Height Change Detection in Antarctica Using Satellite Altimetry Data and Kriging / Kalman Filtering Techniques.

by

An Thanh-Thuy Nguyen

Submitted to the Department of Earth Atmospheric and Planetary Sciences
in partial fulfillment of the requirements for the degree of

Doctor of Philosophy

at the

MASSACHUSETTS INSTITUTE OF TECHNOLOGY

February 2006

Author .....
Department of Earth Atmospheric and Planetary Sciences
Oct 28, 2005

Certified by .....
Thomas A. Herring
Professor of Geophysics
Thesis Supervisor

Accepted by .....
Maria T. Zuber
E.A. Griswold Professor of Geophysics and Planetary Science,
Department Head

Height Change Detection in Antarctica Using Satellite Altimetry Data and Kriging / Kalman Filtering Techniques.

by

An Thanh-Thuy Nguyen

Submitted to the Department of Earth Atmospheric and Planetary Sciences
on Oct 28, 2005, in partial fulfillment of the
requirements for the degree of
Doctor of Philosophy

Abstract

Studies of the response of ice sheets to climate change require data sets with high accuracy and uniform ice-sheet coverage. The most common technique used in analyzing satellite altimetry data to study height change in the ice sheets is the dH/dt technique based on the cross-over geometry. In this thesis two alternative techniques to cross-overs are studied and applied to all ERS radar and ICESat laser altimetry data to study height change in Antarctica. The first technique, block kriging, uses all available data to build a statistical model of the elevation field. Results of height rate of changes dh/dt in Antarctica for the years 1995-2001 produced using block kriging and cross-over analysis are compared. In the Amery Ice Shelf and in the West Antarctic coastal area and near latitude -81°N, the difference in dh/dt between the two methods are statistically significant. A second technique combines kriging and Kalman filtering to allow for time evolutions of the height change rate and other parameters used in the description of the surface elevation field. An application of the technique to laser altimetry data from the current NASA's ICESat mission shows the potential of the technique in detecting height change. In addition, the method can potentially characterize surface elevation in Antarctica at small horizontal scales of the order of the laser footprint size. The quality of laser altimetry data at the present is not sufficient for height change detection at the accuracy level of 2cm/yr required for studying mass balance in Antarctica.

Thesis Supervisor: Thomas A. Herring
Title: Professor of Geophysics

Acknowledgments

My greatest respect and gratitude to Tom Herring my advisor for passing on his wealth of knowledge, for his guidance, patience, and always being available to answer all my questions. I thank my thesis committee members, especially Dr. Zuber for her constructive comments and Dr. Zwally for making his cross-over analysis results available for the comparison between the techniques in this thesis. I also thank Terri Macloon who helped taken care of all the administrative-related issues, Simon McClusky and Linda Meinke for maintaining the computers running, and Eric Hetland for all the great discussions and his help through the years.

Many thanks to my younger sister Linh Nguyen and older sister Chau Nguyen who have helped keeping me sane through all the good and bad times, and for the occasional cargos of food delivered in person or by mails. I would like to also thank my family for their support through the years, and all my friends near and far who have given me a wonderful experience at MIT and are always ready to lend a hand when I need help. Lastly, I'd like to thank my best friend Bao-Chi Nguyen for her great companionship and superb cooking.

Contents

1 Introduction **27**

1.1 Sea level rise 28

1.2 The world's main ice sheets 29

1.3 Ice sheet mass balance 33

1.3.1 Antarctica mass balance 35

1.3.2 Greenland Mass Balance 39

1.3.3 Summary 41

1.4 Satellite altimetry to study the ocean and ice sheets 42

2 Kriging **45**

2.1 Introduction 45

2.2 Ordinary Neighborhood Kriging 46

2.3 Block Kriging using Neighborhood Search 48

2.4 Covariance - Semi-variogram model 52

2.5 Kriging Size Determination 58

3 Kriging Analysis of ERS Data **61**

3.1 Introduction 61

3.2 ERS data 63

3.2.1 Data Corrections 63

3.2.2 Time Step Set Up 66

3.2.3 Block Set Up 67

3.2.4 Anisotropic Variograms 68

3.2.5 Block uncertainties 72
3.2.6 Surface Backscatter Power Correction 75
3.3 Block Kriging Results and Discussion 77
3.3.1 Dh/dt 80
3.3.2 Seasonal Signal 82
3.4 Kriging versus cross-over analysis 88
3.4.1 dh/dt 89
3.4.2 Seasonal signal 97
3.5 Kriging versus Averaging 103
3.6 Conclusion 107

4 The Geoscience Laser Altimeter System 111
4.1 Introduction 111
4.2 The Geoscience Laser Altimeter System (GLAS) 114
4.2.1 ICESat Mission Overview 114
4.2.2 Instrument Description 114
4.2.3 Waveform Analysis 116
4.2.4 Altimetry Precision 119
4.2.5 On-orbit performance 122
4.3 Summary 126

5 Analysis of ICESat Data using Kalman Filter and Kriging to Study Height Changes in East Antarctica 129
5.1 Introduction 129
5.2 Method 130
5.2.1 5-km DEM model 132
5.3 ICESat Data 137
5.4 Results and Discussion 143
5.4.1 5-km DEM 143
5.4.2 dh/dt 149
5.4.3 Seasonal Signals 150

5.4.4 Δ_{DEM} convergence 153
5.4.5 Iterated height residuals 154
5.5 Error assessment 159
5.6 Conclusion 162

6 Conclusion **163**

A Time series for ERS data **165**
A.1 Figure Caption 165

List of Figures

1-1 Sea level change over the last 17000 years. Figure is taken from ICESat Mission Brochure [*http://icesat.gfsc.nasa.gov/ICESat_Brochure.pdf*] referenced to data taken from Fairbanks [1989]. The current sea-level change is approximately $2cm$/decade. 30

1-2 Satellite image of the Antarctic continent showing locations of the Transantarctic Mountains separating East and West Antarctica, the ice-shelves and seas overlaid with a summary of surface roughness, slope, snow accumulation and topography distribution. Original mosaic AVHRR background image at resolution 4km/pixel was obtained from http://TerraWeb.wr.usgs.gov/TRS/projects/Antarctica/AVHRR.html. 31

1-3 Surface bedrock map **(a)** and ice thickness **(b)** in Antarctica. Figures are taken from the Antarctic Environmental Data Center at [*http://www.antarctica.ac.uk/aedc/bedmap/*]. The black line in **(a)** shows location of the grounding line–where bedrock elevation is at sea-level. 32

1-4 Maps of Greenland (a) surface heights, (b) bedrock heights, and (c) ice thickness. (a) and (c) are calculated from radar altimetry and ice-penetrating radar data sets, and (b) is obtained by subtracting (c) from (a) [Bamber et al., 2001a,b]. Data for these figures are available at the National Snow and Ice Data Center [http://nsidc.org/data/docs/daac/nsidc0092_greenland_ice_thickness.gd.html]. . . 34

1-5 Net surface mass balance in Antarctica ($kgm^{-2}yr^{-1}$) based on a compilation of *in situ* and radar satellite measurements done by Vaughan et al. [1999]. Figure is taken from the same reference. 34

1-6 Asymmetric inter-annual change in snow surface elevation associated with firn densification/compaction for Greenland from 1992-1999. Figure is taken from Zwally and Jun [2002]. 37

1-7 Bottom melting at the grounding line due to ocean circulation, which could cause up to 33% of mass loss in the Ice-Shelf. Figure is taken from Jacobs et al. [1992]. 37

1-8 Different accumulation zones in Greenland due to topographic barriers. Figure is taken from Ohmura and Reeh [1991]. 40

1-9 Predicted snow accumulation based on satellite backscatter data. Different symbols correspond to *in-situ* measurement sites. Figure is taken from Drinkwater et al. [2001]. 40

1-10 Elevation rate of change in Greenland for 1994-1999 based on aircraft laser altimetry. Linear features indicate flight tracks. Figure is taken from Krabill et al. [2000]. 41

1-11 Greenland mass balance for 1993-1997 based on GPS measurements of ice discharge. The pattern of elevation rate of change (in mm/yr) is bimodal with very high rates in the Southern tip. Figure is taken from Thomas et al. [2000a]. 41

2-1 Neighborhood for ordinary kriging (a) versus block kriging (b-c). In ordinary kriging (a), the estimate at location indicated by the arrow will be a weighted average of all points in the surrounding area, chosen by certain criteria. In contrast, in block kriging one is interested in the average of a spatial block with area A instead of a single point. As an example, here the block of area A in (b) is divided into 25 sub-blocks prior to calculations of the point-to-block covariance Cv(h) between block A and point B 0.3 miles away, and the block covariance CV (c). The number in each sub-block in (b) is the covariance between its center and point B based on the model $C_{ij}(h) = exp(-h/0.8)$. The number in each sub-block in (c) is the covariance between centers of the dotted and all other sub-blocks, and the number below each large square is the point-to-block covariance Cv between the dotted sub-block and the entire block. By averaging 25 of these point-to-block covariances, we obtain the block covariance CV of 0.855. The example and figures are taken from Olea [1999]. 48

2-2 (a) Variogram models from Table 2.1, with all parameters set to 1. Two sample random fields, one continuous (b) and one discontinuous (c) which corresponds to flat slope in the gaussian variogram (b) and steep slope in the power variogram (c). Continuous here refers to the random field being differentiable at the shot-to-shot scale. Figures are taken from Olea [1999] and Kitanidis [1997]. 54

2-3 (a) One example of raw and modeled semi-variograms for radar altimetry data over the interior flat part of East Antarctica, and relative distance (b) and surface heights (c) of the 200 closest points to the grid point (red square). In (a), the second power model is nested, with two sets of parameters for distance $\leq 0.07^o$ and $> 0.07^o$. 55

2-4 The point covariance C_{ij} (a) and inverse C_{ij}^{-1} (b). In (a), the first subplot (i) shows the separation distance in km between the 200 points used. In (b), the first subplot (i) shows the singular value decomposition values for the following three C_{ij}^{-1}. The gaussian model has the highest ratio of first/last SVD values, and its C_{ij}^{-1} is highly unstable. 56

2-5 (a) The terms in the point-to-block covariance B-vector (Eqn 2.20), and the kriging weights for the three models (b)-(d). In each subplot (b)-(d), the estimated value at the grid point (Figure 2-3a), is shown. The mean of the 200 heights is 0.189m. The weights for the gaussian model (b) are unreasonable so this model is discarded. 57

2-6 Fine tuning process using Q_1 (a), Q_2 (b), and cR (c) tests. The criteria are $Q_1 \approx 0$, $Q_2 \approx 1$, and minimum cR. The solutions are not unique. Based on the raw variogram (Figure 2-3a), a value of α between 250-300 is consistent with the slope of $\gamma(h)$ at short distance. This yields β in the range [0.93,0.97]. (d) The solution using $[\alpha, \beta]$ of [250,0.934] gives [q1,q2,cR] of [-0.0075,0.984,2.21], and the distribution of the residuals ϵ is symmetric with mean and standard deviation of -0.008 and 0.995. 57

2-7 (a) Locations of the grid points (red *) relative to the locations of 500 data points used in the neighborhood analysis. The neighborhood of 10 closest points (N=10) results in discontinuities in both data coverage (b) and $\hat{v}$ (c) and the kriging standard error σ (d). In (b) the 10 points in blue makes the neighborhood of the green grid point, and the 10 black points comprise the neighborhood of the magenta grid point. In (c) the discontinuity in $\hat{v}$ can be seen most clearly for grid points between 114.6^o and 115^o and $N < 300$. 59

2-8 Differences in $\hat{v}$ (a) and σ (b) in log scale as a function of neighborhood size N. Color scale from blue to red corresponding to the Western-most to Eastern-most grid points in Figure 2-7a. $\delta\hat{v} = \hat{v}_{N-1} - \hat{v}_N$ and $\delta\sigma = \sigma_{N+1} - \sigma_N$. Units of $\delta\hat{v}$ and $\delta\sigma$ are in meters. $\delta\hat{v}$ reaches below ~0.05m and $\delta\sigma$ stabilizes at $N \approx 350$ with the exception of two grid points. 59

3-1 A pictorial description of the "dH/dt" method developed by Zwally et al. [1989] to analyze space-borne altimeter data to study height changes. (a) The data are binned into N blocks, each with approximately M number of cross-overs that are (1) within a 100-km diameter search area of the grid center, (2) within ±250m of an a-priori DEM, and (3) within a time interval, 90-day in the case for ERS data (b) [Zwally et al., 2002; Zwally, 2005]. 62

3-2 Height change rate results using cross-over analyses in Antarctica from Wingham et al. [1998] (a) and West Antarctica (b) from Zwally et al. [2002] showing thinning in the Pine Island / Thwaites Glaciers of up to -0.30m/yr (a-b) and thickening at [lon,lat] of [120W,-82N] of up to 0.20m/yr (b). 63

3-3 Definition of footprints and returned waveform parameters (a), slope induced errors and correction (b) and retracking correction (c) for satellite radar altimetry. In (b) α is the surface slope, H the satellite altitude, H_m the range to the nearest point P on the surface, and ΔH the error induced by α in height measurement. In (c), two examples of actual sea (i) and ice (ii) surface returns from SEASAT-1 radar altimetry system showing correction ΔR to the data. Figures are taken from Zwally and Brenner [2001], Brenner et al. [1983], and Martin et al. [1983]. 65

3-4 (a) Locations of four regions RI-RIV and basins AA-MM used in this study and (b) the regions' variograms. In brackets in (b) are parameters $[\alpha_1, \beta_1]$ used in fitting $\gamma(h) = \alpha_i h_i^{\beta_i}$ for each region. Parameters set $[\alpha_1, \beta_1]$ and $[\alpha_2, \beta_2]$ are used for distances [0,0.08^o] and [0.08^o,1^o] respectively. 69

3-5 Neighborhood determination (a-b) for one block and grid set up for region IV (c). Sub-figures a-b are similar to Figure 2-8 from Chapter 2, and δv_{est} level of approximately $10^{-1.3}$ or 5cm (horizontal dashed line in (a)) is used to determine the block size. In this particular example at latitude $\sim -80^o$, a neighborhood N≈430 is sufficient. However at lower absolute latitude, N≈500. (c) The sub blocks have $\Delta lat = 0.25^o$ and $\Delta lon = [2^o, 1^o]$ for latitude ranges [-65^o,-72.5^o] and [-72.5^o,-82.5^o] (grey dots). In the final results, blocks are averaged to approximately $(100km)^2$ (cyan squares) with centers shown as red stars. There is a total of 2340 blocks in the region. The coast line is shown in green. 70

3-6 Azimuthal variations of $[\alpha_1, \beta_1]$. Both α_1 and β_1 (a-b) do not exhibit azimuthal dependence, with larger variations within each azimuth than between azimuths. The magenta, green, red, and cyan colors correspond to regions RI to RIV respectively. 71

3-7 Scatter plots of α versus β as a function of azimuths (a) and the time the data were collected (b). There is no apparent drift in the data as a function of time. The parameters used in this study prior to fine-tuning are those of the isotropic case, shown as the black triangles here for R-III. See Table 3.4 for $[\alpha, \beta]$ in the other three regions. 71

3-8 500 closest points for the block centered at [119.5^{o}E,-74.4^{o}N] (red square) for the time steps 06, 31, and 35 (out of 58 time steps). 72

3-9 Scatter plot of correlation coefficient r and slope of the best fitted line between surface height (H) and received power (AGC). When $|r| < 0.2$ there will be no correction to H(t). When the slope $dH/dAGC < -0.2$ and $dH/dAGC > 0.7$, they are reset back to -0.2 and 0.7 to prevent anomalously large corrections. 76

3-10 Data coverage for three $\sim (100km)^2$ blocks in region IV with each sub-block and corresponding 500 nearest points coded in matched color. In (a), some of the sub-blocks are beyond the ERS coverage area, and their block-kriged results will have very large uncertainties. At the edge of the ice-sheet in (c), data quality deteriorates resulting in insufficient coverage and large block-kriged uncertainties. 77

3-11 (a) Uncertainties in the block height estimates from block-kriging for R-IV time step #01 and (b) H(t) time series for one of the blocks. As discussed in the previous figure, uncertainties are very large at the edge of the ice-sheet and at near latitude -82^o. In the time series, H(t=42) and H(t=84) consistently have heights deviating from other points in the time series, and are excluded from the weighted linear least square fit. Time-step #39 consistently has anomalously large uncertainties. In (b), the label on top of the sub-figure indicates the block number, longitude, and latitude of the block. 78

3-12 Estimated dh/dt (a) and uncertainties (b) with surface slope shown as the background field, and drainage divides shown as black lines. (a) 96% of the blocks in E-Ant have dh/dt less than 0.1m/yr in magnitude with positive mean of 0.03m/yr and RMS 0.03m/yr, and 75% have dh/dt less than 0.05m/yr in magnitude with mean of 0.02m/yr and RMS 0.02m/yr. Large dh/dt magnitudes at the Amery Ice Shelf ([lon,lat] $\approx [70^oE, 80^oE, -76^oN, -72^oN]$) range from -0.05m/yr to 0.26m/yr. In W-Ant 90% of the blocks have dh/dt less than 0.20m/yr in magnitude, and 68% with dh/dt less than 0.10m/yr in magnitude. These blocks lie in the interior of West Antarctica. 79

3-13 Time series for two blocks at the Amery Ice Shelf (a-b) and along the coast in W-Ant (c-d). These blocks have large positive and negative dh/dt that exceeds the mean $\pm$ 2·RMS in each of the corresponding regions. The label on top of each subplot indicates the block number, longitude, latitude, dh/dt and $\sigma_{dh/dt}$ values. . 81

3-14 Statistics of dh/dt for E-Ant (blue) and W-Ant (red) (a), and latitudinal dependence of dh/dt (b). Shown in the brackets in (a) are the mean and RMS scatter for E-Ant (E) and W-Ant (W). There is no clear pattern of dh/dt with latitudes (b). 81

3-15 Seasonal signal amplitude B (a) and uncertainties (b). 83% of the blocks (183/221) have seasonal surface signal amplitude less than 0.15m and 96% of those (176) have uncertainties less than 0.03m. Similar to dh/dt, the concentration of high amplitude is at the Amery Ice Shelf, reaching as high as 0.75m. In West Antarctica, 72% of the blocks have B less than 0.30m. Along the edge of the ice-sheet, the amplitude reaches 1.25m. 84

3-16 Seasonal phase θ maximum (a) and uncertainties (b). θ shows a very strong correlation with the drainage divides in East Antarctica. Along the drainage divides, $\theta \approx 420 - 450(55 - 85)$ days implying surface height maximum at the end of Feb to March. Away from the divides, $\theta \approx 135 - 200$ days yielding surface maxima toward mid-May to mid-Aug. In West Antarctica, most of the interior has $\theta \approx 135 - 225$ days, yielding surface maxima at mid-May to Sept. 85

3-17 Time series for one block in W-Ant with large seasonal signal amplitude of 1.25m. The label at the top of the figure indicates the surface number, longitude, latitude, dh/dt estimate and $\sigma_{dh/dt}$. 86

3-18 Statistics of amplitude B (a) and phase θ maximum (c) for E-Ant (blue) and W-Ant (red), and latitudinal dependencies of B (b) and θ (d). Shown in the brackets in (a) and (c) are mean and RMS scatter for each respective parameter. The bimodal phase maximum in (c) corresponds to end of Feb ($\theta \approx 421$ day) and mid-June ($\theta \approx 160$ day). There is evidence of B increasing southward in both E-Ant and W-Ant. However the RMS scatter for both regions is too large to support this observation. 86

3-19 Relationship between phase maxima and locations of the drainage divides. Statistics in (b) are for blocks along the drainage divides (red squares in (a)), and statistics in (c) are for the blue star blocks in (a). 87

3-20 Zwally [2005]'s unpublished ERS cross-over analysis results for dh/dt. 88

3-21 Profiles of cross-over dh/dt (left panel), kriging dh/dt (middle panel), and $\delta dh/dt$ (right panel) for regions R-I (a), R-II (b), R-III (c, next page), and R-IV(d, next page). $\delta dh/dt$ is the difference between kriging and cross-over results. The six profiles chosen for further analysis are numbered [1] through [6] and identified with the red label of latitude. 91

3-22 Inter-satellite biases for four blocks near the coast in W-Ant (a-d), and potential errors in dh/dt as a result of these biases (e). Across two of these blocks (blocks #39 and #40) the cross-over method yields large negative dh/dt rates, whereas kriging using only ERS-2 data yields near zero to positive dh/dt. The dashed red line in (a-d) separates ERS-1 from ERS-2 data. In (e) dh/dt_{true} is the input rate, dh/dt_{bias} is the pseudo dh/dt due to the inter-satellite bias, and dh/dt_{total} is what the model would predict if the bias is not removed from the data. 95

3-23 Statistics of $\delta dh/dt$ (kriging minus cross-over) for the four regions, which shows a systematic positive difference. The numbers in the brackets are the mean and RMS of $\delta dh/dt$ for each corresponding region. 96

3-24 Zwally [2005]'s unpublished ERS cross-over analysis results for seasonal signal amplitude (a) and phase minimum (b). 99

3-25 Profiles of cross-over B (left panel), kriging B (middle panel), and δB (right panel) for regions R-I (a), R-II (b), R-III (c, next page), and R-IV(d, next page). δB is the difference between kriging and cross-over results. 100

3-26 Statistics of δB (kriging minus cross-over) for the four regions, which show systematic positive difference. Numbers in the brackets are the mean and RMS of δB for the corresponding region. 102

3-27 Profiles of dh/dt estimated using block averaging (left panel), kriging dh/dt (middle panel), and their difference (right panel, kriging minus averaging) for regions R-II (a) and R-IV (b). The six profiles chosen for further analysis are numbered [1] through [6] and identified with the red label of latitude. Profiles [2]-[6] are the same as those used in the comparison of cross-over and kriging results. 104

3-28 Time series of two blocks (i) and (ii) at the Amery Ice Shelf estimated using kriging (a) and averaging (b). On each subplot, the label indicates the block number, longitude, latitude, dh/dt and $\sigma_{dh/dt}$. The blue curve shows the block height estimates using either kriging or averaging, and the green line shows the fitted model using weighted linear least square inversion. 105

3-29 Difference in dh/dt estimates for $(100km)^2$ block #66 in W-Ant between block-kriging (Bk) and block-averaging (Ba) using a 500-point neighborhood. (a) Time series for Bk (blue), Ba (red), and Bk excluding time step with large uncertainties (green). (b) Height residuals distribution for the 500 points in the original $(27km)^2$ block. The point-kriging and block-kriging solutions are 12.8m and 11.4m, as opposed to block-averaging solution of 3.9m. 106

3-30 Statistics of the difference in dh/dt between kriging and averaging for R-I through R-IV. The large negative and positive difference in R-II is at the Amery Ice Shelf, where the difference between the two methods diverges. 106

4-1 Relative sizes and accuracy levels of radar and laser altimetry. Figure is taken from Bufton [1989]. 112

4-2 The Earth Observing System (EOS) plan in 1995 to study the Earth. Figure is taken from EOS [1995]. 113

4-3 Zenith and nadir views of ICESat. Figure is taken from Schutz et al. [2005]. . . . 115

4-4 Views of the transmitting (a), receiving (b) components of GLAS, and a generic block diagram (c) illustrating the general concept of transmitting and receiving. Figures are taken from Abshire et al. [2005] and Bufton et al. [1982] with annotation added. For GLAS, the output energy includes the 1064nm and 532nm channels, where the latter originates from 1064nm but passes through a crystal doubler (to double the wavelength). 116

4-5 Concept of laser altimetry with off-nadir pointing angle ϕ and surface slope S. R is the nadir range from the surface to the altimeter, Z is the slant range to the surface, $\Delta\phi$ is interpreted either as the laser divergence angle or the uncertainty in pointing angle [Bufton, 1989]. 118

4-6 Conceptual illustration of range to the surface measurement showing signal strength (P) as a function of time (t) for transmitted pulse of peak strength P_o, energy E_o, duration ΔT_o and received pulse of P_R, E_R. T_s is the mean round-trip time-of-flight. (Figure is taken from Harding et al. [1994]). 118

4-7 Modeling of the returned waveform (Figure is taken from Zwally et al. [2002]). W indicates the returned pulse or modeled waveform, M waveform mid-point, A waveform amplitude, σ standard deviation of the modeled Gaussian waveform, and subscripts R refers to received pulse, M refers to the Gaussian model waveform. . 119

4-8 Stellar Reference System. **(a)** A fraction of the laser beam is redirected into the Laser Reference Camera, along with the orientation of the star tracker to determine pointing orientation. **(b)** Layouts of image frames from the star tracker to the Laser Profiling Array illustrate how pointing orientation with respect to the star tracker is measured. (Figure is taken from Bae and Schutz [2002]). 120

4-9 Field of view of ICESat receiver telescope (a) and location of Laser 2 beam within the field of view (b) [Abshire et al., 2005]. (a) The power response of the field of view is flat max in the center and falls off exponentially beyond approximately 41 arcsec. The horizontal color bar shows the laser footprint should be within the 20 arcsec of the FOV for height measurements to bias free. Within 20 to 41 arcsec, the laser return energy is clipped (as shown by the laser beam offsetting at +41 arcsec) and height bias has to be corrected for. Beyond 41 arcsec where the FOV response has attenuated to 50%, signal is considered lost. 124

4-10 Geometry of satellite showing height bias due to pointing (a), ocean scan maneuver used to removed pointing bias (b), and ICESat pointing bias (c) which are both time and temperature dependent. In (a), $\delta\alpha$ is the off-nadir pointing, and $\Delta\delta\alpha$ the pointing error. In (c) biases are shown for only the X-axis of the spacecraft, and the top panel shows biases from ocean scans at orbit midnight (blue) and orbit noon (red), and the bottom panel shows bias estimates (red) from a round-the-world-scan (an equivalent of an ocean scan over a full orbit) and a functional fit (blue). The figures are taken from Lisano and Schutz [2001], Luthcke et al. [2005] and a presentation by Scott Luthcke at an ICESat team meeting. 127

5-1 Three regions of study (a) with a sample $(100km)^2$ block DEM centered at [-75.5°,122.5°] (b). Each circle in (a) represents a $(100km)^2$ block. There are 287 blocks, with each having approximately between 600 and 850 5-km pixels (shown as circles with elevation in (b) and 12 to 125 GLA06 tracks within each 33-day cycle (500 to 8000 data points). 135

5-2 Semi-variograms (γ) of height residuals for the three regions shown in Figure 5-1a, along with a raw semi-variogram for region III (x). $\gamma(0)$ corresponds to 1-cov(0). Region III is smoothest (sill $\approx 12m^2$), and region II roughest (sill $\approx 18m^2$). Region I is close to III in characteristics. See Table 5.1 for a complete list of all parameters and Table 5.2 for the numerical values of both the sill σ^2 and variogram γ. The behavior of γ at foot-print spacings is shown in the inset. 136

5-3 Estimates of pointing bias for ICESat height over Antarctica based on differential slopes at cross-overs. The number of cross-overs are consistent for all 33-day operational periods Laser 2a-3b **(a)**. As a function of differential slopes between the two tracks, ascending minus descending, cross-over residual mean increases away from zero $\Delta slope$ indicating the existence of pointing biases **(b)**. The best fitted slope through the means suggests pointing biases for Laser 2a-2c and 3a of 4, 0.96, 3.4, 20, 1.76 arc-sec. The deviation from the mean (STD) is similar for all lasers **(c)**, with Laser 3b having the largest STD at zero-slope of approximately $35cm$ compared to $\leq 30cm$ for Lasers 2a-3a. 138

5-4 Laser 1 cycles 02, 03, 04 saturation statistics. Only shots with returned energy between 1-30fJ are used. In the legend, G is an abbreviation for gain. For cycle 02-03, approximately 42-81% of data have gain < 13 because no lower limit in gain was set. Because only saturation correction for gain $= 13$ is available at this time, shots with gain < 13 are discarded. As the laser strength decreases with time, the received energy decreases from $\sim$ 17fJ on average in cycle 02 to $\sim$ 15fJ in cycle 04. 140

5-5 Laser 2 8-day cycle 28 and 33-day period 2a. At the beginning of 2a, the majority of shots were saturated (gain $= 13$), but with smaller energy ($\sim 15 - 16$fJ than those at the start of Laser 1. With the minimum gain set at 13, more shots become valid. 141

5-6 Laser 2 33-day period 2b and Laser 3 33-day period 3a. The laser strength clearly decreases in period 2b, and becomes significantly lower in Laser 2c (not shown here), which resulted in very high noise and pointing bias in the latter campaign. In all three lasers, Laser 3 is strongest, with energy at the beginning of campaign 3a in the range of 25fJ, highly saturated. Based on the saturated energy and the ratio -2.2cm/fJ, the potential height bias would be approximately -6cm and -24cm for Laser 2a and 3a, resulting in a potential negative dh/dt bias. 142

5-7 Time series of one $(100\text{km})^2$ block at the end of Laser 3a. The first column shows results for dh/dt, Δ_{DEM}, B_1, and B_2 terms, and the second column shows their corresponding standard deviations. Red-x's mark the end of either the 8-day or 33-day campaigns. Unit along the x-axis is in year, referenced to Jan-2003. The inset in the last subplot shows the location of the sample block, with longitudes and latitudes along the x-axis and y-axis respectively. 144

5-8 (a) Dh/dt and (b) uncertainties from the Kalman filter. All blocks in E-Ant has dh/dt between -0.21 to 0.13m/yr $\pm 0.03 m/yr$. Within region LB, dh/dt are more positive and varies in a wider range between -0.28 to 0.37 ± 0.3m/yr. The parameter dh/dt appears to be banded with negative mean between latitude [-81°,-73°], and zero mean north of $-73°$ and south of $-81°$. 145

5-9 Seasonal signal amplitude B (a) and uncertainties (b) from the Kalman filter. B varies between 0.01 and 0.59 ± 0.07m in E-Ant and 0.03 to 0.98 ± 0.07m in LB. The comparison shows that the amplitudes obtained here are at least one order of magnitude higher than those predicted from climate and firn compaction models or inferred from *in-situ* measurements. 146

5-10 Seasonal signal phase maxima (a) and uncertainties (b). θ appears to be banded (similar to dh/dt), with high phase of $\sim$ 90-150 days (Apr - Jul) between latitude [-81°,-73°] and low phase of $\sim$ 0-65 days (Jan - Mar) north of $-73°$ and south of $-81°$. 147

5-11 Block adjustment Δ_{DEM} after 2 iterations (a), after 3 to 24 iterations (b), and uncertainties (c). Within region II (Figure 5-1a), Δ_{DEM} are within -0.25 and 0.25m after only two iterations (a). For region I and III, Δ_{DEM} ranges between -4 to 4m after two iterations. Convergence to within [-0.25,0.25]m in region I and III requires between 6 and 24 iterations (b). Uncertainties are highest near the coast, but low for the whole region II. 148

5-12 Histogram of *dh/dt* (a), B (b), θ (c), and Δ_{DEM} (d). There is a total of 259 100×100km blocks in East Antarctica, with 52 in LB (red) and 207 outside (blue). In brackets are the mean and root-mean-square scatter of each parameter. The inset in subplot **(c)** shows the mean seasonal signal based on climate models (red, Turner et al. [1999]) and scaled seasonal temperature (dashed blue). The temperature profile is scaled to only illustrate the seasonal maximum and minimum locations. 151

5-13 Latitudinal dependency of *dh/dt* (a), B (b), θ (c), and Δ_{DEM} (d) for E-Ant (blue) and LB (red). Each closed circle represents an average of all 100×100km blocks across all longitudes for each 1° latitudinal bin, and the size of of the circle represents the number of blocks N in each bin, with the scale provided for $N = 18$. (a) *dh/dt* is negative in most of E-Ant except north of -73° latitude. In LB, *dh/dt* has positive mean but with large scatter that cover 0.0m/yr rates. Some of the correlations between these estimated parameters with latitudes could be due to pointing bias. 152

5-14 ICESat heights and residuals. (a) Original ICESat height profile from Laser 3a (green) and the interpolated DEM (black). The inset shows the DEM estimates the trend but misses the shorter wavelength details. (b) Height residuals for the profile in (a), along with two additional profiles corresponding to Laser 2a (blue), 2b (red). The inset shows the residuals before (solid line) and after (dot-line) saturation corrections. (c) Residuals after two iterations through the Kalman filter. The inset shows the difference between the repeat tracks for the three laser periods. 157

5-15 Height residuals after two iterations and their PSDs. (a) Residuals along a profile which shows the dominant 5-km wavelength oscillations with magnitude near $\pm 2m$. (b) Residuals along a different profile showing much smaller amplitudes. The shot-to-shot variations and the spatially-correlated behavior can be seen here. (c) Power spectral densities (PSD) for the two profiles above (blue for (a), red for (b)) and a potential fit using a second order Gauss-Markov PSD functional form. 158

5-16 Dh/dt_{bias} assuming a pointing bias of **10 arcsec** and surface slopes up to 0.4° for the cases when pointing bias vector is **(a)** $\perp$ to elevation contours, and **(b)** $\parallel$ to elevation contours. In case **(a)**, dh/dt_{bias} is nearly $1m/yr$: 1° slope at latitude $-86°$ and decreases away from the South Pole. In case **(b)**,dh/dt_{bias} is half of that in case **(a)**. Here the maximum error occurs when cross-over separation angle is 90°, or latitude $-84.3°$. 160

5-17 Dh/dt estimates in region III using (a) ascending only tracks, (b) descending only tracks, and (c) ascending minus descending results. Dh/dt ranges between [-0.12,0.27]m/yr in (a) and [-0.22,0.06]m/yr in (b), and the mean and RMS of their differences are 0.09 and 0.08m/yr. 161

List of Tables

1.1 Glaciers and ice sheets [Church et al., 2001] 29

1.2 Mass Balance in Antarctica (10^{12} kg/yr = 1 Gt/yr) 38

1.3 Mass Balance in Greenland (10^{12} kg/yr = 1 Gt/yr) 42

1.4 Past and present satellite altimetry missions 44

2.1 Most commonly used variograms 53

3.1 Possible Errors in Radar Altimetry over the Ice Sheets 64

3.2 Regions of study 67

3.3 Block Size 67

3.4 Fine tuning of variogram parameters β 67

3.5 ERS Data 109

4.1 Comparison between GLAS, MOLA, and ERS instruments 117

4.2 Single Shot Vertical Error Budget 121

5.1 Regions of study 135

5.2 Semivariograms values $\gamma(h)$ (m^2) 135

5.3 $(100km)^2$ block set up 136

5.4 ICESat height accuracies and biases 137

5.5 Percentage of valid shots used 139

5.6 DEM conversion test 155

A.1 Block Kriging Results 199

Chapter 1

Introduction

Climate change studies require scientific evidence from a network of atmospheric and oceanic sciences and solid earth geophysics, and involve many disciplines including those from the scientific and engineering communities. This research is motivated by my desire to understand and help preserve our planet. One possible way to assess how the Earth is changing due to global warming is by studying changes in the ice sheets and how ice sheets interact with the ocean and atmosphere. This research focuses on obtaining the best possible method to detect height changes in Antarctica using available satellite altimetry. The thesis will be presented in the following order: Chapter 1 will describe our current knowledge of, and the methods that are used, to study the ice sheets and sea level changes. Chapters 2 and 3 will describe kriging, and optimal interpolator, and its application using satellite radar altimetry from the European Remote Sensing satellites. Chapter 4 will cover satellite missions' instruments designed to study the ice sheets, with a strong emphasis on the Geoscience Laser Altimetry System on-board the Ice, Cloud, and land Elevation Satellite (ICESat) mission. In Chapter 5, a method combining kriging and Kalman filtering will be used to analyze laser altimetry data from ICESat. The connection between ERS1/2 and ICESat results will be discussed in the last chapter, Chapter 6, along with a discussion of future work and conclusions.

1.1 Sea level rise

Since the last Glacial Maximum 20000 years ago, sea level has risen by as much as 120m at rates up to 10mm/yr. Based on geological records the rate slowed down to approximately 0.6mm/yr between $15000 - 6000$ years ago, and 0.2mm/yr in the last 6000 years (Figure 1-1, [Church et al., 2001]). Results from tide gauge measurements over the last century give rates ranging from $+1.5\pm0.5$mm/yr [Church et al., 2001] to $+1.9\pm0.1$mm/yr [Douglas, 1997], and show evidence of faster rates in the 20th century than the 19th century [Church et al., 2001]. Our knowledge of current sea level change from satellite altimetry is +2.1 to 2.5 ± 1.3mm/yr based on results of analyses of TOPEX/POSEIDON (T/P) radar altimetry measurements over the ocean from December 1992 to February 1997 ([Nerem et al., 1997; Nerem and Mitchum, 2001b]). Sea level change detection with an accuracy level of 1mm/yr using satellite altimetry requires accurate orbital determination to within 5cm, and accurate ionospheric and tropospheric delays to the centimeter level [Nerem and Mitchum, 2001b; Zelli, 1999]. T/P operated in dual altimeter frequency enabling calculations of ionospheric delay, and used a microwave radiometer to measure water vapor column for tropospheric corrections. In addition, the GPS tracking system on-board T/P enabled orbit determination to 2-3cm radially. Earlier and concurrent radar satellite missions to T/P including SEASAT (1978), Geosat (1985), and ERS1/2 (1991,1995) could not meet these requirements, with some having large errors in orbit or ionospheric corrections, yielding errors in sea level change rates of 3-5mm/yr [Nerem and Mitchum, 2001b]. Current satellite missions ENVISAT (2002) and JASON-1 (2001) are designed similar to T/P. However these missions are still in the early validation phase and have not collected enough data to construct sea level time series for change rate estimation. As a result, T/P is the most accurate set of data to date for analyzing sea level change with single height measurement and height change rate accuracies of $\sim$2cm and 1.3mm/yr [Nerem and Mitchum, 2001a].

Both satellite and tide gauge results of sea level increase in the last century, 1.8 ± 0.1mm/yr and 2.1 ± 1.3mm/yr, are approximately seven to ten times higher than it

Table 1.1 Glaciers and ice sheets [Church et al., 2001]

	Glaciers	Ice caps	Glaciers and ice caps [a]	Greenland ice sheet [b]	Antarctic ice sheet [b]
Number	>160000	70			
Area (10^6km^2)	0.43	0.24	0.68	1.71	12.37
Volume (10^6km^3)	0.08	0.10	0.18±0.04	2.85	21.71
Sea-level rise equivalent [d]	0.24	0.27	0.50±0.10	7.2 [c]	61.1 [c]
Accumulation (sea-level equivalent, mm/yr) [d]			1.9±0.3	1.4±0.1	5.1±0.2

[a] Including glaciers and ice caps on the margins of Greenland and the Antarctic Peninsula.
[b] Grounded ice only, including glaciers and small ice caps.
[c] calculated with allowance for isostatic rebound and sea water replacing grounded ice.
[d] Assuming an oceanic area of 3.62 x 10^8 km^2.

has been in the past 6000 years, although observations from global tide gauges also suggest no acceleration in sea level rise rate within the last century (Figure 1-1, [Fairbanks, 1989; Douglas, 1997; Church et al., 2001]). Factors contributing to this rise include $\sim$ 0.7 to 1.1mm/yr from thermal expansion over the last several decades, $\sim$ 0.2 to 0.4mm/yr from melting of low-latitude glaciers [Church et al., 2001], and an unknown contribution from the two main ice sheets, Antarctica and Greenland. The unknown contributions are due to our current lack of knowledge in the ice sheets' mass balance. Table 1.1 taken from Church et al. [2001] lists the size of the world's glaciers and ice sheets and their corresponding contributions to sea level rise if completely melted.

1.2 The world's main ice sheets

The Antarctic ice sheet contains 90% of the world's ice and if completely melted would contribute approximately 71m and 61m in sea level increase before and after isostatic rebound is taken into account (assuming volume and area of 25.71 x 10^6 km^3 and 3.62 x 10^8 km^2 for the Antarctic ice sheet and the ocean, [Church et al., 2001]). Here we only consider the melting of ice that rests on bed rock (grounded ice), because a change in sea ice or in the ice shelves does not contribute to sea-level change. Given the area of the Antarctic ice sheet of approximately 12.37 x 10^6 km^2, the ice thickness is approximately 2080m, and a 1m change in ice sheet elevation

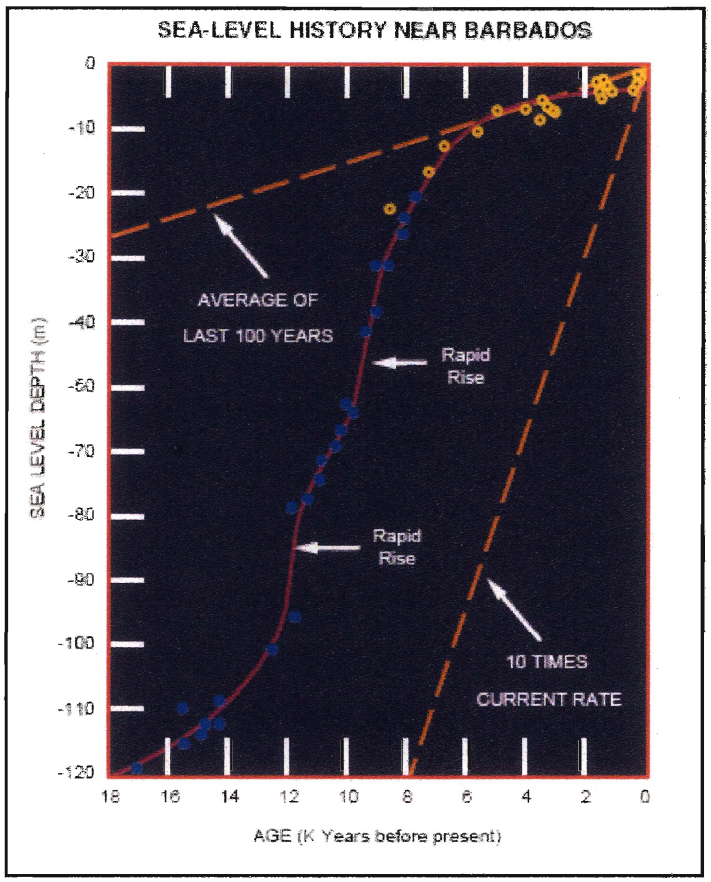

Figure 1-1 Sea level change over the last 17000 years. Figure is taken from ICESat Mission Brochure [*http://icesat.gfsc.nasa.gov/ICESat_Brochure.pdf*] referenced to data taken from Fairbanks [1989]. The current sea-level change is approximately $2cm$/decade.

would result in $\sim$ 3.4cm sea level rise [Church et al., 2001; Fifield, 1987]. Figures 1-2 and 1-3 show the distribution of surface elevation, slopes, and ice thickness in Antarctica. The continent is comprised of two main parts, East and West Antarctica, separated by the Transantarctic Mountains (Figure 1-2). The Eastern part (10.35 x $10^6 km^2$) is mainly terrestrial with maximum elevation of 4000m. Ice slope is low in the interior with gradient $\sim$ 1:1000 and increases toward the coast. The smaller West Antarctic ice sheet comprises of a marine region or inland ice (2 x 10^6 km^2), two large marginal ice shelves (1 x 10^6 km^2), and the mountainous Antarctic Peninsula (0.5 x 10^6 km^2). Elevation in the inland ice reaches 3300m [Brenner et al., 2003]. Over half of Antarctica has slopes $\leq$1:300 and 90% of the area has slopes $\leq$ 3:200. Near the margins where the ice is thin, slopes can get as high has 1:10. Roughness over the ice sheet are of three scales: wind-induced and snow-accumulated features at vertical and

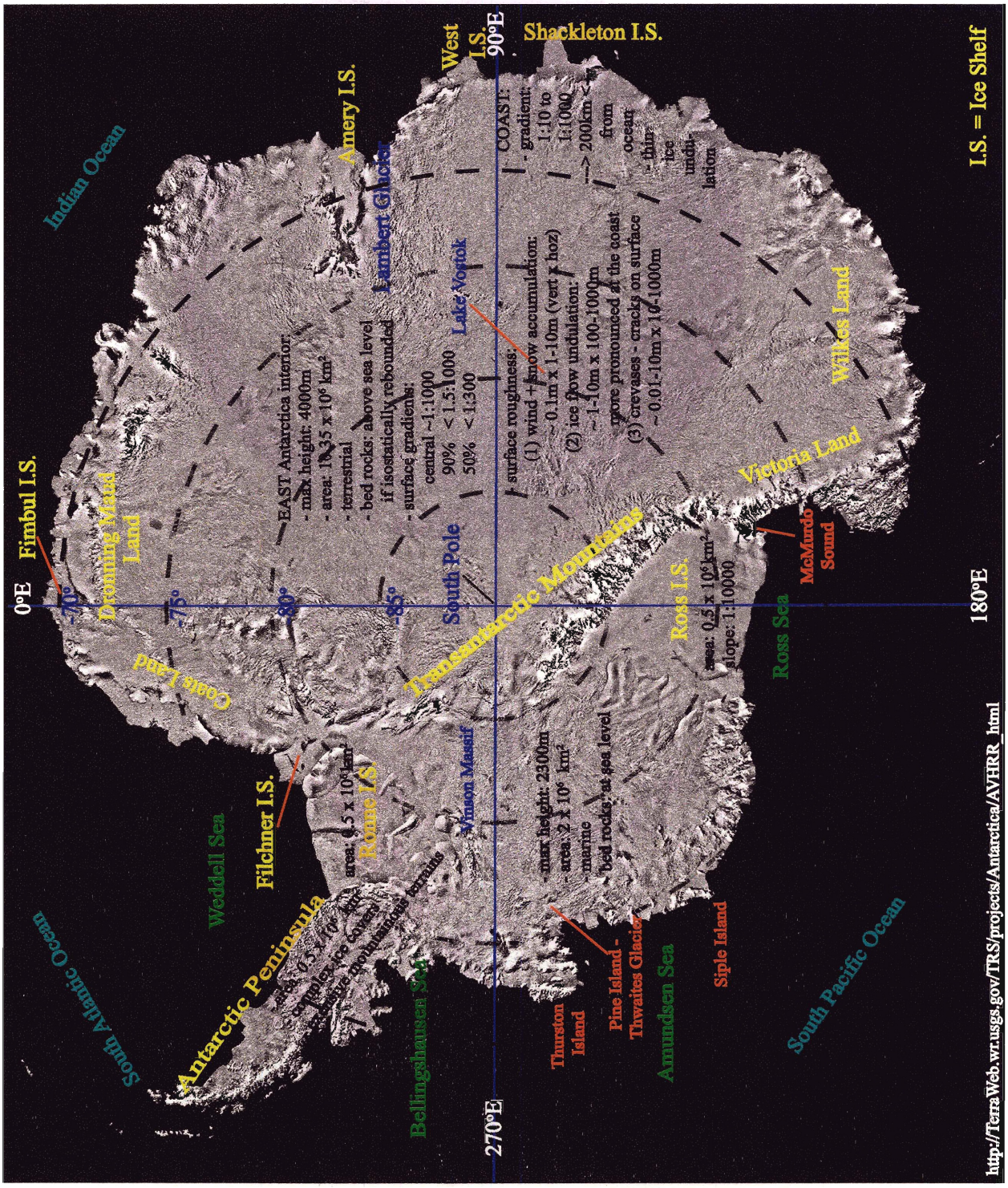

Figure 1-2 Satellite image of the Antarctic continent showing locations of the Transantarctic Mountains separating East and West Antarctica, the ice-shelves and seas overlaid with a summary of surface roughness, slope, snow accumulation and topography distribution. Original mosaic AVHRR background image at resolution 4km/pixel was obtained from http://TerraWeb.wr.usgs.gov/TRS/projects/Antarctica/AVHRR.html.

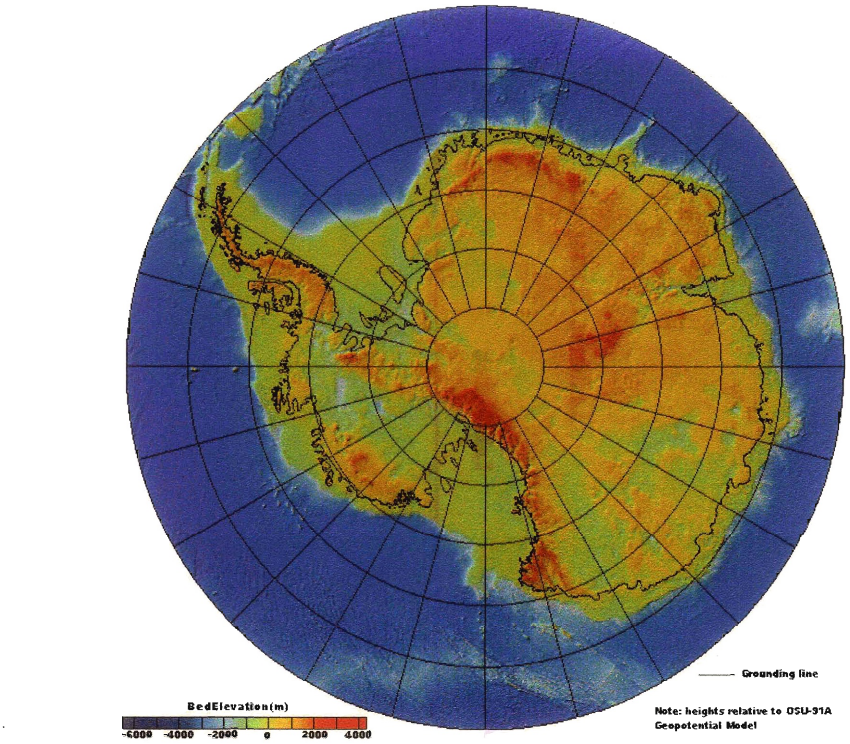

(a)

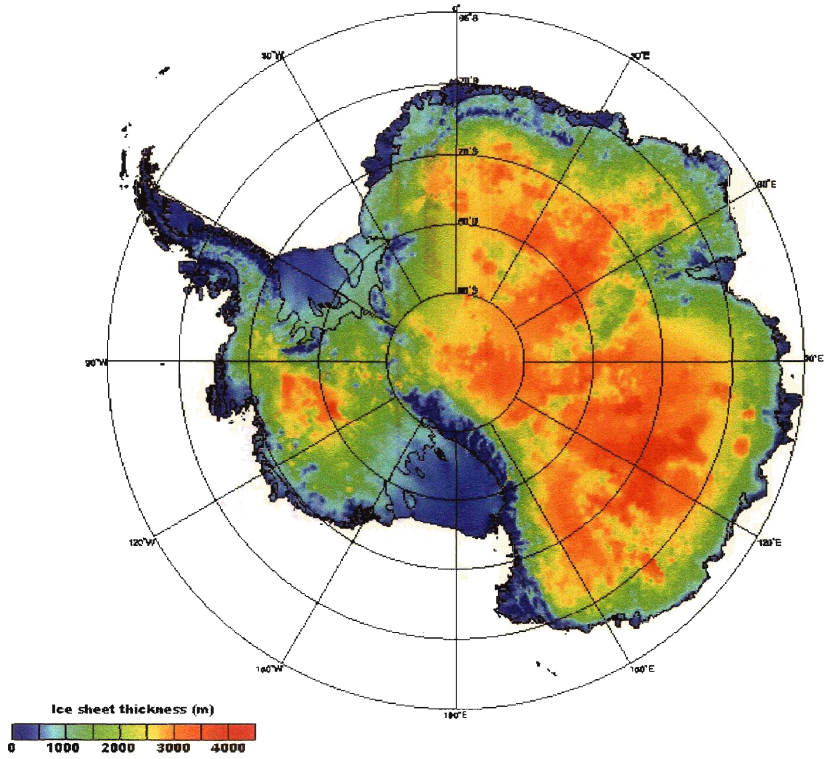

(b)

Figure 1-3 Surface bedrock map **(a)** and ice thickness **(b)** in Antarctica. Figures are taken from the Antarctic Environmental Data Center at [*http://www.antarctica.ac.uk/aedc/bedmap/*]. The black line in **(a)** shows location of the grounding line–where bedrock elevation is at sea-level.

horizontal scales of 0.1-1m and 1-10m; ice flow undulation at 1-10m and 100-1000m; and crevases at 10m and 10-1000m [Brenner et al., 2003].

The Greenland ice sheet is approximately 1/8 the size of Antarctica (1.73 x 10^6 km^2) with elevation reaching 3300m in the interior. Ice flows from the mountainous interior through outlets straight into the ocean. Surface gradients in Greenland are relatively similar in ranges to Antarctica, but with a higher ratio of high sloped margins to low-sloped interior [Brenner et al., 2003]. Similar roughness scales to Antarctica also exist here. Figure 1-4 shows three maps of Greenland surface heights, bedrock heights, and ice thickness at 5-km resolution in polar stereographic projection views. The surface height model is calculated using radar altimetry from the European Remote Sensing Satellite mission [Bamber and Bindschadler, 1997]. The ice thickness map was compiled by Bamber et al. [2001a] using ice penetration radar data. [Bamber et al., 2001b] subtracted ice thickness from surface heights to obtain the bedrock height map.

1.3 Ice sheet mass balance

Each year the Antarctic and Greenland ice sheets exchange $\sim$ 3000$\pm$100 km^3 of water with the ocean, an equivalence of 240 ± 8.1mm ice sheet elevation change or $\sim 8 \pm 2.4mm$ change in sea level [Zwally et al., 1989]. In order to detect a global warming effect on sea level change, we must be able to estimate ice sheet surface height change with an accuracy approximately that of the exchange rate in order to separate out the annual, semi-annual, decadal and post-glacial rebound signals from any overall increasing/decreasing trend. Studies of mass balance in Antarctica have yielded results close to zero change (in balance) or even slightly negative (mass gain) due to an increase in precipitation [Church et al., 2001]. The major factors influencing the calculations of mass balance include *a*) input from snow accumulation, and *b*) output from firn compaction/densification, surface and basal melting, and runoff.

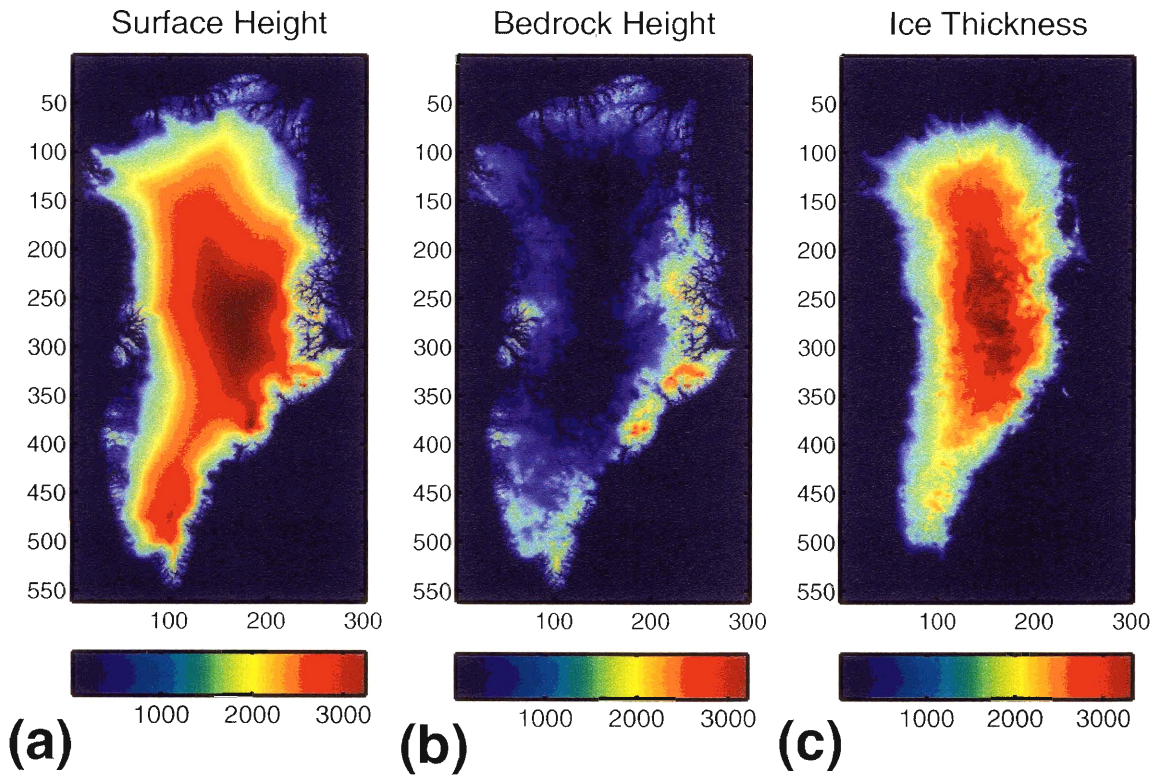

Figure 1-4 Maps of Greenland (a) surface heights, (b) bedrock heights, and (c) ice thickness. (a) and (c) are calculated from radar altimetry and ice-penetrating radar data sets, and (b) is obtained by subtracting (c) from (a) [Bamber et al., 2001a,b]. Data for these figures are available at the National Snow and Ice Data Center [http://nsidc.org/data/docs/daac/nsidc0092_greenland_ice_thickness.gd.html].

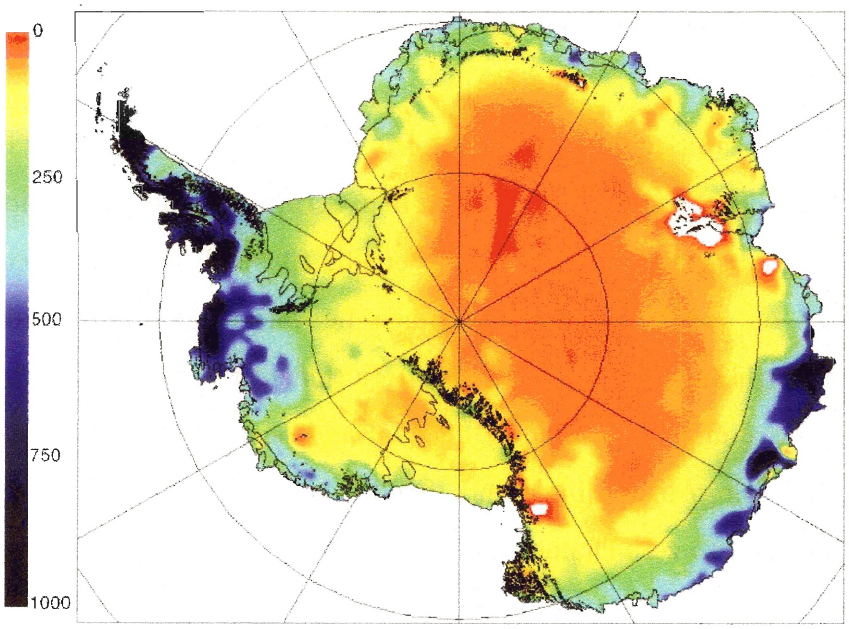

Figure 1-5 Net surface mass balance in Antarctica ($kgm^{-2}yr^{-1}$) based on a compilation of *in situ* and radar satellite measurements done by Vaughan et al. [1999]. Figure is taken from the same reference.

1.3.1 Antarctica mass balance

The interior part of Antarctica is nearly a desert with total accumulation of approximately 0.15m (sea water equivalent) annually, an equivalence of 2106 x 10^{12}kg/yr [Vaughan et al., 1999; Turner et al., 1999; Giovinetto and Zwally, 2000; Lipzig et al., 2002]. Accumulation is the sum of precipitation, sublimation/deposition and ablation (wind-blown, [Frezzotti et al., 2004]). Figure 1-5, taken from Vaughan et al. [1999], shows the distribution of surface mass balance (net accumulation minus ablation) based on *in-situ* ice cores measurements. The dry snow line at a few tens of kilometers from the coast separates the desert from regions of high rates of accumulation up to $2m/yr$ [Giovinetto and Zwally, 2000]. Climate models based on surface temperatures, atmospheric circulation and sparse *in-situ* measurements from 1979-1993 give annual rates from 0.025m/yr in the interior of East Antarctica to ~0.300-0.700m/yr at the coast [Turner et al., 1999]. At Lake Vostok (location shown in Figure 1-2), ice penetrating radar data show rates of accumulation in the last 17000 years varying between 0.005 to 0.045m/yr [Leysinger-Vieli et al., 2004]. In another study traversing from the Ross Ice Shelf to Lake Vostok, ice cores and snow stakes show large homogeneous regions (hundreds of km^2) of uniform precipitation and show that surface wind-driven sublimation produce most of variations at shorter scales. These workers also showed surface mass balance results which differ from those in Vaughan et al. [1999]; Giovinetto and Zwally [2000] by up to 60%, with a 10% difference leading to a difference of 0.5mm/yr in sea level variation [Leysinger-Vieli et al., 2004]. The *in-situ* measurements from these studies provide us with good constraints on surface mass balance estimates. However, their spatial coverage is limited, and climate models can only predict rates at coarse spatial resolution due to poor constraints on some of the atmospheric parameters. The combination of models and limited data can give disagreements of up to 60%, yielding uncertainties ~ 5%-10%, or approximately 0.25-0.5mm in annual sea level [Church et al., 2001; Vaughan et al., 1999; Giovinetto and Zwally, 2000; Frezzotti et al., 2004]. As shown by Fricker et al. [2000] and others, uncertainties in input parameters are the largest source of uncertainties in mass

balance estimations.

The most important mechanism by which grounded ice in the ice sheet loses mass is basal melting. The weight of the ice above causes thermal instability and bottom melting, and ice slides slowly past the bedrock on its way to the sea. Horizontal ice flow rates can vary vertically and horizontally based on bedrock slopes, and are estimated based on numerical models due to lack of *in-situ* measurements in Antarctica. In the interior of the ice sheet, basal melting is considered negligible. Jacobs et al. [1992] had argued that changes in ice shelves directly affect the balance of grounded ice in Antarctica, and should be included in the mass balance equation of the ice sheets. Their numerical simulations showed that at the interface of ice/sea water at the grounding line, basal melting contributes approximately 21% of the mass loss annually, with $\sim$ 3% of which coming from melting in the interior grounded ice. The other 89% comes from iceberg calving which is shown as mechanism 2 in Figure 1-7 [Jacobs et al., 1992]. Jacobs et al. [1992] also quoted errors of $\pm$20%, $\pm$33% and $\pm$50% for their estimated rates of accumulation, iceberg calving, and basal melting. They concluded that their results, while showing negative mass balance equivalent that of a 1.3mm/yr sea level change, have uncertainties of approximately $\pm$1.8mm/yr.

Other less important factors which contribute to the mass balance calculations include surface melting and firn compaction. Zwally and Fiegles [1994] used microwave signals, which reflect changes in moisture content based on changes in dielectric properties of wet/dry firn, to study the melt extent over the Antarctica. Surface melting only occurs within 10km from the coast where the temperature gets above -4 to -2°C in December to January (southern summer). Melting can transfer heat downward faster than thermal conduction, which could contribute to instabilities and disintegrations of ice shelves [Zwally and Fiegles, 1994]. However their results show the melting-freezing cycle is extensive only in the Antarctic Peninsula, the Filchner-Ronne Ice Shelf, Dronning Maud Land coast, Amery Ice Shelf, West Ice Shelf and Shackleton Ice Shelf (Figure 1-2).

Early models of firn compaction / densification which assumed constant surface temperature and surface accumulation rate have produced short-term elevation changes

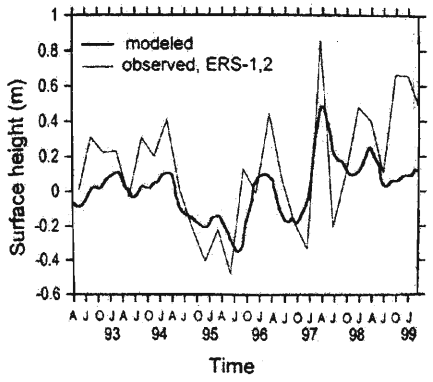

Figure 1-6 Asymmetric inter-annual change in snow surface elevation associated with firn densification/compaction for Greenland from 1992-1999. Figure is taken from Zwally and Jun [2002].

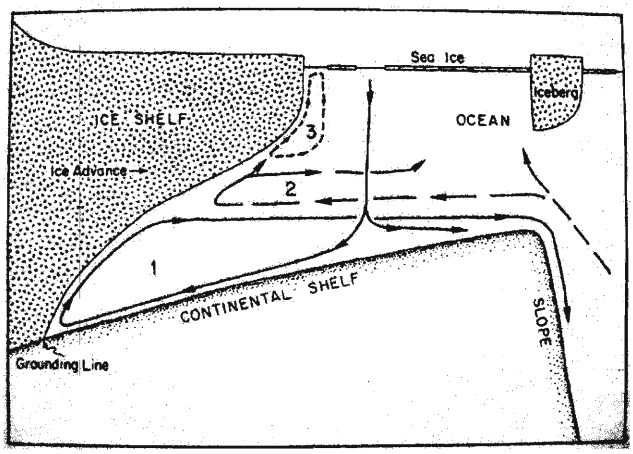

Figure 1-7 Bottom melting at the grounding line due to ocean circulation, which could cause up to 33% of mass loss in the Ice-Shelf. Figure is taken from Jacobs et al. [1992].

an order of magnitude smaller than the observed signal using ERS radar altimetry [Zwally and Jun, 2002]. Zwally and Jun [2002] recalculated compaction rates using temperature-dependent parameters to show the asymmetric nature of this short-term cycle with amplitudes up to $25cm$ in surface elevation changes. Figure 1-6 taken from Zwally and Jun [2002] shows an example of the modeled asymmetric surface change associated with firn compaction in Greenland. The behavior of this signal is the same in Antarctica. However firn compaction annual cycle also depends on snow accumulation, and can not exceed the amplitude of the accumulation signal [Jun, 2005]. For East Antarctica this means the maximum surface height change that can occur via this mechanism is $\sim$0.05m/yr in the interior.

Table 1.2 taken from Church et al. [2001] and Jacobs et al. [1992] shows a collection of current mass balance estimates for Antarctica. The sources of data include both climate-model outputs, 1800+ *in-situ* measurements of ice-cores, and satellite microwave backscatter measurements. Many studies are follow ups of previous ones with better constraints on either the surface mass balance term ("Accumulation" in Table 1.2) or mass loss ("Attrition" in Table 1.2). Some authors also exclude the iceberg calving, ice shelves, and the Antarctica Peninsula from their estimates because changes in the ice shelves do not contribute directly to the sea level change (because they are already floating). In addition, some studies only focused on the surface mass

balance term, in which case there will be no mass loss term or overall mass balance estimates. As mentioned earlier and shown in Table 1.2, common to all estimates, the error bars for mass balance estimates are in the 25% to 100% range, and in some cases are greater than the mass balance estimate itself. As a result, our current knowledge is that the Antarctic ice sheet's contribution to sea level rise is approximately zero to slightly negative (Table 1.2).

Mass balance studies focused mainly in East Antarctica because it is 83% of the

Table 1.2 Mass Balance in Antarctica (10^{12} kg/yr = 1 Gt/yr)

Accumulation			Attrition			Balance	Reference
Grounded ice	Ice Shelf	Total	Calving icebergs	Ice-shelf melting	Run-off		
		2000	-1700	-550		-400	Losev(1963)
1490	356	1885	-1053	-293			Barkov (1971)
		2080	-1450	-200	-10	+420	Bull (1971)
		2000	-2400	-320	-60	-720	Kotlyakov et al., (1978)
		1749	-855	-251		+487	Meier (1983)
		2000	-1800			+200	Budd and Smith (1985)
			-2300			-	Orheim (1985)
1468	495	1963					Giovinetto and Bentley (1985)
		2141					Giovinetto and Bentley (1989)
1817	287	2104					Fortuin and Oerlemens (1990)
		2200	-2200			0	Warrick and Oerlemans (1990)
1660						+180	Bentley and Giovinetto (1991)
1528	616	2144	-2016	-544	-53	-469	Jacobs et al. [1992]
1752 [a]		2279 [a]					Giovinetto and Zwally (1995)
		2190					Budd *et al.*, (1995)
				-756			Jacobs *et al.*, (1996)
		2190					Bromwich *et al.*, (1998)
		2106					Turner et al. [1999]
1811		2288					Vaughan et al. [1999]
1924		2344					Huybrechts et al. [2000]
1883 [b]		2326 [b]					Giovinetto and Zwally [2000]
1843±76 [c]		2246±86 [c]	2072±304	-540±218	-10±10 [d]	-376±384 [d]	Mean and standard deviation

[a] Normalized to include the Antarctic Peninsula.
[b] Normalized to include the Antarctic Peninsula and without applying a combined deflation and ablation adjustment.
[c] Mean and standard deviation based only on accumulation studies published since 1995.
[d] Estimated by Church et al. [2001].

total area (many authors exclude the Antarctic Peninsula from their analyses). However, changes in the ice sheet in response to climate change are expected to occur in West Antarctica because of its larger perimeter to volume ratio. Using ERS radar altimetry from the years 1993-1999, Wingham et al. [1998] and Zwally et al. [2002] showed evidences of large rates of surface thinning and thickening in the West Antarctic ice sheet (WAIS) and Thwaites and Pine Island Glaciers (see Figure 1-2 for their locations). In addition, Zwally and Fiegles [1994] showed that an increase in tem-

perature would likely cause equal surface melting in both West and East Antarctica, even though their surface area ratio is nearly 1 : 10; and that 80% of ice-shelf area is in WAIS and 25% of Antarctica total accumulation occurs in the Western part of the continent. ERS data also showed evidence of an increase in elevation on-land due to increased precipitation, consistent with warmer weather as predicted by climate models [Zwally, 2005].

Another important factor that needs to be accounted for in mass balance calculations is the isostatic uplift of the bedrock due to continuous melting of the ice sheets since the last Glacial Maximum. Currently, constraints on post-glacial rebound are poorly known in the South Pole region. Predictions are made through models using geophysical parameters such as lithospheric thickness and mantle viscosity. The most updated model ICE-4G [Peltier, 1994] has helped improve the knowledge of sea-level change significantly. However due to lack of data over Antarctica, the model could only predict changes in the range of $5mm/yr$ to $10mm/yr$ of uplifts [Church et al., 2001; Schutz, 2002] with no alternative method to verify the results. The current satellite gravity mission GRACE should address this problem well, as GRACE would measure gravity signal and be able to separate out bed-rock elevation changes from those of ice [Velicogna and Wahr, 2002].

1.3.2 Greenland Mass Balance

Approximately 10% of the world's ice is stored in Greenland [Brenner et al., 2003]. Similar to the WAIS, Greenland mass-balance is affected more by and thus serves as a better indicator of climate change than East Antarctica due to its larger parameter:area ratio (8-fold higher compared to Antarctica). Because of its smaller size, snow accumulation and ice flow rates are also higher. Figures 1-8 and 1-9, taken from Ohmura and Reeh [1991] and Drinkwater et al. [2001] show maps of topographic barriers which control snow accumulation rate in Greenland, and estimates of surface accumulation using combined radar backscattered data from ERS, NASA's ADEOS-1, SEASAT missions and *in-situ* ice core measurements. Accumulations increase up

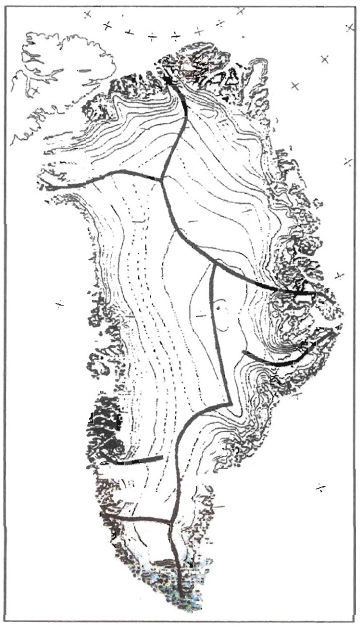

Figure 1-8 Different accumulation zones in Greenland due to topographic barriers. Figure is taken from Ohmura and Reeh [1991].

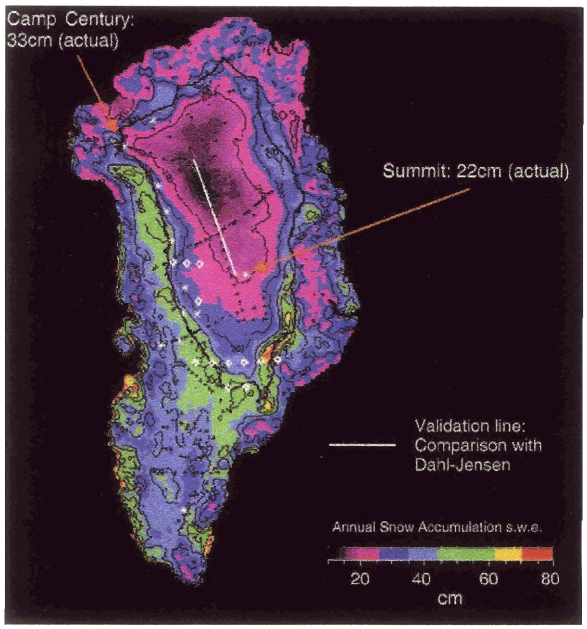

Figure 1-9 Predicted snow accumulation based on satellite backscatter data. Different symbols correspond to *in-situ* measurement sites. Figure is taken from Drinkwater et al. [2001].

to more than 1m/yr (sea water equivalent) at the southern tip, and are controled by weather pattern resulted from Greenland's topography [Ohmura and Reeh, 1991]. An asymmetric annual signal with amplitude ~18-25cm in height change associated with firn densification is found by Zwally and Jun [2002] to be strongly correlated with surface air temperature. ERS radar altimetry measurements support the existence of this signal (see Figure 1-6).

Using microwave measurements Abdalati and Steffen [2001] found evidence for a significant increase in surface melting on the west side, where the surface temperature is on average 2^oC higher than that along the east coast. Repeated aircraft laser altimetry measurements from 1993-1994 and 1998-1999 show strong evidence for surface thickening and thinning rates higher than 1m/yr along the coast below 2000m of elevation (Figure 1-10, [Abdalati and Steffen, 2001; Abdalati et al., 2002]). From another study measuring ice discharge using GPS data, Thomas et al. [2000b] found elevation thickening rates of 0.02-0.20m/yr and thinning of 0.002-0.30m/yr (Figure 1-11). The pattern of thickening/thinning is bimodal, and the large rates suggest that the changes are dynamically driven (surging for example) rather than

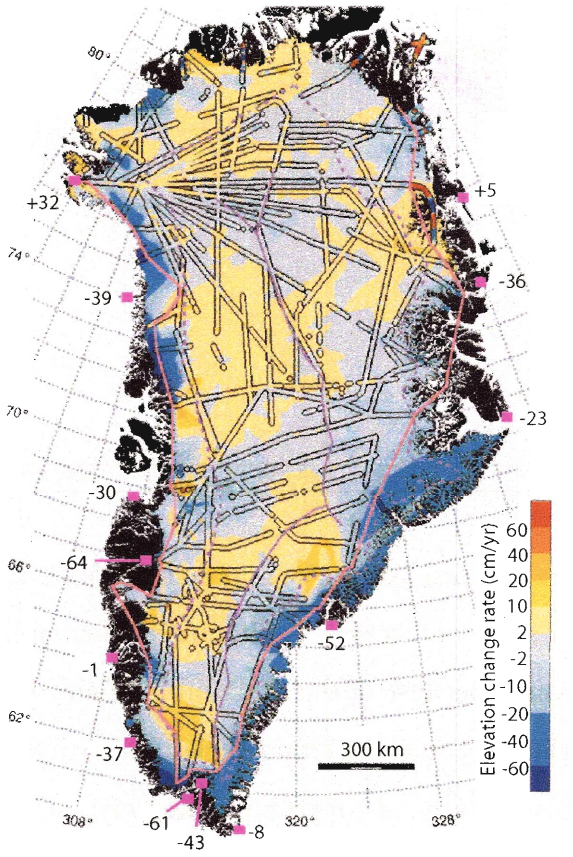

Figure 1-10 Elevation rate of change in Greenland for 1994-1999 based on aircraft laser altimetry. Linear features indicate flight tracks. Figure is taken from Krabill et al. [2000].

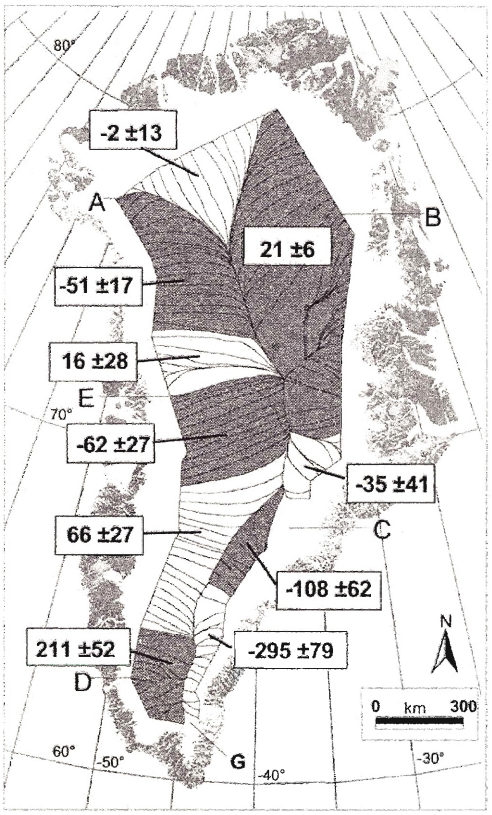

Figure 1-11 Greenland mass balance for 1993-1997 based on GPS measurements of ice discharge. The pattern of elevation rate of change (in mm/yr) is bimodal with very high rates in the Southern tip. Figure is taken from Thomas et al. [2000a].

simple changes in accumulation/basal melting [Abdalati et al., 2002; Thomas et al., 2000b]. Above 2000m, Greenland is in balance with changes only within ranges of 0.5±0.7cm/yr [Krabill et al., 1999; Thomas et al., 2000a]. In the studies by Krabill et al. [1999, 2000], the authors applied a correction of approximately 4mm/yr and 5mm/yr in the southern and northern part of Greenland to account for isostatic uplift. Table 1.3 taken from Church et al. [2001] provides a summary of current knowledge in Greenland ice sheet mass balance.

1.3.3 Summary

The ice sheet mass balance in Antarctica is less well constrained than in Greenland. Based on current available data and numerical models, Antarctica appears to have approximately zero (no mass change) to slightly negative mass change, with evidence

Table 1.3 Mass Balance in Greenland (10^{12} kg/yr = 1 Gt/yr)

Source	Accumulation	Run-off	Net accumulation	Iceberg production	Bottom melting	Balance
Benson (1962)	500	272	228	215		+13
Bauer (1968)	500	330	170	280		-110
Weidick (1984)	500	295	205	205		±0
Ohmura and Reeh (1991)	535					
Huybrechts et al. (1991)	539	256	283			
Robasky and Bromwich (1994)	545					
Giovinetto and Zwally (1995)	461					
Van de Wal (1996)	539	316	223			
Jung-Rothenhausler (1998)	510					
Reeh et al. (1999)	547	276	271	239	32	±0
Ohmura et al. (1999)	516	347	169			
Janssens and Huybrechts (2000)	542	281	261			
Zwally and Giovinetto (2000)			216			
Mean and standard deviation	520±26	297±32	225±41	235±33	32±3	-44±53

of thinning along the coast, at the ice-shelves, in West Antarctica, and small thickening also along the coast but further inland in East Antarctica. A similar conclusion is drawn for Greenland, but with better constraints because of the availability of aircraft altimetry data. With laser altimetry from the Ice Cloud and land Elevation Satellite (ICESat), we anticipate an improvement in surface height measurements with accuracy level of less than 20cm that will help constrain the uncertainties in surface height change to within a few centimeters per year. However considerable effort and new experiments are still needed to obtain more data to improve our understanding in other mass balance factors including basal melting, isostatic uplift, and snow accumulation [Abdalati et al., 2004].

1.4 Satellite altimetry to study the ocean and ice sheets

Satellite measurements of surface topography can provide data sets with high global coverage and uniform accuracy. The first radar altimetry satellite mission was SEASAT in 1978 with height accuracy in the range of tens of centimeters [Zwally and Brenner, 2001]. Table 1.4 taken from Zwally and Brenner [2001] (and addition sources as shown in the Table) provides a list of satellite missions pertaining to ice sheet and ocean studies, along with their spatial and temporal coverage and accuracies. All missions

operate using radar altimeter, with the exception of ICESat which is the first mission designed specifically for studying the ice sheets using a laser altimeter system. Chapters 2- 3 will focus on the description and analysis of ERS1/2 data to study height changes in Antarctica. Chapters 4- 5 will focus on the description and analysis of ICESat data. The main contributors of errors in range measurement in radar altimetry are from satellite orbit determination and delays due to the ionosphere and troposphere. To reduce these errors, many radar altimetry satellites operate using dual frequencies to remove ionospheric delays, carry microwave radiometers to measure water vapor content to correct for tropospheric delays, and use a combination of ground-based laser ranging and tracking devices on-board to constrain orbital errors to within 4cm or less. ERS-2 was a follow-up mission to ERS-1, both of which operated using single frequency and did not have as good orbit precision as the others (Table 1.4, [Nerem and Mitchum, 2001a]). Compared to radar, laser altimeters have many advantages including smaller footprints, reduced ground penetration, and higher accuracy. However with the smaller footprints, additional error sources become magnified, the most significant of which is pointing. Jason-1 was designed as a continuation of TOPEX/POSEIDON, with similar radar altimeter and exact orbit. ENVISAT is the follow up mission to ERS-2, both in the radar altimeter design and orbit. The success of these radar and laser altimetry missions will enable time series construction of 10+ years for both sea level and ice sheet surface height change studies.

Table 1.4 Past and present satellite altimetry missions

Satellite	Ops Period	Latitude range (deg)	Wave-length (cm)	Repeat cycle (day)	inter-track spacing at equator (km)	footprint size (km)	Orbit accuracy (cm)	Height accuracy (cm) [a]
SEASAT	Jul-Oct 1978	±72	2.2	-	163	1.7	50-70	>40
Geosat	1985-1989	±72	2.2	-	163	1.7	50-70	>40
TOPEX/ POSEIDON	1991-2001	±66.0	2.3,5.8	10	300	2.2	2-3	4.2[b]
ERS-1	1991-1996	±82.4	2.2	3,35	85	1.7	8-9 (5 [c])	>73
ERS-2	1996-2001	±82.4	2.2	3,35	85	1.7	8-9 (5 [c])	>73
Jason-1	2002-present	±66.0	2.3,5.8	10	300	2.2	2	< 2.5[b],[d]
ENVISAT	2002-present	±82.4	2.3,9.3	3,35,	85	1.7	2-3	∼35[e]
ICESat[f]	2002-present	±86.0	1024nm 532nm	8,33		70m	2	<20

[a] over the ice sheet unless noted otherwise; [b] over the ocean;
[c] post processing accuracy; [d] science goal;
[e] over ice sheet, estimated by DiMarzio et al. [2004]; [f] laser altimetry;
Additional sources include the ENVISAT instrument website http://envisat.esa.int/instruments/ra2, Jason-1 homepage http://topex-www.jpl.nasa.gov/mission/jason-1.html, and the National Snow and Ice Data Center GEOSAT and SEASAT altimetry data for the Antarctic and Greenland ice sheets http://nsidc.org/data/docs/daac/nsidc0053_scasat_geosat.gd.html.

Chapter 2

Kriging

2.1 Introduction

The method currently being used to analyze satellite altimetry data to detect height change is the cross-over analysis. This method will be mentioned briefly here and covered in detail in the next chapter. Cross-over uses four points at the locations where the ascending and descending satellite tracks meet on the ground at different time to study height changes. One main disadvantage of the cross-over technique is that it uses only a small fraction of the available data (<10%). We seek an alternative method that will enable us to use all of the data and the data statistics to estimate height changes and other surface characteristics. In addition, we want an optimal linear estimator, where optimal implies that the estimator error variance is minimized in the least-square sense. Kriging satisfies all of these criteria, and is chosen as the alternative method to cross-over. In this and the next chapter, kriging will be described and used to analyze radar altimeter data, and results obtained by both kriging and cross-overs will be compared. One fundamental question we wish to address in introducing kriging as an alternative method is whether more data and a more sophisticated method yield more accurate dh/dt estimates.

2.2 Ordinary Neighborhood Kriging

Kriging is named after Danie Krige who among others in the early 1950s developed a statistically-optimized interpolator to analyze gold mining-related problems [Olea, 1999]. Ordinary kriging is a technique of interpolating between points using weights where the weights w_i are determined based on statistics of the data set. The assumption is such that the data are second-order stationary, *i.e.*, the data mean is the same in all locations and data covariance is a function of only the separation distance. In addition, the estimate will be unbiased (zero mean error) and has minimum error variance. Given a set of measurements (data points) $[v(\mathbf{x}_1), ..., v(\mathbf{x}_N)]$ with mean $\bar{v}$, variance $C_{ii}(0) = \sigma^2$ and covariance $C_{ij}(h) = \sum_{k=1}^{N}(v(\mathbf{x}_i) - \bar{v})(v(\mathbf{x}_j) - \bar{v})$ between all pairs of points $\mathbf{x}_i$ and $\mathbf{x}_j$ separated by the distance h (Figure 2-1a), the estimated value $\hat{v}(\mathbf{x}_e)$ at an interpolated point $\mathbf{x}_e$ is:

$$\hat{v}(\mathbf{x}_e) = \sum_{i=1}^{N} w_i \cdot v(\mathbf{x}_i) \tag{2.1}$$

When it is unambiguous, the notation for $v(\mathbf{x}_i)$ is shortened to v_i. From the assumptions, the mean and variance of the estimation error are:

$$\begin{aligned} E[\hat{v}_e - v_e] &= E[\sum_{i=1}^{N} w_i v_i] - E[v_e] \\ &= \sum_{i=1}^{N} w_i E[v_i] - E[v_e] \\ &= (\sum_{i=1}^{N} w_i - 1)E[v_e] = 0 \end{aligned} \tag{2.2}$$

$$\begin{aligned} E[(\hat{v} - v_e)^2] &= E[v_e^2] + E[(\hat{v})^2] - 2E[\hat{v}v_e] \\ &= E[v_e^2] + E[(\sum_{i=1}^{N} w_i v_i)(\sum_{j=1}^{N} w_j v_j)] - 2E[(\sum_{i=1}^{N} w_i v_i)v_e] \\ &= E[v_e^2] + \sum_{i=1}^{N}\sum_{j=1}^{N} w_i w_j E[v_i v_j] - 2\sum_{i=1}^{N} w_i E[v_i v_e] \end{aligned}$$

$$= (\sigma^2 + \bar{v}^2) + (\sum_{i=1}^{N}\sum_{j=1}^{N} w_i w_j C_{ij} + \bar{v}^2) - 2(\sum_{i=1}^{N} w_i C_{ie} + \bar{v}^2)$$

$$= \sigma^2 + \sum_{i=1}^{N}\sum_{j=1}^{N} w_i w_j C_{ij} - 2\sum_{i=1}^{N} w_i C_{ie} \tag{2.3}$$

subject to the constraint:

$$\sum_{i=1}^{N} w_i = 1, \tag{2.4}$$

where C_{ie} is the covariance function between the interpolated point $\mathbf{x}_e$ and data point $\mathbf{x}_i$. The constraint Eqn 2.4 is necessary to ensure that the error mean is zero (Eqn 2.2). Using the Lagrangian method (with Lagrange parameter μ) to minimize the estimate variance (Eqn 2.3) with the constraint (Eqn 2.4) leads to:

$$\sigma_E^2 \equiv \sigma^2 + \sum_{i=1}^{N}\sum_{j=1}^{N} w_i w_j C_{ij} - 2\sum_{i=1}^{N} w_i C_{ie} \quad + \quad 2\mu(\sum_{i=1}^{N} w_i - 1) \tag{2.5}$$

$$\frac{\partial(\sigma_E^2)}{\partial w_i} = 2\sum_{j=1}^{N} w_j C_{ij} - 2C_{ie} + 2\mu = 0 \quad \Rightarrow \quad \sum_{j=1}^{N} w_j C_{ij} + \mu = C_{ie} \tag{2.6}$$

$$\frac{\partial(\sigma_E^2)}{\partial \mu} = 2\sum_{i=1}^{N} w_i - 2 = 0 \quad \Rightarrow \quad \sum_{i=1}^{N} w_i = 1. \tag{2.7}$$

Equivalently in matrix form:

$$\begin{bmatrix} C_{11} & \cdots & C_{1N} & 1 \\ \vdots & \ddots & \vdots & \vdots \\ C_{N1} & \cdots & C_{NN} & 1 \\ 1 & \cdots & 1 & 0 \end{bmatrix} \cdot \begin{bmatrix} w_1 \\ \vdots \\ w_N \\ \mu \end{bmatrix} = \begin{bmatrix} C_{1e} \\ \vdots \\ C_{Ne} \\ 1 \end{bmatrix} \tag{2.8}$$

If we define $\mathbf{C}$, $\mathbf{w}$, and $\mathbf{B}$ to be the matrix containing C_{ij} and the vectors containing w_i and C_{ie} above, then in short notation, the kriging weights can be solved for at each interpolated point e as:

$$\mathbf{Cw} = \mathbf{B} \tag{2.9}$$

$$\mathbf{w} = \mathbf{C^{-1}B} \tag{2.10}$$

$$\Rightarrow \hat{v}_e = \textstyle\sum_{i=1}^{N} w_i v_i \tag{2.11}$$

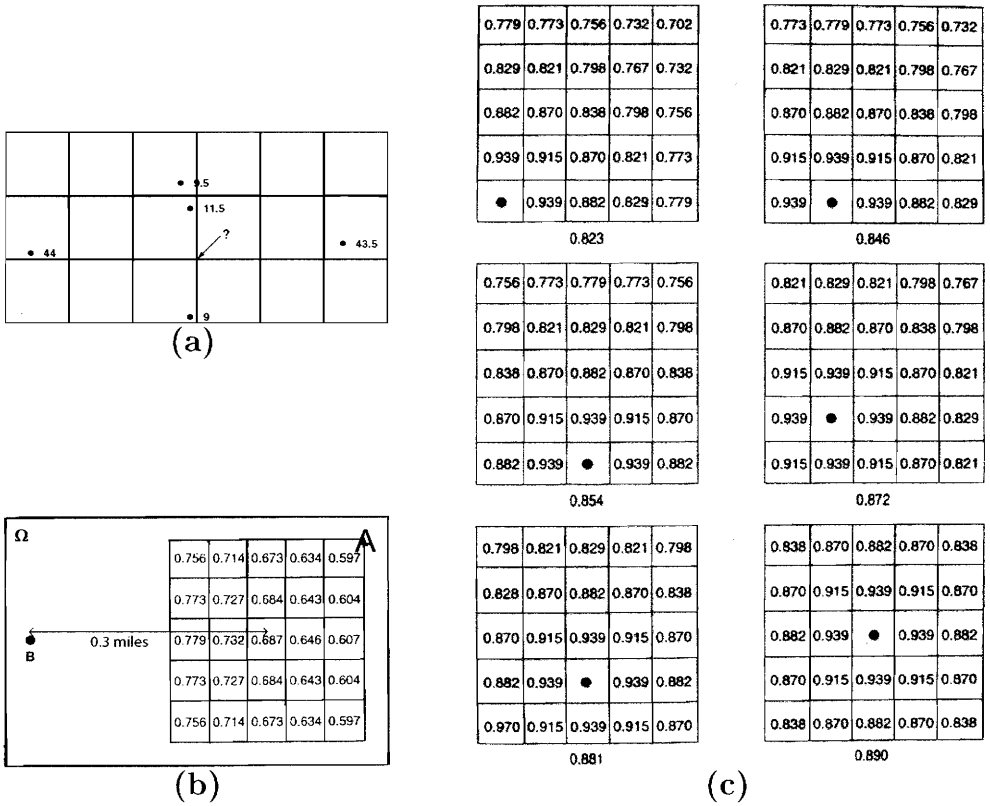

Figure 2-1 Neighborhood for ordinary kriging (a) versus block kriging (b-c). In ordinary kriging (a), the estimate at location indicated by the arrow will be a weighted average of all points in the surrounding area, chosen by certain criteria. In contrast, in block kriging one is interested in the average of a spatial block with area A instead of a single point. As an example, here the block of area A in (b) is divided into 25 sub-blocks prior to calculations of the point-to-block covariance Cv(h) between block A and point B 0.3 miles away, and the block covariance CV (c). The number in each sub-block in (b) is the covariance between its center and point B based on the model $C_{ij}(h) = exp(-h/0.8)$. The number in each sub-block in (c) is the covariance between centers of the dotted and all other sub-blocks, and the number below each large square is the point-to-block covariance Cv between the dotted sub-block and the entire block. By averaging 25 of these point-to-block covariances, we obtain the block covariance CV of 0.855. The example and figures are taken from Olea [1999].

$$\sigma_E^2 = \sigma^2 - \sum_{i=1}^{N} w_i C_{ie} - \mu \tag{2.12}$$

2.3 Block Kriging using Neighborhood Search

In dealing with large sets of data, block kriging has the advantage over ordinary kriging if one is only interested in the average of a block of certain size. Similar to the steps in ordinary kriging, we obtain the weights w_j in order to calculate the estimates $\hat{V}$ of the blocks [Olea, 1999]. Here the upper-case V will be used for the block, and small-case v for the raw data / random field. Given the set of data $\{v_1, v_2, ..., v_N\}$

inside a search neighborhood Ω (Figure 2-1b), the point-to-block covariance Cv between block k of area A_k inside Ω and its surrounding data points $v_i, i \leq N$, and the block covariance CV between the k and all other blocks j in Ω are defined as,

$$Cv_{ik} = \frac{1}{A_k} \int_{A_k} C_{il} dA_l \tag{2.13}$$

$$CV_{jk} = \frac{1}{A_k A_j} \int_{A_k} \int_{A_j} C_{mn} dA_m dA_n \tag{2.14}$$

where C_{mn} is again the covariance function between two points m and n inside Ω. In practice, as shown in Figure 2-1b, the block of area A_k is usually divided into sub-blocks with equal areas, and the integrals in Eqn 2.14 and 2.14 become discrete sums:

$$\begin{aligned} Cv_{ik} &\approx \frac{1}{N\delta A_k} \sum_{l=1}^{N} C_{il} \delta A_l \\ &= \frac{1}{N} \sum_{l=1}^{N} C_{il} \end{aligned} \tag{2.15}$$

$$\begin{aligned} CV_{jk} &\approx \frac{1}{NM\delta A_j \delta A_k} \sum_{n=1}^{N} \sum_{m=1}^{M} C_{mn} \delta A_n \delta A_m \\ &= \frac{1}{NM} \sum_{n=1}^{N} \sum_{m=1}^{M} C_{mn} \end{aligned} \tag{2.16}$$

In the example shown in Figure 2-1b, the covariance model is given as $C_{ij}(h) = e^{-h/0.8)}$, the block dimension is 0.25x0.25 mile^2, and the sub-block dimension is 0.05x0.05 mile^2. The distance between point B and the center of A is 0.3 miles. To calculate the point-to-block covariance Cv_{AB}, one first obtain the point-to-point covariance between point B and the centers of all sub-blocks (25 numbers in Figure 2-1b), then average to obtain $\mathrm{Cv}_{AB}(0.3) = 0.682$. To calculate the block covariance CV, one first calculate the point-to-point covariance between the centers of sub-block i and all other sub-blocks j and average to get point-to-block covariances (values under each large square in Figure 2-1c). Then CV is obtained by averaging these 25 point-to-block values, CV = ((0.890 + 4(0.823 + 0.854 + 0.872 + 0.881) + 8(0.846))/25 = 0.855.

The equations for the estimate $\hat{V}_k$ of block k is similar to that for ordinary kriging,

$$\hat{V}_k = \sum_{i=1}^{N} w_i v_i \tag{2.17}$$

However the kriging weights are now calculated based on block covariances. Again, the block estimate is unbiased:

$$\begin{aligned} E[\hat{V}_k - V_k] &= E[\sum_{i=1}^{N} w_i V_i - V_k] \\ &= (\sum_{i=1}^{N} w_i - 1)E[V_k] = 0 \end{aligned} \tag{2.18}$$

with a variance

$$\begin{aligned} E[(\hat{V}_k - V_k)^2] &= E[(V_k)^2] - 2E[\hat{V}_k V_k] + E[(\hat{V}_k)^2] \\ &= E[\frac{1}{A_k}\frac{1}{A_k}\int_{A_k}\int_{A_k} v_i v_j dA_i dA_j] \\ &- 2E[\sum_{i=1}^{N} w_i v_i V_k] + E[\sum_{i=1}^{N}\sum_{j=1}^{N} w_i w_j v_i v_j] \\ &= CV_{kk} - 2\sum_{i=1}^{N} w_i Cv_{ik} + \sum_{i=1}^{N}\sum_{j=1}^{N} w_i w_j C_{ij} \end{aligned} \tag{2.19}$$

where in Eqn 2.18 the block mean $E[V_k]$ is assumed the same as the random field mean $E[v]$ which equals to a constant based on our second order stationary assumption:

$$V_k = \frac{1}{A_k}\int_{A_k} v dA \Leftrightarrow E[V_k] = \frac{1}{A_k}\int_{A_k} E[v] dA = E[v] = constant \tag{2.20}$$

and that the constraint $\sum_{i=1}^{N} w_i = 1$ holds to ensure unbiasedness. When the estimation error variance is parametrized to include the Lagrange multiplier μ for the constraint and minimized, we obtain the solution for the block kriging weights:

$$\begin{aligned} \sigma_E^2 &\equiv E[(\hat{V}_k - V_k)^2] + 2\mu(\sum_{i=1}^{N} w_i - 1) \\ &= CV_{kk} - 2\sum_{i=1}^{N} w_i Cv_{ik} + \sum_{i=1}^{N}\sum_{j=1}^{N} w_i w_j C_{ij} + 2\mu(\sum_{i=1}^{N} w_i - 1) \end{aligned} \tag{2.21}$$

$$\frac{\partial(\sigma_E^2)}{\partial w_i} = -2Cv_{ik} + 2\mu + 2\sum_{j=1}^{N} w_j C_{ij} = 0$$

$$\Rightarrow \sum_{j=1}^{N} w_j C_{ij} + \mu = Cv_{ik} \tag{2.22}$$

$$\frac{\partial(\sigma_E^2)}{\partial \mu} = \sum_{i=1}^{N} w_i - 1 = 0$$

$$\Rightarrow \sum_{i=1}^{N} w_i = 1 \tag{2.23}$$

Substituting Eqn 2.23 into the third term in the estimation error covariance n Eqn 2.21 gives:

$$\begin{aligned} \sigma_E^2 &= CV_{kk} - 2\sum_{i=1}^{N} w_i Cv_{ik} + \sum_{i=1}^{N} w_i (Cv_{ik} - \mu) \\ &= CV_{kk} - \sum_{i=1}^{N} w_i Cv_{ik} - \mu \end{aligned} \tag{2.24}$$

We can now summarized the derivations above, Eqn 2.23 to Eqn 2.24 in matrix notation:

$$\begin{bmatrix} C_{11} & \cdots & C_{1N} & 1 \\ \vdots & \ddots & \vdots & \vdots \\ C_{N1} & \cdots & C_{NN} & 1 \\ 1 & \cdots & 1 & 0 \end{bmatrix} \cdot \begin{bmatrix} w_1 \\ \vdots \\ w_N \\ \mu \end{bmatrix} = \begin{bmatrix} Cv_{1k} \\ \vdots \\ Cv_{Nk} \\ 1 \end{bmatrix} \tag{2.25}$$

or in short notation (using the same symbols as in ordinary kriging)

$$\mathbf{Cw} = \mathbf{B} \tag{2.26}$$

$$\mathbf{w} = \mathbf{C}^{-1}\mathbf{B} \tag{2.27}$$

$$\Rightarrow \hat{V_k} = \textstyle\sum_{i=1}^{N} w_i v_i \tag{2.28}$$

$$E[\hat{V_k} - V_k] = 0 \tag{2.29}$$

$$\sigma_{\hat{v_k}}^2 = \sigma_E^2 = CV_{kk} - \mathbf{B}^T\mathbf{w} = CV_{kk} - \mathbf{B}^T\mathbf{C}^{-1}\mathbf{B} \tag{2.30}$$

2.4 Covariance - Semi-variogram model

Traditionally kriging uses semi-variograms instead of covariance functions in its calculations [Kitanidis, 1997; Olea, 1999; Deutsch and Journel, 1998]. A semi-variogram is a function which describes how statistically similar two data points are as a function of their separation distances. Because the true first and second order statistics of the random field are not known, semi-variograms are generally used as an approximation. Semi-variogram estimation does not require knowledge of the mean, and offers ways to obtain the variance of the data if existed [Olea, 1999]. The theoretical semi-variogram between all pairs of measurements separated by an average distance h is defined as:

$$\begin{aligned}
\gamma(h) &= \frac{1}{2}E[v(x_i) - v(x_i+h)^2] && (2.31)\\
&= \frac{1}{2}E[v(x_i)^2 + v(x_i+h)^2 - 2v(x_i)v(x_i+h)]\\
&= \frac{1}{2}E[v(x_i)^2 - \bar{v}^2] + \frac{1}{2}E[v(x_i+h)^2 - \bar{v}^2] - E[v(x_i)v(x_i+h) - \bar{v}^2]\\
&= \sigma^2 - C(h) && (2.32)
\end{aligned}$$

where σ^2 and $C(h)$ are the variance and covariance function of the random field $v(x)$, and $\bar{v}$ the mean. Again the covariance is only a function of the separation distance and the mean is a constant at all locations because we assume the random field is second order stationary. The estimated or raw semi-variogram is calculated as:

$$\begin{aligned}
\hat{\gamma}(h) &= \frac{1}{2N}\sum_{i=1}^{N}\{v(x_i) - v(x_i+h)\}^2 && (2.33)\\
&= \frac{1}{2N}\sum_{i=1}^{N}\{v(x_i)^2 + v(x_i+h)^2 - 2v(x_i)v(x_i+h)\}\\
&= \frac{1}{2N}\sum_{i=1}^{N}\{(v(x_i)^2 - 2\bar{v}v(x_i) + \bar{v}^2) + (v(x_i+h)^2 - 2\bar{v}v(x_i+h) + \bar{v}^2)\\
&\qquad +2\bar{v}v(x_i) + 2\bar{v}v(x_i+h) - 2\bar{v}^2 - 2v(x_i)v(x_i+h)\}\\
&= \frac{1}{2N}\sum_{i=1}^{N}\{(v(x_i) - \bar{v})^2 + (v(x_i+h) - \bar{v})^2 - 2(v(x_i) - \bar{v})(v(x_i+h) - \bar{v})\}\\
&= \hat{\sigma}^2 - \hat{C}(h) && (2.34)
\end{aligned}$$

where N is the number of pairs of measurements $v(x_i)$ and $v(x_i + h)$ at average separation distance h. Table 2.1 and Figure 2-2a show some semi-variogram functions most commonly used in geostatistics. At short h, the slope of the variogram reflects whether the data is continuous (flat slope) or discontinuous (steep slope) ([Kitanidis, 1997], Figure 2-2b,c). Figure 2-3a shows one example of a raw semi-variogram of surface elevation in the interior of Antarctica based on radar altimetry data, and the fitted variograms. Variogram fittings near the origin is more important than at large h because of the higher weights w_i associated with short separation distance [Kitanidis, 1997]. There are many different schemes being used in variogram fitting, with most emphasizing on minimizing the "residuals" and keeping the variogram models as simple as possible. Some workers prefer to minimize the residuals between the modeled and raw semi-variograms using weights that are proportion to the inverse of the scatter of the variograms [Olea, 1999]. Others favor minimizing the normalized residuals ϵ between actual measurements and predicted values based on kriging at the measurement locations (the kriging standard error is used for normalization, [Kitanidis, 1997]). In the latter case, if the modeled variogram correctly model the surface, the residuals are expected to be the uncorrelated noise associated with measurement errors and have zero mean. Furthermore, if the noise is assumed normal with variances equal to those from the kriging σ_E^2, ϵ is then $\sim$N[0,1]. Two additional tests, the Q_1 and Q_2 tests, where $Q_1 = \frac{1}{N-1}\sum_{i=2}^{N}\epsilon_i$ and $Q_2 = \frac{1}{N-1}\sum_{i=1}^{N}\epsilon_i^2$ are used in the

Table 2.1 Most commonly used variograms

Model	Functional form	parameters
Spherical	$\gamma(h) = C(\frac{3}{2}\frac{h}{a} - \frac{1}{2}(\frac{h}{a})^3), 0 \le h < a$	C,a
	$= C \quad , a \le h$	
Exponential	$\gamma(h) = C(1 - e^{-\frac{h}{a}})$	C,a
Gaussian	$\gamma(h) = C(1 - e^{-(\frac{h}{a})^2})$	C,a
Power	$\gamma(h) = \alpha h^\beta, 0 < \beta < 2$	α, β
Cubic	$\gamma(h) = C(7(\frac{h}{a})^2 - \frac{35}{4}(\frac{h}{a})^3 + \frac{7}{2}(\frac{h}{a})^5 - \frac{3}{4}(\frac{h}{a})^7), 0 \le h < a$	C,a
	$= C \quad , a \le h,$	
Hole effect	$\gamma(h) = C(1.0 - cos(\frac{h}{a}\pi))$	C,a
Nugget effect	$\gamma(h) = C, h > 0$	C
	$= 0$, h $= 0$	

variogram fitting procedure. Q_1 is the sum of N-1 normal variables ϵ and has a normal distribution with zero mean and variance 1/(N-1). (N-1)Q_2 is the sum of squares of N-1 normal $\epsilon \sim N[0,1]$ random variables and has a χ^2 distribution of (N-1) degrees of freedom. Combining these tests with a functional form of minimizing the kriging variance σ_E^2 results in the most reasonable / appropriate variogram model for the data. Kitanidis [1997] suggests the functional form $cR = Q_2 exp(\frac{1}{N-1}\sum_{i=1}^{N} ln((\sigma_E)_i^2))$ for this last step. In practice, these tests are carried out as follows, (a) inspecting visually the raw variograms and fitting the two to three appropriate models from Table 2.1 using linear least square inversion, (b) inspecting the residuals ϵ (mean and variance) and calculating Q_1 and Q_2 to test and eliminate models which give grossly large residuals ϵ, (c) fine tuning using Monte-Carlo method to search for the set of variogram parameters that yields the smallest cR under the conditions that $Q_1 \approx 0$

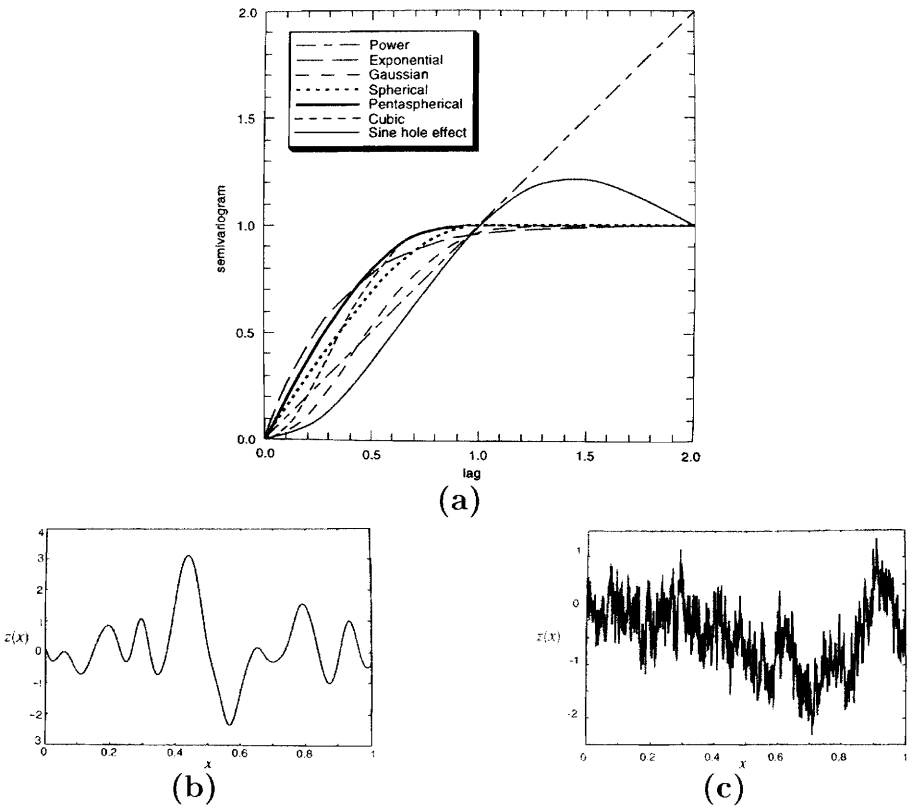

Figure 2-2 (a) Variogram models from Table 2.1, with all parameters set to 1. Two sample random fields, one continuous (b) and one discontinuous (c) which corresponds to flat slope in the gaussian variogram (b) and steep slope in the power variogram (c). Continuous here refers to the random field being differentiable at the shot-to-shot scale. Figures are taken from Olea [1999] and Kitanidis [1997].

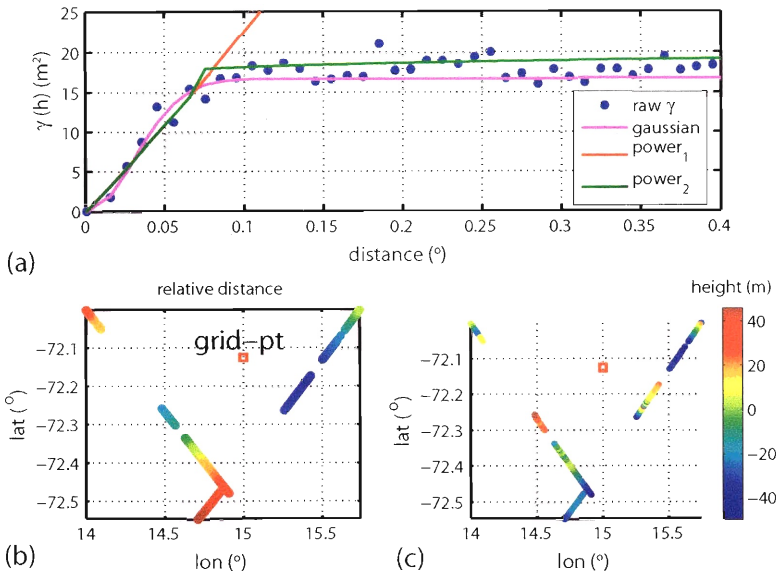

Figure 2-3 (a) One example of raw and modeled semi-variograms for radar altimetry data over the interior flat part of East Antarctica, and relative distance (b) and surface heights (c) of the 200 closest points to the grid point (red square). In (a), the second power model is nested, with two sets of parameters for distance $\leq 0.07^o$ and $> 0.07^o$.

and $Q_2 \approx 1$ [Kitanidis, 1997].

Using the raw variogram in Figure 2-3a, and the 200 closest points to a grid (Figure 2-3b), the structure of C_{ij} (Eqn 2.18) and their inversions are shown in Figure 2-4. Based on the inversion, the gaussian model is eliminated due to its instability. This is also reflected in the singular-value-decomposition of C_{ij}^{-1} (Figure 2-5a). Figure 2-5b-d shows the weights as a function of distance from the grid point, with a 1-to-1 color correspondent with the color scale in Figure 2-3b. The mean of 200 heights is 0.189m, compared to the predicted 3804m, -1.55m, and -1.11m from the gaussian, power1 and power models. The Q_1 and Q_2 tests eliminated the power2 model, and a Monte-Carlo search yields Q_1, Q_2 and cR as shown in Figure 2-6. There is no unique solution for parameters $[\alpha, \beta]$. Based on visual inspection, an α in the range 250-300 would be consistent with the slope of the raw variogram at small h. This yields β in the range of [0.93,0.97]. Care should be taken to make sure the raw variograms used for fitting is representative of the data.

The geostatistic software GSLIB, developed by Deutsch and Journel [1998], is used to process both radar and laser data, with some modifications made to convert X-Y to LON-LAT coordinates.

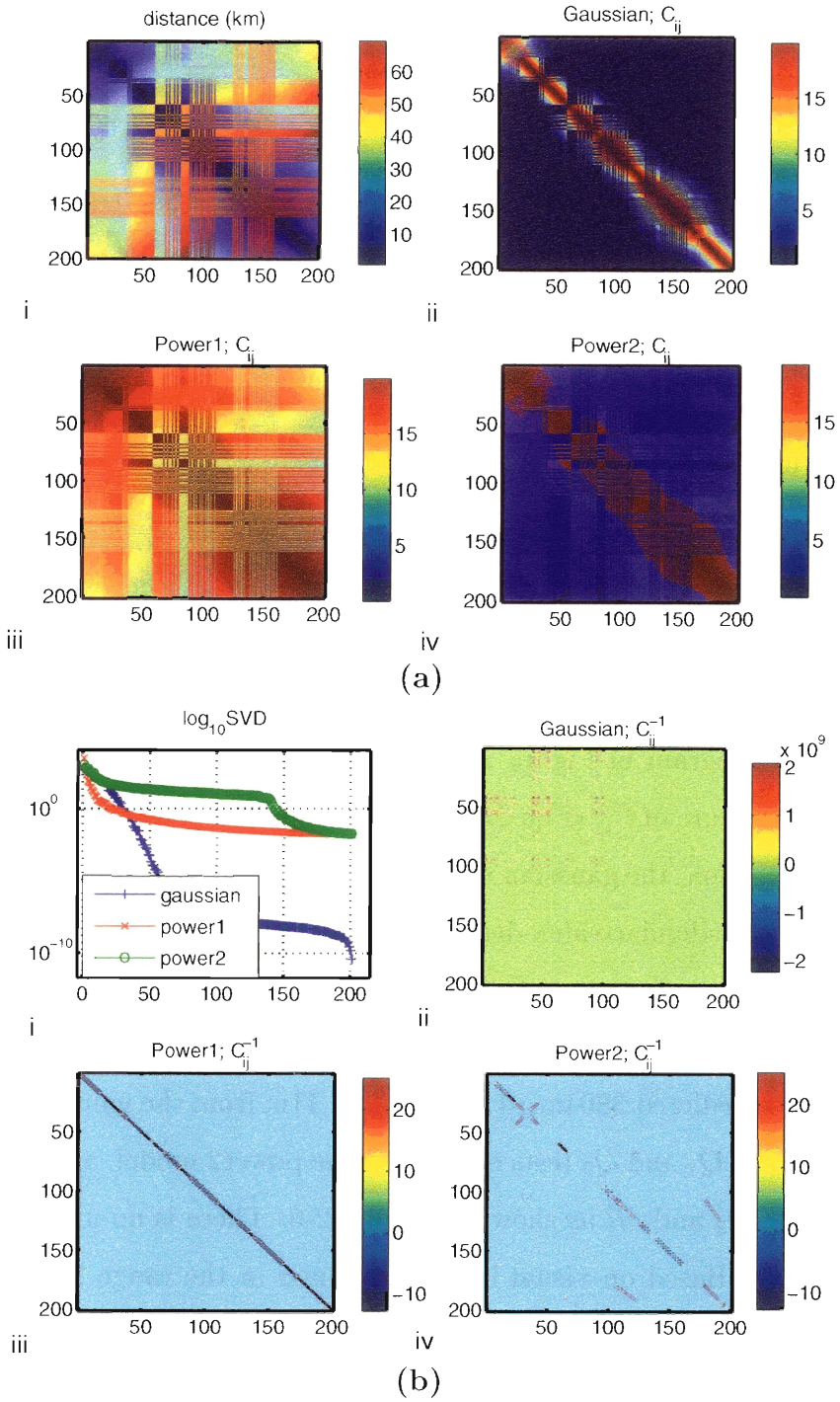

Figure 2-4 The point covariance C_{ij} (a) and inverse C_{ij}^{-1} (b). In (a), the first subplot (i) shows the separation distance in km between the 200 points used. In (b), the first subplot (i) shows the singular value decomposition values for the following three C_{ij}^{-1}. The gaussian model has the highest ratio of first/last SVD values, and its C_{ij}^{-1} is highly unstable.

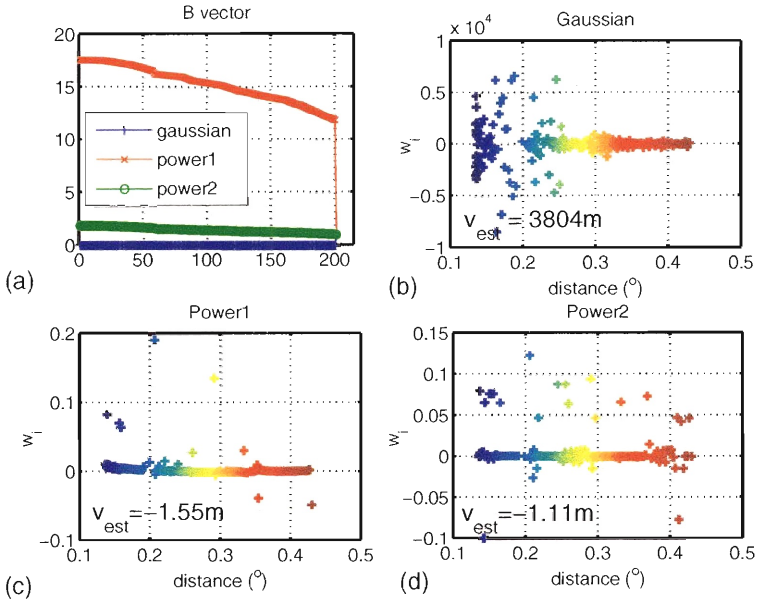

Figure 2-5 (a) The terms in the point-to-block covariance B-vector (Eqn 2.20), and the kriging weights for the three models (b)-(d). In each subplot (b)-(d), the estimated value at the grid point (Figure 2-3a), is shown. The mean of the 200 heights is 0.189m. The weights for the gaussian model (b) are unreasonable so this model is discarded.

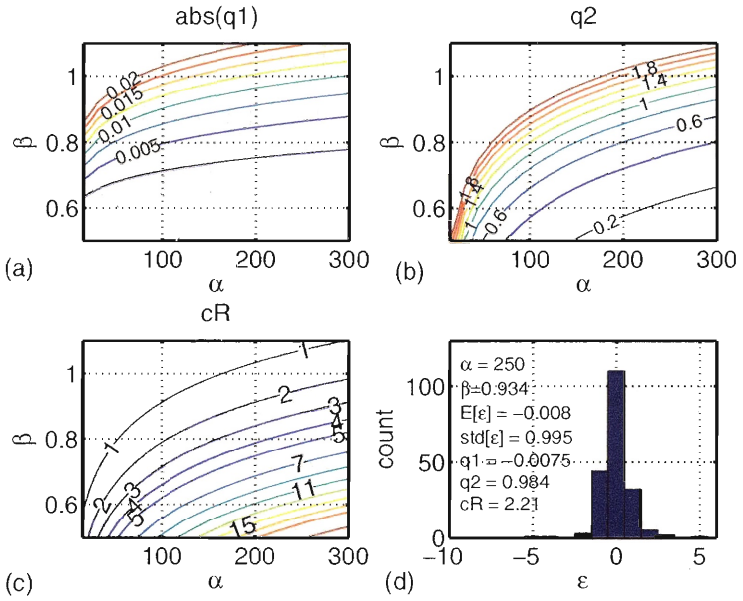

Figure 2-6 Fine tuning process using Q_1 (a), Q_2 (b), and cR (c) tests. The criteria are $Q_1 \approx 0$, $Q_2 \approx 1$, and minimum cR. The solutions are not unique. Based on the raw variogram (Figure 2-3a), a value of α between 250-300 is consistent with the slope of $\gamma(h)$ at short distance. This yields β in the range [0.93,0.97]. (d) The solution using $[\alpha, \beta]$ of [250,0.934] gives [q1,q2,cR] of [-0.0075,0.984,2.21], and the distribution of the residuals ϵ is symmetric with mean and standard deviation of -0.008 and 0.995.

2.5 Kriging Size Determination

Kriging size, *i.e.*, the number of points in the neighborhood Ω, is determined by considering the trade-off between kriging stability and computer time. For satellite altimetry data, the most important factor is cross-track coverage. Figure 2-7 shows how cross tracks influence the kriging results. For a lay-out of block centers as shown in Figure 2-7a, the goals are to (a) obtain a smooth transition in kriging estimates $\hat{v}$ from West to East that is consistent with the statistics of the elevation field, and (b) to obtain stable kriging estimates $\hat{v}$ and variances σ^2. The first point is addressed partly in the previous section by choosing the appropriate modeled variogram. The second point implies that we should choose a neighborhood such that cross-tracks do not introduce discontinuities into the results, and that boundary effect is minimized. Take the case when we only use the closest 10 points (N=10) to estimate the kriging height $\hat{v}$ and variance σ^2 at each grid point (red squares in Figure 2-7a-b). As we go from West to East, the 10 closest points will first be from the track West of the grid points, then abruptly change to the 10 data points East of the grid (Figure 2-7b). This causes a discontinuity in $\hat{v}$, as shown in Figure 2-7b for $N < 300$ approximately. The discontinuity for each grid point can be located by calculating $\delta\hat{v} = \hat{v}_{N+1} - \hat{v}_N$ and plot $\delta\hat{v}$ as a function of N. A similar calculation is done for σ^2, and their results are shown in Figure 2-8. This example is at latitude -70.5^o, the lowest absolute latitude being considered, where data coverage is coarsest. As absolute latitude increases (toward the South Pole), the neighborhood Ω can be adjusted accordingly by repeating this procedure for each 1^o latitudinal band. For this particular example, $\delta\hat{v}$ drops below 0.05m between N of [250,420], and $\delta\sigma$ decreases steadily after N = 350, except of two grid points. Note that σ is highest where there is no data (between the cross-tracks). As a results, even though their $\delta\sigma$ has not stabilized after N = 300 (Figure 2-7d), the magnitudes of these $\delta\sigma$ are still much smaller than their actual values, $\delta\sigma \sim 10^{-2} - 10^{-3}$m compared to $\sigma \sim 3.5 - 5$m. In this case, N is chosen where $\delta\hat{v}$ is at the 5cm level, or $N \approx 350$.

In practice, both the variogram parameters and the neighborhood size are determined

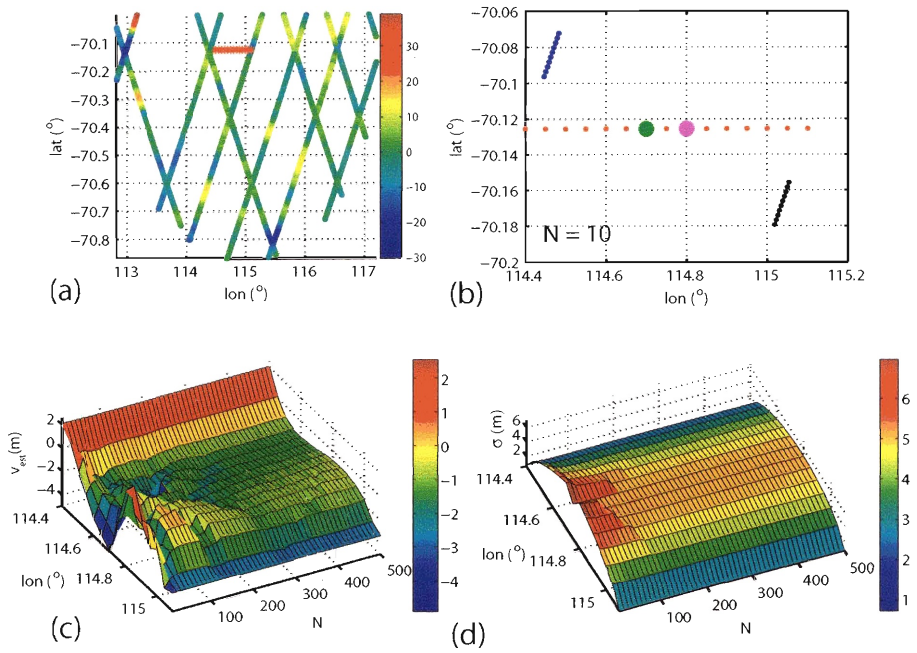

Figure 2-7 (a) Locations of the grid points (red *) relative to the locations of 500 data points used in the neighborhood analysis. The neighborhood of 10 closest points (N=10) results in discontinuities in both data coverage (b) and $\hat{v}$ (c) and the kriging standard error σ (d). In (b) the 10 points in blue makes the neighborhood of the green grid point, and the 10 black points comprise the neighborhood of the magenta grid point. In (c) the discontinuity in $\hat{v}$ can be seen most clearly for grid points between 114.6° and 115° and $N < 300$.

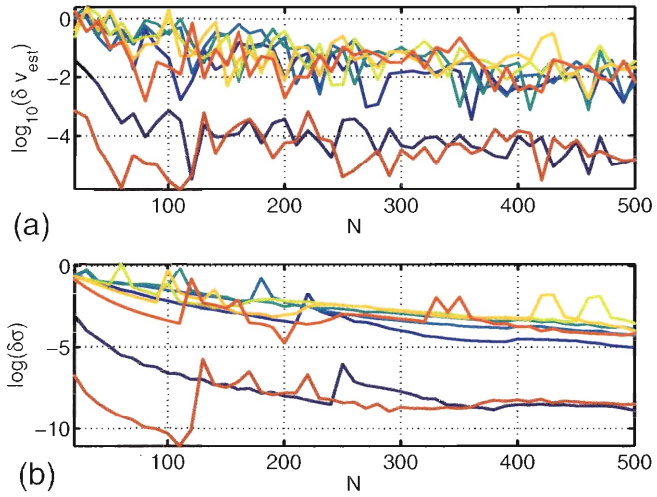

Figure 2-8 Differences in $\hat{v}$ (a) and σ (b) in log scale as a function of neighborhood size N. Color scale from blue to red corresponding to the Western-most to Eastern-most grid points in Figure 2-7a. $\delta\hat{v} = \hat{v}_{N+1} - \hat{v}_N$ and $\delta\sigma = \sigma_{N+1} - \sigma_N$. Units of $\delta\hat{v}$ and $\delta\sigma$ are in meters. $\delta\hat{v}$ reaches below ~0.05m and $\delta\sigma$ stabilizes at $N \approx 350$ with the exception of two grid points.

by averaging α, β, and N for blocks at various latitudes and time steps. For neighborhood size, the emphasis is on the stability of block estimates at lower absolute latitudes where data coverage is coarsest.

Chapter 3

Kriging Analysis of ERS Data

3.1 Introduction

The European Remote Sensing Satellites ERS-1 launched in July 1991 and ERS-2 launched in April 1995 used two nearly identical radar altimetry systems to measure continuous surface heights over the ocean and the ice-sheets from 1992-2001. Both satellites operated at an altitude of approximately 800km with inclination -98.52^o giving coverage on the ground $[-81.5^o, 81.5^o]$ in latitude. The radar beam-width of 1.3^o yields foot-prints on the ground of approximately 1.7km, and the along-track spacing of 325m gives overlapping footprint area of approximately 80%. Two operational cycles, 168-day and 35-day, give cross-track spacings are approximately 2-3km and 25km at latitude -71^oN [Fricker et al., 2000].

Previous studies using ERS data to detect height change in Antarctica include work done using the cross-over "dH/dt" method by Wingham et al. [1998], Zwally and Brenner [2001], Zwally et al. [2002], DiMarzio et al. [2004], and Zwally [2005] (Figure 3-1). In this method, all M numbers of cross-overs within 100km diameter of a grid point, with residual elevations (to an *a-priori* surface) less than ±250m, and within each non-overlapping 90-day (35-day in Wingham et al. [1998]) period are binned into N consecutive boxes (Figure 3-1). Between any two boxes i and j, the average cross-over residual is computed as $\overline{dH_{ij}} = 1/2\{\frac{\sum_{k=1}^{P_{ij}}(A_i - D_j)_k}{P_{ij}} + \frac{\sum_{k=1}^{Q_{ij}}(D_i - A_j)_k}{Q_{ij}}\}$ where P and Q are the number of ascending A and descending D tracks in their corresponding time

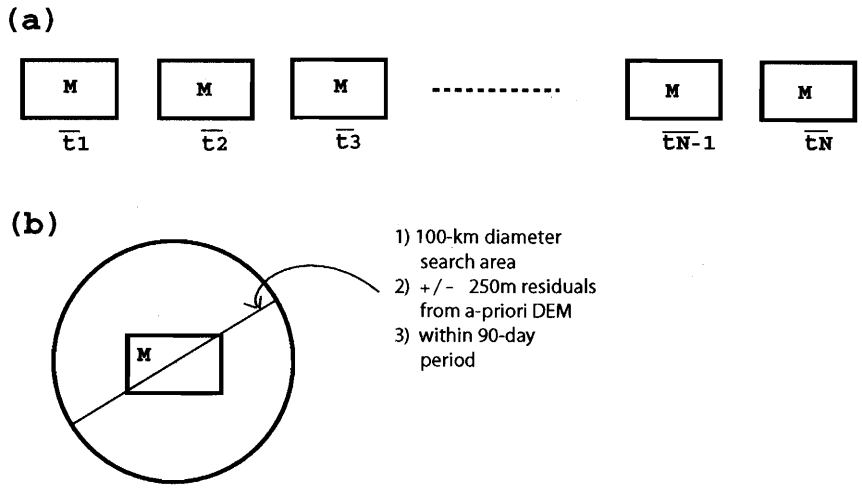

Figure 3-1 A pictorial description of the "dH/dt" method developed by Zwally et al. [1989] to analyze space-borne altimeter data to study height changes. (a) The data are binned into N blocks, each with approximately M number of cross-overs that are (1) within a 100-km diameter search area of the grid center, (2) within ±250m of an a-priori DEM, and (3) within a time interval, 90-day in the case for ERS data (b) [Zwally et al., 2002; Zwally, 2005].

interval, and averaging is used to reduce both the single-shot error and the potential bias between ascending and descending tracks. Finally a time series is constructed using the weighted average of all combinations of $\overline{dH_{ij}}$, with initial time referenced back to $\overline{dH_{11}}$. The weights are such that at any given time t_i, the time series at that time $H_i(t_i)$ is defined as $\frac{1}{i-1}[dH_{1i} + (H_2 + dH_{2i}) + \cdots + (H_{i-1} + dH_{i-1,i})]$ As an example, the time series at time t_3 is $H_3(t_3) = 1/2[(dH_{13} + (H_2 + dH_{23})]$. Using this method, both Wingham et al. [1998] and Zwally et al. [2002] found evidence for negative height rate of change (dh/dt) in West Antarctica near the Pine Island/Thwaites Glaciers ($\sim [-76^oN, 260^oE]$) of -11.7 ± 1.0 to -17.6 ± 3.5cm/yr and Zwally et al. [2002] found positive dh/dt of similar amplitudes near $\sim [-82^oN, 235^oE]$ (Figure 3-2). The seasonal amplitudes are in the range of a few tens of centimeters peak-to-peak, and have been modeled by both accumulation and surface-temperature-dependent seasonal firn compaction [Zwally and Jun, 2002; Zwally et al., 2002]. The eight-year span of ERS-1/2 missions has also made it possible to connect time series of height change with past (SEASAT, GEOSAT) and current/future missions (ENVISAT, ICE-Sat, CRYOSAT). One potential problem is the height bias between any two missions and their different range uncertainties [DiMarzio et al., 2004].

In this chapter, I will investigate height change detection over Antarctica using two

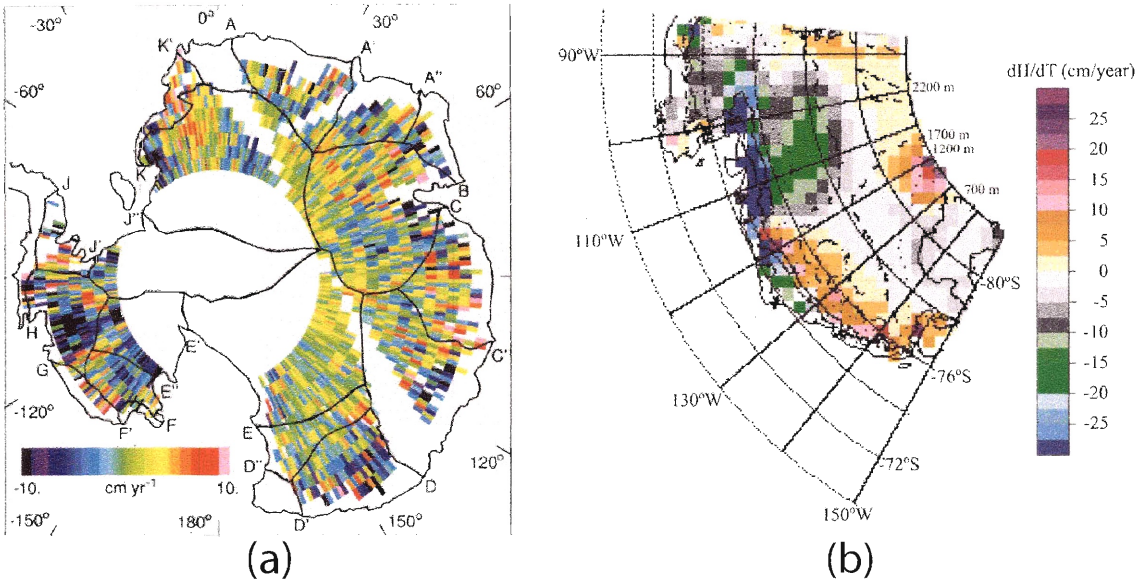

Figure 3-2 Height change rate results using cross-over analyses in Antarctica from Wingham et al. [1998] (a) and West Antarctica (b) from Zwally et al. [2002] showing thinning in the Pine Island / Thwaites Glaciers of up to -0.30m/yr (a-b) and thickening at [lon,lat] of [120W,-82N] of up to 0.20m/yr (b).

methods, one taking average of data within each "snap-shot" as used by Smith et al. [2001b] to analyze MOLA results, and one using block kriging, the method described in Chapter 2. A snap-shot is defined as a period of time during which height change is assumed negligible. For ERS data, a snap-shot of 35 days is used, which coincides with the 35-day sub-repeat cycle of the mission. Results will be compared with those from cross-over analyses in Antarctica when appropriate. Background on kriging is covered in Chapter 2.

3.2 ERS data

3.2.1 Data Corrections

Radar altimeters (RA) measure ranges to the surface using two-way time of flight similar to the laser altimetry system which will be described in Chapter 4. The fundamental difference between laser and radar lies in the wide beam-width of radar at the source, which illuminates on the ground a footprint of sizes several kilometers

Table 3.1 Possible Errors in Radar Altimetry over the Ice Sheets

Source	Range (m)	Correction	Reference
Retracking	±15	GSFC[a]V4 retracker	[GSFC-website, 2005]
Slope	0 to 150	GSFC	[GSFC-website, 2005]
Tropospheric delays	1.5 to 2.5	GSFC - ECMWF[b]	[GSFC-website, 2005]
Ionospheric delays	0.02 to 0.10	GSFC - IRI90[c]	[GSFC-website, 2005]
Tides	-3 to 3	GSFC - UTCSR[d]	[GSFC-website, 2005]
Orbit	-0.3 to 0.25	GSFC - DGM-E04[e]	ERS-1 data, Fricker et al. [2000]

[a]Goddard Space Flight Center, Ice Altimetry group

[b]European Center for Medium Range Weather Forecasts

[c]International Reference Ionosphere 1990

[d]University of Texas Center for Space Research tide model developed by Richard Eanes

[e]Delft University DGM-E04 gravity model

instead of hundreds of meters in the laser case. The pulse-limited and beam-limited footprints are defined as "the maximum circular area from which backscattering can be simultaneously received, and the "area within which the beam attenuated to 3dB in power" [Martin et al., 1983]. For ERS-1/2, the pulse-limited footprint size is approximately 1.7km, and the beam-limited footprint size is approximately 21km (Figure 3-3a). Due to the frequency used in radar, RA experiences ground penetration of up to several meters. In addition, the wide footprints result in slope-induced and surface-tracking errors that are not as critical in the laser altimetry case due to the small laser footprints size. Figure 3-3c illustrates these two errors and how to correct for them.

When the satellite travels in the direction of increasing slope, the wide beam hits a point up-slope first prior to hitting the point at nadir (directly down, Figure 3-3b). This results in an apparent surface higher than that in reality. Removing this error requires knowledge of both local and regional slopes in the along-track and across-track direction. Due to under-sampling in the across-track direction, only regional slope is available, which results in potential errors up to several meters still remaining in the surface height measurements [Brenner et al., 1983]. Tracking error is another consequence of the wide-beam width in RA. When the surface undulation is changing faster than the on-board circuit electronics can handle, the leading edge as shown in Figure 3-3a,c is mis-detected to a location earlier or later in time. A functional fit to the actual returned waveform would identify the correct leading-edge time,

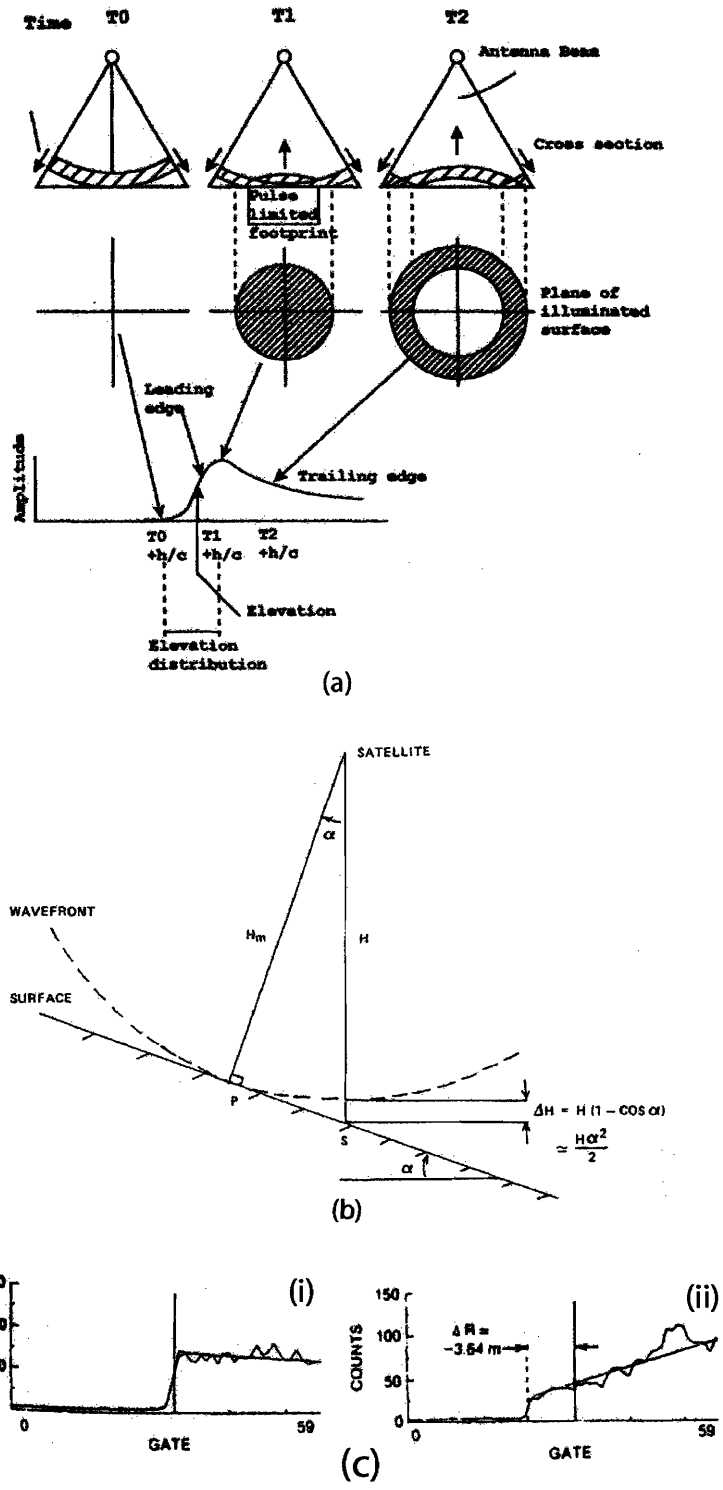

Figure 3-3 Definition of footprints and returned waveform parameters (a), slope induced errors and correction (b) and retracking correction (c) for satellite radar altimetry. In (b) α is the surface slope, H the satellite altitude, H_m the range to the nearest point P on the surface, and ΔH the error induced by α in height measurement. In (c), two examples of actual sea (i) and ice (ii) surface returns from SEASAT-1 radar altimetry system showing correction ΔR to the data. Figures are taken from Zwally and Brenner [2001], Brenner et al. [1983], and Martin et al. [1983].

and the range measurement can be corrected for accordingly (Figure 3-3c, [Martin et al., 1983]). There are three known methods of fitting the waveforms, each with its own advantages and disadvantages as described in detailed at the Goddard Space Flight Center (GSFC) Ice Altimetry website GSFC-website [2005]. In this chapter, the GSFC retracking correction is used. Retracking and slope errors limit ERS-1/2 altimetry precision to $> 70cm$ ([Zwally and Brenner, 2001], Table 3.1).

Other corrections applied to height measurements, as listed in Table 3.1, include orbital corrections, dry/wet atmospheric delays, ionospheric delay, solid/ocean tides. In addition, Arthern et al. [2001], Wingham et al. [1998], and Zwally [2005] found a correlation between changes in surface backscatter coefficients and false surface height temporal variation (dh/dt) in Antarctica that could result in errors in dh/dt of a few tens of cm/yr. Corrections to height rate of change will include those from isostatic uplift of bedrock ($\sim$ 2cm/yr) and seasonal cycles (tens of centimeters to several meters in amplitude along the coast, Chapter 1, [Zwally et al., 2002]).

3.2.2 Time Step Set Up

Ice-mode ERS data obtained from the GSFC-website [2005] (Table 3.1), and ERS-1 168-day and 35-day repeat cycles beginning April 1994 and ERS-2 35-day repeat cycles beginning June 1996 were obtained for this study (Table 3.5). Biases between ERS-1 and ERS-2 height measurements include a constant 40.9cm offset [GSFC-website, 2005] and an additional $11 \pm 6.5cm$ that varies with elevation [DiMarzio et al., 2004; Zwally, 2005], and were observed in this study. A full investigation has not been done on this elevation-dependent inter-satellite bias. As a result, two years of 168-day ERS-1 data are excluded from, and only ERS-2 data were used in analysis of height change. A 5-km digital elevation model (DEM) constructed using ICESat 33-day (Laser 2a) data is used as *a-priori* background. Residuals of ERS data with the DEM yield near-zero means and estimated variances as shown in Table 3.3 for the four regions of study.

Table 3.2 Regions of study

Region	lat range (^{o})	lon range (^{o})	σ^2 (m^2)	# blocks
I	[-82,-72]	[0,50]	53.53	1950
II	[-82,-72]	[50,90]	78.39	1560
III	[-82,-70]	[100,140]	25.37	1720
IV	[-82,-72]	[210,270]	180.13	2340

3.2.3 Block Set Up

Table 3.3 Block Size

Lat(^{o})	-82	-80	-78	-76	-74	-72.5	-72	-71	-70
$\Delta lon(km)$	15.5	19.3	23.1	26.9	30.6	33.4	68.6	72.3	75.9
$\Delta lat(km)$					27.75				

Modified GSLIB block-kriging subroutines from Deutsch and Journel [1998] are used in this study. Due to the increase in density of data poleward, the size of blocks decreases so that the number of data points per block remains approximately constant. Figure 3-4a shows the locations of the four regions of study, and Figure 3-5 shows one example of the block-size analyses, and the grid set-up for a region in West Antarctica (W-Ant) with uniform $\Delta lat = 0.25^o$ and non-uniform $\Delta lon = [2^o, 1^o]$ for latitudinal ranges $[-70^o, -72.5^o]$ and $[-72.5^o, -82.5^o]$ respectively. Block-size as a function of latitude is given in Table 3.3 with a near-squared block of size $(28km)^2$ at latitude -75.5^o. This set-up allows the 500 closest points to block centers to

Table 3.4 Fine tuning of variogram parameters β

		α									final
Region	block	100	200	300	400	500	600	700	800	900	$[\alpha, \beta]$
	325	0.87	0.99	1.06	1.10	1.13	1.16	N/A	N/A	N/A	
1	1225	0.97	1.20	1.15	1.19	1.22	1.25	N/A	N/A	N/A	[375,1.1]
	1720	0.85	0.97	1.02	1.07	1.11	1.14	N/A	N/A	N/A	
	17	0.89	0.96	1.02	1.07	1.10	1.13	1.16	1.18	N/A	
2	23	0.83	0.92	0.98	1.03	1.07	1.10	1.12	1.14	N/A	[275,0.68]
	580	0.42	0.53	0.58	0.67	0.73	0.79	0.82	0.84	N/A	
	1060	0.42	0.55	0.64	0.70	0.74	0.77	0.80	0.83	N/A	
	48	0.83	0.95	1.02	1.06	N/A	N/A	N/A	N/A	N/A	
3	1620	0.91	0.98	1.03	1.07	N/A	N/A	N/A	N/A	N/A	[200,0.98]
	1700	0.97	1.03	1.09	1.13	N/A	N/A	N/A	N/A	N/A	
	58	N/A	N/A	N/A	0.88	0.93	0.96	0.99	1.01	1.03	
4	410	N/A	N/A	N/A	0.35	0.39	0.44	0.48	0.52	0.54	
	1130	N/A	N/A	N/A	1.11	1.15	1.58	1.20	1.22	1.24	[800,1.1]
	1850	N/A	N/A	N/A	1.04	1.08	1.11	1.13	1.15	1.17	

approximately cover the whole block, minimizing boundary problems in block-kriging. Because kriging involves matrix inversions of the number of data N used within each block, one must limit N in order to balance out between stability of kriging and computer time. Neighborhood determination and variogram fitting procedures are discussed in Chapter 2. In each of the four regions, three to four blocks at latitudes $\sim -72^o, -76^o, -78^o, -80^o$ were used to determine both variogram parameters and neighborhood size. Figure 3-5a,b shows the neighborhood size determination for one particular block in region R-IV. Note an increase in uncertainties with the size of the neighborhood is often observed, and shows the potential boundary problem. In other words, when the block size expands to include a new cross-track, both the block estimates and uncertainties increase, then stabilize again when the neighborhood expands further to include more data within that cross-track. In addition, orbital or tracking problems could result in loss of data and cause an increase in uncertainty as a function of time. Based on the criteria of $\delta v_{est} \sim 0.05m$, 500 closest points to the block center is used for all regions (N=500). δv_{est_i} is defined as the difference between the block estimate using a the neighborhood size N_{i+1} and that at neighborhood size N_i, where $N_i < N_{i+1}$. The size of the neighborhood is dictated by blocks whose centers are in between cross-tracks (see Figure 2-7b in Chapter 2). It takes approximately 13 to 17 minutes per time step for N = 500, or approximately 13.5 to 17 hours to process all of ERS-1/2 data per region using a Pentium-4 2GHz processor with 2GB random access memory.

3.2.4 Anisotropic Variograms

Figure 3-4b and Table 3.4 show the raw semi-variograms and parameters $[\alpha, \beta]$ for the four regions of study. The variogram function used for ERS RA residuals has the form $\gamma(h) = \alpha h^\beta$ where h is distance in degrees, and parameters $[\alpha, \beta]$ are first solved for using linear least-square inversion, then fine-tuned using the procedure outlined in Chapter 2. In the first step, linear inversion, ERS elevation residuals (with respect to the ICESat DEM) can be fitted using two sets of parameters $[\alpha_1, \beta_1]$ and $[\alpha_2, \beta_2]$ for distances $h < 0.08^o$ and $h \leq 0.08^o$ respectively (Figure 3-4b). At

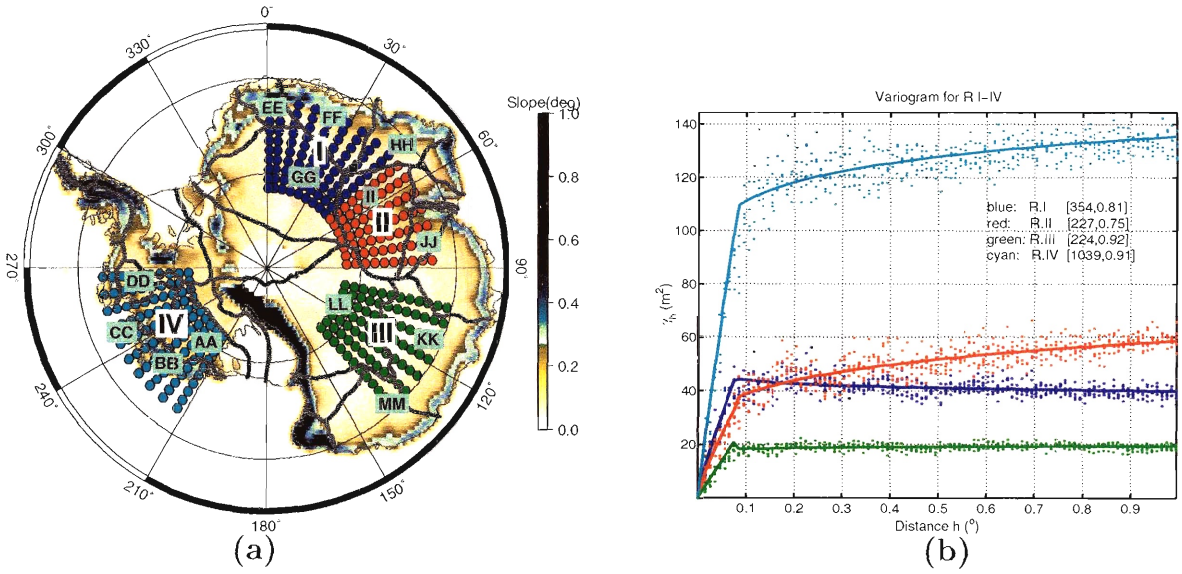

Figure 3-4 (a) Locations of four regions RI-RIV and basins AA-MM used in this study and (b) the regions' variograms. In brackets in (b) are parameters $[\alpha_1, \beta_1]$ used in fitting $\gamma(h) = \alpha_i h_i^{\beta_i}$ for each region. Parameters set $[\alpha_1, \beta_1]$ and $[\alpha_2, \beta_2]$ are used for distances [0,0.08°] and [0.08°,1°] respectively.

$h > 0.08^o$ residuals approach white noise with near zero β_2. At shorter distances the DEM is not sufficient to model the elevation field, and $[\alpha_1, \beta_1]$ are parameters of semi-variograms of the actual elevation field rather than the residuals. Using the statistical tests Q_1 and Q_2 as described in Chapter 2, the variogram function of the form $\gamma(h) = \alpha_1 h^{\beta}{}_1$ using only α_1 and β_1 fits the data the best. Solutions for $[\alpha, \beta]$ in each region is non-unique, and the final $[\alpha, \beta]$ is controlled by a combination of the variance of the residuals, which varies from $\approx 25m^2$ for R.III to $\approx 200m^2$ for R.IV (Table 3.5), and the slope of the raw-variogram near the origin. In Table 3.4, α is shown across the head of each column, and the values in the Table are of β, with the final parameter set listed in the last column. Figure 3-6 and 3-7 shows variations of $[\alpha_1, \beta_1]$ for all four regions as a function of azimuth and time. Variations in both α_1 and β_1 are smaller than those within individual azimuths. As a result, for the remainder of the chapter, the isotropic α and β as shown in Table 3.4 and Figure 3-7 are used (black triangles in Figure 3-7).

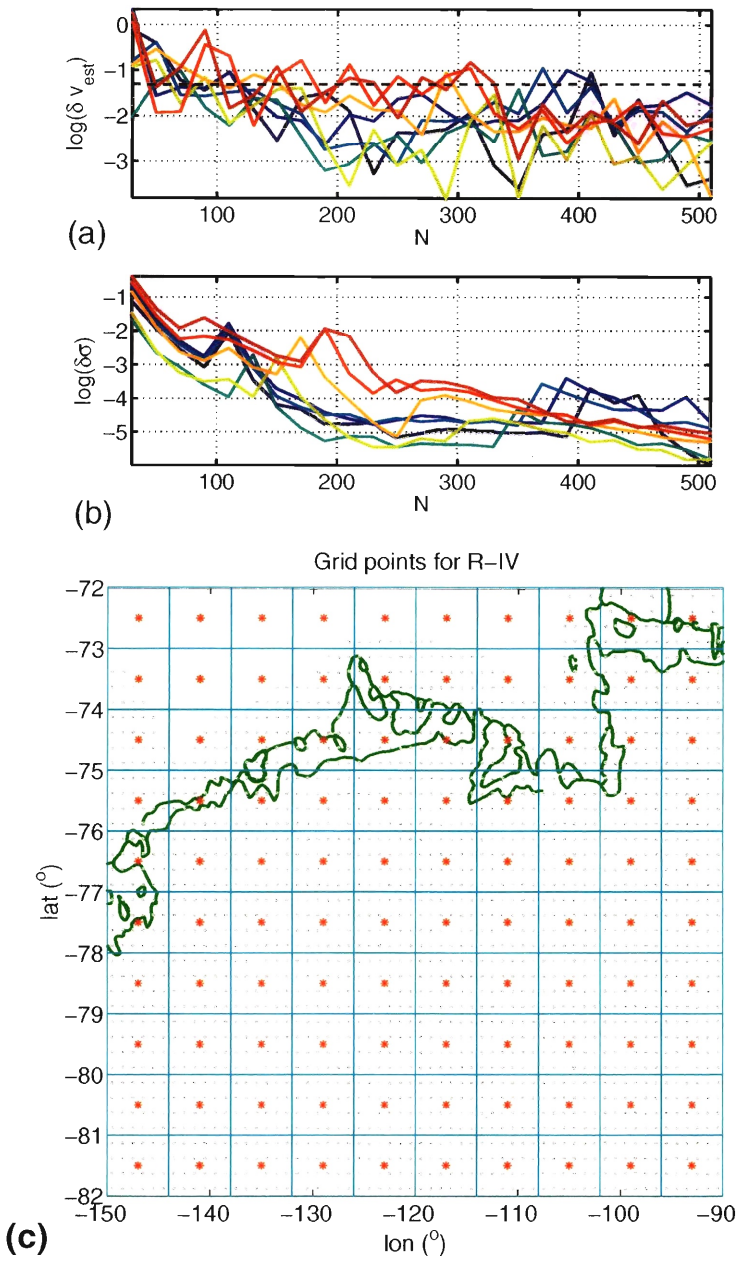

Figure 3-5 Neighborhood determination (a-b) for one block and grid set up for region IV (c). Sub-figures a-b are similar to Figure 2-8 from Chapter 2, and δv_{est} level of approximately $10^{-1.3}$ or 5cm (horizontal dashed line in (a)) is used to determine the block size. In this particular example at latitude $\sim -80^o$, a neighborhood N≈430 is sufficient. However at lower absolute latitude, N≈500. (c) The sub blocks have $\Delta lat = 0.25^o$ and $\Delta lon = [2^o, 1^o]$ for latitude ranges [-65^o,-72.5^o] and [-72.5^o,-82.5^o] (grey dots). In the final results, blocks are averaged to approximately $(100km)^2$ (cyan squares) with centers shown as red stars. There is a total of 2340 blocks in the region. The coast line is shown in green.

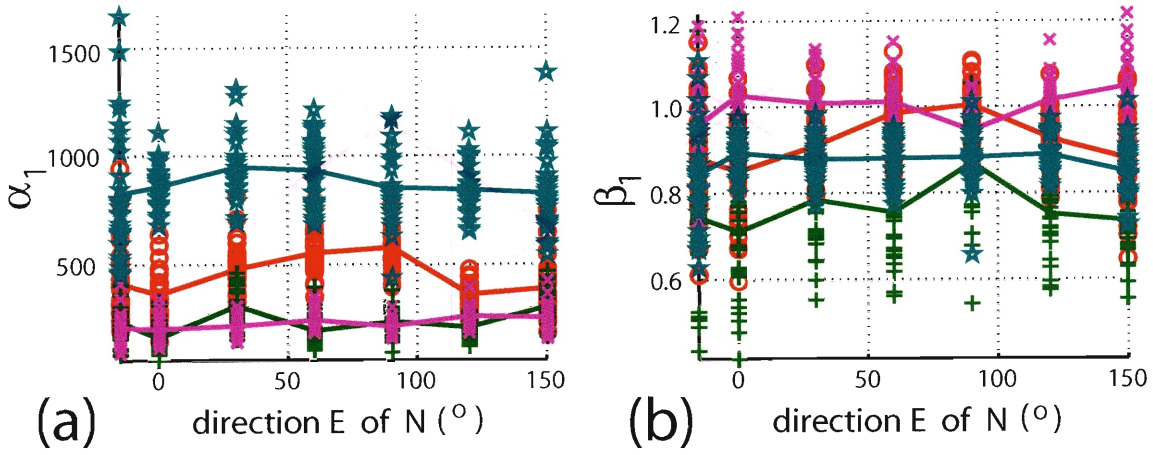

Figure 3-6 Azimuthal variations of $[\alpha_1, \beta_1]$. Both α_1 and β_1 (a-b) do not exhibit azimuthal dependence, with larger variations within each azimuth than between azimuths. The magenta, green, red, and cyan colors correspond to regions RI to RIV respectively.

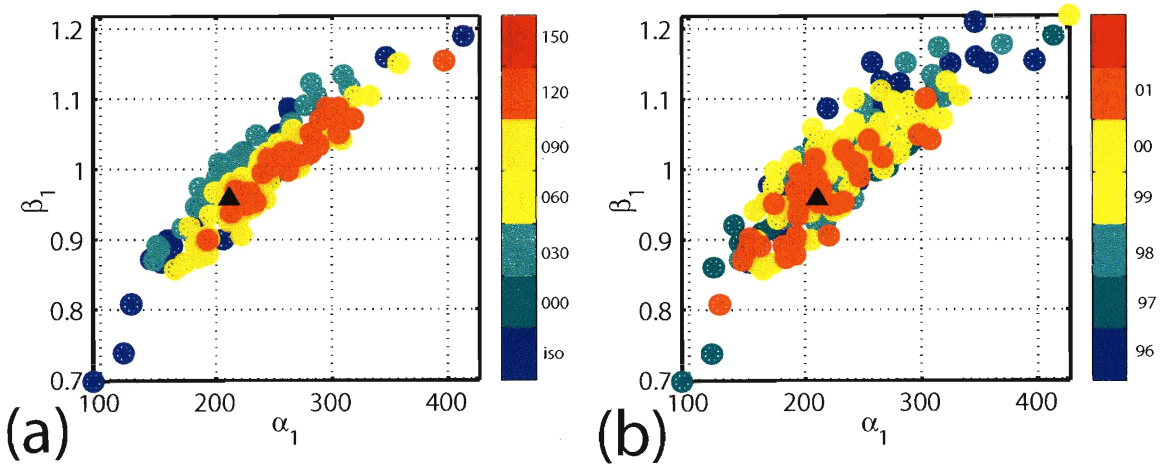

Figure 3-7 Scatter plots of α versus β as a function of azimuths (a) and the time the data were collected (b). There is no apparent drift in the data as a function of time. The parameters used in this study prior to fine-tuning are those of the isotropic case, shown as the black triangles here for R-III. See Table 3.4 for $[\alpha, \beta]$ in the other three regions.

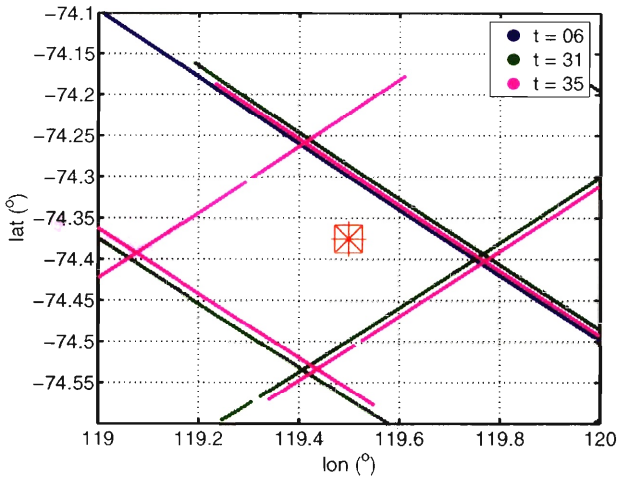

Figure 3-8 500 closest points for the block centered at [119.5°E,-74.4°N] (red square) for the time steps 06, 31, and 35 (out of 58 time steps).

3.2.5 Block uncertainties

The calculation for the block kriging uncertainty at each time step is given in Eqn 2.30 in Chapter 2. A full covariance matrix for the block estimates at different time steps t_i and t_j is needed to calculate the uncertainty in the height rate of change dh/dt. Assume a data vector $\mathbf{d} = [\hat{v}_{t_1}, \hat{v}_{t_2}, \cdots, \hat{v}_{t_N}]^T$ corresponding to time $[t_1, t_2, \cdots, t_N]$, and a model containing four terms $\mathbf{m} = [h0, dh/dt, B_1, B_2]^T$ for the surface height, height change, and sinusoidal components for the seasonal signal, the linear least square inversion solution is:

$$\mathbf{Gm} = \mathbf{d} \tag{3.1}$$

$$\mathbf{m} = (\mathbf{G}^T\mathbf{G})^{-1}\mathbf{G}^T\mathbf{d} = \mathbf{Kd} \tag{3.2}$$

$$\mathbf{cov}_m = \mathbf{K}(\mathbf{cov}_d)\mathbf{K}^T \tag{3.3}$$

where $\mathbf{cov}_m$ is the covariance matrix of the model parameters, and $\mathbf{cov}_d$ the covariance matrix of the block height estimates. The 2×2 matrix $\mathbf{cov}_d$ between two time steps t_i and t_j is calculated using the kriging weights w_i and data covariance function $C(h)$ where $C(h) = C(0) - \gamma(h)$. $C(h)$ between different time steps will simply be a function of separation distance, and its structure for the 500 points at time step t_i and 500 points at time step t_j is:

$$\mathbf{C}(t_i,t_j)=\begin{bmatrix} C_{11}(t_i) & \cdots & C_{1N}(t_i) & C_{11}(t_i,t_j) & \cdots & C_{1N}(t_i,t_j) \\ \vdots & \ddots & \vdots & \cdots & \ddots & \cdots \\ C_{N1}(t_i) & \cdots & C_{NN}(t_i) & C_{N1}(t_i,t_j) & \cdots & C_{NN}(t_i,t_j) \\ C_{11}(t_i,t_j) & \cdots & C_{1N}(t_j) & C_{11}(t_j) & \cdots & C_{1N}(t_j) \\ \vdots & \ddots & \vdots & \cdots & \ddots & \cdots \\ C_{N1}(t_i,t_j) & \cdots & C_{NN}(t_i,t_j) & C_{N1}(t_j) & \cdots & C_{NN}(t_j) \end{bmatrix} \tag{3.4}$$

and $\mathbf{cov}_d$ is:

$$\mathbf{cov}_d=\begin{bmatrix} w_1(t_i) & \cdots & w_N(t_i) & 0 & \cdots & 0 \\ 0 & \cdots & 0 & w_1(t_j) & \cdots & w_N(t_j) \end{bmatrix}\mathbf{C}(t_i,t_j)\begin{bmatrix} w_1(t_i) & 0 \\ \vdots & \vdots \\ w_N(t_i) & 0 \\ 0 & w_1(t_j) \\ \vdots & \vdots \\ 0 & w_N(t_j) \end{bmatrix} \tag{3.5}$$

A full scale calculation of $\mathbf{cov}_d$ for each block using 500 closest points and for 58 time steps (spanning ERS-2 temporal coverage) will require calculations of matrices of the size $500 \cdot 58 \times 500 \cdot 58$ or 29000×29000. Due to lack of computer memory, only two pairs of time steps are calculated and used as a guideline for approximating the off-diagonal terms in $\mathbf{cov}_d$. Figure 3-8 shows the data coverage (500 closest points) in one block centered at [119.5°E,-74.4°N] in region R-III for three time steps $t=[6,31,35]$. Time step $t=6$ has the least amount of data coverage, and $t=[31,35]$ have approximately the same coverage. Point kriging is used here to obtain an insight into the correlation between the block height estimates $\hat{v}_{t_i}$ and $\hat{v}_{t_j}$. Using Eqn 3.5, the covariance matrices for the pairs t=[35,31], [35,06], and [31,06] are:

$$\mathbf{cov}_d(35,31)=\begin{bmatrix} 171.5 & 171.0 \\ 171.0 & 170.8 \end{bmatrix} \tag{3.6}$$

$$\mathbf{cov}_d(35,06) = \begin{bmatrix} 171.5 & 173.6 \\ 173.6 & 181.0 \end{bmatrix} \tag{3.7}$$

$$\mathbf{cov}_d(31,06) = \begin{bmatrix} 170.8 & 168.5 \\ 168.5 & 169.6 \end{bmatrix} \tag{3.8}$$

Based on this calculation, with the correlation of the block estimates between different time steps highly correlated, an approximation scheme for the off-diagonal terms in $\mathbf{cov}_d$ between time steps t_i and t_j will be:

$$\mathbf{cov}_d(t_i,t_j) = \begin{bmatrix} \sigma_k^2(t_i) & min(\sigma_k^2(t_i),\sigma_k^2(t_j)) \\ min(\sigma_k^2(t_i),\sigma_k^2(t_j)) & \sigma_k^2(t_j) \end{bmatrix} \tag{3.9}$$

The covariance matrix in Eqn 3.6 is then approximated as:

$$\mathbf{cov}_d(35,31) \approx \begin{bmatrix} 171.5 & 170.8 \\ 170.8 & 170.8 \end{bmatrix} \tag{3.10}$$

A similar calculation is done to obtain the covariance matrix between kriging and averaging at the three time steps by replacing the weights w_i in Eqn 4.5 with the factor 1/N for the corresponding time step. The off-diagonal terms in $\mathbf{cov}_d$ between the block estimates using kriging and averaging are also positive with approximate magnitudes as those along the diagonal. As a result, these off-diagonal terms will be approximated similarly using $min(\sigma_k^2(t_i),\sigma_a^2(t_j))$, where the subscripts k and a are for kriging and averaging. The block estimate variances for $t = [06, 31, 35]$ are [3.83,0.49,0.23] using Eqn 2.30 (compared to $\approx$[181.0,171.5,170.8] in point kriging). When the kriging weights in Eqn 2.30 are replaced with 1/N, the variances for the blocks' averages are [2.67,3.77,4.09]. The data covariance matrix $\mathbf{cov}_d$ for the three time steps between kriging and averaging is now approximated as:

$$\mathbf{cov}_d \approx \begin{bmatrix} 3.83 & 0.49 & 0.23 & 2.67 & 3.77 & 3.83 \\ 0.49 & 0.49 & 0.23 & 0.49 & 0.49 & 0.49 \\ 0.23 & 0.23 & 0.23 & 0.23 & 0.23 & 0.23 \\ 2.67 & 0.49 & 0.23 & 2.67 & 2.67 & 2.67 \\ 3.77 & 0.49 & 0.23 & 2.67 & 3.77 & 3.77 \\ 3.83 & 0.49 & 0.23 & 2.67 & 3.77 & 4.09 \end{bmatrix} \tag{3.11}$$

When a full $\mathbf{cov}_d$ is approximated for all 58 time steps, the covariance matrix $\mathbf{cov}_m$ for the model parameters can be then calculated using Eqn 3.3 and used for comparison between kriging and averaging.

3.2.6 Surface Backscatter Power Correction

Using ERS elevation data, Wingham et al. [1998] and Arthern et al. [2001] found a correlation between backscatter power temporal variation and surface height change of 0.7 or higher, and Wingham et al. [1998] made a constant 0.38m/dB correction to all surface height change rate. The correction removed rates ranging between -0.257m/yr to .388m/yr with mean 0.011m/yr and standard deviation 0.0611m/yr across Antarctica. Zwally [2005] studied the relationship between received power and surface height as a function of time, and made corrections based on how strong / how weak their correlations are. Their final corrections, which are also used in this study, are as follows,

$$\begin{aligned} H(t)_{corr} &= H(t)_{uncorr} - (H_o + \tfrac{dH}{dAGC} \times AGC(t)) \quad |r| \geq 0.2 \\ &= H(t)_{uncorr} \quad |r| < 0.2 \end{aligned} \tag{3.12}$$

where $H(t)_{corr}$ and $H(t)_{uncorr}$ are the surface height time series before and after correction is applied, H_o and dH/dAGC are the y-intercept and slope of the best fitted line between surface height H and received power AGC, and r is the correlation coefficient between H and AGC. A scatter plot of r versus dH/dAGC is shown in Figure 3-9 for one block in W-Ant. In addition, a maximum and minimum dH/dAGC

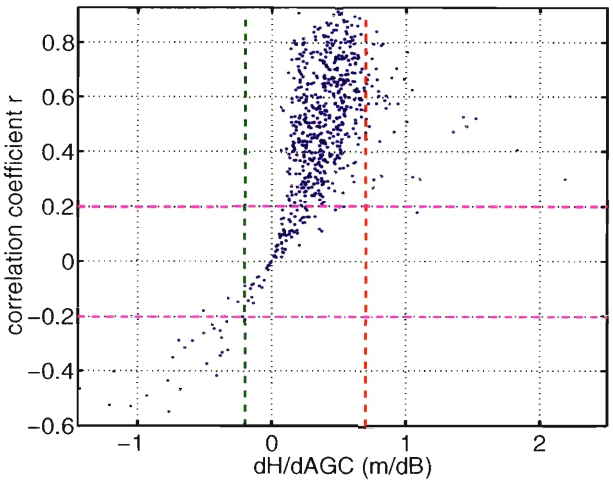

Figure 3-9 Scatter plot of correlation coefficient r and slope of the best fitted line between surface height (H) and received power (AGC). When $|r| < 0.2$ there will be no correction to H(t). When the slope $dH/dAGC < -0.2$ and $dH/dAGC > 0.7$, they are reset back to -0.2 and 0.7 to prevent anomalously large corrections.

were set at [-0.2,0.7] to prevent anomalously large corrections applied to surface height time series [Zwally, 2005].

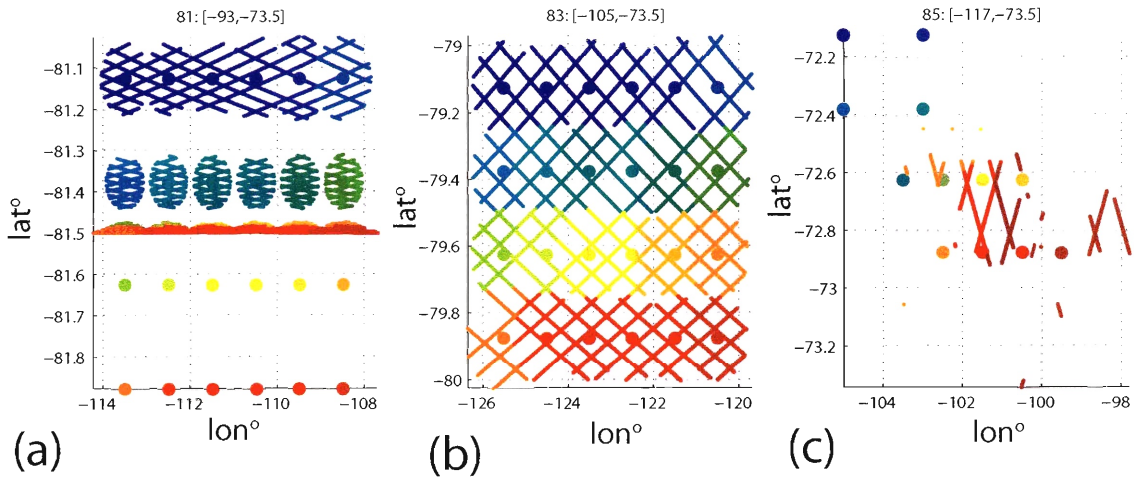

Figure 3-10 Data coverage for three $\sim (100km)^2$ blocks in region IV with each sub-block and corresponding 500 nearest points coded in matched color. In (a), some of the sub-blocks are beyond the ERS coverage area, and their block-kriged results will have very large uncertainties. At the edge of the ice-sheet in (c), data quality deteriorates resulting in insufficient coverage and large block-kriged uncertainties.

3.3 Block Kriging Results and Discussion

Data coverage over 35 days for a few blocks in R-IV are shown in Figure 3-10, and Figure 3-11 shows uncertainties as obtained from block kriging for time step #01 over the entire R-IV, along with uncertainties in the time series for one block. The parameter H(t) at time steps #42 and #84 consistently deviates from other points in the time series and were omitted during the weighted linear least square fitting procedure. The weighting factor is inversely proportional to the block estimate uncertainty σ_k for the corresponding time step. The model includes a surface height term, a surface height change term, and two terms for the sine and cosine components of the seasonal signal, and has the form $H(t_i) = h0 + \frac{dh}{dt}(t_i) + B_1 cos(2\pi t_i) + B_2 cos(2\pi t_i)$. Figure 3-12, 3-15, and 3-16 show results for dh/dt, seasonal signal amplitude B and phase θ for all ERS-2 data. Uncertainty of individual $H(t_i)$ (Figure 3-11b) are mapped to the model parameters via the weighted linear least square general inverse matrix. The color scales for dh/dt, B, and θ figures are adapted from Zwally [2005] to facilitate cross-comparisons of the results. In general, blocks at latitudes -81.5^o and further south, and along the coast have very large uncertainties due to insufficient data coverage, and are excluded from the analysis. Plots of all blocks' time series are shown

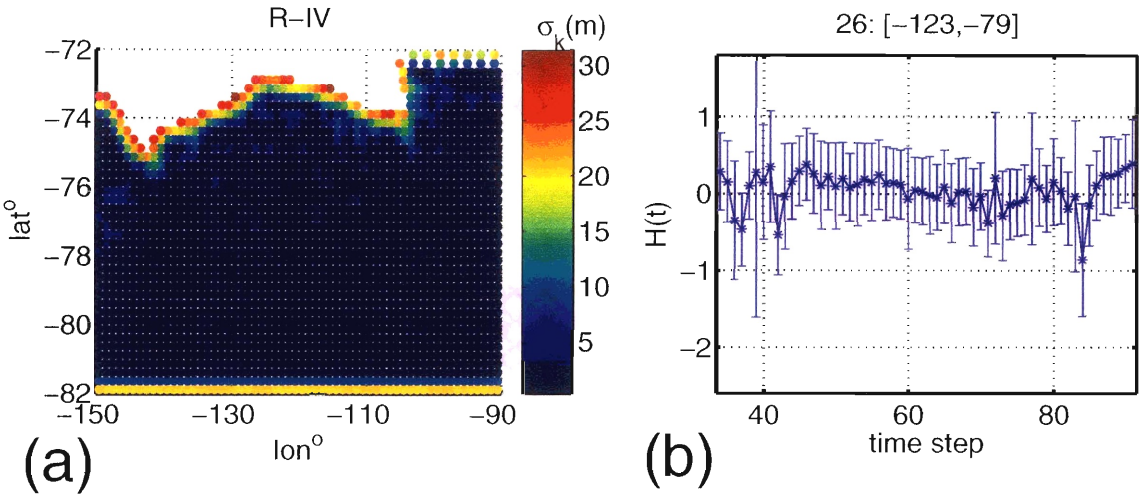

Figure 3-11 (a) Uncertainties in the block height estimates from block-kriging for R-IV time step #01 and (b) H(t) time series for one of the blocks. As discussed in the previous figure, uncertainties are very large at the edge of the ice-sheet and at near latitude -82^o. In the time series, H(t=42) and H(t=84) consistently have heights deviating from other points in the time series, and are excluded from the weighted linear least square fit. Time-step #39 consistently has anomalously large uncertainties. In (b), the label on top of the sub-figure indicates the block number, longitude, and latitude of the block.

in Appendix A, and numerical results for the parameters are shown in Table A.1.

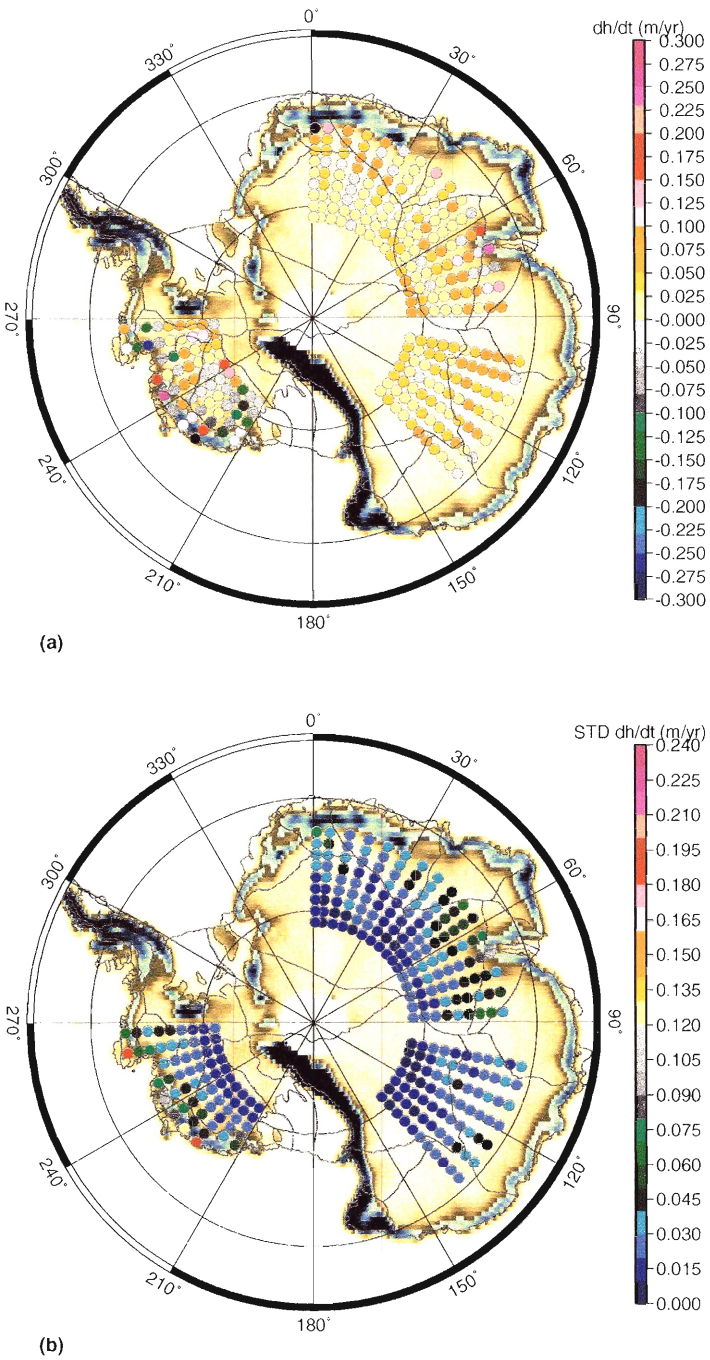

Figure 3-12 Estimated dh/dt (a) and uncertainties (b) with surface slope shown as the background field, and drainage divides shown as black lines. (a) 96% of the blocks in E-Ant have dh/dt less than 0.1m/yr in magnitude with positive mean of 0.03m/yr and RMS 0.03m/yr, and 75% have dh/dt less than 0.05m/yr in magnitude with mean of 0.02m/yr and RMS 0.02m/yr. Large dh/dt magnitudes at the Amery Ice Shelf ([lon,lat] $\approx [70^o E, 80^o E, -76^o N, -72^o N]$) range from -0.05m/yr to 0.26m/yr. In W-Ant 90% of the blocks have dh/dt less than 0.20m/yr in magnitude, and 68% with dh/dt less than 0.10m/yr in magnitude. These blocks lie in the interior of West Antarctica.

3.3.1 *Dh/dt*

96% of the blocks (212/221) in the interior of East Antarctica (E-Ant) have *dh/dt* less than 0.1m/yr in magnitude with positive mean and root mean square (RMS) scatter of 0.03m/yr and 0.03m/yr, and 75% (169/221) have *dh/dt* less than 0.05m/yr in magnitude with mean and RMS of 0.02m/yr and RMS 0.02m/yr (Figure 3-12a). Uncertainties in E-Ant are less than $\pm 0.05 m/yr$ for all blocks in the interior (204/221), and increase to between 0.06 and 0.10m/yr along the coast and at the Amery Ice Shelf. (Figure 3-12b). Two blocks with *dh/dt* significantly larger than average are at the Amery Ice Shelf, 0.17±0.07m/yr and 0.26±0.10m/yr. (Figure 3-12a between [lon,lat] of $[60^o, 80^o, -76^o, -72^o]$). The time series and model fit for these two blocks are shown in Figure 3-13a,b. In West Antarctica (W-Ant) 90% of the blocks (62/69) have *dh/dt* less than 0.20m/yr in magnitude, and 68% with *dh/dt* less than magnitude 0.10m/yr. All blocks within latitude range $[-81^o, -78^o]$ have uncertainties less than $\pm 0.05 m/yr$ (Figure 3-12b). Closer to the coast line, uncertainties increase to between 0.05m/yr and 0.15m/yr. Along the coast the two blocks with the largest uncertainties $\sim$ 0.20m/yr have *dh/dt* of -1.03m/yr and 0.48m/yr (Figure 3-12a). The time series for these two blocks are shown in Figure 3-13c,d.

Histograms of *dh/dt* shows a positive mean and an RMS of 0.03m/yr and 0.06m/yr in E-Ant, and mean and RMS of 0.01m/yr and 0.18m/yr in W-Ant (Figure 3-14a). As a function of latitude, *dh/dt* has positive mean across all latitudes except at latitude -71°N. However the RMS scatter at each latitude band is approximately equal to the mean, which gives *dh/dt* ranges that include 0.00m/yr (Figure 3-14b). The large RMS scatter at latitude -73°N is due to the inclusion of the Amery Ice Shelf. In W-Ant, there is no clear pattern of *dh/dt* with latitude, and RMS scatters are nearly one order of magnitude larger than in E-Ant at each corresponding latitude. Backscatter corrections bring *dh/dt* in the interior of E-Ant from near zero (mean 0.001 m/yr, RMS 0.069 m/yr) to positive (mean 0.03 m/yr, RMS 0.06 m/yr), and those between $[-72^o, -70^o]$ in region III from mean 0.1m/yr and RMS 0.08m/yr down to mean 0.008m/yr and RMS 0.03m/yr.

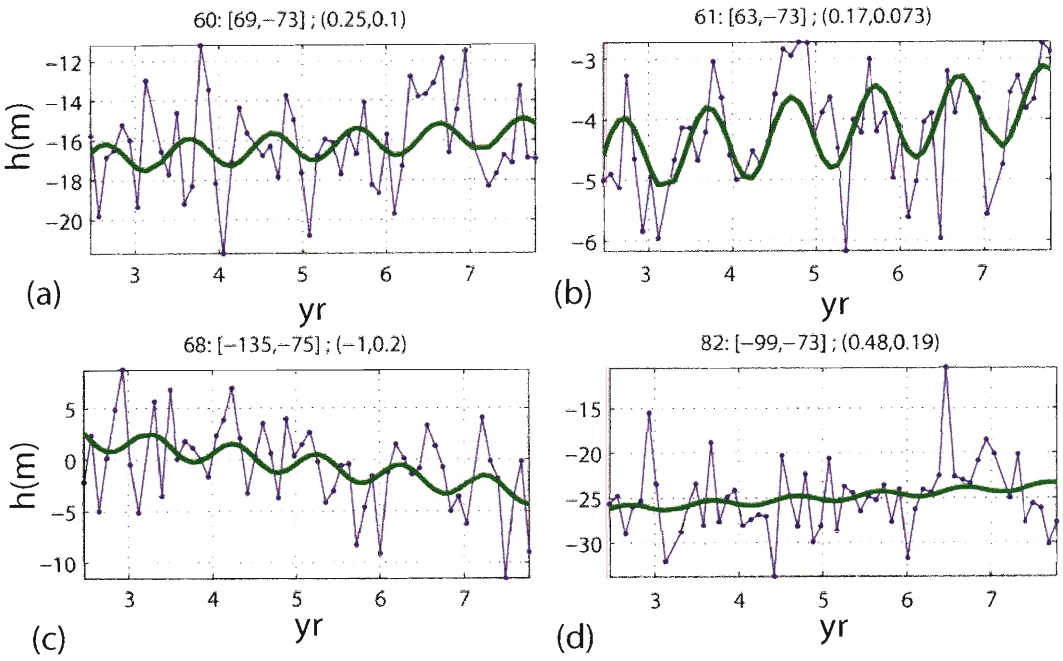

Figure 3-13 Time series for two blocks at the Amery Ice Shelf (a-b) and along the coast in W-Ant (c-d). These blocks have large positive and negative dh/dt that exceeds the mean ± 2·RMS in each of the corresponding regions. The label on top of each subplot indicates the block number, longitude, latitude, dh/dt and $\sigma_{dh/dt}$ values.

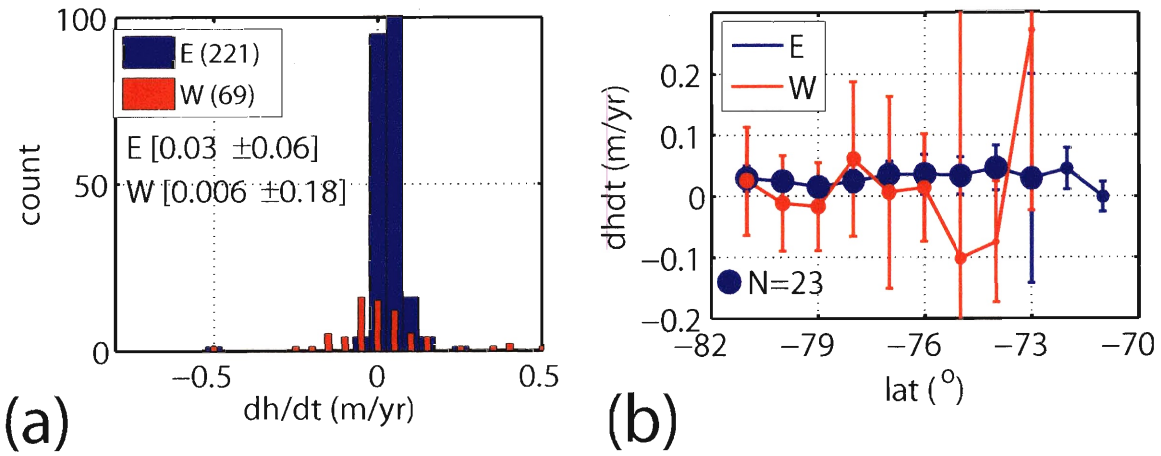

Figure 3-14 Statistics of dh/dt for E-Ant (blue) and W-Ant (red) (a), and latitudinal dependence of dh/dt (b). Shown in the brackets in (a) are the mean and RMS scatter for E-Ant (E) and W-Ant (W). There is no clear pattern of dh/dt with latitudes (b).

3.3.2 Seasonal Signal

Figure 3-15 and 3-16 show amplitude and phase results. Unit of the seasonal signal amplitude B is kept in meters of snow height to facilitate cross-comparison with cross-over results produced by Zwally [2005]. All blocks have amplitude uncertainties $\leq$ 0.05m. 83% of the blocks in the interior of E-Ant (183/221) have amplitude B less than 0.15m and within those, 176 have uncertainties less than $\pm$0.03m (Figure 3-15a). At the Amery Ice Shelf ([lon,lat] = [60^{o}E,80^{o}E,-76^{o}N,-72^{o}N]) amplitudes are systematically larger with B ranging from 0.15 to 0.75m and mean and RMS of 0.37m and 0.18m. Uncertainties are also systematically larger in the Amery Ice Shelf region, with σ_B ranging from 0.06m to 0.12m (Figure 3-15b). The two blocks with the largest B, 0.75$\pm$0.03m and 0.63$\pm$0.04m, coincide with those with the largest dh/dt magnitudes and are shown in Figure 3-13a,b. In W-Ant, blocks in the interior (50 blocks) have amplitudes less than 0.30$\pm$0.04m, and 32 of those blocks have amplitudes less than 0.10m. Between latitudes $[-76^o, -74^o]$ uncertainties are between 0.06 and 0.12m, and the amplitudes range from 0.30m to 1.25m (Figure 3-15). One block at the coast with large amplitude, 1.25$\pm$0.06m, is shown in Figure 3-17. The large uncertainties along the coast are due to limited data as shown in Figure 3-10c and Figure 3-11a. Overall, amplitudes have mean and RMS of 0.11m and 0.11m in E-Ant, and 0.20m and 0.23m in W-Ant repsectively (Figure 3-18a). There is a trend of increasing amplitude northward in both E-Ant and W-Ant (Figure 3-18b). The large-amplitude mean and RMS at latitude -73^{o}N is due to the inclusion of the Amery Ice Shelf (Figure 3-18b).

Phase maximum θ in E-Ant shows a strong correlation with locations of drainage divides (Figure 3-16a). Specifically, within R-I and R-II, as shown in Figure 3-19, the mean and RMS of θ are 421 (56-day) and 27 days along or within 1 block of the divides, and 178 and 61 days away from the divides respectively. The relationship between phase and drainage divides is less obvious in R-III. Uncertainties are larger along the drainage divides ($\sigma_\theta \sim \pm 45$ to ± 135) than in other part of E-Ant ($\sigma_\theta \sim \pm 5$ to ± 60). The overall distribution of θ is bimodal, with θ between Jan-Apr along

drainage divides and in R-III and May-Aug in other parts of E-Ant interior (Figure 3-18c, 3-19b,c). In W-Ant, θ does not exhibit bimodal statistics, and is between 88-225 days with mean and RMS of 187 and 65 days respectively (Figure 3-18c). There is no clear pattern of θ with latitude for either E-Ant or W-Ant (Figure 3-18d). The backscatter correction affects both phase and amplitude, with mean phases shifting from 15 days to 421 (or 56) days and 180 days to 160 days in the bimodal distribution, and amplitudes shifting from mean 0.17m to 0.11m with smaller RMS.

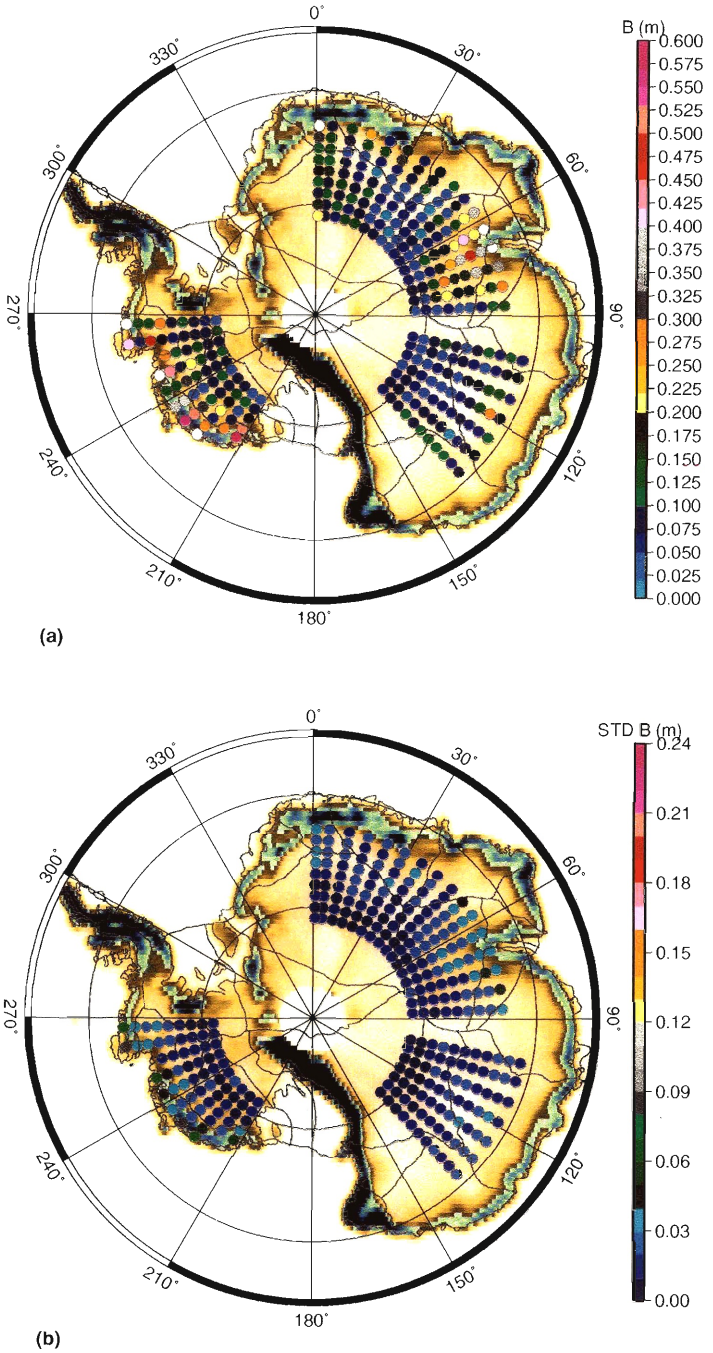

Figure 3-15 Seasonal signal amplitude B (a) and uncertainties (b). 83% of the blocks (183/221) have seasonal surface signal amplitude less than 0.15m and 96% of those (176) have uncertainties less than 0.03m. Similar to dh/dt, the concentration of high amplitude is at the Amery Ice Shelf, reaching as high as 0.75m. In West Antarctica, 72% of the blocks have B less than 0.30m. Along the edge of the ice-sheet, the amplitude reaches 1.25m.

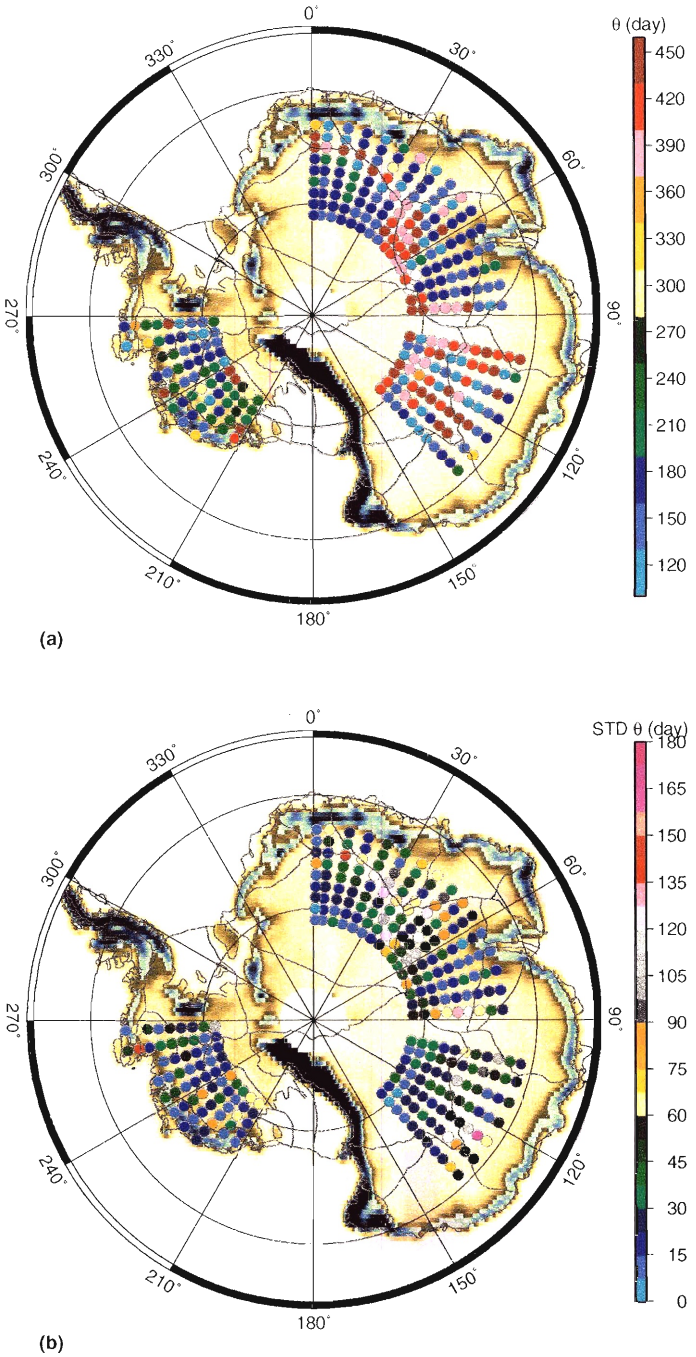

Figure 3-16 Seasonal phase θ maximum (a) and uncertainties (b). θ shows a very strong correlation with the drainage divides in East Antarctica. Along the drainage divides, $\theta \approx 420-450(55-85)$ days implying surface height maximum at the end of Feb to March. Away from the divides, $\theta \approx 135-200$ days yielding surface maxima toward mid-May to mid-Aug. In West Antarctica, most of the interior has $\theta \approx 135-225$ days, yielding surface maxima at mid-May to Sept.

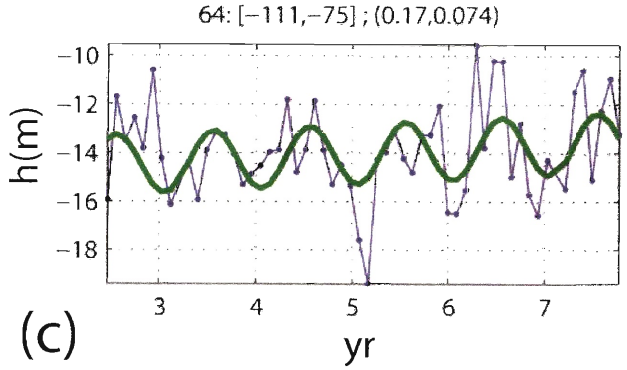

Figure 3-17 Time series for one block in W-Ant with large seasonal signal amplitude of 1.25m. The label at the top of the figure indicates the surface number, longitude, latitude, dh/dt estimate and $\sigma_{dh/dt}$.

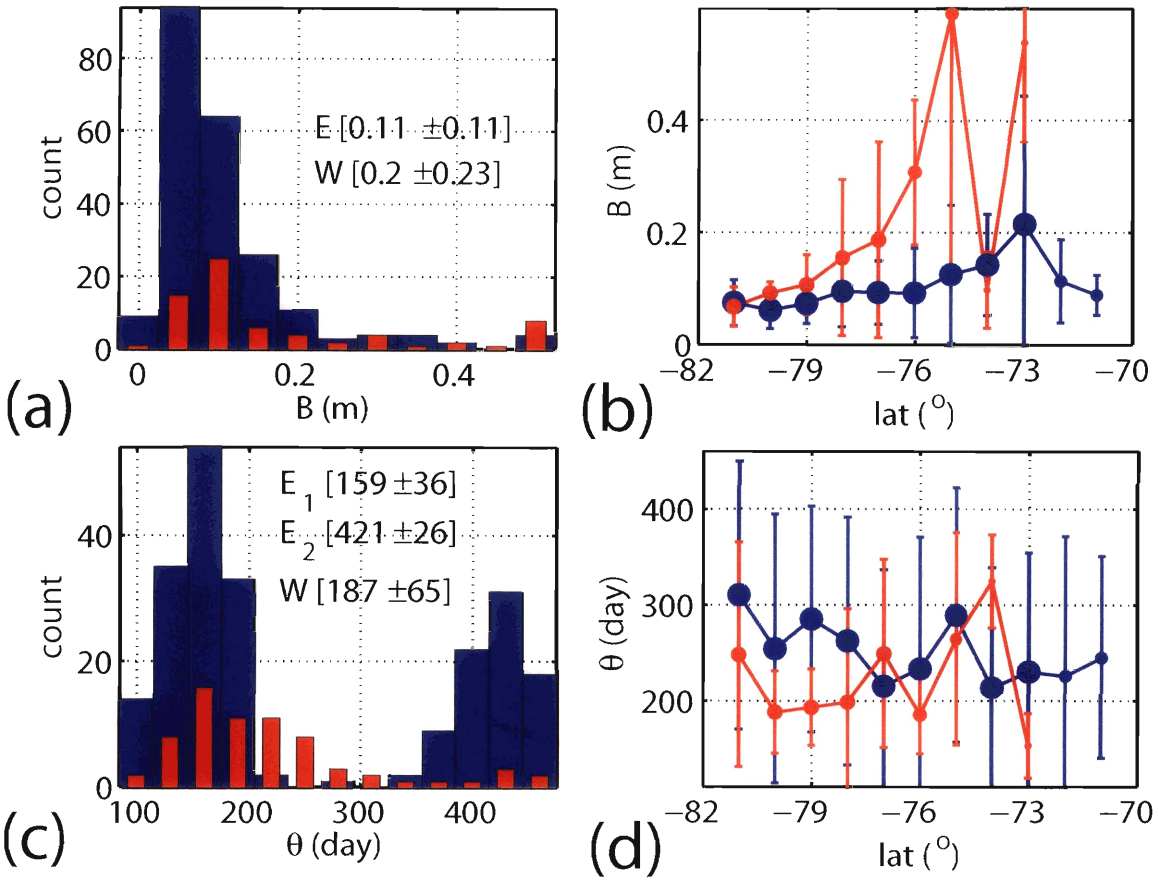

Figure 3-18 Statistics of amplitude B (a) and phase θ maximum (c) for E-Ant (blue) and W-Ant (red), and latitudinal dependencies of B (b) and θ (d). Shown in the brackets in (a) and (c) are mean and RMS scatter for each respective parameter. The bimodal phase maximum in (c) corresponds to end of Feb ($\theta \approx 421$ day) and mid-June ($\theta \approx 160$ day). There is evidence of B increasing southward in both E-Ant and W-Ant. However the RMS scatter for both regions is too large to support this observation.

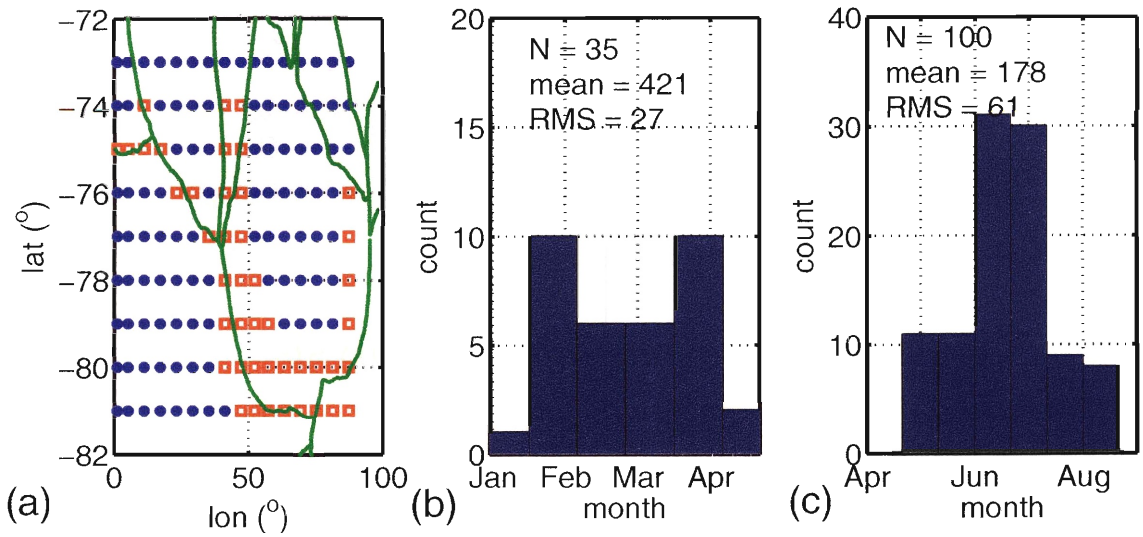

Figure 3-19 Relationship between phase maxima and locations of the drainage divides. Statistics in (b) are for blocks along the drainage divides (red squares in (a)), and statistics in (c) are for the blue star blocks in (a).

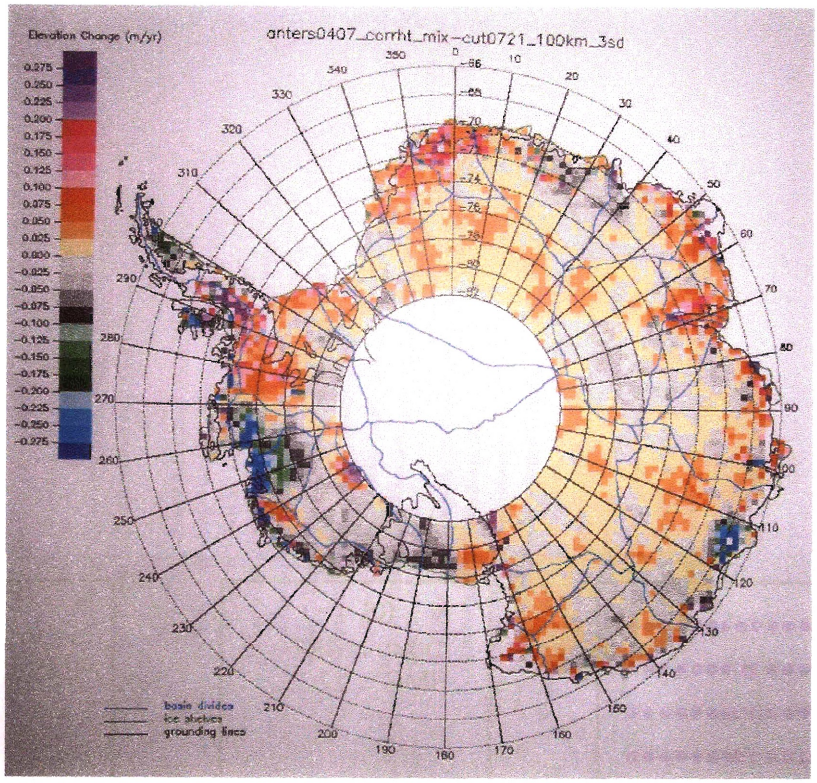

Figure 3-20 Zwally [2005]'s unpublished ERS cross-over analysis results for dh/dt.

3.4 Kriging versus cross-over analysis

Direct comparison of dh/dt results with Wingham et al. [1998] is not feasible because of a different grid resolution and that only ERS-1 data were used with a different backscatter correction in Wingham et al. [1998]. Results from Zwally et al. [2002]; DiMarzio et al. [2004]; Zwally [2005] are more appropriate for comparison because these workers used ERS-1/2 data with the same retracking algorithm and backscatter correction. A copy of unpublished results from Zwally [2005] is shown in Figure 3-20 and Figure 3-24.

Original cross over results are at 50-km grid resolution. For direct comparison, cross-over results are averaged into each approximate 100x100km^2 block which are used in kriging analysis. Based on the search radius of 100-km, the 50-km dh/dt estimates are expected to be highly correlated (~40% overlapping). As a result, uncertainties of the block average dh/dt from cross-over will be approximated using Eqn 3.9, with σ_k^2 replaced by σ_{xover}^2. Thus uncertainties for the 100kmx100km block will have values

in the same order of magnitude as those in the original 50-km grid. A more accurate calculation of the correlations between the adjacent 50-km blocks is still being investigated. For cross comparison between the methods, it is assumed that the two methods generate independent dh/dt estimates. This assumption is based on the fact that the cross-over analysis uses less than 10% of the data. As an example, for the block centered at [lon,lat] of [119.5,-74.4] (Figure 3-8), there are approximately 240 cross-overs (or 960 data points, 4 per cross-over) per time step, which gives ~55680 data points being used in cross-over analysis for all 58 time steps. In comparison, kriging uses 8000 points per time step (500 x 16 subblocks), which results in ~464000 data points being used for all 58 time steps. In reality, due to the fast drop-off in the weights with distance, the effective number of points used in kriging could be less. However the geometry difference between the two methods will result in approximately independent data points being used. For blocks at higher absolute latitude, the number of cross overs increases. However the spatial distribution of cross-overs within the 100km radius search is different than the 500 closest points to each subblock.

3.4.1 dh/dt

Based on this uncorrelated assumption between the two methods, profiles of dh/dt from each method, and their differences are generated in Figure 3-21. Six profiles, one from the smoothest region R-III, two from the Amery Ice Shelf, and three from W-Ant are chosen for detailed comparison. Figure 3-21 identifies the six profiles with red labels for latitudes, and with profile numbers [1]-[6] shown in the brackets. Profile [1], centered at latitudes -78°N and longitudes [100°E,140°E] shows dh/dt in the range -0.009±0.003 to 0.017±0.015m/yr for cross-over, and 0.021±0.019m/yr to 0.066±0.029m/yr for kriging (Figure 3-21c). The differences between the two methods range from 0.024±0.022 to 0.065±0.033m/yr. The pattern of dh/dt across all longitudes is similar in both methods. However kriging systematically gives higher dh/dt than cross-over analysis, with the mean difference across all longitudes of 0.039

for this profile. This systematic difference is observed in all profiles across R-III (Figure 3-21c).

Profile [2] and [3] are from R-II at latitudes -74°N and -73°N, which covers the upper part of the Amery Ice Shelf (Figure 3-21b). Here both methods observe large positive dh/dt (0.059±0.055m/yr for cross-over and 0.25±0.10m/yr for kriging) at [-73°N,69°E]. However along profile [2], cross-over yields negative dh/dt (-0.044±0.036m/yr) where kriging yields large positive dh/dt of 0.11±0.08m/yr (Figure 3-21b). The time series for this particular block is shown earlier in Figure 3-13a. Both profiles show differences between the two methods at the Amery Ice Shelf that are significantly different, specifically kriging yielding dh/dt of approximately 0.15 to 0.19 ±0.11m/yr higher than cross-overs (Figure 3-21b). In the interior of R-II, kriging again yields systematically higher dh/dt than cross-overs (Figure 3-21b). One example is along the profile at latitude -81°N (Figure 3-21b), where dh/dt patterns are similar in both methods, with a difference of approximately 0.05±0.02m/yr across all longitudes.

Profiles [4]-[6] are from R-IV in W-Ant at latitudes -81°N, -77°N, and -75°N (Figure 3-21d). Profile [5] at -81°N shows the same pattern of negative and positive dh/dt in both methods, with kriging having larger magnitudes. The large positive dh/dt here correspond to the positive signal observed in Figure 3-2b at [lon,lat] of [120°W,-82°N]. In this case, the large uncertainties in cross-over estimates are the limiting factors in the comparison. Specifically the large uncertainties in cross-over maps directly into the difference, yielding differences that are not significantly different from 0.00m/yr (Figure 3-21d). In the last two profiles, profiles [5]-[6], the cross-over method shows pervasive negative rates across longitudes -93°E to -123°E. Uncertainties for these negative rates are also large, ±0.07 to ±0.77m/yr. Kriging results only show the negative dh/dt along profile [5], and a large positive dh/dt signal across longitudes -111°E to -117°E in profile [6]. For one block, dh/dt is 0.17±0.07m/yr in kriging and -1.02±0.77m/yr in cross-over. This block at [lon,lat] of [-111°E,-75°N] is shown earlier in Figure 3-17. Despite the large uncertainties in both methods, the difference for this block and others along these two profiles are significantly different from 0.00m/yr.

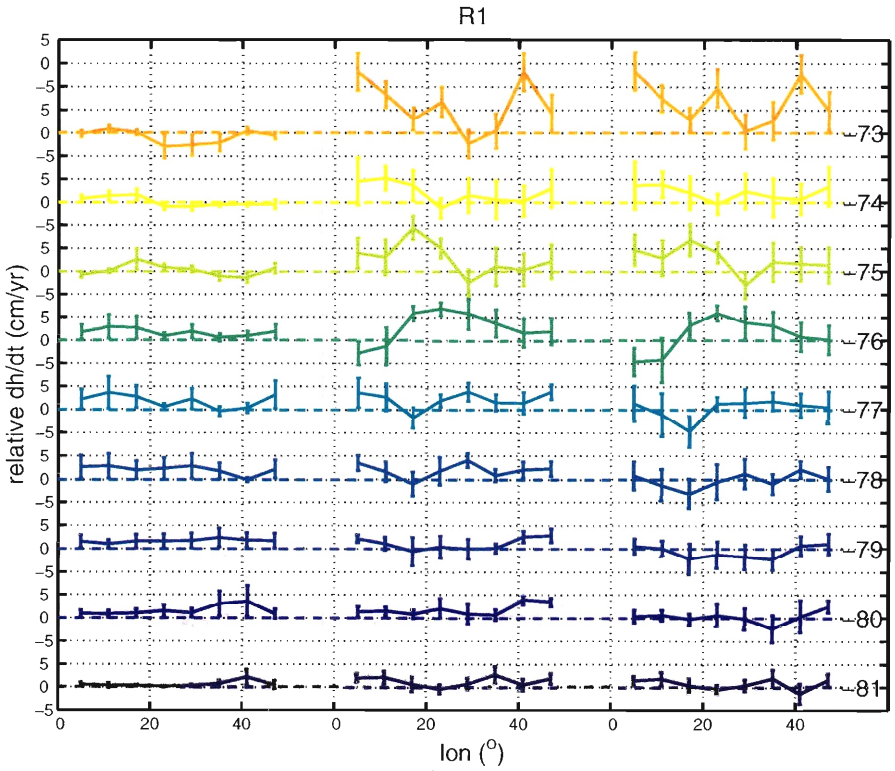

(a)

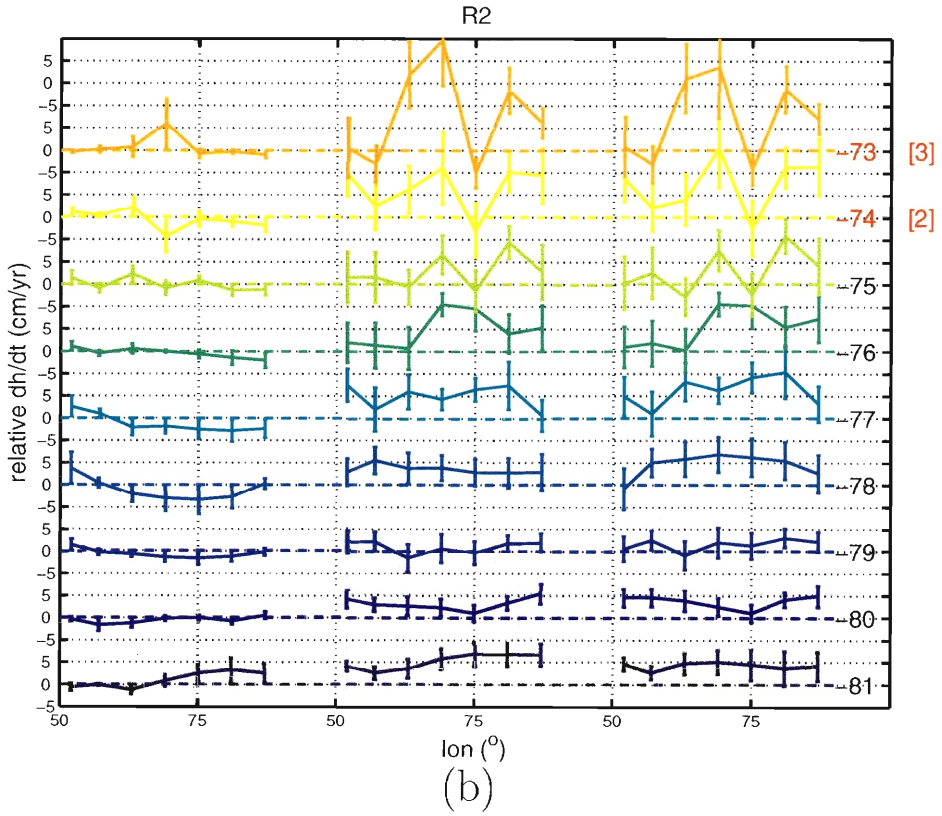

(b)

Figure 3-21 Profiles of cross-over dh/dt (left panel), kriging dh/dt (middle panel), and $\delta dh/dt$ (right panel) for regions R-I (a), R-II (b), R-III (c, next page), and R-IV(d, next page). $\delta dh/dt$ is the difference between kriging and cross-over results. The six profiles chosen for further analysis are numbered [1] through [6] and identified with the red label of latitude.

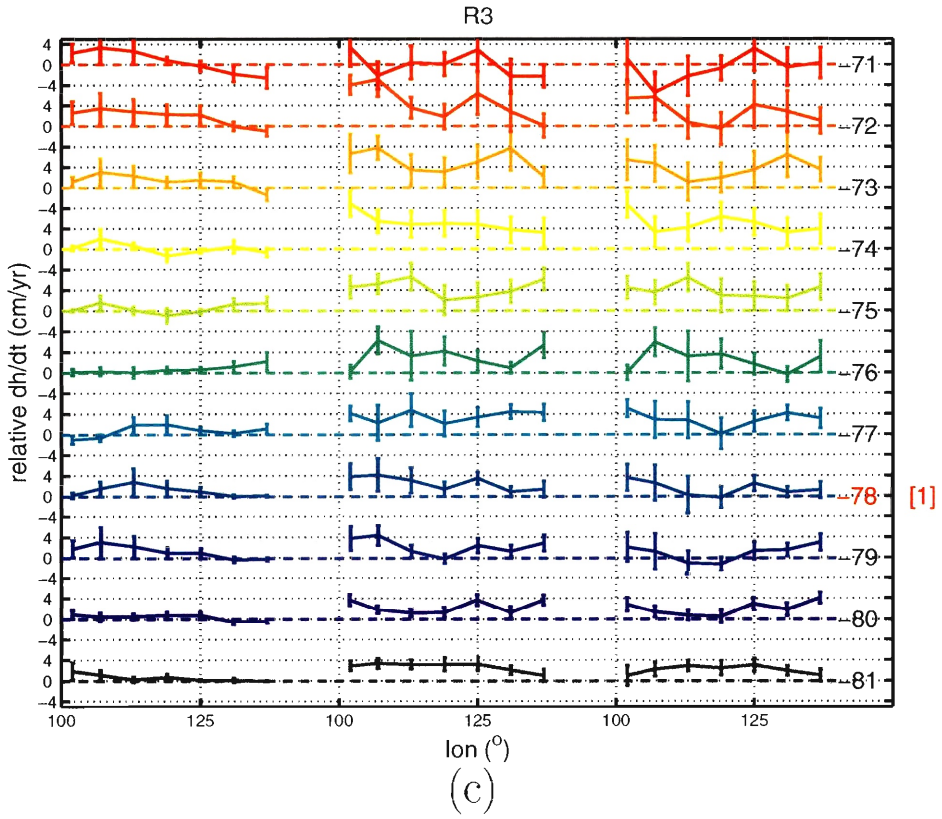

(c)

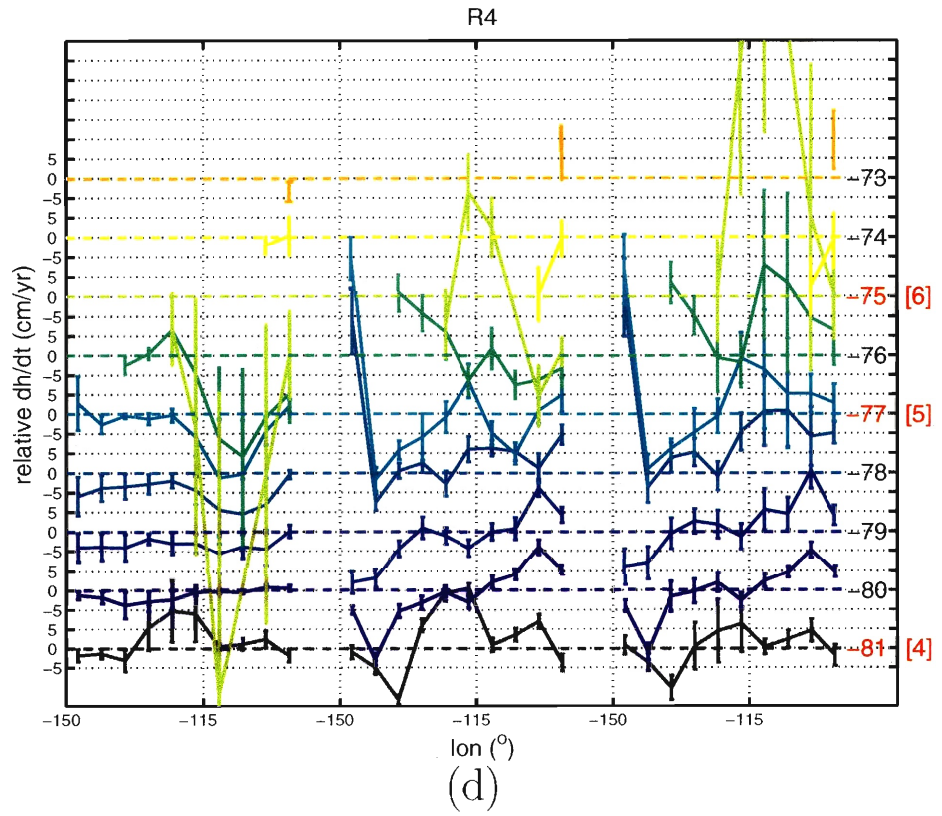

(d)

Figure 3-21 cont'd . The y-axis labels are dh/dt on the left, and latitude on the right.

One possible explanation for the large difference in dh/dt observed between the two methods is that cross-over analyses use both ERS-1 and ERS-2 data, whereas kriging uses only ERS-2 data. If we assume that the dh/dt in each block is deterministic and constant with time, then there should not be a difference in dh/dt estimates when ERS-1 data were used or excluded. However, a bias exists between ERS-1 and ERS-2 and varies spatially based on local surface heights [DiMarzio et al., 2004]. Particularly for a few blocks in West-Ant, it was observed that the bias can reach up to several meters, with both senses of bias occurring, *i.e.*, ERS-2 higher than ERS-1 for some blocks but lower for others. Figure 3-22 shows four examples of these inter-satellite biases for blocks across profiles [5]-[6]. Because of the non-systematic nature of the bias, ERS-1 data were excluded from this study. The adjustments to these biases can significantly change the dh/dt estimate, especially because the added data is at the beginning of the time series. A sensitivity test is done using the $\mathbf{G}$ matrix in Eqn 3.1 and the time ERS-1/2 data were collected (approximately 0.3yr to 7.8yr at spacing of 0.09yr). Figure 3-22e shows the effect of positive biases (ERS-1 higher than ERS-2) between 0.1m to 1m on a block with true dh/dt of 0.01m/yr. For a positive bias, ERS-1 is higher than ERS-2 heights, resulting in negative dh/dt. When the bias is negative, the pseudo dh/dt will be positive with the same magnitudes as those shown in this example. Figure 3-23 summarizes the statistics of the difference between cross-over and kriging estimates for dh/dt. Overall kriging method yields systematically higher dh/dt than cross-overs, with means of 0.014, 0.046, 0.025, and 0.07m/yr for regions R-I through R-IV respectively. The effect of this bias in the positive difference (kriging minus cross-over) in the interior of E-Ant will be investigated in the near future. When both methods yield similar dh/dt patterns across longitudes, kriging results are larger in magnitudes. This is because kriging estimates dh/dt in each individual block with no overlapping data, whereas cross-over uses overlapping data (more than 50% overlapping between adjacent 50-km grid points when a search radius of 100km is used), which essentially smooths out (or smears out) large but localized variations. In addition, toward the coast, the overlaps result in bias toward inland data.

Two important factors that need to be removed from the dh/dt using kriging obtained here are the isostatic adjustments and firn compaction rates. Isostatic uplift of the bedrock is approximately 0.0 to 0.3cm/yr in the interior of E-Ant, 0.3 to 1.1cm/yr in the Amery Ice Shelf, and 0.3 to 2.2cm/yr in West Antarctica [Zwally et al., 2004]. The firn-compaction rate is approximately < 0.004m/yr in E-Ant, and between 0.004m/yr to -0.02m/yr in W-Ant [Zwally et al., 2004]. However the cross-over dh/dt results do not have these two corrections applied, and Zwally et al. [2004] combined dh/dt, bedrock isostatic adjustments, and the firn-compaction rate to obtain an overall change in the ice thickness change. As a result, a direct comparison between dh/dt between the kriging and cross-over is still valid here.

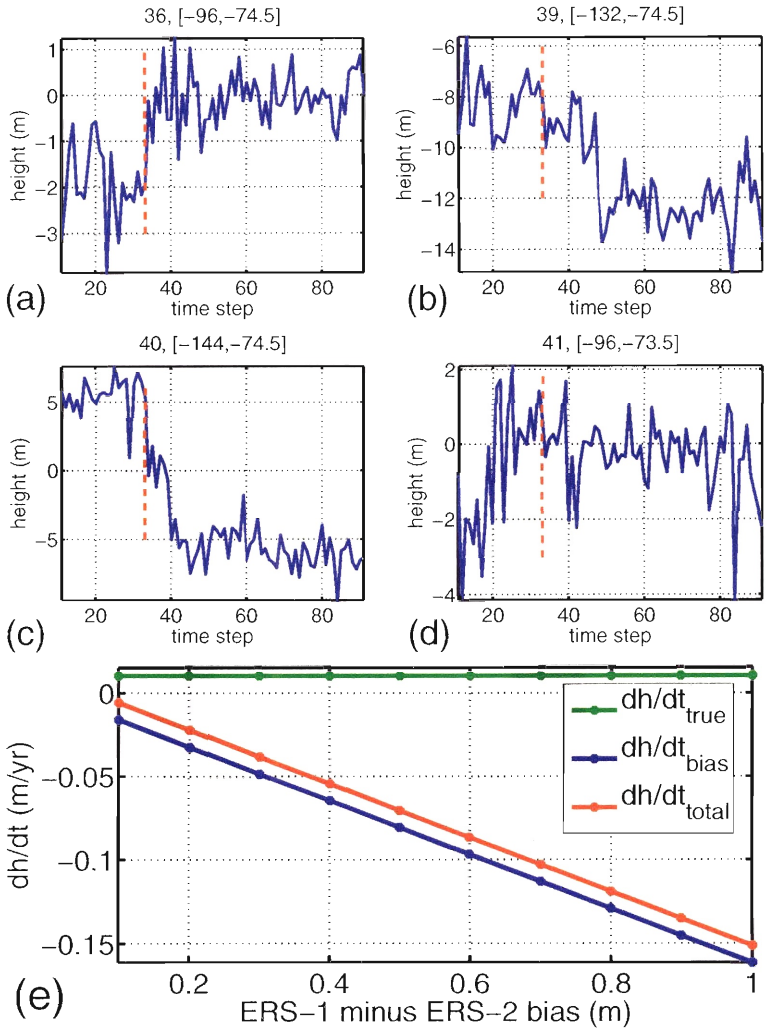

Figure 3-22 Inter-satellite biases for four blocks near the coast in W-Ant (a-d), and potential errors in dh/dt as a result of these biases (e). Across two of these blocks (blocks #39 and #40) the cross-over method yields large negative dh/dt rates, whereas kriging using only ERS-2 data yields near zero to positive dh/dt. The dashed red line in (a-d) separates ERS-1 from ERS-2 data. In (e) dh/dt_{true} is the input rate, dh/dt_{bias} is the pseudo dh/dt due to the inter-satellite bias, and dh/dt_{total} is what the model would predict if the bias is not removed from the data.

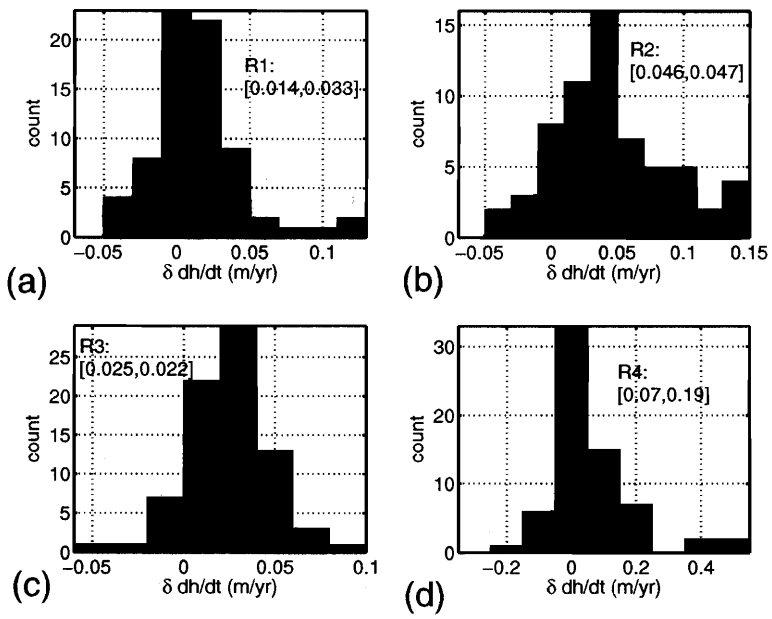

Figure 3-23 Statistics of $\delta dh/dt$ (kriging minus cross-over) for the four regions, which shows a systematic positive difference. The numbers in the brackets are the mean and RMS of $\delta dh/dt$ for each corresponding region.

3.4.2 Seasonal signal

Figure 3-24 shows unpublished results of B and θ from cross-over analysis [Zwally, 2005], and Figure 3-25 shows the profiles of amplitudes B and the δB between the two methods. δB is defined as the difference between kriging amplitude (B_{krig}) and cross-over ones (B_{xover}). When a full covariance matrix is approximated using Eqn 3.9, uncertainties in B from cross-overs are large, in the range of $\pm$0.7m, and only 6 blocks have δ_B that are significantly different from zero (out of 221 blocks). As a result, amplitude estimates in cross-over technique are assumed uncorrelated in the calculation of the variance of the block average. Using this assumption, σ_{δ_B} are significantly smaller, and 91% of the blocks show δ_B significantly different from zero (Figure 3-25). Spatially, B_{xover} has a bimodal distribution with low amplitudes at the drainage divides ([mean,RMS] of [0.126m,0.041m]) and high amplitudes away from the divides ([mean,RMS] of [0.203m,0.113m]). This correlation is less visible in kriging results. Using the same block distribution shown in Figure 3-19a for blocks along and away from the drainage divides, B_{krig} have [mean,RMS] of [0.05m,0.03m] along the divides, and [0.16m,0.14m] elsewhere respectively (compare Figure 3-15 with Figure 3-24). In profile view (Figure 3-25), the pattern of B is similar in both methods in R-I and R-III, but with kriging results consistently having smaller B than cross-overs. However in R-II, over the Amery Ice Shelf, kriging predicts higher B (one of only a few cases where kriging yields larger B than cross-over). In W-Ant, one block at [-111°E, -75°N] shows significant difference in B between the methods. The amplitude fit for this block is shown earlier in Figure 3-13c. Overall, both methods show the bimodal distribution of B along and away from the drainage divides in R-I and R-II. However, kriging consistently yields lower B than cross-overs in the smooth interior part of Antarctica, with mean δ_B of [-0.07,-0.05,-0.07,-0.04]m for R-I through R-IV (Figure 3-26).

The strong correlation between phase maximum/minimum and drainage divides in E-Ant are observed clearly in both methods. However, phases are approximately 1 month earlier for kriging when compared to cross-over. Specifically along the drainage

divides $\theta_{max} \approx 421$ day $\Leftrightarrow \theta_{min}$ in Aug to Oct for kriging versus Sep to Nov for cross-over, and away from the divides $\theta_{max} \approx 178$day $\Leftrightarrow \theta_{min}$ at mid-Nov to mid-Jan for kriging versus Jan to Mar for cross-over (compare Figure 3-19 with Figure 3-24). Uncertainties of θ in kriging range from ± 45 to ± 135 days along the drainage divides, and ± 10 to ± 45 day away from the drainage. Cross-over analysis did not generate uncertainties for θ. Despite the systematic off-set of 1 month between the two methods, uncertainties in θ estimates from kriging imply that the phase difference is not significantly different from zero. Firn compaction models, based on temperature cycles with a maximum in Dec, would predict phase min/max approximately one to two months earlier than the temperature cycle, or Oct-Nov/Apr-May [Jun, 2005].

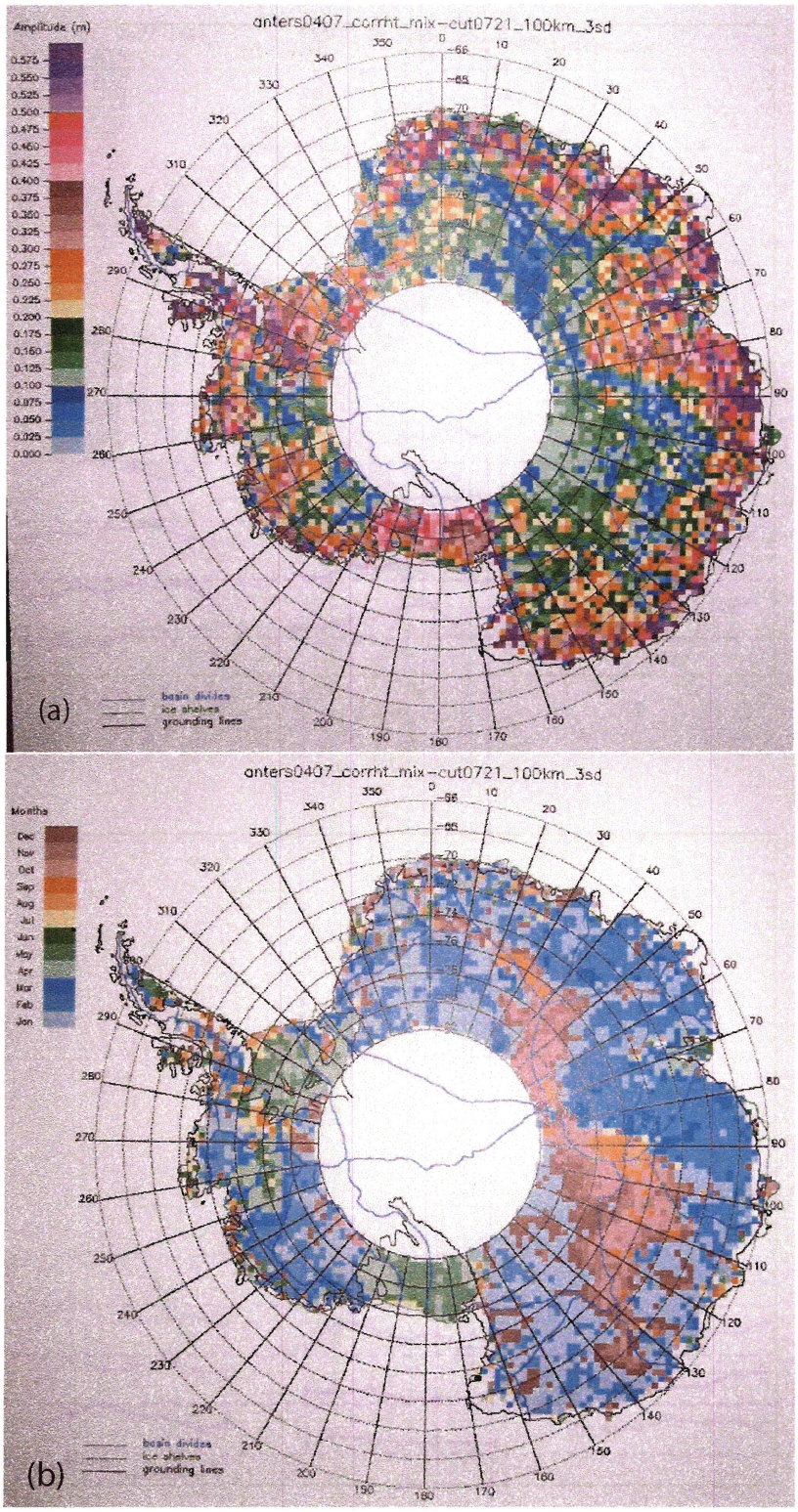

Figure 3-24 Zwally [2005]'s unpublished ERS cross-over analysis results for seasonal signal amplitude (a) and phase minimum (b).

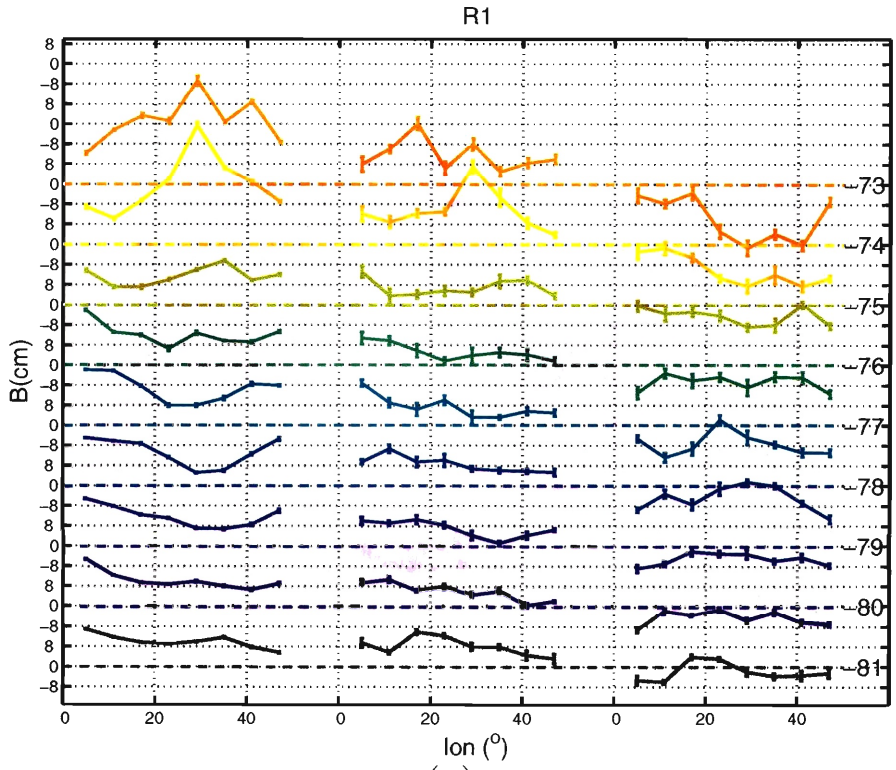

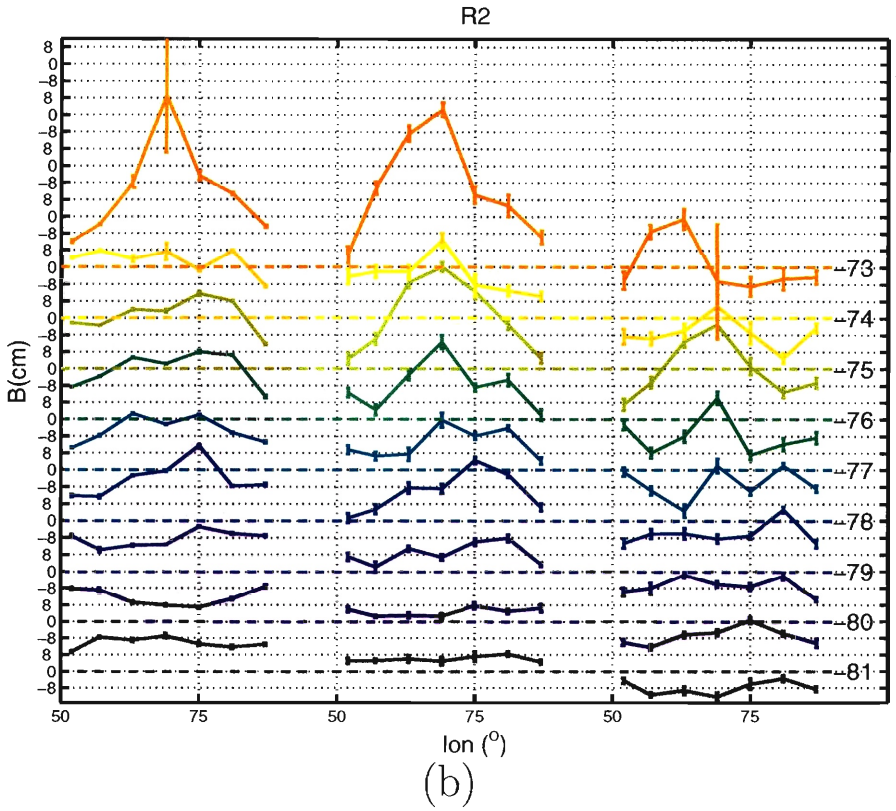

Figure 3-25 Profiles of cross-over B (left panel), kriging B (middle panel), and δB (right panel) for regions R-I (a), R-II (b), R-III (c, next page), and R-IV(d, next page). δB is the difference between kriging and cross-over results.

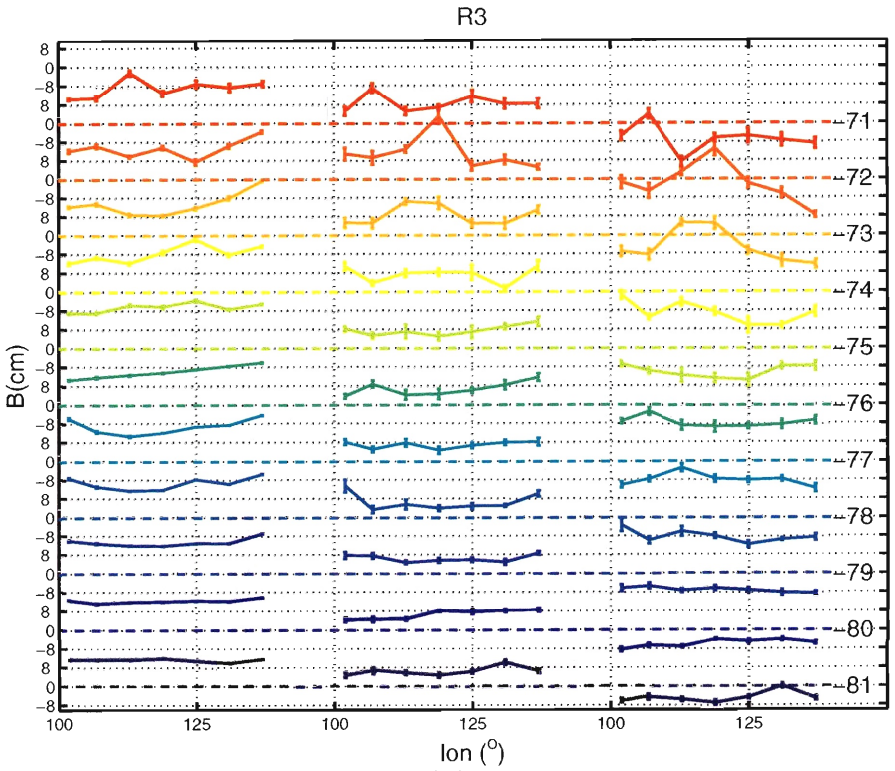

(c)

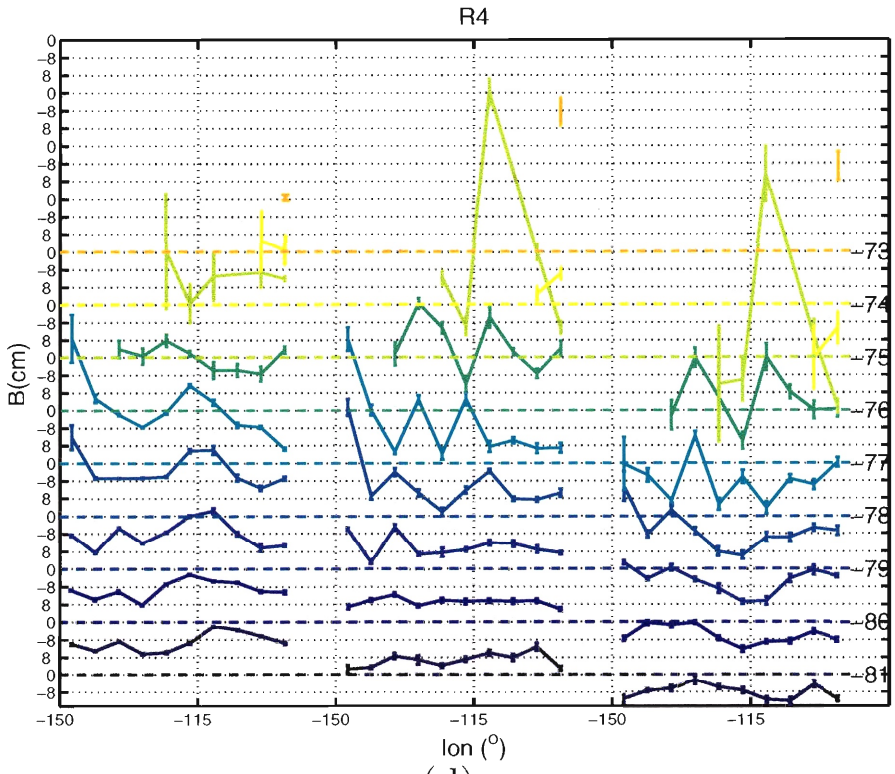

(d)

Figure 3-25 cont'd . The y-axis labels are B on the left, and latitude on the right.

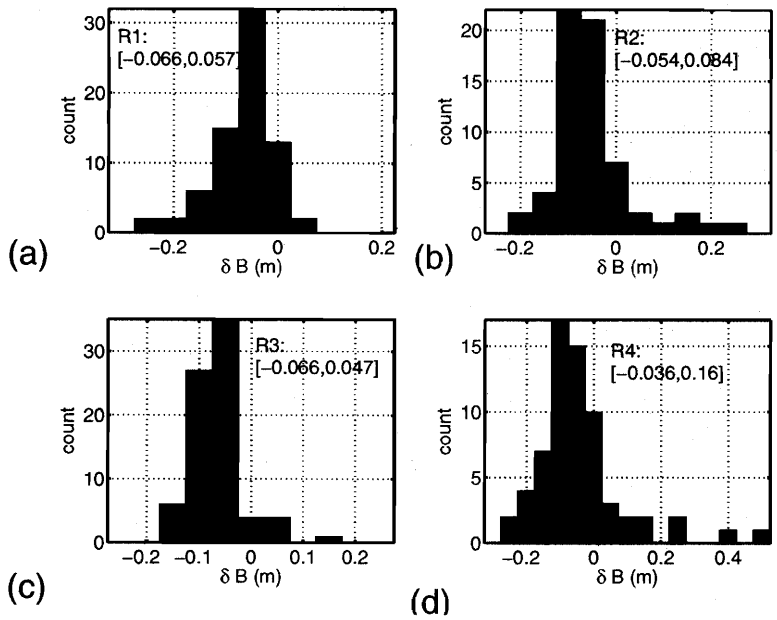

Figure 3-26 Statistics of δB (kriging minus cross-over) for the four regions, which show systematic positive difference. Numbers in the brackets are the mean and RMS of δB for the corresponding region.

3.5 Kriging versus Averaging

Uncertainties in block height estimates σ_a^2 using averaging is several times larger than those from kriging (see the diagonal terms in Eqn 3.11). As a result, when a full approximation of the covariance matrix in Eqn 3.11 is used, the off-diagonal terms in $\mathbf{cov}_d$ are scaled according to the kriging uncertainties σ_k^2, resulting in very small off-diagonal terms in $\mathbf{cov}_m$ in the order of $10^{-4}m^2$. The combination of large σ_a^2 and small correlations between predicted dh/dt_k and dh/dt_a gives large uncertainties in the difference $\delta dh/dt_{ka}$ such that no blocks have $\delta dh/dt_{ka}$ significantly different from 0.00m/yr. To gain an insight into the correlation between dh/dt_k and dh/dt_a, the block height estimates were assigned the same uncertainties as block kriging, *i.e.*, $\sigma_a^2 \equiv \sigma_k^2$. In this case, the off-diagonal terms in $\mathbf{cov}_d$ is more reflective of the correlation between block heights estimates between the two methods. The evidence of the existence of this correlation is discussed in the section 3.2.5 earlier. The results using this approach for regions R-II and R-IV are shown in Figure 3-27.

Six profiles are chosen for comparison, again numbered as profile [1] – [6] in Figure 3-27. Profiles [2]-[6] are the same as those used in the kriging versus cross-over comparison. Profile [1], located at latitudes -81^o in region R-II shows positive dh/dt estimates in both kriging and averaging. This is also observed in the interior of E-Ant in R-I and R-III (not shown here). Profiles [2]-[3] at the Amery Ice Shelf are where dh/dt estimated by the two methods diverges. Figure 3-28 shows the time series of the two blocks in profile [3] where the discrepancies are approximately +0.15m/yr in one block and -0.15m/yr in the adjacent one. The large negative dh/dt_a in profile [2] at longitude 63^{o}E-69^{o}E is also observed in cross-over analysis, with a 100-km eastward shift, however (compare Figure 3-27a with Figure 3-21b).

Profiles [4] in R-IV shows consistent dh/dt estimates between the two methods. At the coast, profiles [5]-[6] diverges, particularly at longitude -147^{o}E. Similar to cross-over, block averaging does not produce the large positive dh/dt seen in profile [6] at longitude -147^{o}E. However averaging also does not produce the pervasive negative dh/dt that cross-over results show. An example of block height estimates using krig-

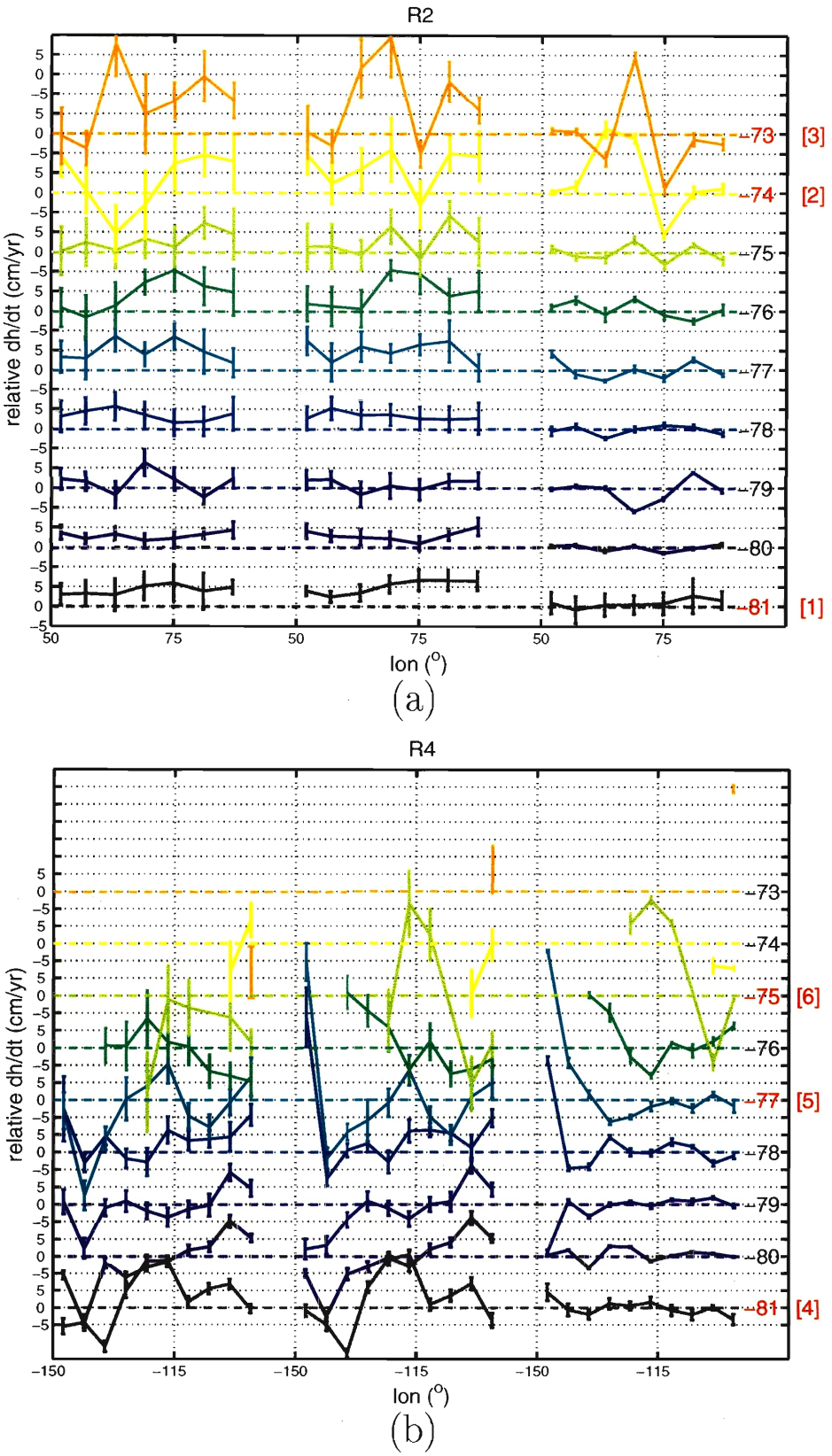

Figure 3-27 Profiles of dh/dt estimated using block averaging (left panel), kriging dh/dt (middle panel), and their difference (right panel, kriging minus averaging) for regions R-II (a) and R-IV (b). The six profiles chosen for further analysis are numbered [1] through [6] and identified with the red label of latitude. Profiles [2]-[6] are the same as those used in the comparison of cross-over and kriging results.

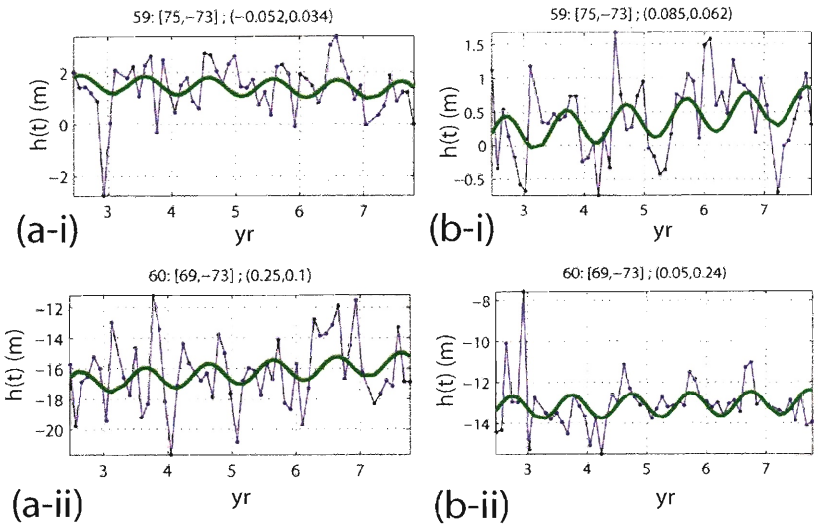

Figure 3-28 Time series of two blocks (i) and (ii) at the Amery Ice Shelf estimated using kriging (a) and averaging (b). On each subplot, the label indicates the block number, longitude, latitude, dh/dt and $\sigma_{dh/dt}$. The blue curve shows the block height estimates using either kriging or averaging, and the green line shows the fitted model using weighted linear least square inversion.

ing and averaging is shown in Figure 3-29 to illustrate the fundamental difference between the two methods. A systematic offset is commonly observed between kriging and averaging. In this example, the linear fit through H(t) gives dh/dt_a of 0.011m/yr, and block kriging dh/dt_k of 0.23±0.23m/yr. Large error bars in the block height estimates are due to degrading data quality near / at the coast. The block center is closer to height residual maxima in this example (at one particular time step), and the geometry gives point kriging and block kriging heights of 12.8m and 11.4m, as oppose to 3.9m from block averaging. When the offsets are not time independent, we obtain different estimates of block dh/dt. In this example the error bar for dh/dt_k is large enough to include dh/dt_a as a possible solution. However, as shown in profiles [3]-[4] in R-II and [5]-[6] in R-IV, block kriging yields dh/dt that are significantly different from block averaging near the coast. Figure 3-30 shows the statistics of $\delta dh/dt_{ka}$ for all four regions.

Acknowledgment I thank Dr. Zwally for making his unpublished cross-over analysis results available for the comparison between the methods in this chapter, and Helen Cornejo for her help with the back scatter correction and the data and results files.

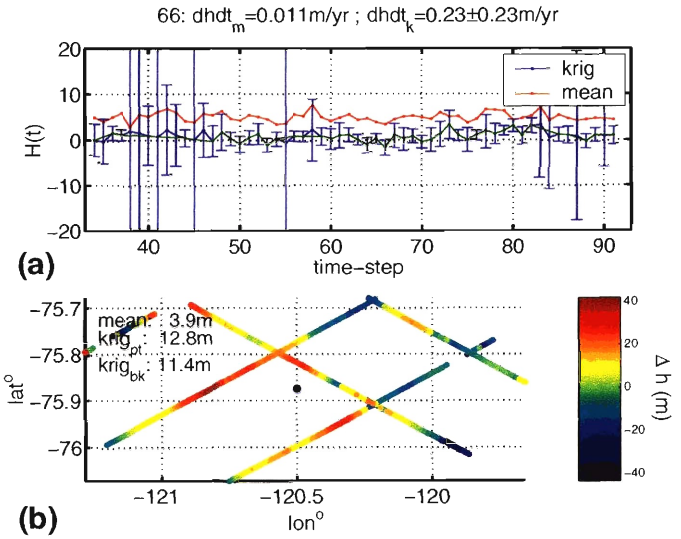

Figure 3-29 Difference in dh/dt estimates for $(100km)^2$ block #66 in W-Ant between block-kriging (Bk) and block-averaging (Ba) using a 500-point neighborhood. (a) Time series for Bk (blue), Ba (red), and Bk excluding time step with large uncertainties (green). (b) Height residuals distribution for the 500 points in the original $(27km)^2$ block. The point-kriging and block-kriging solutions are 12.8m and 11.4m, as opposed to block-averaging solution of 3.9m.

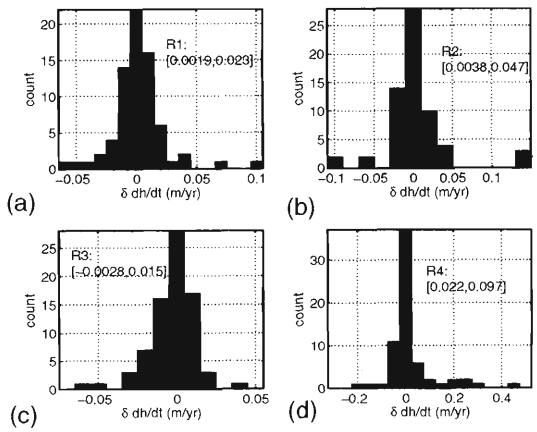

Figure 3-30 Statistics of the difference in dh/dt between kriging and averaging for R-I through R-IV. The large negative and positive difference in R-II is at the Amery Ice Shelf, where the difference between the two methods diverges.

3.6 Conclusion

Block-kriging is an alternative method to cross-over analysis to detect height change and other temporal variations in the ice-sheets using radar and laser altimetry data. The advantages of kriging are that it uses nearly all of the available data, and the data statistics. Results obtained from kriging shows significantly difference in dh/dt estimates in Antarctica from cross-overs. Specifically kriging gives higher positive dh/dt at the Amery Ice Shelf, and does not show the pervasive negative dh/dt in the Pine Island / Thwaites Glaciers area. In addition, kriging results also show a systematic positive difference of approximately 0.03±0.02m/yr over the smoothest part in East Antarctica. Both methods detect the large positive dh/dt at approximately [lon,lat] of [-120^{o}E, -82^{o}N], with kriging showing higher positive dh/dt. When both methods yield consistent pattern of dh/dt as a function of longitude, kriging produces estimates with higher magnitudes. This is expected because the large and overlapping search neighborhood used in cross-over smooths out any large localized deviations in height. Moreover, cross-over search neighborhood will result in dh/dt estimates that are biased toward in-land values. The bias of approximately 0.03m/yr between kriging and cross-over will be investigated further in the near future. In addition, both the dh/dt and corresponding uncertainties will be calculated at the same resolution between the two methods using the same data period to better assess their differences.

Seasonal signal amplitudes predicted using kriging combining with linear inversion are systematically lower than those estimated from cross-overs in the interior of E-Ant, with a mean difference of approximately 0.05m to 0.06m with an RMS of approximately 0.06m. Phase maxima predicted in kriging are approximately one month earlier than those predicted using cross-overs. The uncertainties in phase are not calculated in the cross-over method. Uncertainties from kriging results are in the range ±15 to ±45 days, making the one month off-set not significantly different statistically. The systematic offsets in dh/dt (higher in kriging), B (lower in kriging), and θ (one month earlier in kriging) could potentially be the result of different time coverage in

the data used by the two methods. In this study ERS-1 data were excluded due to a geographically dependent bias between ERS-1/2 that had not been fully investigated. Cross-over analyses use both ERS-1/2 data. The additional 2.5 years at the beginning of the time series, combining with a geographically dependent bias can significantly impact the rate of change, as well as the seasonal signal amplitude and phase. A sensitivity test using the **G** matrix from the linear least square fit, and the time data were collected for ERS-1/2 data shows that a bias of 0.1m to 1.0m result in a pseudo dh/dt in the range 0.016m/yr to 0.16m/yr.

Differences between block kriging and averaging are less than between kriging and cross-over methods. In the smooth interior part in East Antarctica, averaging and kriging yields consistent results with mean difference of 0.00m/yr and RMS of approximately 0.01m/yr to 0.02m/yr. Significant differences are found at the Amery Ice Shelf, where kriging yields both large negative and positive rates which averaging does not produce. In the Pine Island / Thwaites Glaciers area, averaging and kriging results do not show the pervasive large negative in the range -0.7m/yr to -1.0m/yr found in cross-over analyses. Instead, kriging shows positive dh/dt of approximately 0.15m/yr that block averaging again does not show. The uncertainties at the coast in this area for cross-over method are $\sim$0.5m/yr to 0.8m/yr.

An independent data set is needed to validate the results obtained in this study. The next two chapters will cover description and analysis of laser altimetry data over Antarctica.

Table 3.5: ERS Data

step	JD_1	JD_2	YR_1	MO_1	DAY_1	YR_2	MO_2	DAY_2
				ERS-1				
t11	2449453	2449486	1994	4	10	1994	5	13
t12	2449487	2449520	1994	5	14	1994	6	16
t13	2449521	2449554	1994	6	17	1994	7	20
t14	2449555	2449588	1994	7	21	1994	8	23
t15	2449589	2449622	1994	8	24	1994	9	26
t16	2449624	2449657	1994	9	28	1994	10	31
t17	2449658	2449691	1994	11	1	1994	12	4
t18	2449692	2449725	1994	12	5	1995	1	7
t19	2449726	2449759	1995	1	8	1995	2	10
t20	2449760	2449793	1995	2	11	1995	3	16
t21	2449798	2449832	1995	3	21	1995	4	24
t22	2449833	2449866	1995	4	25	1995	5	28
t23	2449867	2449901	1995	5	29	1995	7	2
t24	2449902	2449936	1995	7	3	1995	8	6
t25	2449937	2449971	1995	8	7	1995	9	10
t26	2449972	2450006	1995	9	11	1995	10	15
t27	2450007	2450041	1995	10	16	1995	11	19
t28	2450042	2450076	1995	11	20	1995	12	24
t29	2450077	2450111	1995	12	25	1996	1	28
t30	2450112	2450146	1996	1	29	1996	3	3
t31	2450147	2450181	1996	3	4	1996	4	7
t32	2450182	2450216	1996	4	8	1996	5	12
t33	2450217	2450251	1996	5	13	1996	6	16
				ERS-2				
t34	2450238	2450271	1996	6	3	1996	7	6
t35	2450272	2450305	1996	7	7	1996	8	9
t36	2450306	2450339	1996	8	10	1996	9	12
t37	2450340	2450373	1996	9	13	1996	10	16
t38	2450374	2450407	1996	10	17	1996	11	19
t39	2450408	2450441	1996	11	20	1996	12	23
t40	2450442	2450476	1996	12	24	1997	1	27
t41	2450477	2450510	1997	1	28	1997	3	2
t42	2450511	2450544	1997	3	3	1997	4	5
t43	2450545	2450578	1997	4	6	1997	5	9
t44	2450579	2450612	1997	5	10	1997	6	12
t45	2450613	2450646	1997	6	13	1997	7	16
t46	2450647	2450680	1997	7	17	1997	8	19
t47	2450681	2450714	1997	8	20	1997	9	22
t48	2450715	2450748	1997	9	23	1997	10	26
t49	2450749	2450782	1997	10	27	1997	11	29
t50	2450783	2450816	1997	11	30	1998	1	2
t51	2450817	2450850	1998	1	3	1998	2	5
t52	2450851	2450884	1998	2	6	1998	3	11
t53	2450885	2450918	1998	3	12	1998	4	14
t54	2450919	2450952	1998	4	15	1998	5	18
t55	2450953	2450986	1998	5	19	1998	6	21
t56	2450987	2451020	1998	6	22	1998	7	25
t57	2451021	2451054	1998	7	26	1998	8	28
t58	2451055	2451088	1998	8	29	1998	10	1
t59	2451089	2451122	1998	10	2	1998	11	4
t60	2451123	2451156	1998	11	5	1998	12	8
t61	2451157	2451190	1998	12	9	1999	1	11
t62	2451191	2451224	1999	1	12	1999	2	14
t63	2451225	2451258	1999	2	15	1999	3	20
t64	2451259	2451292	1999	3	21	1999	4	23
t65	2451293	2451326	1999	4	24	1999	5	27
t66	2451327	2451360	1999	5	28	1999	6	30
t67	2451361	2451394	1999	7	1	1999	8	3
t68	2451395	2451428	1999	8	4	1999	9	6
t69	2451429	2451462	1999	9	7	1999	10	10
t70	2451463	2451496	1999	10	11	1999	11	13
t71	2451497	2451530	1999	11	14	1999	12	17
t72	2451531	2451564	1999	12	18	2000	1	20

t73	2451565	2451598	2000	1	21	2000	2	23
t74	2451599	2451633	2000	2	24	2000	3	29
t75	2451634	2451667	2000	3	30	2000	5	2
t76	2451668	2451701	2000	5	3	2000	6	5
t77	2451702	2451735	2000	6	6	2000	7	9
t78	2451736	2451769	2000	7	10	2000	8	12
t79	2451770	2451803	2000	8	13	2000	9	15
t80	2451804	2451837	2000	9	16	2000	10	19
t81	2451838	2451871	2000	10	20	2000	11	22
t82	2451872	2451905	2000	11	23	2000	12	26
t83	2451906	2451941	2000	12	27	2001	1	31
t84	2451942	2451975	2001	2	1	2001	3	6
t85	2451976	2452009	2001	3	7	2001	4	9
t86	2452010	2452043	2001	4	10	2001	5	13
t87	2452044	2452077	2001	5	14	2001	6	16
t88	2452078	2452111	2001	6	17	2001	7	20
t89	2452112	2452145	2001	7	21	2001	8	23
t90	2452146	2452179	2001	8	24	2001	9	26
t91	2452180	2452213	2001	9	27	2001	10	30

Chapter 4

The Geoscience Laser Altimeter System

4.1 Introduction

Radar altimetry has been used to measure sea level and ice sheet changes since 1978 (Chapter 1, 3). However, the large footprint size of ~10km in radar yields large uncertainties in height measurements in the range of several tens of centimeters due to slope-induced errors. In addition, over surfaces with rapidly-varying local slopes at spatial wavelengths approximately that of the footprint size, typical along the coast, the tracking device in radar fails to locate the surface, resulting in loss of data (Chapter 3, [Fricker et al., 2000; Brenner et al., 1983; Martin et al., 1983]). Martin et al. [1983] showed that data loss occurs when surface slopes reach 1° or higher. Because changes in the ice sheets in response to climate are expected to occur at the coast where radar altimetry is limited in capacity, laser altimetry was proposed as an alternative. Satellite laser altimeter was first critically reviewed for ice sheet studies in 1981 [Zwally et al., 1981; Bufton et al., 1982]. With its smaller footprints ~ 70m, laser can measure heights over high sloped surfaces and quantify surface roughness at footprint scale with smaller uncertainties. Figure 4-1 taken from Bufton [1989] shows the relative sizes of radar and laser footprints. Subsequent instrument concept reviews showed height measurement at sub-meter accuracy can be achieved [Bufton

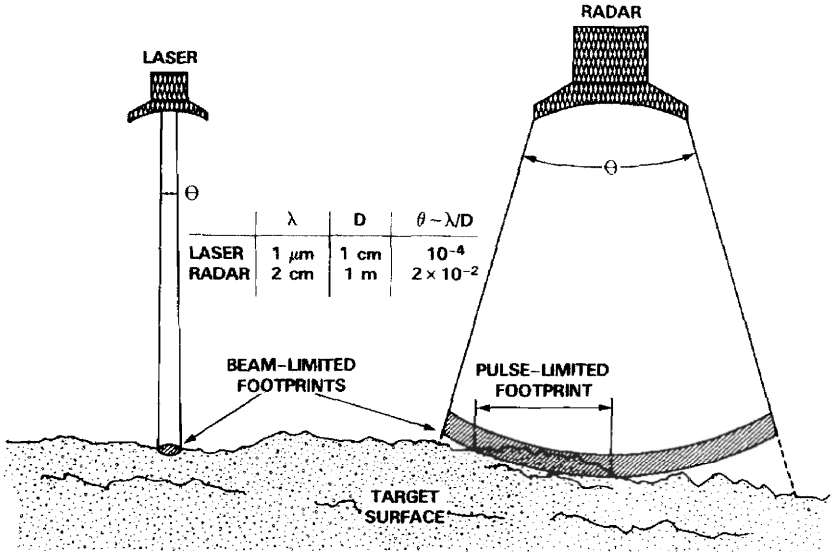

Figure 4-1 Relative sizes and accuracy levels of radar and laser altimetry. Figure is taken from Bufton [1989].

et al., 1982; Zwally et al., 1981; Bufton, 1989; Harding et al., 1994], with pointing knowledge of the laser identified as the chief limiting factor. In 1992, the Intergovernmental Panel on Climate Change (IPCC) noted that our lack of knowledge in sea level change stemmed from our inadequate knowledge of the ice sheet mass balance [Houghton et al., 1992; Zwally et al., 2002; Schutz et al., 2005]. Specifically, our understanding of the mass input-output in the ice sheet is limited by the $\pm 25\%$ uncertainties, or equivalently $\sim$ 2mm/yr in sea level change (Chapter 1, [Zwally et al., 2002]). Following IPCC's assessment, NASA had designated the Geoscience Laser Altimeter System (GLAS) as the chief instrument to study ice sheet mass balance, and planned to allocate three successive laser altimetry satellites (2003, 2008, 2013) to study ice volume and mass changes fifteen years following GLAS launch date (Figure 4-2, [EOS, 1995]). The predecessor of GLAS, the Mars Orbiter Laser Altimeter (MOLA) successfully mapped the surface of Mars with sub-meter accuracy enabling the detection of the seasonal CO_2 cycle of the martian ice caps [Smith et al., 2001b; Aharonson et al., 2004]. In this chapter, GLAS and its ability to measure ice sheet height change will be reviewed.

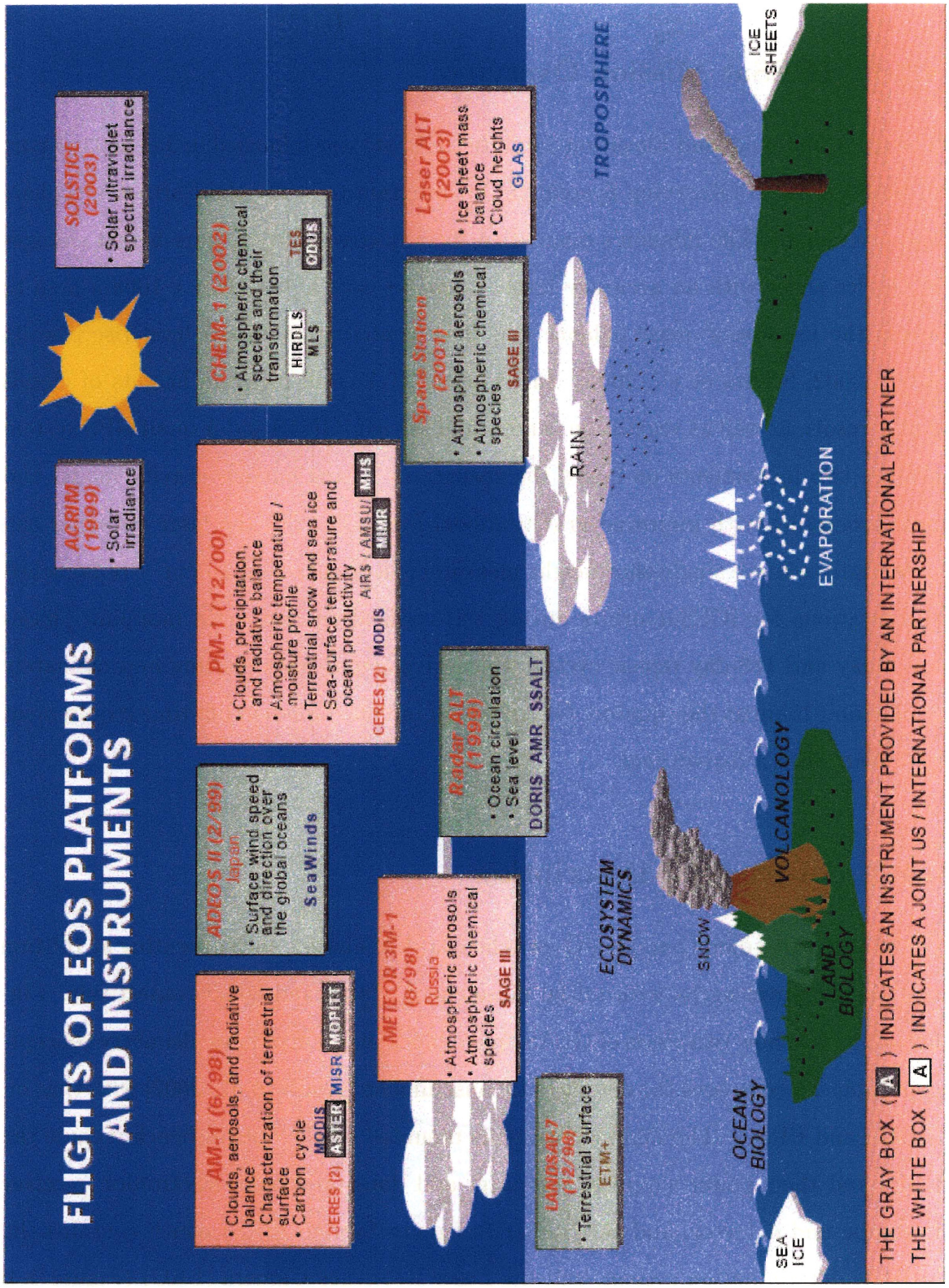

Figure 4-2 The Earth Observing System (EOS) plan in 1995 to study the Earth. Figure is taken from EOS [1995].

4.2 The Geoscience Laser Altimeter System (GLAS)

4.2.1 ICESat Mission Overview

The Ice, Cloud and land Elevation Satellite (ICESat) was launched in Jan 2003 as part of NASA's Earth Observing System (EOS) program to study the Earth atmosphere and cryosphere. The mission's main scientific objective is to measure height changes in the ice sheet with an accuracy level $\sim$ 2cm/yr over a $\sim$ 100km x 100km area to assess the ice sheets' mass balance and their contribution to sea level rise [Zwally et al., 2002; Schutz et al., 2005]. In addition GLAS will measure heights of clouds and aerosols, as well as vegetation canopy and sea ice. GLAS and a small GPS system are the two instruments on-board the spacecraft. Using current gravity model and post-processing with improved gravity model from GRACE, the laser altimeter can potentially achieve single-shot height measurement accuracy of 15-cm. Pre-launched specifications for ICESat orbits during the verification and main mapping phases are 8-day and 183-day repeat cycles, which give across-track spacing approximately 340km and 15km at the equator. GLAS has an intended mission life-time requirement of 3 years with a *5-year* goal.

4.2.2 Instrument Description

GLAS uses three diode pumped, Q-switched Nd:YAG lasers, each operating at 1064nm and 532nm wavelengths with initial pulse energy 74mJ and 30mJ respectively. Figure 4-3 to 4-4 show two views of GLAS, and a block diagram of laser altimetry concept, and Table 4.1 compares the details of the instrument [Zwally et al., 2002] with that on MOLA and ERS-1. The main components mounted on the optical bench include the lasers and their power supplies, computer and data processing electronics, receiver telescope and detector, and the Stellar Reference System (SRS) which contains the attitude determination system, and the Laser Reference Camera (LRC) (Figure 4-4, [Bae and Schutz, 2002]). Other components necessary for determining the orientation of the optical bench include the instrument star tracker and gyros. Accurate GLAS

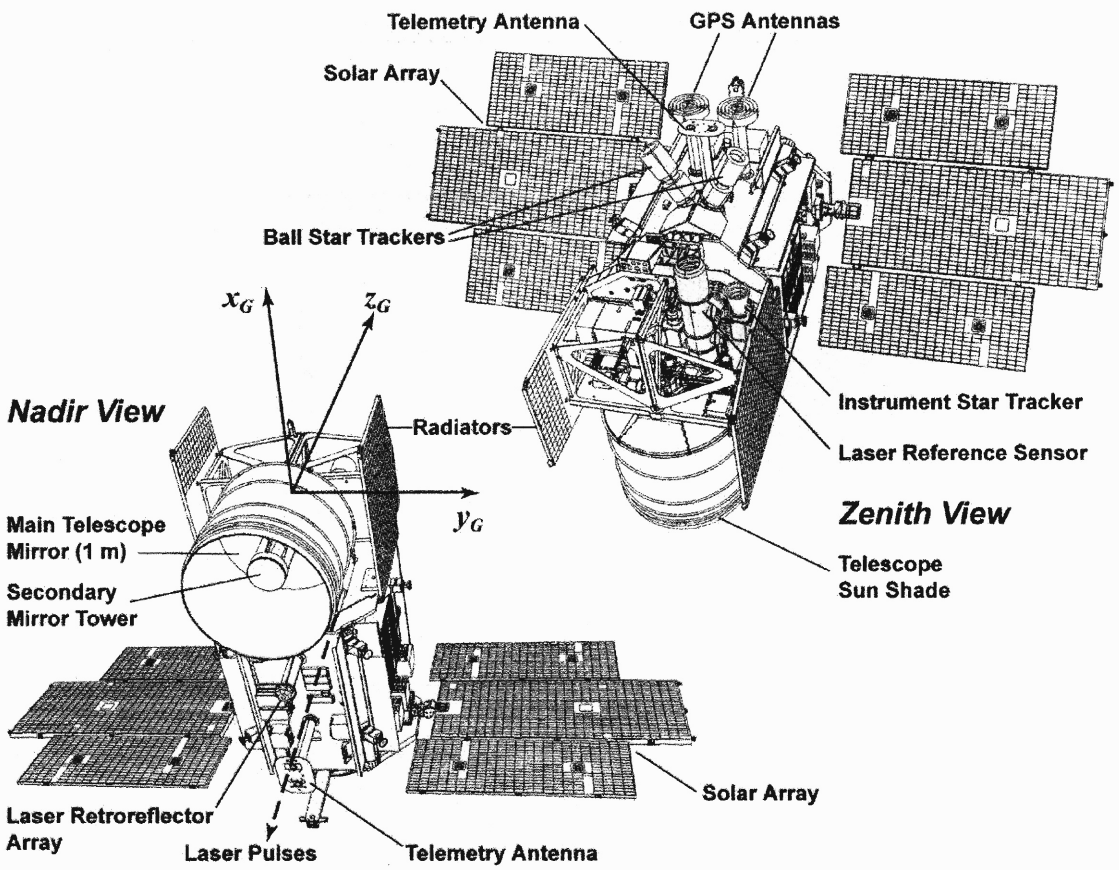

Figure 4-3 Zenith and nadir views of ICESat. Figure is taken from Schutz et al. [2005].

orbit is achieved using a GPS tracking system [Schutz et al., 2005].

At a near-circular orbit at altitude 600km, the system's beam divergence of 0.110mrad ($\sim$ 22 arcsec) and frequency 40Hz correspond to a footprint size of $\sim$ 70m in diameter with 172m spacing along track on the surface. Figure 4-5 taken from Bufton [1989] illustrates the geometry between the altimeter and ground target. For GLAS the off-nadir angle ϕ will be approximately 0.33^o in order to avoid specular reflection [Schutz et al., 2005]. The *8-day* and *91-day* repeat cycles (a modification from pre-launch specs) produce cross-track spacing of $\sim$340km and $\sim$30km at the equator and $\sim$29km and $\sim$2.5km at latitude 85^o. An orbit that optimizes the cross-over geometry for coverage of the ice-streams in West Antarctica which extends to latitude -86^o puts the spacecraft at an inclination of 94^o [Schutz, 1995]. This near-polar orbit corresponds to maximum latitude coverage of 86^o North-South, with $\sim$ 70, 150, 485 and 11,340 cross-overs in an average $100 \times 100km^2$ area centered at

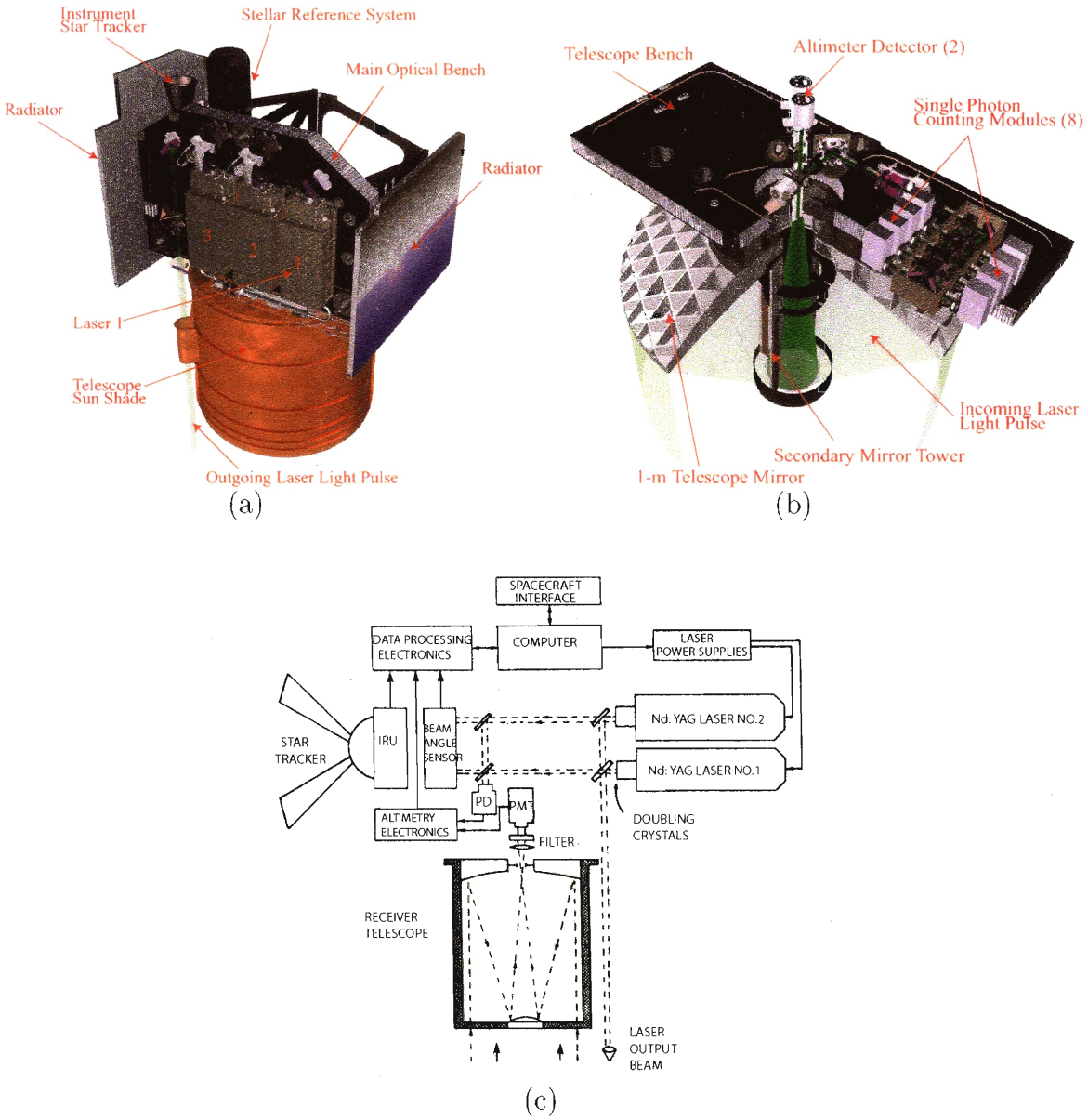

Figure 4-4 Views of the transmitting (a), receiving (b) components of GLAS, and a generic block diagram (c) illustrating the general concept of transmitting and receiving. Figures are taken from Abshire et al. [2005] and Bufton et al. [1982] with annotation added. For GLAS, the output energy includes the 1064nm and 532nm channels, where the latter originates from 1064nm but passes through a crystal doubler (to double the wavelength).

latitudes *[-70.5°,-75.5°,-80.5°,-85.5°]*.

4.2.3 Waveform Analysis

Over the ice-sheet, pulses of energy 74mJ (1064nm) and duration 5ns are transmitted from the Nd:YAG laser (Figure 4-4c, 4-6). The returned signal passes through

Table 4.1 Comparison between GLAS, MOLA, and ERS instruments

Description	GLAS[a]	MOLA[b]	ERS-1[c]
Mass	300kg	23.8kg	888.2kg
Altimeter	diode-pumped Q-Switched Nd:YAG laser	same	radar
wavelength	1064nm, 532nm	1064nm	2.2cm (13.8GHz)
Pulse energy	74mJ, 30mJ	48mJ	
Shot frequency	40 Hz	10 Hz	20Hz
Beam Divergence	0.110 μrad	0.42 μrad	0.110 mrad
Pulse duration	5ns	8 ns	5 ns
Altitude	600km	400km	780-785km
Inclination	94^o	92.8^o	82^o
Power consumption	330 Watts (on avg)	28 Watts	2600 Watts
telescope diameter	100cm	50cm	120cm
Vert. precision	~2cm [d]	37.5cm	70^+cm
Vert. accuracy	$< 20cm$	1m(include orbit error)	
Horz. accuracy	$< 350m$[e]	100m	
footprint diameter	70m	168m	1-20km
footprint along-track spacing	170m	300m	
footprint across-track spacing at equator	30km,340km	4km	
Data Rate	450 bit/sec	618 bits/sec	2000 bits/sec

[a] Zwally et al. [2002]
[b] Zuber et al. [1992]; Smith et al. [2001a].
[c] ERS instrument website http://earth.esa.int/rootcollection/eeo4.64/
[d] Shuman et al. [2005]
[e] Estimated using ICESat repeat tracks over the ice sheet

the receiver telescope, reduced in energy due to scattering ($\sim 10^{-16}J \approx 10000$ photoelectrons), is detected using a photoelectron counter ([Brenner et al., 2003]). A coarse resolution DEM stored in the on-board computer helps determine the range gate as shown in Figure 4-6. The signal is then digitized at 1-ns interval, and a series of matched filters identify the type of surface or cloud each pulse has sampled [Bufton et al., 1982; Brenner et al., 2003]. Surface characteristics and range determination from waveform analysis is covered in detail in Bufton et al. [1982]; Harding et al. [1994]; Brenner et al. [2003] and will be summarized here. Many factors contribute to the spreading of the laser transmitted pulse including surface slope and roughness within the footprint, cloud, and pointing uncertainty. A modeled Gaussian curve as shown in Figure 4-7 is fitted to the returned waveform using a non-linear least square inversion procedure to locate its centroid time, shape, and amplitude. Widened pulses with reduced amplitudes result in larger uncertainty in the centroid time location, and map directly into range error. Range here is defined as half the traveled time (T_s in Figure 4-6) multiplied by the speed of light, and corrected for tropospheric and atmospheric delays. Harding et al. [1994] found the largest error

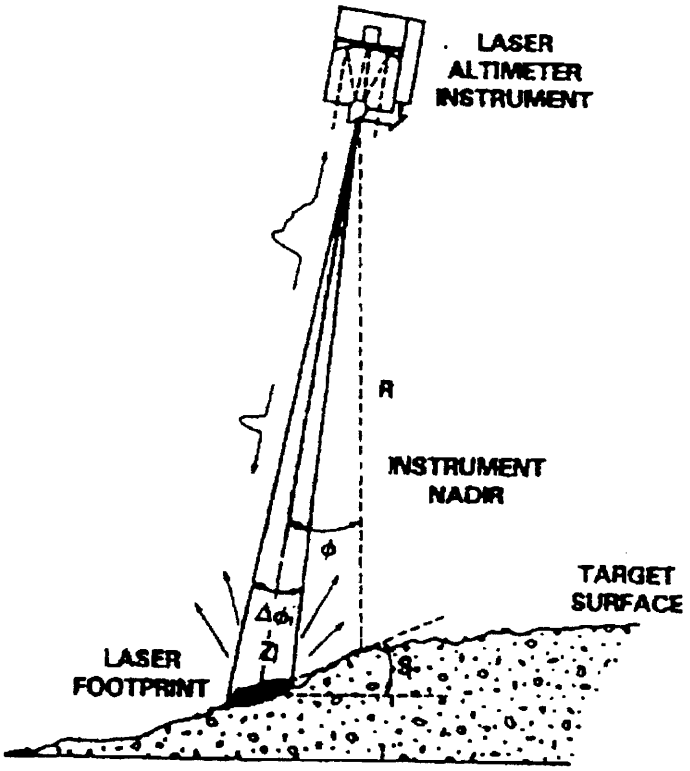

Figure 4-5 Concept of laser altimetry with off-nadir pointing angle ϕ and surface slope S. R is the nadir range from the surface to the altimeter, Z is the slant range to the surface, $\Delta\phi$ is interpreted either as the laser divergence angle or the uncertainty in pointing angle [Bufton, 1989].

contribution in range determination comes from surface slope (S in Figure 4-5), which can also be interpreted as off-nadir pointing.

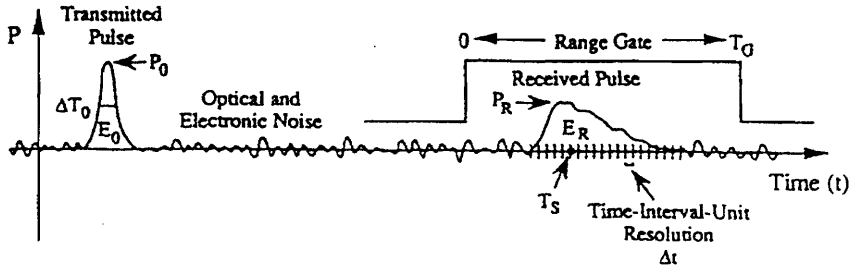

Figure 4-6 Conceptual illustration of range to the surface measurement showing signal strength (P) as a function of time (t) for transmitted pulse of peak strength P_o, energy E_o, duration ΔT_o and received pulse of P_R, E_R. T_s is the mean round-trip time-of-flight. (Figure is taken from Harding et al. [1994]).

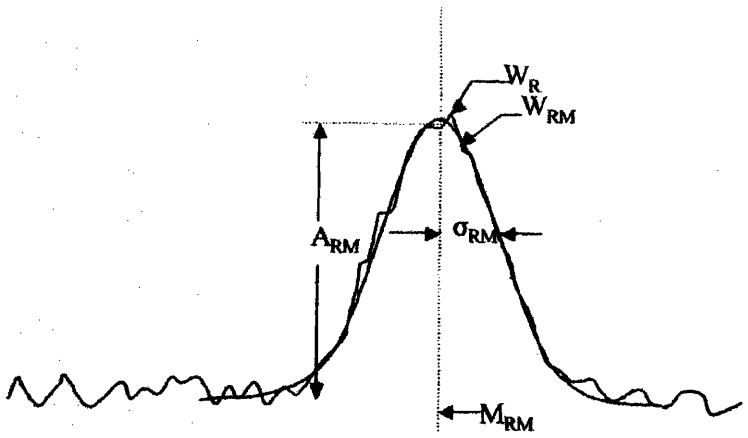

Figure 4-7 Modeling of the returned waveform (Figure is taken from Zwally et al. [2002]). W indicates the returned pulse or modeled waveform, M waveform mid-point, A waveform amplitude, σ standard deviation of the modeled Gaussian waveform, and subscripts R refers to received pulse, M refers to the Gaussian model waveform.

4.2.4 Altimetry Precision

Laser altimeters can achieve ranging precision and accuracy to within ±3cm and ±15cm [Shuman et al., 2005; Zwally et al., 1981; Zwally and Jun, 2002; DiMarzio et al., 2004]. Table 4.2 breaks down the error budget for the mission which includes contributions from the instrument, orbital determination, and atmospheric delay. Orbital determination for GLAS is done using GPS and validated using ground-based Satellite Laser Ranging (SLR) data [Rim and Schutz, 2002]. Using the current gravity model, JGM-3 or EGM96 or TEG-4, orbit determination is accurate to 16-36cm, which is greater than the $5cm$ radial orbit error budget [Schutz, 1998; Rim and Schutz, 2002]. However in-flight tuning of orbital parameters can improved uncertainties to less than $5cm$ and $20cm$ in the radial and horizontal directions respectively [Rim and Schutz, 2002]. In addition, post-processing of GRACE gravity and GLAS cross-over data could potentially improve the orbit precision [Schutz, 1998; Rim and Schutz, 2002]. However Rim and Schutz [2002] noted that the requirement of 5cm radial orbit accuracy can be achieved using any of the gravity model available during operation, JGM-3, EGM-96, TEG-4, or an improved gravity model using GRACE as the initial gravity field prior to on-orbit fine tuning.

The satellite attitude and laser pointing are determined using the on-board star trackers and Laser Reference Camera system (Figure 4-8a, taken from Bae and Schutz

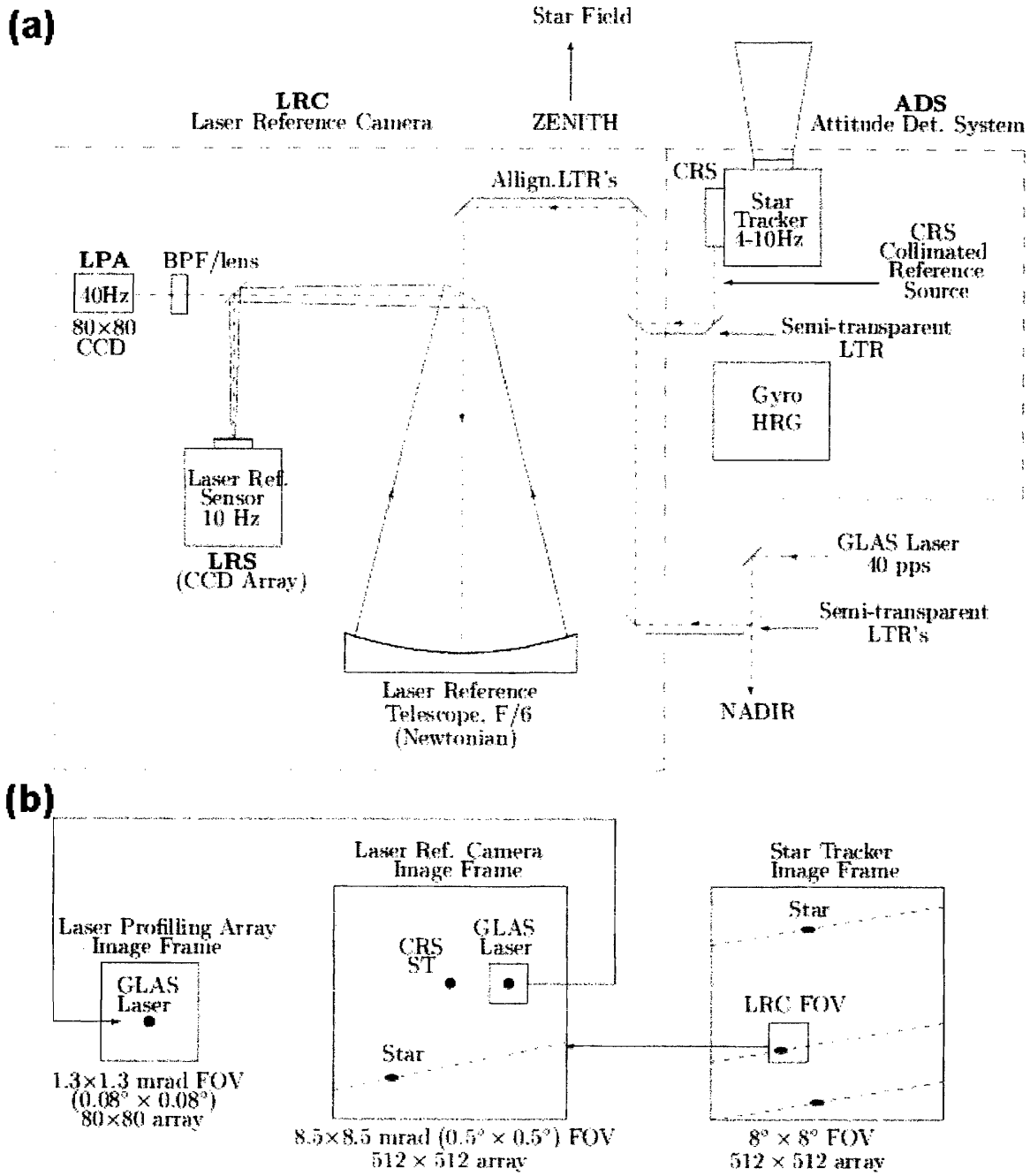

Figure 4-8 Stellar Reference System. **(a)** A fraction of the laser beam is redirected into the Laser Reference Camera, along with the orientation of the star tracker to determine pointing orientation. **(b)** Layouts of image frames from the star tracker to the Laser Profiling Array illustrate how pointing orientation with respect to the star tracker is measured. (Figure is taken from Bae and Schutz [2002]).

Table 4.2 Single Shot Vertical Error Budget

Source	Pre-launch Error(cm)	Post-launch Error(cm) [a]	Reference[b]
Instrument precision	10	2 [c]	Bufton [1989]; Schutz [1998]; Zwally et al. [2002]
Orbit determination	5 (& 20[d])	<3	Rim and Schutz [2002]; Zwally and Jun [2002]
Pointing determination	1.5 arcsec	1.5 to 25 arcsec	Schutz [1998]; Zwally and Jun [2002]
Troposphere delay	1	1	Schutz [1998]
Atmospheric scattering	2	2	Schutz [1998]; Zwally and Jun [2002]
Saturation	unknown	0-40	
Forward scattering	unknown	4 to 7	
Field of view shadowing	0-30	same[e]	
Tides	1	unknown [f]	Schutz [1998]; Zwally and Jun [2002]
Total	13.8	20 to 70	Zwally and Jun [2002]

[a] Post-launch values are from post-launch evaluations of the ICESat team during team meetings.
[b] references for pre-launch error values.
[c] Shuman et al. [2005]'s estimation over flat terrain in Lake Vostok, East Antarctica.
[d] radial and horizontal directions respectively.
[e] The error due FOV shadowing can be in-separable from that due to pointing.
[f] Tidal model is considered in-correct for the ice-sheet, the team is still investigating how to best calculate and apply this correction.

[2002]). The term *attitude* refers to the angular orientation of the optical bench containing the lasers and the receiving telescope [Bae and Schutz, 2002] with respect to an external reference frame such as the Celestial Reference Frame. *Pointing* is referred to the direction of the out-going laser with respect to the optical bench [Bae and Schutz, 2002; Schutz et al., 2005]. For every transmitted laser pulse, a fraction of the energy is redirected into the Laser Reference Camera, along with alignment information with respect to the star tracker (Figure 4-8). Within the Laser Reference Camera, a Laser Profiling Array will digitize and determine the orientation of the laser pointing with respect to the spacecraft to within 1.5 arcsec (Figure 4-8b). The error in geolocation of the laser footprints on the ground associated with pointing results in $\sim$ 5cm of vertical error per arcsec per degree of total slope (surface slope plus off-nadir angle) [Schutz, 1998; Schutz et al., 2005].

Atmospheric correction can achieve accuracy of 1cm, which corresponds to modeling surface pressure accurate to $\pm$ 5mbar [Schutz, 2002; Herring and Quinn, 1999]. Ocean tidal loads can cause displacement in the range of tens of millimeters over Antarctica. Using the current tide model, this displacement can be measured to within $\pm$3mm and corrected for [Yi et al., 1999]. Other sources of error include GPS clock synchronization and atmospheric scattering (Table 4.2). The presence of low altitude thin clouds causes forward scattering which will both delay and decrease the magnitude

of the return waveform, and results in height biases of several centimeters and an increase in range uncertainties. In summary, the pre-launch vertical error budget for a single shot totals $\sim 14.8cm$ [Zwally et al., 2002].

4.2.5 On-orbit performance

4.2.5.1 Mission plan modification

After launch, Laser 1 performed well with a couple of unexpected major drops in the output energy. Thirty eight days after activation, Laser 1 abruptly failed. An Independent GLAS Anomaly Review Board (IGARB) concluded that a failure in the laser pump diode array due to a temperature-dependent chemical erosion that had taken place in the wire bonds was the main cause [IGARB, 2003]. IGARB also concluded that the problem would most likely exist in the remaining two lasers on-board ICESat. The mission plan was modified in September 2003 to operate the lasers (one at a time) at a lower temperature to slow down the erosion, and to operate them in short durations of approximately 33 days three times a year. Laser 2 was activated in October 2003, and performed well in its first 50 days (Laser 2a). At the start and end of its third campaign (Laser 2c) in May 2004, the 532nm and 1064nm energy diminished below the usable level (~3mJ) respectively. Following recommendations from the instrument team, Laser 3 was activated at lower temperature in an attempt to slow down the energy decline rate. As a consequence, the 532nm energy dropped below the 3mJ threshold required for detection, and was not usable. However the strategy had slowed down the rate of energy decrease for the 1064nm channel, enabling the completion of Laser 3a,b,c campaigns by May 2005. The instrument team anticipates seven more operational periods before the 1064nm energy drops below the critical threshold of 3mJ, assuming that the energy decline rate remains consistent with what is observed currently [Abshire et al., 2005].

4.2.5.2 Boresight alignment – field of view shadowing

The alignment of the laser footprint within the field of view (FOV) of the receiving telescope is critical for the return energy to be detected. For GLAS, the FOV of the receiving telescope is $\sim$ 63 arcsec in radius, with approximately flat maximum response at the center, attenuation of 50% at $\sim$ 41 arcsec, and 5% at $\sim$ 62 arcsec (Figure 4-9a). The 1064nm laser beam is approximately 17 arcsec. A height accuracy of $\sim$ 15cm (and height rate of change accuracy of 2cm/yr) requires the laser beam to be within the 90% FOV response, or $\sim$ 23 arcsec radius (Figure 4-9a). Outside of this radius, the return waveform would be clipped resulting in height biases. This phenomenon is sometimes refered to as the FOV shadowing effect. Prior to launch, the misalignments between all three lasers and the receiving telescope due to different sources were identified. The most important of which is the thermally-driven drift which can cause misalignments of 10 to 28 arcsec over the range of expected operational temperatures of ICESat in space. Figure 4-9a also shows height biases due to misalignments of 41 arcsec for a surface slope of 3^o.

When the 532nm channel was available in orbit, misalignments could be observed. Figure 4-9b taken from Abshire et al. [2005] shows the 1064nm laser beam pattern for Laser 2a as seen from the Laser Profile Array within the Stellar Reference System. The return waveform (Figure 4-9b) clipped by the misalignment is biased either at the leading edge or at the tail, resulting in height bias in both directions. As temperature on the optical bench changes across the day and night side and with time, the misalignment can also drift in an unpredictable fashion. In addition, each laser has a different offset which could cause height bias between lasers if not accounted for. Current assessment by ICESat team is approximately $\sim$ 15 arcsec in pointing errors associating with this misalignment, which due to the lack of the 532nm channel is still not corrected for (except in Laser 2a).

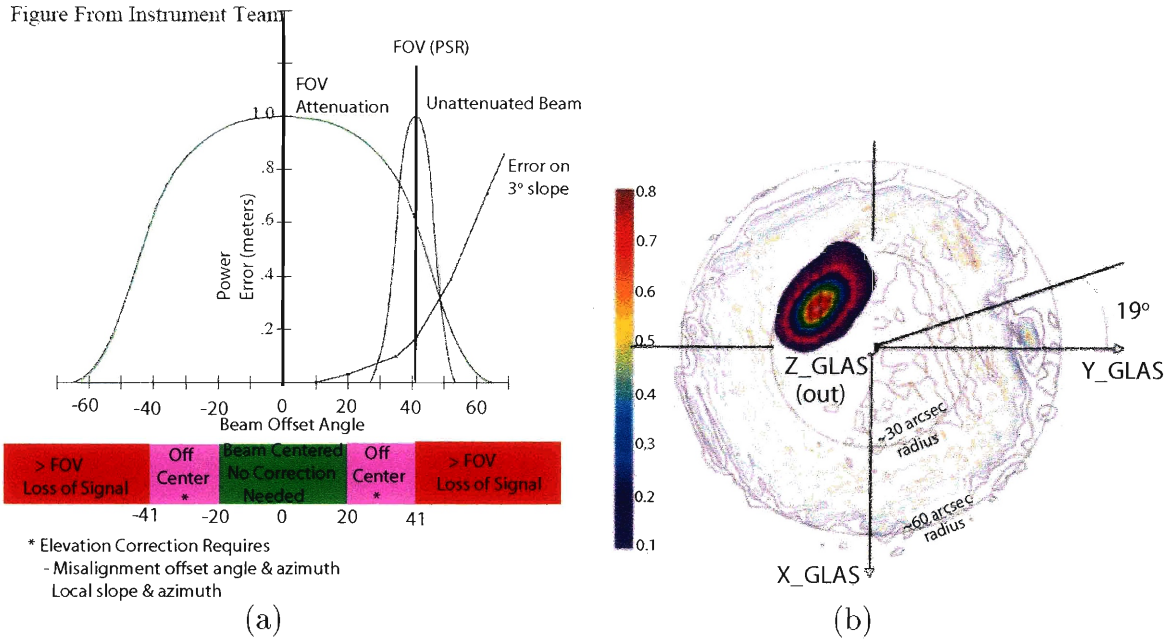

Figure 4-9 Field of view of ICESat receiver telescope (a) and location of Laser 2 beam within the field of view (b) [Abshire et al., 2005]. (a) The power response of the field of view is flat max in the center and falls off exponentially beyond approximately 41 arcsec. The horizontal color bar shows the laser footprint should be within the 20 arcsec of the FOV for height measurements to bias free. Within 20 to 41 arcsec, the laser return energy is clipped (as shown by the laser beam offsetting at +41 arcsec) and height bias has to be corrected for. Beyond 41 arcsec where the FOV response has attenuated to 50%, signal is considered lost.

4.2.5.3 Pointing errors

A detailed discussion of the pointing biases and methods to correct for them are in Luthcke et al. [2005] and Lisano and Schutz [2001], and a summary is given here. Figure 4-10a taken from Lisano and Schutz [2001] shows how an error in pointing maps into error in height measurement. A height $H_{measured}$ is obtained with an off-nadir pointing $\delta\alpha_{est}$. However an error in pointing $\Delta\delta\alpha$ means that the actual off-nadir pointing is $\delta\alpha$, and that we have erroneously assign the height $H_{measured}$ at point A to point B whose height is H_{true}. Pointing errors can be tracked using ocean scan maneuvers, as shown in Figure 4-10b [Luthcke et al., 2005]. A series of ocean scans by ICESat reveals the time / temperature / geographically-dependent pointing biases (Figure 4-10c). A combined solution using Stellar Reference System data, ocean scan, and minimized cross-over residuals can reduce these pointing errors (Figure 4-10c) down to 0.00±0.94 arcsec for the first 50 days of Laser 2 [Luthcke et al., 2005]. When data from the Stellar Reference System are not available, the

short-period component of pointing errors and some of the long term trend (including those from FOV shadowing) can not be removed, and pointing errors remain higher than the science requirement of 1.5 arcsec.

4.2.5.4 Forward Scattering

Forward scattering was covered in a presentation by Spinhirne [2005] during an ICE-Sat team meeting and in Duda et al. [2001], and will be summarized here. In the presence of thin clouds, the transmitted photons can be scattered within one degree of the pulse path prior to surface encounter, and mixed in with the non-scattered photons on the returning path. The effect on the return waveform includes broadening of the main peak and stretching at the tail. Detection of thin clouds is done using the 532nm atmospheric channel, and the 1064nm atmospheric channel when the former channel is weak in energy or not available. Range bias can be calculated based on a combination of cloud thickness, inferred optical depth along the photons' path, receiver's field of view radius, and cloud heights. Range delays can reach up to 20cm for optically thin cloud within 2km of the surface [Duda et al., 2001]. The cloud sensitivity in the 1064nm channel is weaker than in the 532nm channel for all particle sizes with optical depth less than 0.2 [Spinhirne, 2005]. As a result, when the 1064nm is used to detect cloud, the error would be approximately 2cm on average for East Antarctica, and $>$ 5cm for West Antarctica [Spinhirne, 2005].

4.2.5.5 Saturation

Saturation of the GLAS detector is due to a combination of high reflection of energy off very flat surfaces in Antarctica and the instrument inability to adjust the gain below its preset lower limit [Sun, 2005]. The onset of non-linear response of the instrument detector occur when the receive energy exceeds approximately twice the pre-launch calibration values. Over Antarctica, when the laser was at full strength at the beginning of each campaign, the received energy was four times the pre-launch expected value on average for clear sky condition and flat surfaces [Sun, 2005]. The characteristics of a saturated received energy waveform include a flat top, a longer

tail with ringings at both the peak and tail [Fricker et al., 2005; Sun, 2005]. Both standard centroid and alternate Gaussian fits to the saturated return waveforms yield longer than the true ranges, which results in a lower derived surface heights [Sun, 2005]. Range errors can reach up to 40cm over the flat surface in Antarctica when saturation is not corrected for. The distribution of saturated shots and correction procedure will be discussed in more detail in the next chapter.

4.3 Summary

The last column in Table 4.2 shows the post-launch GLAS single-shot accuracy. Contributions from orbits and atmospheric delays are at or better than pre-launch requirements. However pointing biases, FOV shadowing, forward scattering, and saturation errors are still above the science requirements. The post-launch accuracy is approximately 20-70cm. The ICESat team has formed a sub-panel to address the precision - range determination of GLAS, and progress has been made. We anticipate the removal of both saturation and forward scattering errors to within 2-4cm accuracy. In addition, the pointing errors are anticipated to be constrained to less than 1.5 arc-sec (7.5cm).

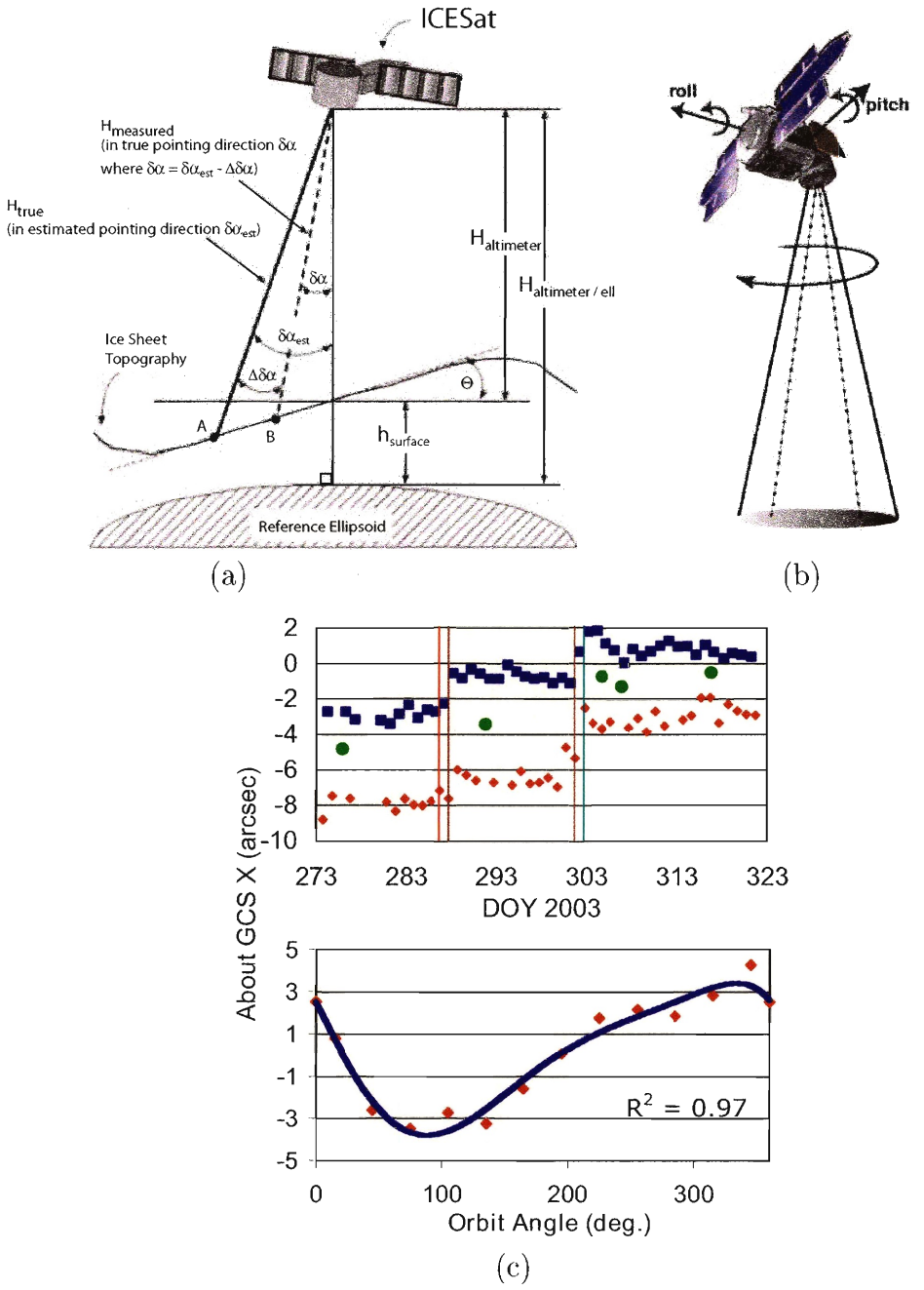

Figure 4-10 Geometry of satellite showing height bias due to pointing (a), ocean scan maneuver used to removed pointing bias (b), and ICESat pointing bias (c) which are both time and temperature dependent. In (a), $\delta\alpha$ is the off-nadir pointing, and $\Delta\delta\alpha$ the pointing error. In (c) biases are shown for only the X-axis of the spacecraft, and the top panel shows biases from ocean scans at orbit midnight (blue) and orbit noon (red), and the bottom panel shows bias estimates (red) from a round-the-world-scan (an equivalent of an ocean scan over a full orbit) and a functional fit (blue). The figures are taken from Lisano and Schutz [2001], Luthcke et al. [2005] and a presentation by Scott Luthcke at an ICESat team meeting.

Chapter 5

Analysis of ICESat Data using Kalman Filter and Kriging to Study Height Changes in East Antarctica

(A shortened version of this chapter is being submitted to Geophys. Res Letts. for publication.)

5.1 Introduction

In 2003, NASA launched the Ice Cloud and land Elevation Satellite (ICESat) with the Geoscience Laser Altimeter System (GLAS) on-board. One of ICESat scientific objectives is to study changes in the ice-sheet surface heights to improve our understanding of the ice-sheet mass balance and the contributions of the ice sheets to sea-level changes. With a global coverage of $\pm 86°$N at along-track spacing of $\sim$172m, GLAS is the first laser altimeter to offer us a high-precision set of data with uniform spatial and sufficient temporal coverages to address the mass balance issue in Antarctica ([Schutz et al., 2005], Chapter 1, Chapter 4).

Over the Antarctic ice sheet, height change (dh/dt) detections using space-borne altimetry measurements are typically calculated by averaging height differences at

cross-over locations over large areas and long periods of time [Zwally et al., 1989]. The main advantage of this method is that measurements are interpolated over short distances (less than the along-track spacing) to the same locations, and that any change likely reflects real *dh/dt*. Errors are typically large per cross-over, but decrease when averaged over large areas and time as $N^{-1/2}$, where N is the number of cross-overs used [Zwally et al., 1989]. However this approach only uses $< 10\%$ of the available data. In addition, implementation of cross-over analysis often bins data as a function of time, adding an additional assumption that during the binning interval, the heights remain constant. In this chapter we develop an alternate approach to the spatio-temporal *dh/dt* detection problem to assess whether height change detection with accuracy of ~2cm/yr over $(100\text{km})^2$ areas is possible. We present preliminary results of processed ICESat ice-sheet height data using a combined kriging/Kalman filtering technique to evaluate the technique's capability and current data releases quality.

5.2 Method

Kalman filtering, which is based on Bayesian estimation, is a minimum-variance estimator that is ideal for systems that stochastically evolve with time [Sorenson, 1970; Maybeck, 1979]. For ICESat mission, the data are collected at different time-steps of 1/40 sec (shot-to-shot), 8 days (8-day cycle), and between 91 to 139 days (33-day sub-cycle). In cross-over analysis, one would assume that the surface elevation has not changed within each, and that height changes occur between each 8-day or 33-day duration. The use of Kalman filtering would remove this arbitrary decision by improving the estimate of height changes continuously each time a new data point is collected. We formulate the filter for ice-sheet height change problem as follows,

- Update

$$\mathbf{x}_{t+\Delta t}^{t} = \mathbf{S}_{t+\Delta t} \cdot \mathbf{x}_{t}^{t} \tag{5.1}$$

$$\mathbf{C}_{t+\Delta t}^{t} = \mathbf{S}_{t+\Delta t} \cdot \mathbf{C}_{t}^{t} \cdot (\mathbf{S}_{t+\Delta t})^{T} + \mathbf{Q} \tag{5.2}$$

• Observation equation

$$\mathbf{z} = \mathbf{A} \cdot \mathbf{x} + \mathbf{v} \tag{5.3}$$

• Kalman Gain

$$\mathbf{K} = \mathbf{C}^{t}_{t+\Delta t} \cdot (\mathbf{A}_{t+\Delta t})^{T} \cdot (\mathbf{A}_{t+\Delta t} \cdot \mathbf{C}^{t}_{t+\Delta t} \cdot (\mathbf{A}_{t+\Delta t})^{T} + \mathbf{R})^{-1} \tag{5.4}$$

$$\mathbf{x}^{t+\Delta t}_{t+\Delta t} = \mathbf{x}^{t}_{t+\Delta t} + \mathbf{K} \cdot \mathbf{z} \tag{5.5}$$

$$\mathbf{C}^{t+\Delta t}_{t+\Delta t} = \mathbf{C}^{t}_{t+\Delta t} - \mathbf{K} \cdot \mathbf{A}_{t+\Delta t} \cdot \mathbf{C}^{t}_{t+\Delta t} \tag{5.6}$$

with

$$\mathbf{x} = \begin{bmatrix} \delta dem_1 & \cdots & \delta dem_N & P_1 & \cdots & P_M & \Delta DEM & \frac{dh}{dt} \end{bmatrix}^{T} \tag{5.7}$$

$$\mathbf{S} = \begin{bmatrix} 1 & \cdots & 0 & 0 & \cdots & 0 & 0 & 0 \\ \vdots & \ddots & \vdots & \vdots & \ddots & \vdots & \vdots & \vdots \\ 0 & \cdots & 1 & 0 & \cdots & 0 & 0 & 0 \\ 0 & \cdots & 0 & 1 & \cdots & 0 & 0 & 0 \\ \vdots & \ddots & \vdots & \vdots & \ddots & \vdots & \vdots & \vdots \\ 0 & \cdots & 0 & 0 & \cdots & 1 & 0 & 0 \\ 0 & \cdots & 0 & 0 & \cdots & 0 & 1 & \Delta t \\ 0 & \cdots & 0 & 0 & \cdots & 0 & 0 & 1 \end{bmatrix} \tag{5.8}$$

$$\mathbf{A} = \begin{bmatrix} w_1 & \cdots & w_N & \eta_1 & \cdots & \eta_M & 1 & 0 \end{bmatrix} \tag{5.9}$$

Definitions of variables are as follows:

x: the state vector containing the model parameters

S: the state transition matrix

A: the partial derivative matrix

C: the model covariance matrix

Q: the model process noise covariance matrix

v: the data noise, assumed Gaussian $N(0, \mathbf{R})$

R: the data noise covariance matrix

z: measured minus predicted heights at ICESat location at time $t + \Delta t$ (length L)

K: the Kalman gain matrix

$[]_t^t$: estimate at previous time step

$[]_{t+\Delta t}^t$: estimate at current time step prior to data input (a-priori)

$[]_{t+\Delta t}^{t+\Delta t}$: estimate at current time step after data input (a-posteriori)

δdem: change in the modeled 5km DEM pixel height (length N)

P: additional modeled parameters related to topography field (length M)

ΔDEM: change in the overall $(100\text{km})^2$ DEM block height

$\frac{dh}{dt}$: rate of height change for the whole $(100\text{km})^2$ block

w_i: weight contribution of each DEM pixel to the predicted height at ICESat location

η_i: "weight" contribution of each additional parameter P

5.2.1 5-km DEM model

In this model, we start with a crude DEM using Laser 2a (Release 14) data with a resolution approximately 5km as the *a-priori* model. The DEM is calculated by averaging all data points within each $(5\text{km})^2$ block, and is done in polar stereographic projection (parallel $= -80°$) to maintain the regular spacing. Height residuals are calculated using bi-cubic interpolation from the closest 16-elements in the DEM to ICESat location on the ground. For each approximately $(100\text{km})^2$ block as a function of time, we estimate improvements to the DEM 5km elements $(\delta_{dem})_i$, the over-all height change of the block Δ_{DEM}, and the block height rate of change dh/dt. Also estimated are two additional parameters $P_1 = B_1$ and $P_2 = B_2$ related to the amplitude and phase of the seasonal surface height signal. The DEM pixel uncertainties are assumed uncorrelated with a uniform *a-priori* value of $400m^2$. Uncertainties for $\Delta_{DEM}, dh/dt, B_1, B_2$ are also assumed $400m^2, 400m^2/yr^2, 400m^2, 400m^2$. These values are loosely constrained relative to the data. Model process noise is assumed zero ($Q = 0$), and data noise v is assumed $\sim N(0, R) = N(0, 1m^2)$. Thus **x**, **S**, **A**, and **z**

in Eqn 5.7 to 5.9 and Eqn 5.3 are as follows,

$$x = \begin{bmatrix} \delta dem_1 & \cdots & \delta dem_N & B_1 & B_2 & \Delta DEM & \frac{dh}{dt} \end{bmatrix}^T \tag{5.10}$$

$$S = \begin{bmatrix} 1 & \cdots & 0 & 0 & 0 & 0 & 0 \\ \vdots & \ddots & \vdots & \vdots & \vdots & \vdots & \vdots \\ 0 & \cdots & 1 & 0 & 0 & 0 & 0 \\ 0 & \cdots & 0 & 1 & 0 & 0 & 0 \\ 0 & \cdots & 0 & 0 & 1 & 0 & 0 \\ 0 & \cdots & 0 & 0 & 0 & 1 & \Delta t \\ 0 & \cdots & 0 & 0 & 0 & 0 & 1 \end{bmatrix} \tag{5.11}$$

$$A = \begin{bmatrix} w_1 & \cdots & w_N & cos(2\pi(\frac{t-t_{jan}}{365})) & sin(2\pi(\frac{t-t_{jan}}{365})) & 1 & 0 \end{bmatrix} \tag{5.12}$$

$$\begin{aligned} \mathbf{z} = \sum_{i=1}^{N} w_i \cdot \delta dem_i \quad &+ \quad cos(2\pi(\frac{t-t_{jan}}{365})) \cdot B_1 \\ &+ \quad sin(2\pi(\frac{t-t_{jan}}{365})) \cdot B_2 + \Delta DEM + \mathbf{v} \end{aligned} \tag{5.13}$$

and the amplitude B and phase θ of the seasonal change are related to B_1 and B_2 by:

$$B_1 = B \cdot cos(\theta) \tag{5.14}$$

$$B_2 = B \cdot sin(\theta) \tag{5.15}$$

or:

$$B = \sqrt{B_1^2 + B_2^2} \tag{5.16}$$

$$\theta = tan^{-1}\frac{B_2}{B_1} \tag{5.17}$$

$$h_{seasonal} = B \cdot cos(2\pi(\frac{t-t_{jan}}{365}) - \theta) \tag{5.18}$$

t_{jan} in Eqn 5.18 refers to Jan 01, 2003. In this model, w_i in Eqn 5.12 are the kriging weights calculated based on statistics of heights within the regions of study. See Chapter 2 for a review of the kriging method. In contrast to the radar satellite data, the fine spacing along track of ICESat gives continuous surface height residuals (ICESat height minus DEM) with raw semi-variograms following a gaussian function of the form

$$\gamma(h) = \sigma^2(1 - exp(-(\frac{h}{L})^2)) \tag{5.19}$$

where σ^2 and L are called the sill and range of the variograms, and h the lag (separation distance) in unit degree [Olea, 1999]. The parameter σ^2 is an approximate estimation of the field's covariance at zero lag, and the range L represents the distance of separation beyond which, correlation between the height residuals approaches zero asymptotically. Figure 5-1 shows the locations of the three studied regions along with an example of a $(100km)^2$ DEM block. These regions are chosen to facilitate comparisons of results between ICESat and ERS data. Their corresponding raw semi-variograms are shown in Figure 5-2 and Table 5.1- 5.2. Because fitting the raw semi-variogram at short lags is more important than fitting the whole shape [Olea, 1999], a weighted linear least square inversion with weights corresponding to $1/h^2$ is used for fitting, and only lags $\leq 0.1^o$ are used. As seen in Figure 5-2, the fit is badly over-estimating at lags larger than 0.25km. However it is essential to capture the continuous behavior of residuals at the shot-to-shot separation, and beyond lags 0.25km, the kriging weights have decreased significantly compared to at shorter lags. In addition, the spacing between the DEM pixels are approximately 5km. This means at any time t_0, four closest pixels will be at lags $\leq$ 5km to the ICESat footprint, and a gaussian variogram model will produce a smooth transition in height at the next ICESat shot at time t_1. In contrast, when the whole shape of the raw variogram is fitted, the fit will grossly over-estimate at small lags and result in dis-continuous jumps at the shot-to-shot length scale.

The set up for the approximate $(100km)^2$ blocks is listed in Table 5.3. The block size

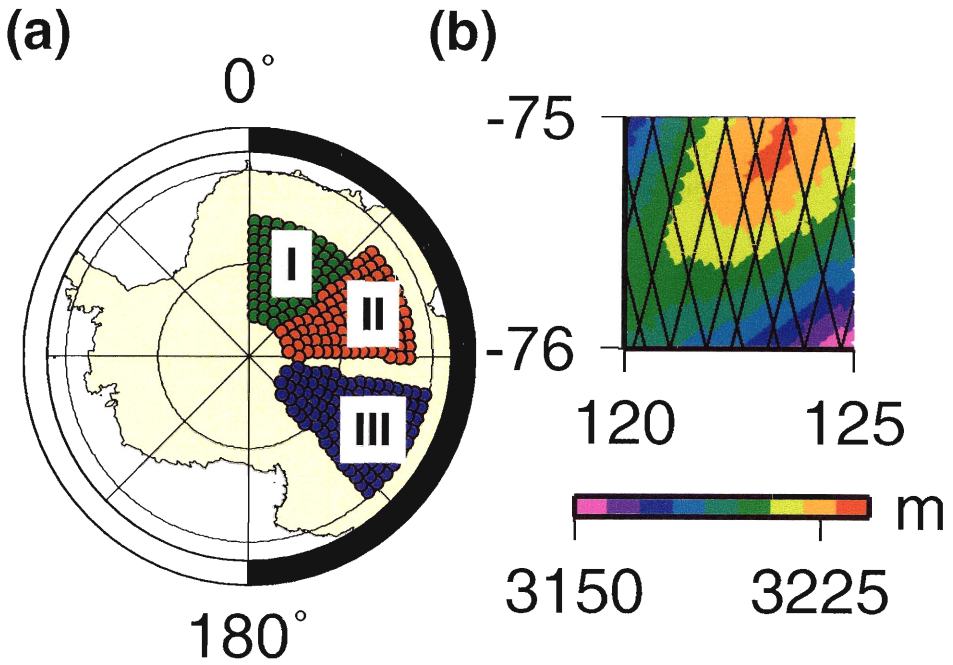

Figure 5-1 Three regions of study (a) with a sample (100km)^2 block DEM centered at [-75.5^o,122.5^o] (b). Each circle in (a) represents a (100km)^2 block. There are 287 blocks, with each having approximately between 600 and 850 5-km pixels (shown as circles with elevation in (b) and 12 to 125 GLA06 tracks within each 33-day cycle (500 to 8000 data points).

is always 1^o in the latitudinal direction, corresponding to approximately $111km$. In the longitudinal direction, due to the $cos(\phi)$ decrease, the block size is changing from approximately 4^o at latitude -70^oN to 15^o at -86^oN.

Table 5.1 Regions of study

Region	lat range (°)	lon range (°)	σ^2 (m^2)	L(^{o})	h$_{max}$ (^{o})	cov (m^2)
I	[-86,-75]	[0,50]	13.75	0.033	0.10	21.6
II	[-86,-72]	[50,90]	18.17	0.019	0.08	33.6
III	[-86,-70]	[100,140]	12.05	0.033	0.10	17.0

Table 5.2 Semivariograms values $\gamma(h)$ (m^2)

Region \ lag(km)	0.1	0.3	0.5	0.8	1	3	5	10
I	0.010	0.093	0.258	0.650	1.002	6.79	11.68	13.74
II	0.042	0.378	1.032	2.526	3.789	15.96	18.12	18.17
III	0.009	0.082	0.226	0.569	0.878	5.95	10.23	12.04

Table 5.3 $(100km)^2$ block set up

lat	[-70,-75]	[-75,-78]	[-78,-80]	[-80,-82]	[-82,-83]	[-83,-84]	[-84,-85]	[-85,-86]
Δlat (^{o})	1	1	1	1	1	1	1	1
Δlon (^{o})	4	5	6	7.5	9	10	12	15
Δlon (km)	[152,115]	[144,116]	[139,116]	[145,116]	[139,122]	[136,116]	[139,116]	[145,116]

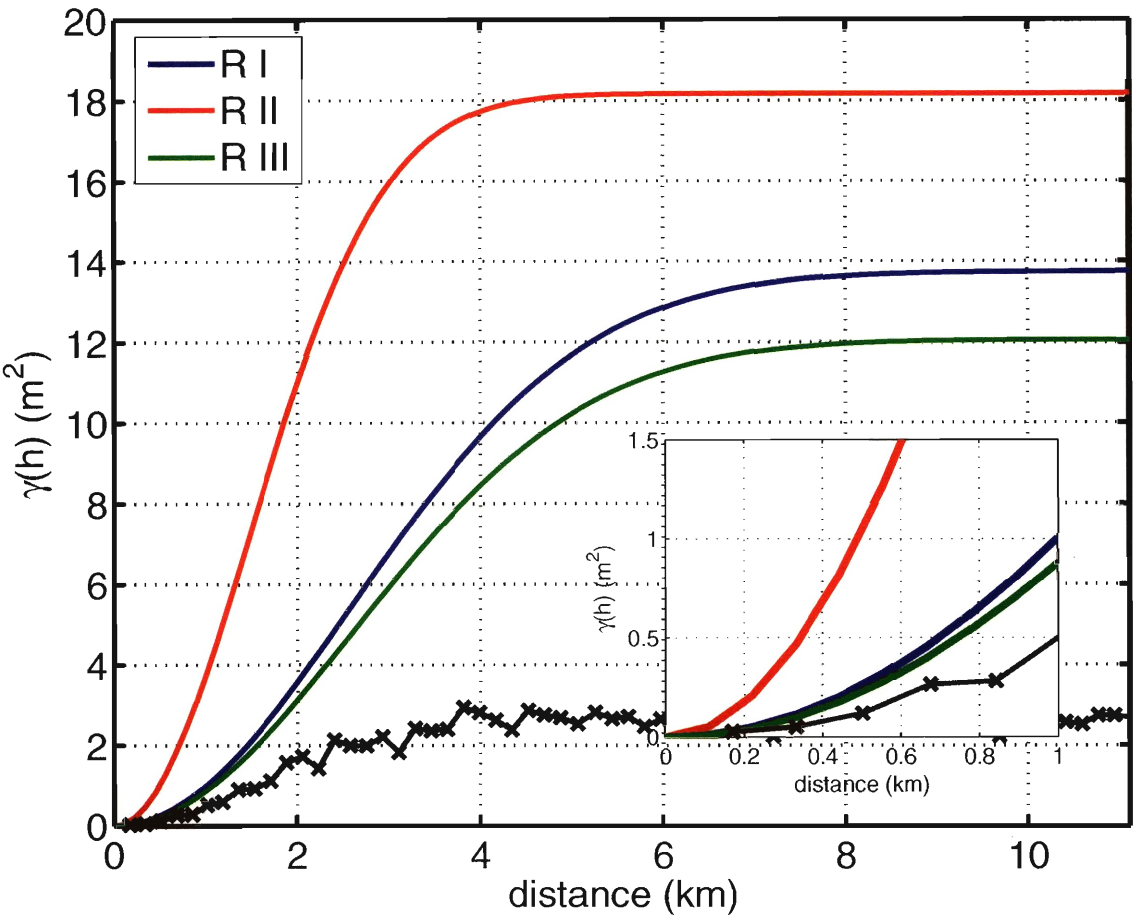

Figure 5-2 Semi-variograms (γ) of height residuals for the three regions shown in Figure 5-1a, along with a raw semi-variogram for region III (x). $\gamma(0)$ corresponds to 1-cov(0). Region III is smoothest (sill $\approx 12\text{m}^2$), and region II roughest (sill $\approx 18\text{m}^2$). Region I is close to III in characteristics. See Table 5.1 for a complete list of all parameters and Table 5.2 for the numerical values of both the sill σ^2 and variogram γ. The behavior of γ at foot-print spacings is shown in the inset.

5.3 ICESat Data

We use estimates of geodetic height above the reference ellipsoid from the most recent releases of GLA06 Global Elevation Data Product and energy and gain from GLA01 Global Altimetry Data Product and GLA05 Global Waveform-based Range Corrections Data (Table 5.4, [Schutz et al., 2005]). Also shown in Table 5.4 are the data releases, range accuracies, and pointing biases. Standard GLA06 data have all instruments and other corrections already applied, including atmospheric, tropospheric delays and tides. Two outstanding issues, saturation and pointing, remain in the data and control the range measurement accuracy. Pointing errors are due to different factors including the motion of the instrument's different components and the mis-alignment of the receiver's field of view with the center of the laser's footprint on the ground (Chapter 4). As discussed in Chapter 4, lack of pointing knowledge is due to the absence of the 532nm channel, and correction for these errors are not straight forward due to the dependency of orbit time, laser energy, temperature, and other factors. Luthcke et al. [2004] showed that pointing biases induce height change biases that are geographically correlated that reaches $\sim$ 5cm/yr in Antarctica. Our estimates of pointing errors based on differential slopes over the ice-sheet are consistent with (but slightly lower than) those estimated globally by Luthcke et al. [2004] (Figure 5-3, the last column in Table 5.4). Related to the pointing problem are the height differences between ascending and descending tracks at cross-over locations, with mean varying between 0-0.05m in magnitudes, and root-mean-square (RMS)

Table 5.4 ICESat height accuracies and biases

Laser	REL	start date (mmddyy)	end date (mmddyy)	RSS[1] (cm)	global [2] pointing bias (arc-sec)	Surface slope vertical bias due to pointing bias (cm) [2] 0.1°	0.3°	0.5°	Antarctica bias (arc-sec)[3]
1	18	02/20/03	03/29/03	18	5.83	2.96	8.88	14.80	4
2a	21	09/25/03	11/18/03	16	0.94	0.48	1.43	2.39	0.96
2b	16	02/17/04	03/21/04	17	8.07	4.10	12.29	20.49	3.4
2c	17	10/04/04	11/08/04	21	23.99	12.18	36.54	61.90	20
3a	22	10/04/04	11/08/04		2.21	1.12	3.36	5.60	1.76

[1] DiMarzio et al. [2004], [2] Luthcke et al. [2005], [3] Figure 5-4 (this study)

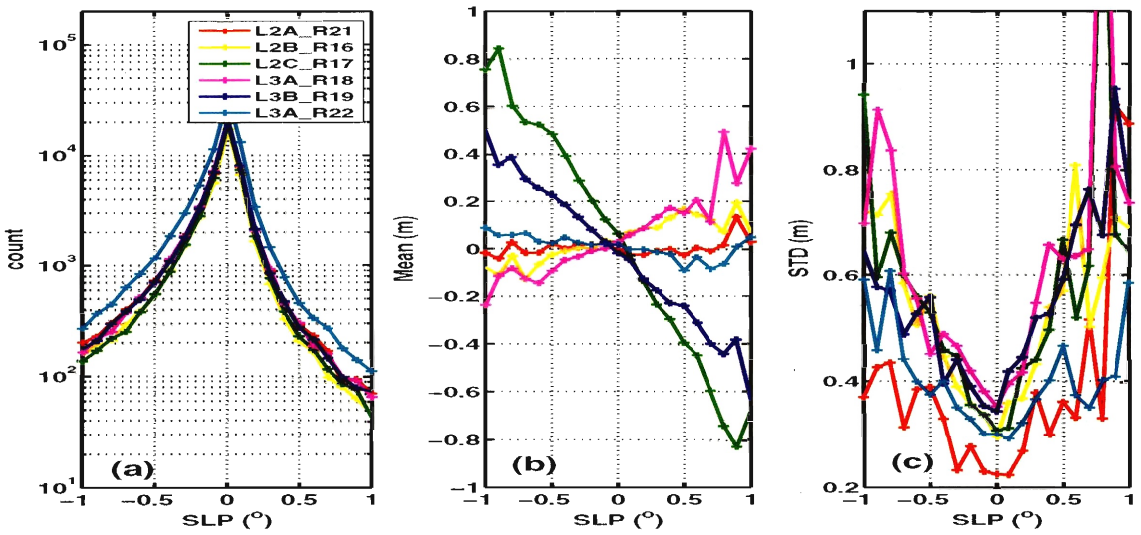

Figure 5-3 Estimates of pointing bias for ICESat height over Antarctica based on differential slopes at cross-overs. The number of cross-overs are consistent for all 33-day operational periods Laser 2a-3b **(a)**. As a function of differential slopes between the two tracks, ascending minus descending, cross-over residual mean increases away from zero $\Delta slope$ indicating the existence of pointing biases **(b)**. The best fitted slope through the means suggests pointing biases for Laser 2a-2c and 3a of 4, 0.96, 3.4, 20, 1.76 arc-sec. The deviation from the mean (STD) is similar for all lasers **(c)**, with Laser 3b having the largest STD at zero-slope of approximately $35cm$ compared to $\leq 30cm$ for Lasers 2a-3a.

scatter of 0.20-0.30 m (Figure 5-3b,c). Laser 2c is excluded from this study because of its current large pointing errors of nearly 20 arc-sec (Figure 5-3b).

The cause of saturation in the return waveform was covered in Chapter 4. Based on initial analyses in the lab, the ICESat team has recommended to correct for saturation for any return waveform with energy higher than a threshold value of $E_{sat} = 13.1fJ$ and gain = 13. We apply the saturation correction to all shots with gain = 13 using the formula shown below (for releases earlier than 22, we multiply the received energy by a factor 1.21, and for releases earlier than 19, we correct for the gain record mis-registration [Donghui Yi, 2005, *per comm*]). We exclude all shots with gain less than 13 (saturated) or more than 100 (a pseudo cloud-filter). For shots with gain between 14 and 100, we use only those shots with energy < 13.1fJ. The two-way time-delay formula for gain = 13 is $t_{delay} = \alpha(E - E_{sat})$ with $\alpha = 0.149$ns/fJ, and the sense of correction is such that the corrected heights are higher than the saturated ones [Sun, 2005]. This scheme will not remove all of the saturation related problems because $E_{sat} = 13.1$fJ is only applicable for gain = 13, and parameters E_{sat} and α have not been derived for other gains. The saturation correction parameter $\alpha = 0.149ns/fJ$

translates to approximately -2.2cm/fJ of height bias. Figures 5-4- 5-6 and Table 5.5 show the statistics of the number of valid ICESat elevation used. The upper limit in gain of 100 is arbitrary because the majority of valid shots have gain < 50 and those in the presence of cloud have gain ≈ 200. This editing eliminated $\sim 80\%$ of Laser 1 and $\sim 2-5\%$ of Laser 2-3 data. In addition to saturation correction, individual height profiles were compared across the laser operation periods to remove spurious data that are due to low-altitude clouds.

Table 5.5 Percentage of valid shots used

Region	time	Laser	GAIN < 13		GAIN $= 13$	GAIN $(13, 100]$		Total valid shots (%)
			total	valid	valid	total	valid	
	t02	1	41.9	0.24	4.9	28.6	20.9	25.8
	t03	1	64.4	0.49	7.6	19.2	12.2	19.8
	t04	1	10.3	0.08	54.9	26.4	18.7	73.6
R1	t28	2a	0	0	75.6	20.0	18.1	93.7
	d290	2a	0	0	85.6	12.1	10.4	96.0
	d413	2b	0.76	0.76	39.5	57.5	53.4	92.9
	d643	3a	0	0	88.4	10.7	7.5	95.9
	t02	1	51.2	0.24	6.9	23.6	14.2	21.1
	t03	1	81.2	0.20	6.7	8.4	3.1	9.8
	t04	1	11.2	0.03	48.5	22.4	14.1	62.6
R2	t28	2a	0	0	74.4	23.2	22.2	96.6
	d290	2a	0	0	88.0	10.8	9.6	97.6
	d413	2b	0.16	0.16	36.5	60.8	57.7	94.2
	d643	3a	0	0	82.0	15.2	13.6	95.6
	t02	1	56.8	0.79	10.5	14.2	6.7	17.2
	t03	1	74.2	0.33	8.3	11.2	6.6	14.9
	t04	1	14.4	0.04	62.2	12.7	5.7	67.9
R3	t28	2a	0	0	75.0	22.3	21.8	96.8
	d290	2a	0	0	91.0	8.1	7.6	98.6
	d413	2b	0.18	0.18	35.3	60.0	58.2	93.5
	d643	3a	0	0	87.25	11.6	9.1	96.4

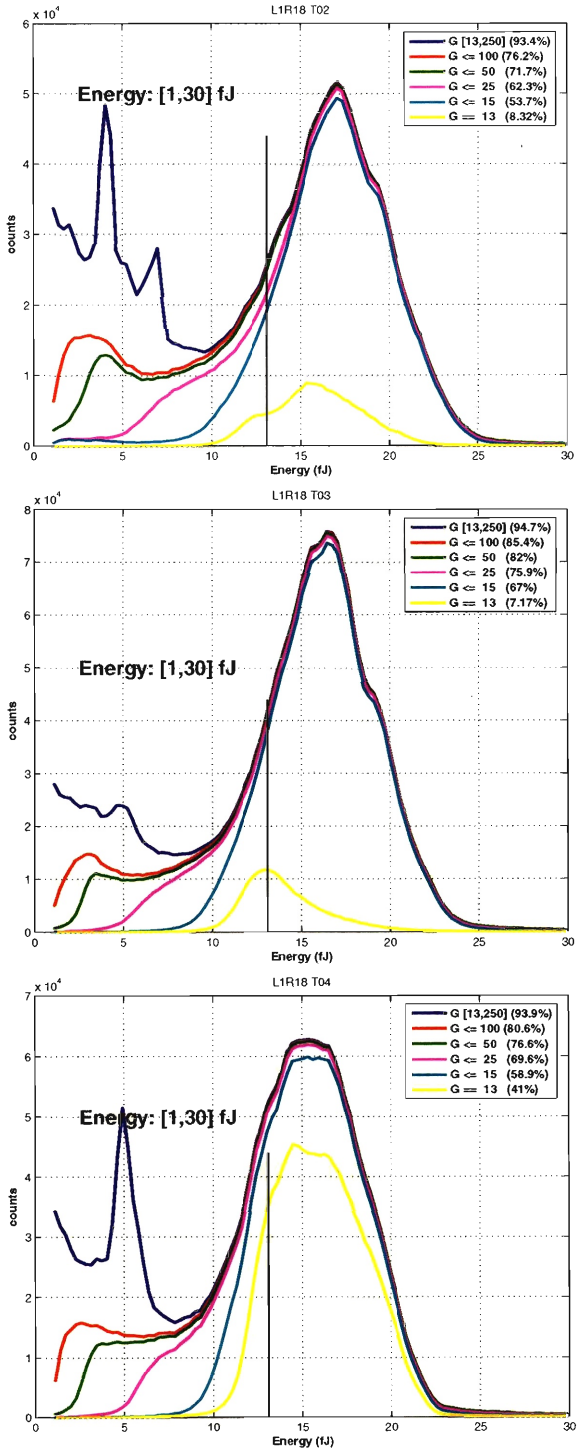

Figure 5-4 Laser 1 cycles 02, 03, 04 saturation statistics. Only shots with returned energy between 1-30fJ are used. In the legend, G is an abbreviation for gain. For cycle 02-03, approximately 42-81% of data have gain < 13 because no lower limit in gain was set. Because only saturation correction for gain $= 13$ is available at this time, shots with gain < 13 are discarded. As the laser strength decreases with time, the received energy decreases from $\sim$ 17fJ on average in cycle 02 to $\sim$ 15fJ in cycle 04.

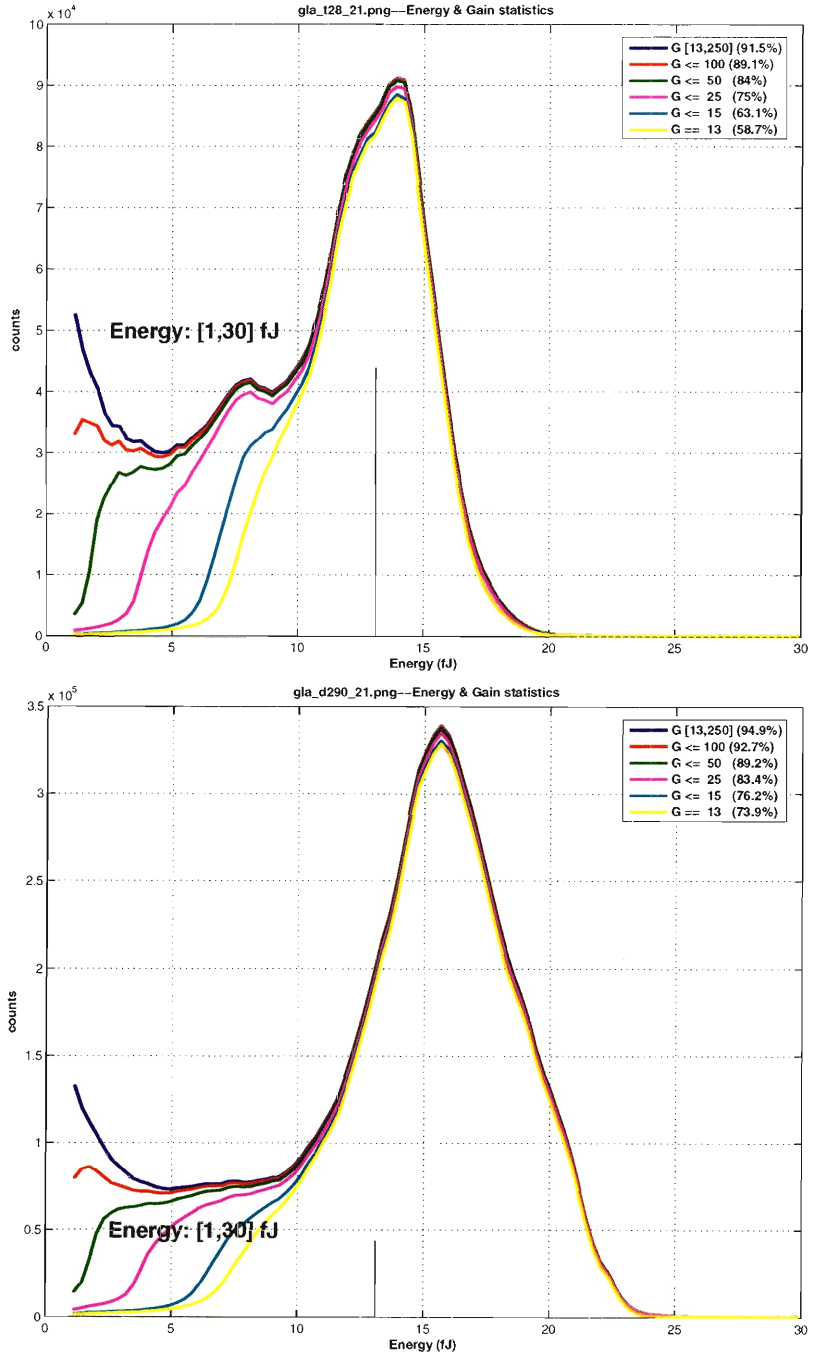

Figure 5-5 Laser 2 8-day cycle 28 and 33-day period 2a. At the beginning of 2a, the majority of shots were saturated (gain = 13), but with smaller energy ($\sim 15 - 16$fJ than those at the start of Laser 1. With the minimum gain set at 13, more shots become valid.

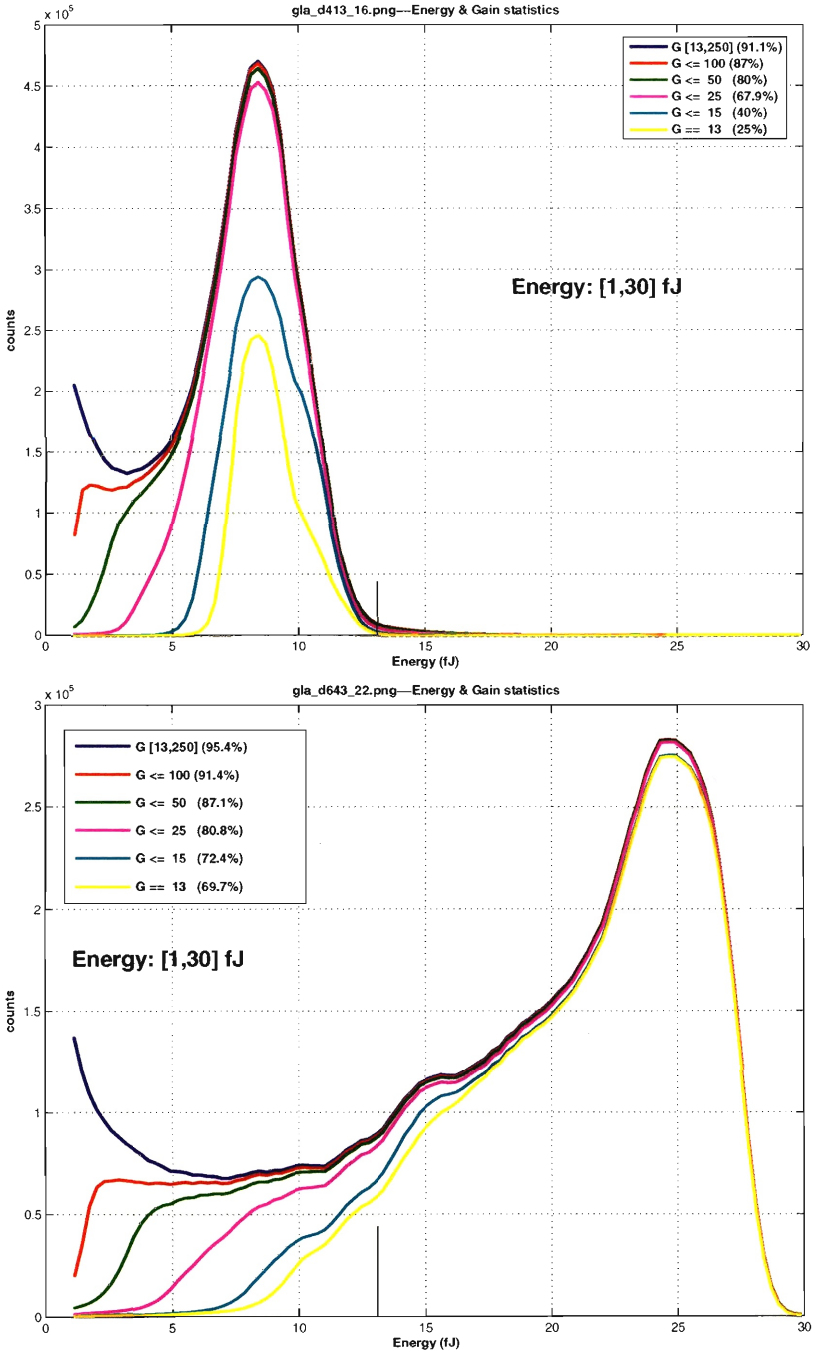

Figure 5-6 Laser 2 33-day period 2b and Laser 3 33-day period 3a. The laser strength clearly decreases in period 2b, and becomes significantly lower in Laser 2c (not shown here), which resulted in very high noise and pointing bias in the latter campaign. In all three lasers, Laser 3 is strongest, with energy at the beginning of campaign 3a in the range of 25fJ, highly saturated. Based on the saturated energy and the ratio -2.2cm/fJ, the potential height bias would be approximately -6cm and -24cm for Laser 2a and 3a, resulting in a potential negative dh/dt bias.

5.4 Results and Discussion

5.4.1 5-km DEM

Figure 5-7 shows the time series for one $(100\text{km})^2$ block to illustrate the general improvement behavior of the Kalman filter for this system. Figures 5-8 to 5-11 show the results of adjustment in dh/dt (a), periodic terms B (b) and θ (c) and block average Δ_{DEM} (d), along with their estimated uncertainties. We divide our studied area into 2 regions based on surface slope. The first region, we refer to as LB, includes the steepest part of the Lambert Glacier / Amery Ice Shelf drainage basin where slope reaches 0.3° over a 5-km length scale (Figure 5-8a, with LB outlined by the drainage basin between [lon,lat] of $\sim [45°E, 95°E, -70°N, -80°N]$). The second region, we refer to as E-Ant, consists of all blocks outside LB. The surface slopes in E-Ant are $< 0.1°$. Within LB between latitudes $[72°, -75°]$, dh/dt estimates have unreasonably large scatters, and the results there will be excluded (28 blocks out of 80) from the discussion below. In general, the filter only begins to stabilize toward the end of Laser 2b period (Figure 5-7). Figure 5-12 shows the statistics of each estimated parameter for E-Ant and LB. To investigate latitudinal dependency, we average all parameters within each 1° latitudinal bin across all longitudes. The results are shown in Figure 5-13, with each circle representing the number of blocks per latitudinal bin.

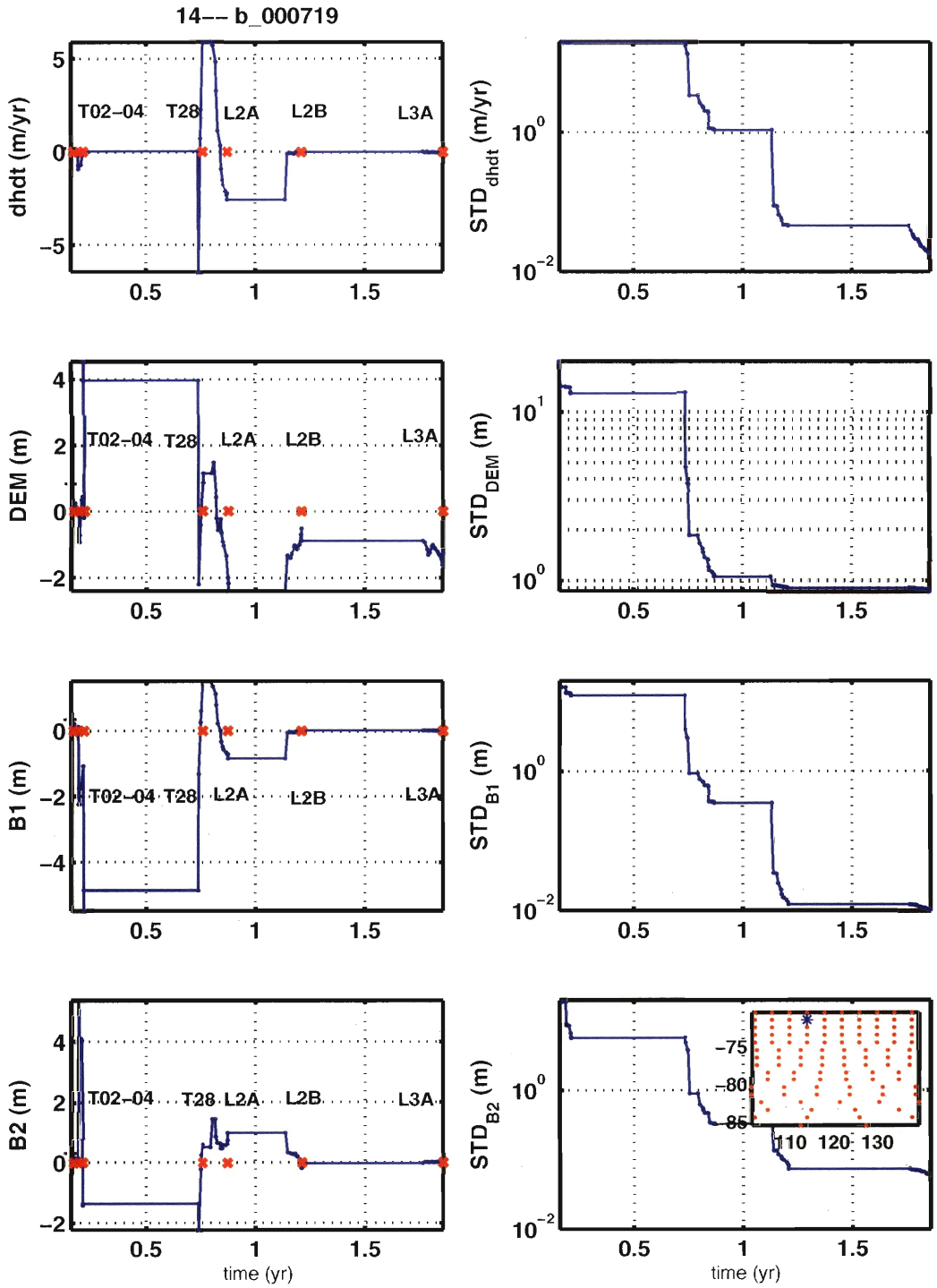

Figure 5-7 Time series of one $(100\text{km})^2$ block at the end of Laser 3a. The first column shows results for dh/dt, Δ_{DEM}, B_1, and B_2 terms, and the second column shows their corresponding standard deviations. Red-x's mark the end of either the 8-day or 33-day campaigns. Unit along the x-axis is in year, referenced to Jan-2003. The inset in the last subplot shows the location of the sample block, with longitudes and latitudes along the x-axis and y-axis respectively.

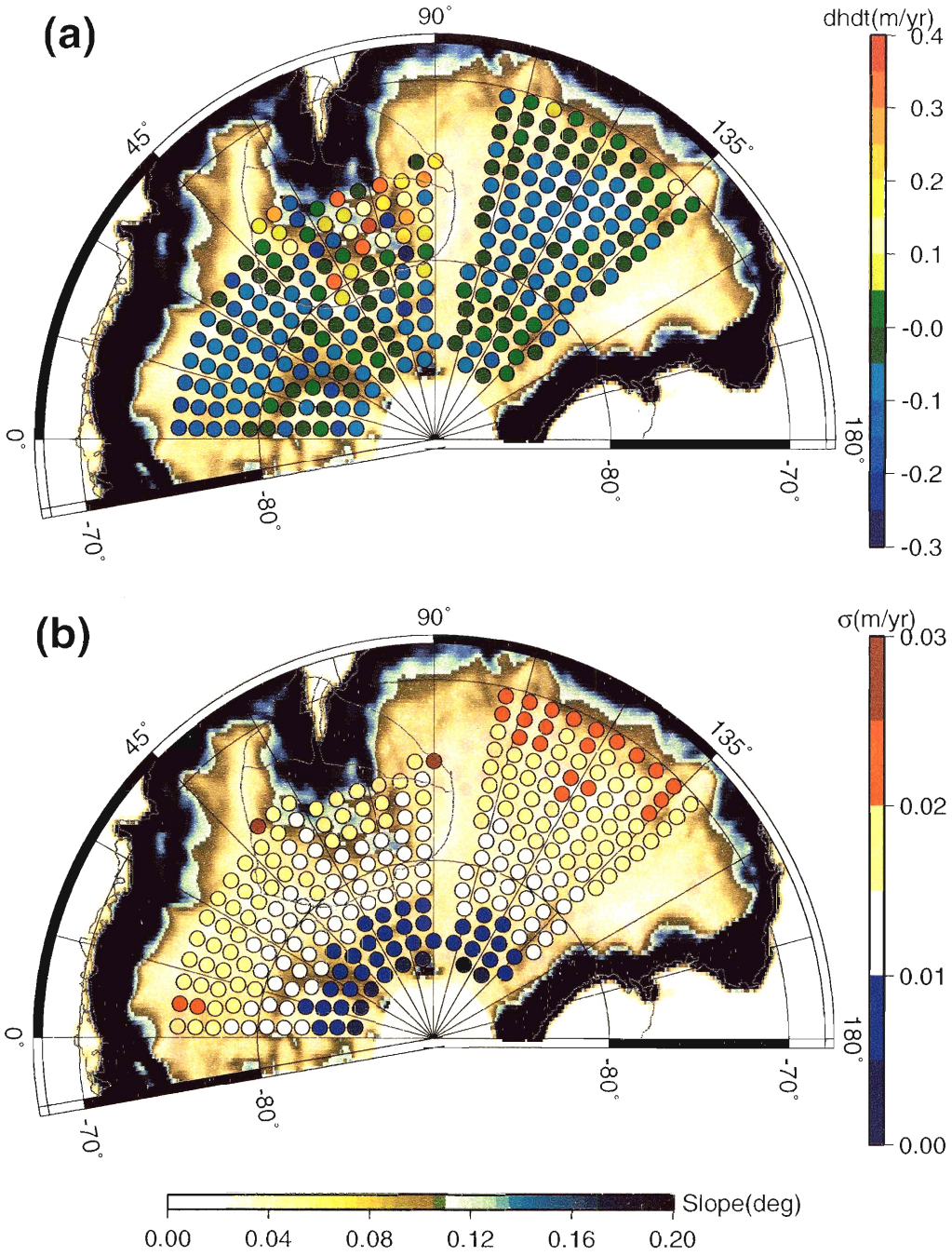

Figure 5-8 (a) Dh/dt and (b) uncertainties from the Kalman filter. All blocks in E-Ant has dh/dt between -0.21 to 0.13m/yr $\pm 0.03 m/yr$. Within region LB, dh/dt are more positive and varies in a wider range between -0.28 to 0.37 ± 0.3m/yr. The parameter dh/dt appears to be banded with negative mean between latitude [-81°,-73°], and zero mean north of $-73°$ and south of $-81°$.

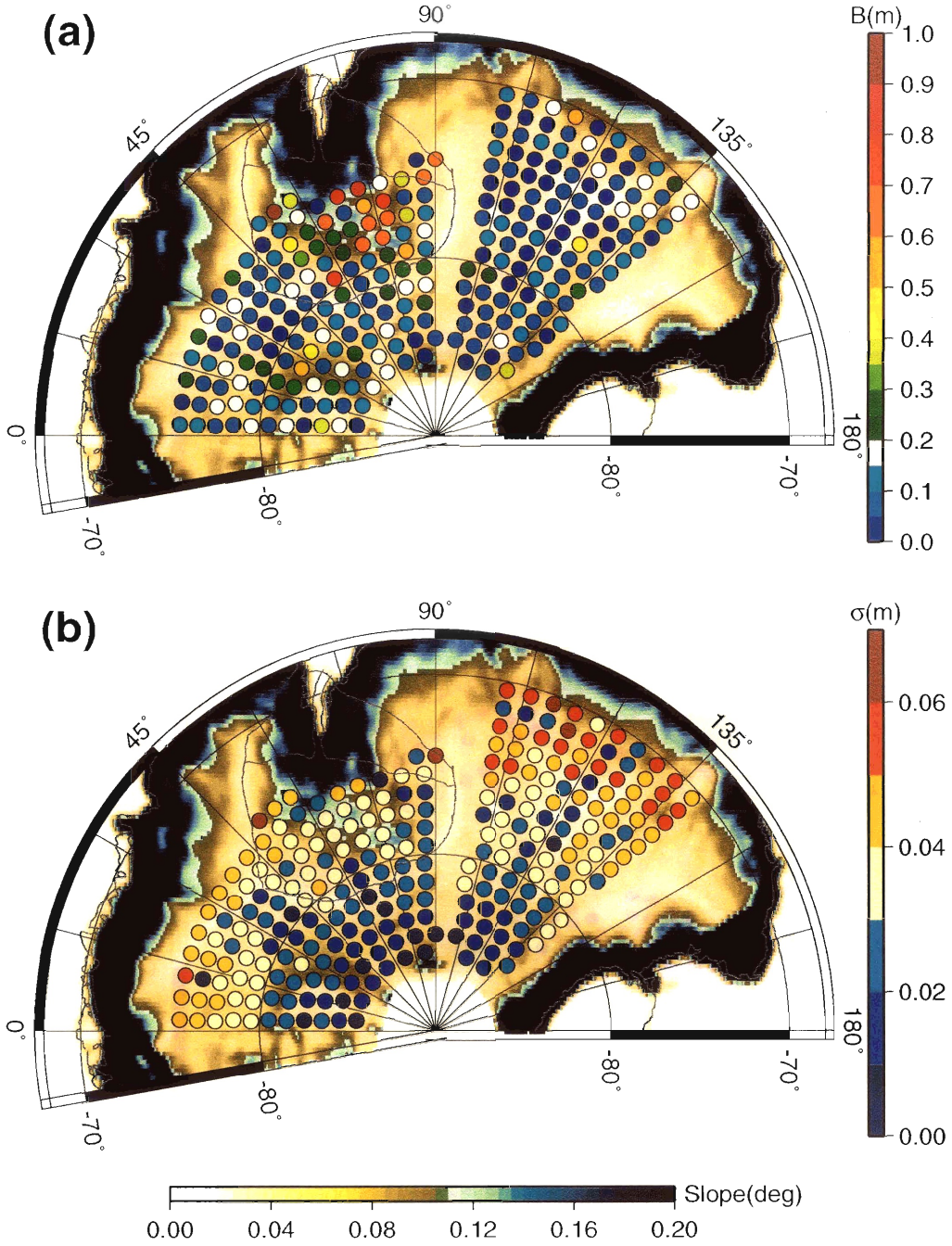

Figure 5-9 Seasonal signal amplitude B (a) and uncertainties (b) from the Kalman filter. B varies between 0.01 and 0.59±0.07m in E-Ant and 0.03 to 0.98±0.07m in LB. The comparison shows that the amplitudes obtained here are at least one order of magnitude higher than those predicted from climate and firn compaction models or inferred from *in-situ* measurements.

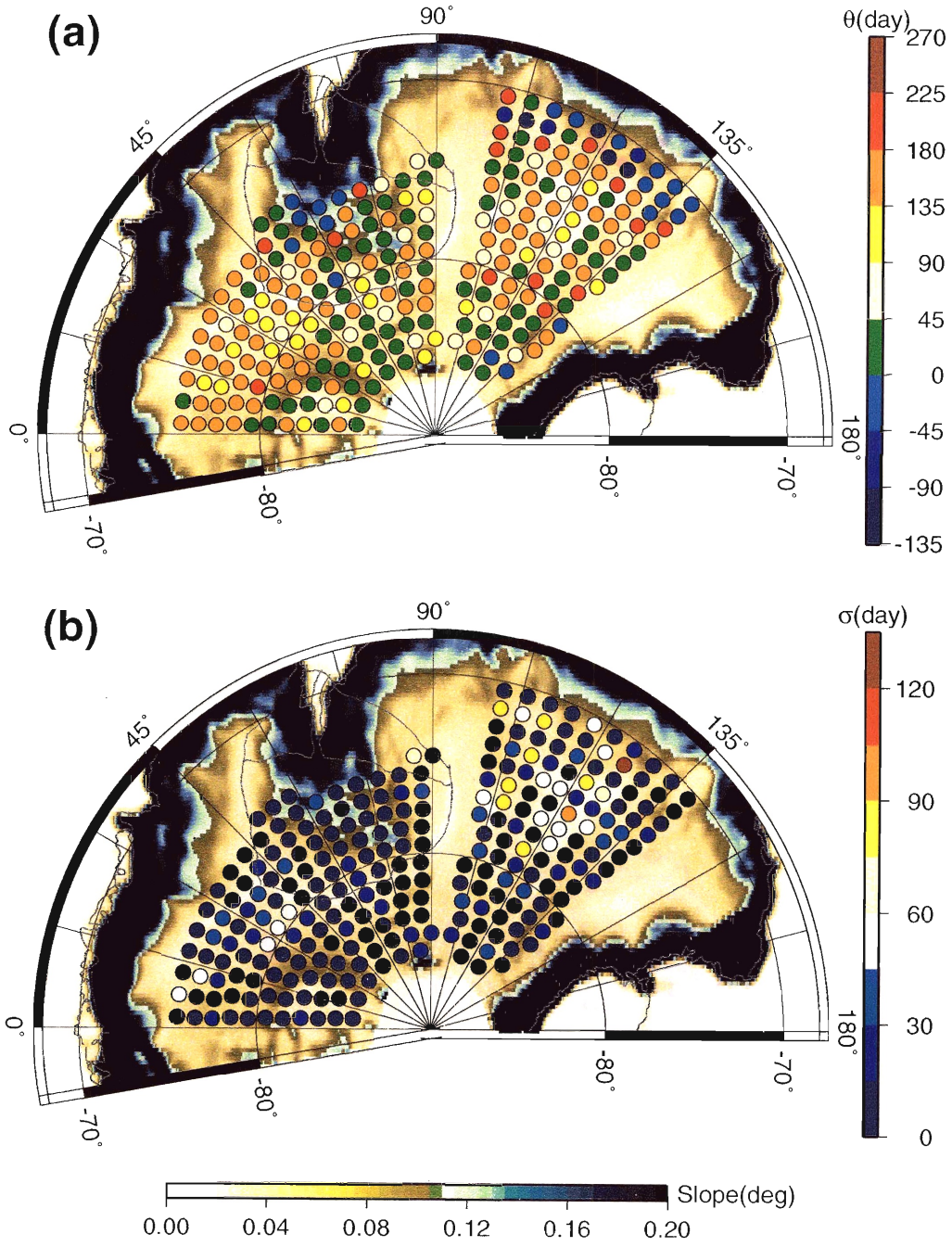

Figure 5-10 Seasonal signal phase maxima (a) and uncertainties (b). θ appears to be banded (similar to dh/dt), with high phase of $\sim$ 90-150 days (Apr - Jul) between latitude [-81°,-73°] and low phase of $\sim$ 0-65 days (Jan - Mar) north of $-73°$ and south of $-81°$.

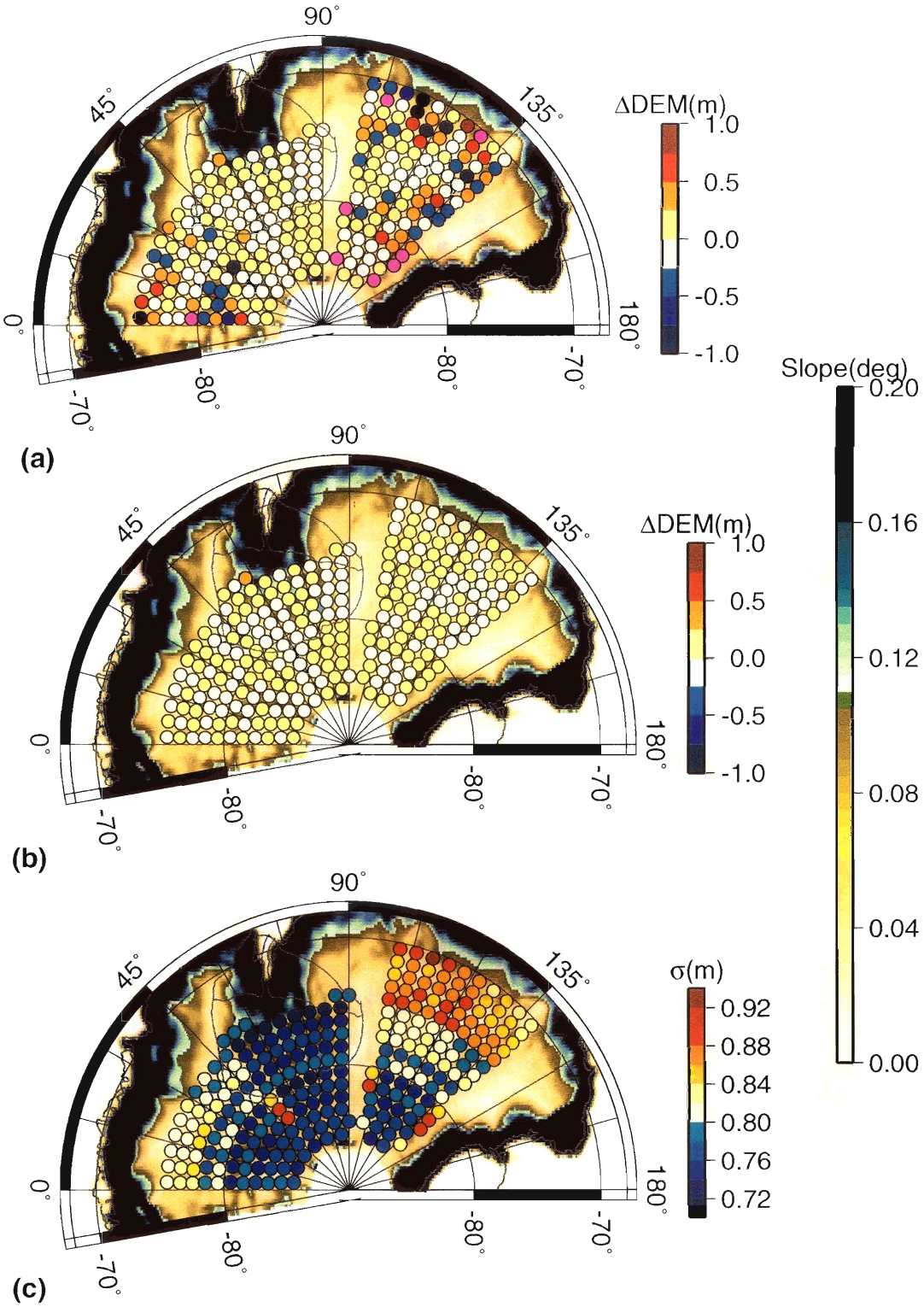

Figure 5-11 Block adjustment Δ_{DEM} after 2 iterations (a), after 3 to 24 iterations (b), and uncertainties (c). Within region II (Figure 5-1a), Δ_{DEM} are within -0.25 and 0.25m after only two iterations (a). For region I and III, Δ_{DEM} ranges between -4 to 4m after two iterations. Convergence to within [-0.25,0.25]m in region I and III requires between 6 and 24 iterations (b). Uncertainties are highest near the coast, but low for the whole region II.

5.4.2 *dh/dt*

In E-Ant, *dh/dt* varies between -0.21 to 0.13m/yr with negative mean and RMS of -0.05 and 0.05m/yr, respectively (Figure 5-8, 5-12). Typical uncertainties of dhdt are ~0.03 m/yr (Kalman filter covariance matrix estimate which depends on the assumed data noise, Figure 5-8). The spatial distribution of *dh/dt* suggests a latitudinal dependency, with rates between -0.05 and 0.05m/yr at latitudes $[-70°, -73°]$ or $[-86°, -81°]$, and between -0.13 and -0.05 m/yr at latitudes $[-81°, -73°]$ (Figure 5-8a, 5-13a). In region LB, *dh/dt* varies between -0.28 to 0.37m/yr, with mean and RMS of 0.05 and 0.15m/yr (Figure 5-8a, 5-12a). As a function of latitude, *dh/dt* in region LB are positive with large RMS that includes the possibility of zero *dh/dt* (Figure 5-13a). The effect of detector saturation are strongest in the latitude band [-81°,-73°] where the surface is flattest ($< 0.05^o$). Prior to saturation correction, *dh/dt* here varies systematically with latitude from -0.05m/yr at -81° to -0.20m/yr at -73°. After the first-order removal of saturation, *dh/dt* is still more negative within this band than outside the band.

As the first attempt to remove the effect of pointing biases, we used data from only the two periods with the best pointing knowledge, Lasers 2a and 3a (Table 5.4). The results of *dh/dt* are nearly identical to those shown in Figure 5-8. To verify the results of *dh/dt* from the Kalman filter, profiles from repeated tracks are compared, and one example is shown in Figure 5-14. In this example, repeat tracks #1297 from Lasers 2a, 2b, and 3a which are close to Lake Vostok ([-78.45°N, 106.87°E]) are shown before and after saturation correction. GLA06 heights are subtracted from the 5-km *a priori* DEM (Figure 5-14a) to obtain the first level of residuals (Figure 5-14b). Prior to saturation correction, heights from Laser 3a are lower than those from Laser 2a by approximately -0.17m, with Laser 2b in between (Figure 5-14). Received energies are ~25.1±2.2fJ and 25.7±1.4fJ for Lasers 3a and 2a, resulting in negative height biases of -0.26±0.05m and -0.28±0.03m. After the correction, heights in Laser 3a remain lower than those in Laser 2a by approximately -0.15m, resulting in a *dh/dt* of -0.15m/yr for this single profile (the time separation is ~ 1 year between Lasers

2a and 3a). When all profiles within the block closest to Lake Vostok (block #221 [-78.5°N, 105°E]) are compared, height differences (Laser 3a minus 2a) are approximately -0.13m and -0.06m before and after saturation correction, and the Kalman filter estimate of *dh/dt* for the block is -0.06m/yr.

To gain more insights into the *dh/dt* uncertainties, we evaluate *dh/dt* using ascending and descending tracks separately. For block #221 above, the mean and RMS of *dh/dt* are -0.01±0.05m/yr and -0.12±0.08m/yr for ascending and descending tracks respectively. The 40 cross-overs within this block have residuals (ascending minus descending) with mean and RMS of -0.05±0.17m and 0.13±0.21m for Laser 2a and 3a respectively. A crude estimate of *dh/dt* at the 40 cross-over locations yields a mean and RMS of -0.08 and 0.29m/yr. Based on cross-over residuals, there are still clear biases between ascending and descending tracks in both laser periods. The shot-to-shot along-track slope mean and RMS for this block is 0.02 and 0.06°. In general received energies are higher in Laser 3a than in 2a (~24.0fJ versus 22.3fJ for the block mentioned above), resulting in smaller height corrections for the latter. However, height differences (Laser 3a minus 2a) are consistently negative, approximately -0.10 to -0.04m after corrections for the flattest part of E-Ant (Figure 5-8a). We suspect that pointing errors contribute to the negative *dh/dt* estimated here.

5.4.3 Seasonal Signals

We model the periodic signal as shown in Eqn 5.18. In E-Ant, B ranges between 0.01 to 0.59m with mean and RMS of 0.11m and 0.09 m (Figure 5-9a, 5-12b). There is no clear pattern of B with latitude in E-Ant (Figure 5-13b). In region LB, B varies from 0.03 to 0.98m, with a mean and RMS of 0.31m and 0.26m. As a function of latitude, B increases in the mean but with large scatters (Figure 5-13b). Uncertainties from the Kalman filter range from 0.004m near 86° latitude to 0.07m near the coast (Figure 5-9b).

If $\theta = 0$, the signal would be maximum at the beginning of January and minimum at the beginning of July. After unit conversion to day, the phase maxima have bi-

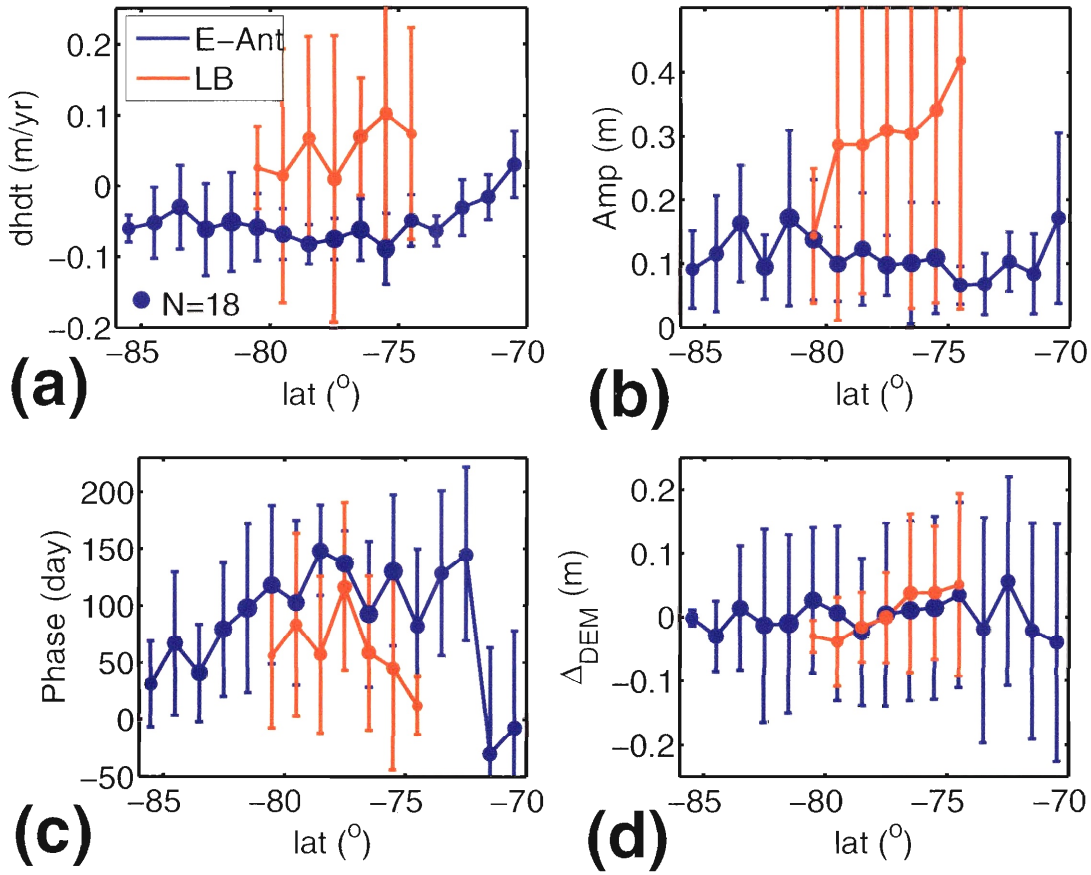

Figure 5-12 Histogram of dh/dt (a), B (b), θ (c), and Δ_{DEM} (d). There is a total of 259 100×100km blocks in East Antarctica, with 52 in LB (red) and 207 outside (blue). In brackets are the mean and root-mean-square scatter of each parameter. The inset in subplot **(c)** shows the mean seasonal signal based on climate models (red, Turner et al. [1999]) and scaled seasonal temperature (dashed blue). The temperature profile is scaled to only illustrate the seasonal maximum and minimum locations.

modal distributions in all regions, with peaks at ~25-day and 170-day for E-Ant, and ~5-day and 180-day for LB (Figure 5-10a). Uncertainties from the Kalman filter are ±10 day for 60% and ±60 day for 96% of the blocks. As a function of latitude, θ in E-Ant appears to be banded similar to dh/dt, with mean ~90-150 day (Apr-Jul) at latitudes $[-81.5°, -72.5°]$ and 0-65 day at other latitudes (Figure 5-10a, 5-13c).

The inset in Figure 5-12c shows climate models' average accumulation for the four seasons [Turner et al., 1999]. Annual temperature signal shows maximum during Dec-Jan and minimum during June-July (dashed blue curve in Figure 5-13c inset). Accumulation (precipitation minus evaporation) annual signal is maximum during southern winter (June-August) and minimum during southern summer (Dec-Feb) (red curve in the inset, Figure 5-12c). Based on the temperature cycle, firn compaction models

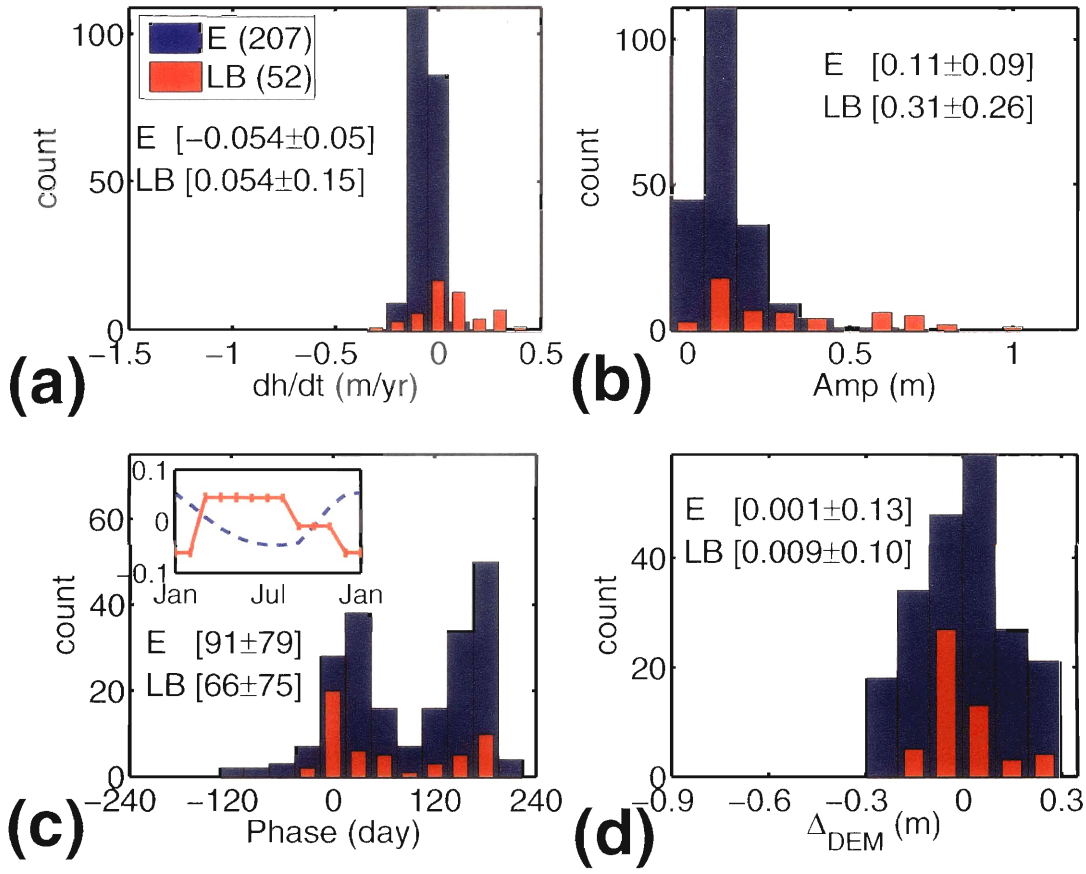

Figure 5-13 Latitudinal dependency of dh/dt (a), B (b), θ (c), and Δ_{DEM} (d) for E-Ant (blue) and LB (red). Each closed circle represents an average of all 100×100km blocks across all longitudes for each 1° latitudinal bin, and the size of of the circle represents the number of blocks N in each *bin*, with the scale provided for $N = 18$. (a) dh/dt is negative in most of E-Ant except north of -73° latitude. In LB, dh/dt has positive mean but with large scatter that cover 0.0m/yr rates. Some of the correlations between these estimated parameters with latitudes could be due to pointing bias.

predict phase maxima in Apr-May [Jun, 2005]. These phase maxima are consistent with our results at latitude range $[-81.5°, -72.5°]$. However, amplitudes obtained here are at least one order of magnitude higher than the 4 to 12 mm of accumulation along the coast predicted by the models. Turner et al. [1999] mentioned in their paper that the climate model they used consistently underestimates accumulation when compared to *in-situ* observations. A study using ground penetration radar found accumulation rate over Lake Vostok ([106.87°E,-78.45°N]) varying between 0.005 m/yr to 0.045 m/yr in the last 17000 years [Leysinger-Vieli et al., 2004]. Assuming that these rates are the results of integrations under the seasonal signal, the inferred maximum amplitude would be ~0.001m to 0.008m. The B found in this study is 0.14m for the block containing Lake Vostok ([105°E,-78.5°N]) and 0.09m with RMS 0.03m

for the 7 closest blocks (Fig 2b). A test is performed by removing both sinusoidal and rate of change dh/dt terms from the state vector and running the Kalman filter again. The results showed consistent values of θ for all Antarctica (not shown here). When Laser 2c period data were included, phase maximum is $\approx$ 165 day, coinciding with this period. When only Laser 2a and 3a are used, the filter did not achieve stability for all parameters, and the seasonal terms can not be estimated. We suspect these high amplitudes are the result of pointing errors [Luthcke et al., 2005] and will discuss further in the Error Assessment section below [Luthcke et al., 2005].

5.4.4 Δ_{DEM} convergence

Our assumption of the overall adjustment term in each block is such that when convergence is achieved, Δ_{DEM} should approach zero within the error limit of the data. Per (100km)^2 block, there are approximately 500-8000 data points, each with the assumed $1m^2$ noise (Figure 5-1b). Thus the error in the block average will scale as one over the square root of the number of data point, $\sim$ 0.01 to 0.05m over each 33-day period, or $\sim$ 0.007 to 0.03m when all data from Laser 1-3a are used. The rate of convergence appears to be independent of the magnitude of height residuals. Within region II (and within LB) first-level residuals are $\approx \pm 50$ to ± 500m (ICESat height minus *a-priori* DEM), and Δ_{DEM} converges to within ± 0.25m after only 2 iterations. In contrast, both regions I and III have first-level residuals in the range of approximately $\pm 20m$ but requires up to 24 iterations before converging to within ± 0.25m (Figure 5-14, 5-11a). Nine blocks in region III with values outside the scale provided in Figure 5-11d are chosen for the DEM convergence test, and their results are listed in Table 5.6. For a few blocks, the values of dh/dt, B, and θ shifts systematically before stabilizing at the smallest Δ_{DEM} (Table 5.6). In one particular block (#111), Δ_{DEM} decreases from $\sim$ 4m to zero, then became negative before stabilizing at approximately -0.006m (still within the error bar of Δ_{DEM}). Overall, by iterating all the blocks to within $\pm 0.25m$, the seasonal signal amplitude fluctuates within $\pm 15cm$, and the maximum B for the three regions of study decreases by $\sim 10cm$ (Figure 5-13b,d). However dh/dt has the same mean and RMS at all iterations.

Uncertainties in Δ_{DEM} from the Kalman filter are in the range ± 0.72m to ± 0.93m (Figure 5-11c). The banded nature of uncertainties with latitudes is likely the result of the way the block were set up (Table 5.3). For example between latitudes $[-70°, -75°]$, the block-size is approximately squared at latitude -72.5°, and blocks south and north of it will have more and less data, respectively (Figure 5-11c, Table 5.3).

5.4.5 Iterated height residuals

As mentioned earlier, first-level residuals between ICESat height and the *a-priori* DEM are in the range approximately $\pm 20m$ for both regions I and III, and reach $\pm 500m$ within LB. Figure 5-14 shows and example of an ICESat height profile and residuals before and after analyses using the Kalman filter. A closer look at the residuals after two iterations shows two distinct characteristics: a sinusoidal behavior at wavelength $\approx$ 5km corresponding to surface undulations at wavelengths shorter than that of the DEM, and a spatially correlated variation at the shot-to-shot length scale (Figure 5-15). It is important to note that the difference between residuals in Figure 5-14c is seen as "height change" in our model, even though it could be a result of both height change as well as height off-sets due to the off-sets of the lasers' tracks from the 33-day referenced tracks. In other words, our current model is insufficient to distinguish between these two cases. This problem will be addressed in future work, and a brief discussion is given here. A crude power spectral density (PSD) analysis of the residuals shows that power drops off as f^{-2} where f is the frequency in unit 1/km (or increases as λ^2 where λ is the wavelength in unit km). A closer look shows that when the oscillation at wavelength $\approx$ 5km dominates, the PSD peaks over a range of λ near 5km and can be fitted with a functional PSD with a resonance frequency/wavelength at this range (Figure 5-15). In the absence of this strong oscillation, the f^{-2} (or λ^2) behavior dominates. One approach to model the residuals with such PSDs is by using a second-order Gauss-Markov noise process, with a PSD function of the form $S(j\omega) = \frac{k^2\sigma^2}{4k^2\omega^2+(\omega^2-\omega_o^2)^2}$ where $k, \sigma^2, \omega, \omega_o$ are the time-constant, noise variance of the process, frequency (1/time), and natural frequency of

Table 5.6 DEM conversion test

		iteration								
	block	1	2	3	5	7	9	11	18	22
	4	-4.86	-3.90	-2.84	-1.61	-1.04	-0.74	-0.57	-0.33	-0.25
	8	1.29	1.07	0.64	0.34	0.23	0.18	0.15		
	12	1.50	1.03	0.66	0.32	0.18	0.12	0.08		
	14	-1.15	-1.21	-0.98	-0.76	-0.59	-0.47	-0.37	-0.22	
Δ_{DEM}	87	1.04	1.36	1.15	0.68	0.40	0.24	0.14		
(m)	98	2.12	1.89	1.31	0.62	0.29	0.13	0.05		
	103	6.27	3.58	2.11	0.73	0.26	0.094	0.036		
	108	4.04	1.24	0.42	0.056	0.012	0.006	0.004		
	111	3.16	1.81	0.81	0.15	0.025	0.000	-0.005	-0.007	
	4	-.0028	-0.012	-0.012	-0.004	-0.004	0.010	0.016	0.025	0.029
	8	0.039	0.037	0.036	0.036	0.036	0.036	0.037		
	12	0.005	0.001	-0.004	-0.009	-0.012	-0.014	-0.014		
	14	-0.005	-0.014	-0.018	-0.021	-0.022	-0.023	-0.023	-0.022	
dh/dt	87	-0.085	-0.085	-0.086	-0.087	-0.087	-0.088	-0.088		
(m/yr)	98	-0.11	-0.11	-0.11	-0.11	-0.11	-0.11	-0.11		
	103	-0.000	-0.003	-0.004	-0.006	-0.007	-0.007	-0.008		
	108	-0.020	-0.019	-0.019	-0.019	-0.019	-0.019	-0.019		
	111	0.017	0.018	0.019	0.020	0.020	0.020	0.020	0.020	
	4	0.58	0.65	0.65	0.63	0.61	0.57	0.57	0.53	0.52
	8	0.18	0.16	0.15	0.14	0.14	0.14	0.14		
	12	0.045	0.033	0.026	0.021	0.020	0.020	0.020		
	14	0.060	0.066	0.069	0.070	0.070	0.070	0.070	0.072	
B	87	0.23	0.24	0.24	0.24	0.25	0.25	0.25		
(m)	98	0.030	0.026	0.027	0.030	0.034	0.037	0.039		
	103	0.071	0.068	0.067	0.066	0.066	0.066	0.066		
	108	0.054	0.055	0.056	0.056	0.056	0.056	0.056		
	111	0.35	0.35	0.36	0.36	0.36	0.36	0.36	0.36	
	4	-17.8	-17.1	-17.0	-17.2	-17.4	-17.7	-17.9	-18.3	-18.5
	8	-17.1	-18.7	-19.9	-21.6	-22.4	-22.9	-23.0		
	12	-24.1	-33.8	-48.7	-76.0	-90.7	-97.9	-101.1		
	14	3.5	3.3	3.5	3.7	3.7	3.5	3.4	3.1	
θ	87	179.2	179.2	179.3	179.1	179.1	179.1	179.1		
(day)	98	139.6	131.0	132.1	138.6	143.6	147.1	149.6		
	103	155.9	156.3	156.5	156.9	157.2	157.3	157.4		
	108	68.7	66.2	65.5	65.2	65.2	65.3	65.4		
	111	-1.4	-1.4	-1.4	-1.3	-1.3	-1.3	-1.3	-1.3	

the system [Brown and Hwang, 1997]. The relationship between wavelength λ and time lag τ of the corresponding correlation function $R(\tau) = F^{-1}(S(j\omega))$ comes from the conversion of 1/40sec to 172m for each ICESat shot (where F^{-1} is the inverse Fourier transform). This approach is typically used in GPS data processing to model the time-correlated noise processes Herring [2005]; Brown and Hwang [1997]. The behavior of $R(\tau)$ is controlled by both the exponential damping term containing the time-constant k parameter, and the oscillation term controlled by the natural frequency ω_o (0.73sec or 5km in λ, Figure 5-15). This second order noise process requires two additional terms in the state vector, and its implementation will be incorporated in the future.

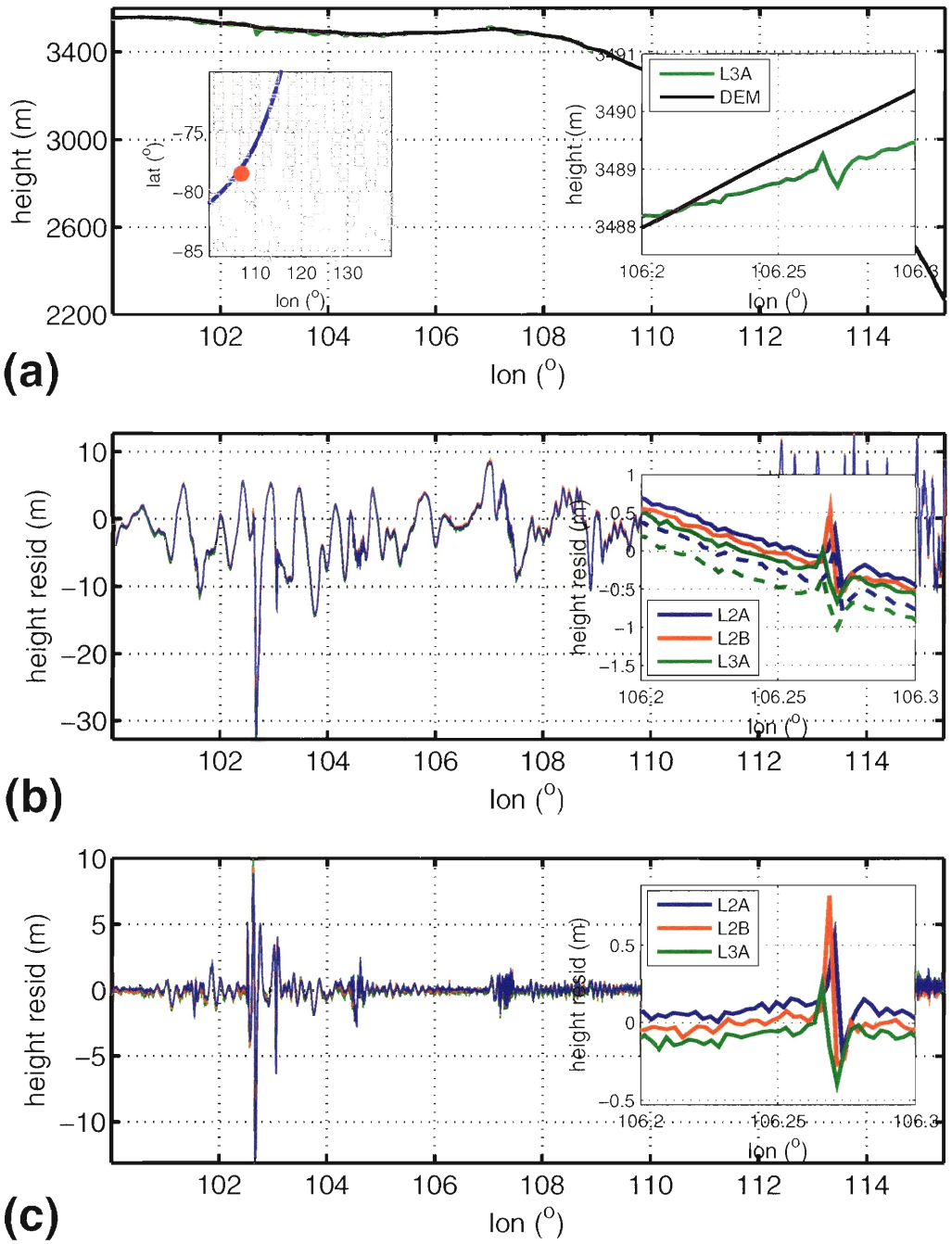

Figure 5-14 ICESat heights and residuals. (a) Original ICESat height profile from Laser 3a (green) and the interpolated DEM (black). The inset shows the DEM estimates the trend but misses the shorter wavelength details. (b) Height residuals for the profile in (a), along with two additional profiles corresponding to Laser 2a (blue), 2b (red). The inset shows the residuals before (solid line) and after (dot-line) saturation corrections. (c) Residuals after two iterations through the Kalman filter. The inset shows the difference between the repeat tracks for the three laser periods.

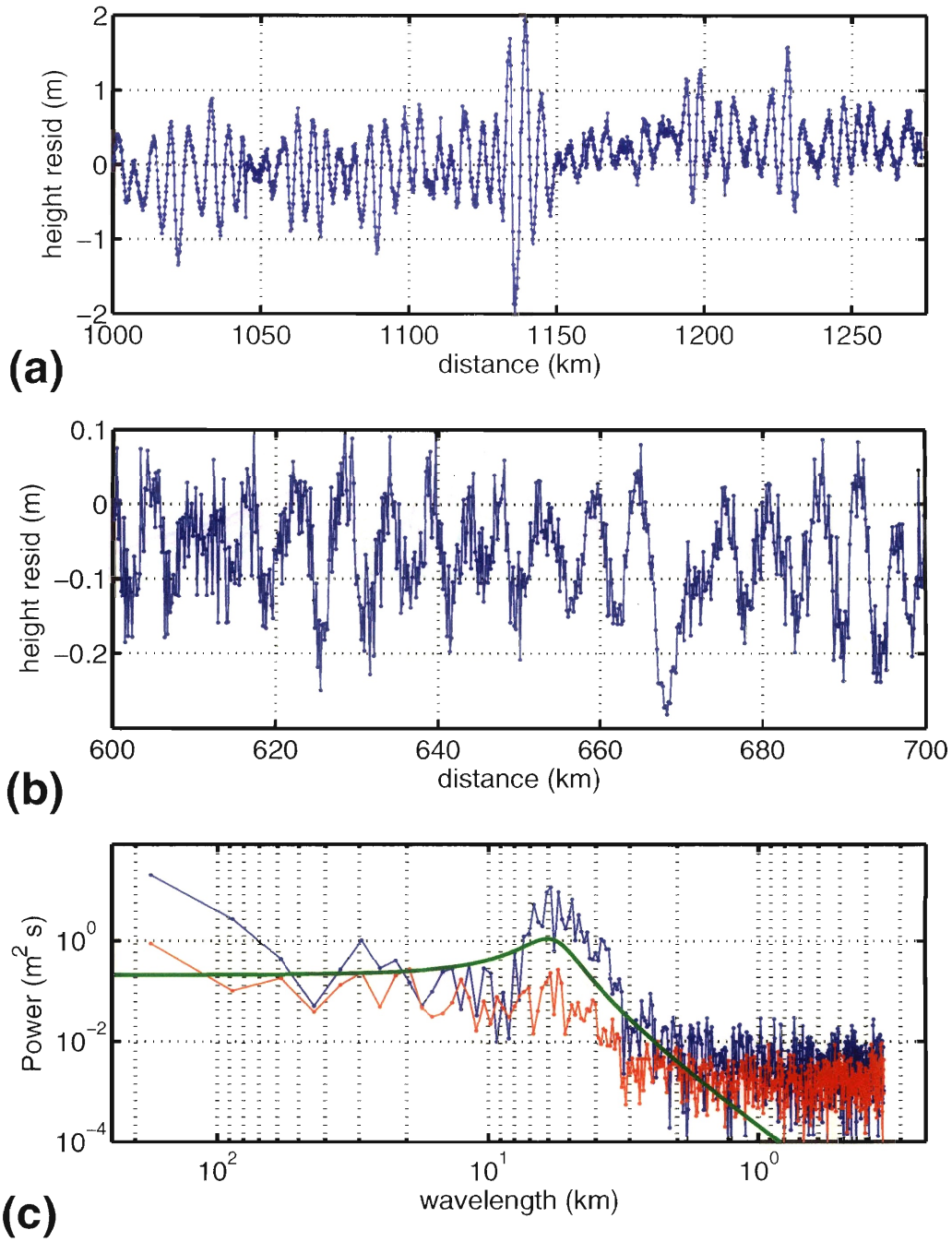

Figure 5-15 Height residuals after two iterations and their PSDs. (a) Residuals along a profile which shows the dominant 5-km wavelength oscillations with magnitude near $\pm 2m$. (b) Residuals along a different profile showing much smaller amplitudes. The shot-to-shot variations and the spatially-correlated behavior can be seen here. (c) Power spectral densities (PSD) for the two profiles above (blue for (a), red for (b)) and a potential fit using a second order Gauss-Markov PSD functional form.

5.5 Error assessment

In our model we assumed non-correlated single-shot error of 1 m^2 and DEM uncertainty of 400 m^2, and that the model parameters are deterministic *i.e.*, no process noise. The large single-shot error 1 m^2 is the first attempt to account for the pointing errors and coarseness in the parametrization of the surface. At the end of Laser 3a, the filter suggests uncertainties of ±0.03 m/yr, ±0.07 m, ±30 to ±60 day for dh/dt, B, and θ. However, pointing bias produces systematic errors that are not accounted for in the filter. Current assessments of single-shot vertical accuracy is ~16 cm for Laser 2a [Shuman et al., 2005], and with pointing bias increase to ~21-33 cm for surface slope 0.1-0.5°. Our estimates of pointing bias obtained by differential slopes at cross-overs across Antarctica are comparable with the global estimates (Table 5.4). Per 33-day operations period, each $(100km)^2$ block has between 500-8000 data points, or 12-125 tracks (Figure 5-1b). If slope distribution is random, errors due to pointing would decrease by a factor of $N^{-1/2}$ when averaged over all N elements within a $(100km)^2$ area. In that case, estimates of uncertainties for dh/dt would be close to those from the Kalman filter results because we have assumed a data noise that accounts for the pointing errors. However toward the coast or near -86° latitude, slope becomes more systematic and contributes pseudo dh/dt, B and θ within the blocks.

Figure 5-16 shows predicted height discrepancy Δh between ascending and descending tracks for cross-overs at different combinations of latitudinal ranges and surface slopes. For ICESat's 94° inclination, separation angles are approximately [19.5°, 25.9°, 48.5°, 61.0°, 84.3°, 106.7°, 180.0°] at latitudes [-60°, -70°, -80°, -82°, -84°, -85°, -86°] using the crude conversion $sin(\phi/2) = 4°/lat$ where ϕ is the separation angle [Schutz, 1995]. When the pointing-bias vector is perpendicular to elevation contour for one of the two tracks, we get almost a 1:1 ratio between Δh and surface slope for a pointing bias of 10 arc-sec (Figure 5-16a) at high absolute latitudes (where ϕ is large). The error is halved if pointing bias is parallel to elevation contour for one of the two tracks (Figure 5-16b). A simple test using only ascending or descending tracks in the Kalman filter shows that the descending tracks yield all negative dh/dt

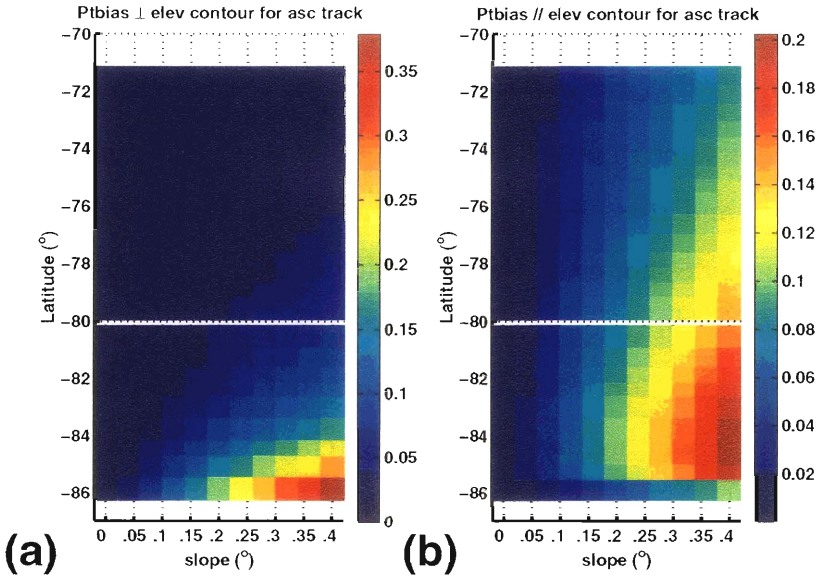

Figure 5-16 Dh/dt_{bias} assuming a pointing bias of **10 arcsec** and surface slopes up to 0.4° for the cases when pointing bias vector is **(a)** ⊥ to elevation contours, and **(b)** ‖ to elevation contours. In case **(a)**, dh/dt_{bias} is nearly $1m/yr$: 1° slope at latitude −86° and decreases away from the South Pole. In case **(b)**,dh/dt_{bias} is half of that in case **(a)**. Here the maximum error occurs when cross-over separation angle is 90°, or latitude −84.3°.

in region III (Figure 5-17b). The difference in dh/dt estimates between ascending and descending tracks ranges between -0.05 to 0.31m/yr.

Pointing errors affect dh/dt estimates even where surface slopes are close to zero because ICESat orbits with a ~0.33° tilt to avoid specular reflection [Schutz et al., 2005]. This tilt results in a total pointing bias equivalent to that of 0.33° plus local slopes. A sensitivity test between the time data were obtained (t≈[0.21,0.79,1.13,1.38,1.76] yr for Lasers 1-3a) and the model parameters shows that Laser 2c contributes the least to dh/dt estimates, and Lasers 2b-c contribute the most to B and θ . When Laser 2c is removed, contributions from all other operation periods become nearly equivalent. Assuming positive height biases from columns 7-9 in Table 5.4, dh/dt_{bias} for lasers [1, 2a, 2b, 3a] are ~[-0.04, -0.02, 0.07, 0.04]m/yr for 98% of the blocks with total slopes < 0.5° in E-Ant, and [-0.05, -0.02, 0.08, 0.05]m/yr for region LB where total slope reaches 0.63°. When only Laser 2a and 3a are used, the contributions to the dh/dt estimate from both lasers are the same with opposite signs. Again assuming positive height biases from columns 6-8 in Table 5.4, dh/dt_{bias} for Laser [2a, 3a] are ~[-0.02, +0.04]m/yr for 98% of the blocks with total slopes < 0.4° in E-Ant, and

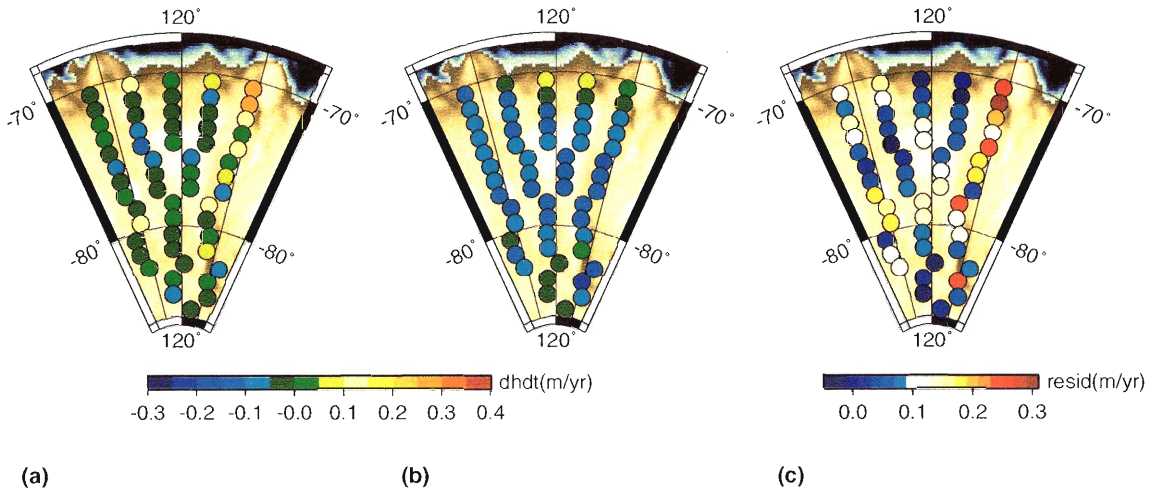

Figure 5-17 *Dh/dt* estimates in region III using (a) ascending only tracks, (b) descending only tracks, and (c) ascending minus descending results. *Dh/dt* ranges between [-0.12,0.27]m/yr in (a) and [-0.22,0.06]m/yr in (b), and the mean and RMS of their differences are 0.09 and 0.08m/yr.

[-0.03, +0.08]m/yr for region LB where total slope reaches 0.63°. If negative height biases are assumed, dh/dt_{bias} would have the same magnitudes but with signs reversed. In the worst case scenario, based on current pointing knowledge with Laser 3a having twice the height bias compared to Laser 2a, combined dh/dt_{bias} could reach ±0.06m/yr when 2 periods (2a and 3a) are used, and $\pm 20 cm/yr$ when Lasers 1-3a are used over nearly flat terrains. In addition we only consider cases with one standard sigma of errors for pointing.

In their analysis, Luthcke et al. [2005] showed that pointing errors can be both temporally and geographically correlated. Fricker et al. [2005] found over flat and smooth terrains, forward scattering and/or pointing errors give negative height biases of ~16cm for Laser 2a. They also showed that, under clear sky conditions, pointing errors contribute negative height biases of about -1.9 and -1.2cm for Laser 2a and 3a, and positive bias of 0.5 to 1.2cm for Laser 2b. This would produce a seasonal signal with phase maximum near Laser 2b with amplitude ~0.035cm or more over sloped terrains. Between 82-91% of the data we use have gain = 13 for Laser 2a and 3a, and and ~76% of Laser 2b data have gain < 25. Our data filtering scheme removes potential cloud (gain between 100 and 250). Thus pointing is the likely source of errors in our estimates of *dh/dt*, B and θ.

5.6 Conclusion

We have demonstrated the potential of ICESat data for surface change detection over Antarctica, using ICESat repeat track altimetry data and a combination of Kalman filtering and kriging. Currently only two laser operational periods (2a and 3a) have adequate pointing calibration to be used for height change detection. Results from the Kalman filter show over the smooth interior part of East Antarctica, *dh/dt* is negative with means between -0.10 to -0.05m/yr. The mean error due to pointing biases is ~0.06m/yr based on the data model / sensitivity when the two data periods with best pointing knowledge are used. Due to a combination of lack of data and larger pointing errors than the science requirement of 2-arcsec, height change detection with an accuracy of ~0.02m/yr is not possible at this time. However, the ICESat team anticipates the reduction pointing errors in all laser operational periods to the same level as that in Laser 2a in the near future [Schutz et al., 2005; Luthcke et al., 2005]. When all available data, Lasers 1-3c become available with adequate pointing knowledge, our sensitivity test shows *dh/dt* uncertainties of 0.02m/yr and 0.03m/yr over surfaces with total slope of 0.33° (flat terrain) and 0.43° can be achieved. We are currently refining the technique to include parameters to account for pointing biases within each laser operational period, and will re-analyze using future data releases to improve *dh/dt* estimates and include the seasonal signal parameters.

Chapter 6

Conclusion

Satellite radar and laser altimetry in the last decade have provided the scientific community large sets of data with uniform accuracy and good temporal and spatial coverage to study height change in the ice sheets. Two techniques were developed in this thesis to use all the available data to study height change in Antarctica. The first technique combining block kriging with linear inversion and was used with radar altimetry measurements from the European Remote Sensing Satellite from 1995-2001. Kriging results show that dh/dt are near zero (0.02 ± 0.06m/yr) in the interior part of East Antarctica, and that large positive and negative rates are observed at the Amery Ice Shelf and in West Antarctica. Comparison with the existing and widely used cross-over method shows that differences between the two methods for both East and West Antarctica are significantly different from zero. Specifically kriging yields higher rates of approximately 0.01 to 0.05 m/yr in East Antarctica, and does not produce the pervasive negative rates observed in cross-over method. Seasonal signal amplitude and phase parameters are also different between the two methods, with kriging producing consistently lower amplitudes and a one-month shift in the phase maxima. The effect of post-glacial rebounding was not assessed, and could potentially remove the systematic difference in the interior smooth part of the ice sheet. A full study of the bias between the satellites ERS-1 and ERS-2 will be done in the near future to assess ERS-1 effect on the dh/dt estimated in this thesis, and to re-assess the difference between kriging and cross-over analysis. In addition, laser altimetry

from the ICESat mission would offer an independent data set to validate the kriging results, as well as give additional data to extend the time series of surface height in Antarctica.

A new method of combining kriging with Kalman filtering was developed to enable modeling surface height change and the seasonal signals as a non-deterministic quantities. In addition, the new method also enable modeling surface heights as a random field. The method was applied to ICESat data and yielded dh/dt estimates over East Antarctica. However the large pointing bias still existing in ICESat data has made dh/dt estimates unreliable at this time. With the anticipation by the ICESat team that pointing error will be removed in the near future, ICESat *data will be* re-analyzed using the second method and compared with ERS results.

The kriging / Kalman filtering technique will be improved further to take advantage of the parallel repeat tracks in laser altimetry to model detailed surface heights and slopes at the spatial scale approximately that of the along-track spacing in ICESat. A detailed map of surface heights and slopes is necessary for accurate dh/dt estimates. Specifically, a well-determined surface will allow both the removal of pointing errors using the local slopes and pseudo dh/dt that are currently observed in the kriging/Kalman filtering technique. In the later case, when a new parallel data track is used, the kriging / Kalman filtering technique is not able to distinguish between spatially offset tracks and height change within our blocks due to the low resolution digital elevation map being used. It remains to be seen an accuracy of $\sim$2cm/yr can be achieved using laser altimetry. When pointing knowledge improve, dh/dt estimates using the improved method will also be applied to study height changes in West Antarctica, specifically along the coast where radar altimetry was limited.

Appendix A

Time series for ERS data

A.1 Figure Caption

Titles on each subfigure a: [b,c]; (d,e) indicate block#: [lon,lat]; (dh/dt,$\sigma_{dh/dt}$). Units along the axes are in meter (y-axis) and year (x-axis) referenced to Jan 01, 1994.

Region I

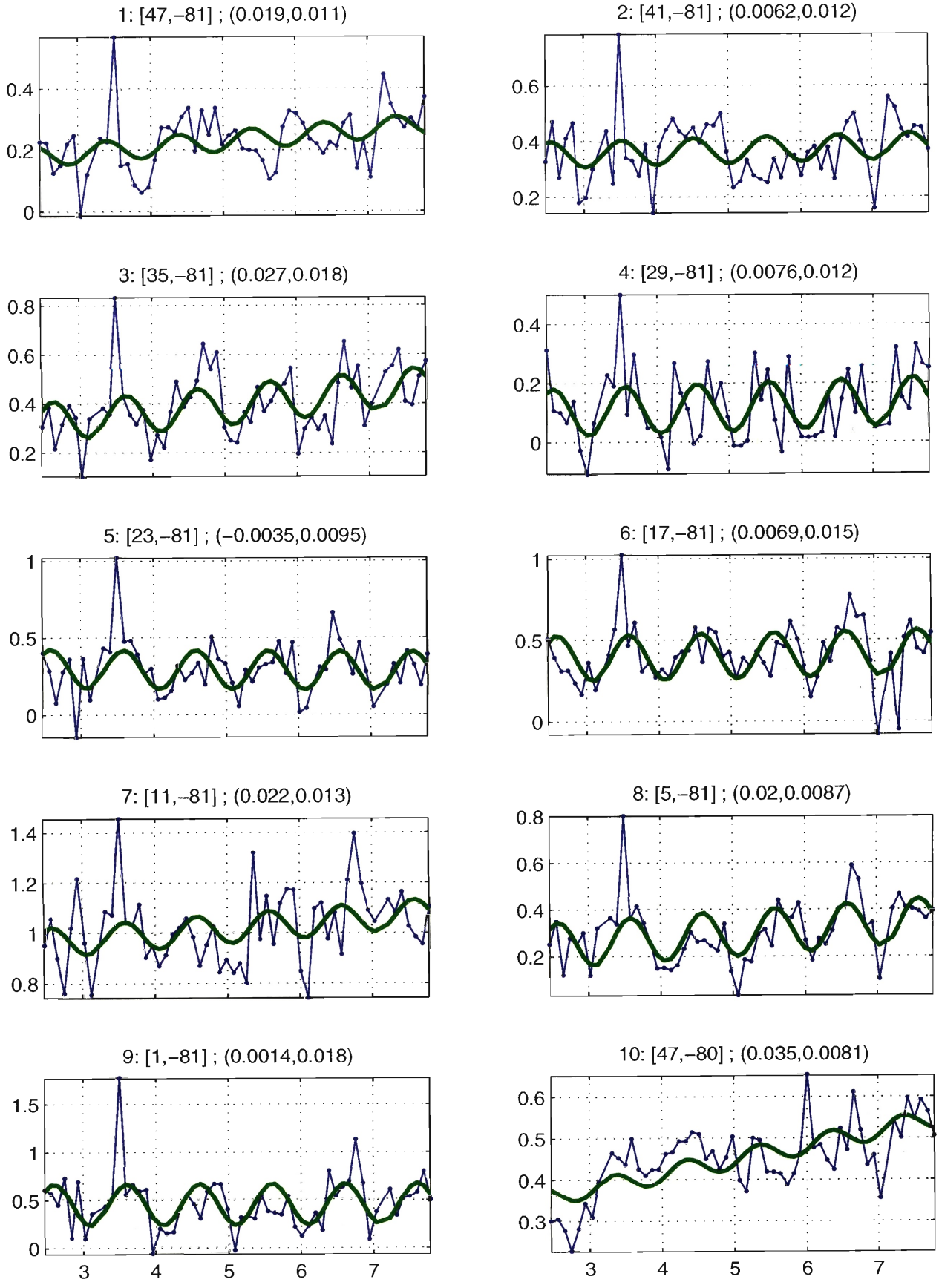
1: [47,−81] ; (0.019,0.011)
2: [41,−81] ; (0.0062,0.012)
3: [35,−81] ; (0.027,0.018)
4: [29,−81] ; (0.0076,0.012)
5: [23,−81] ; (−0.0035,0.0095)
6: [17,−81] ; (0.0069,0.015)
7: [11,−81] ; (0.022,0.013)
8: [5,−81] ; (0.02,0.0087)
9: [1,−81] ; (0.0014,0.018)
10: [47,−80] ; (0.035,0.0081)

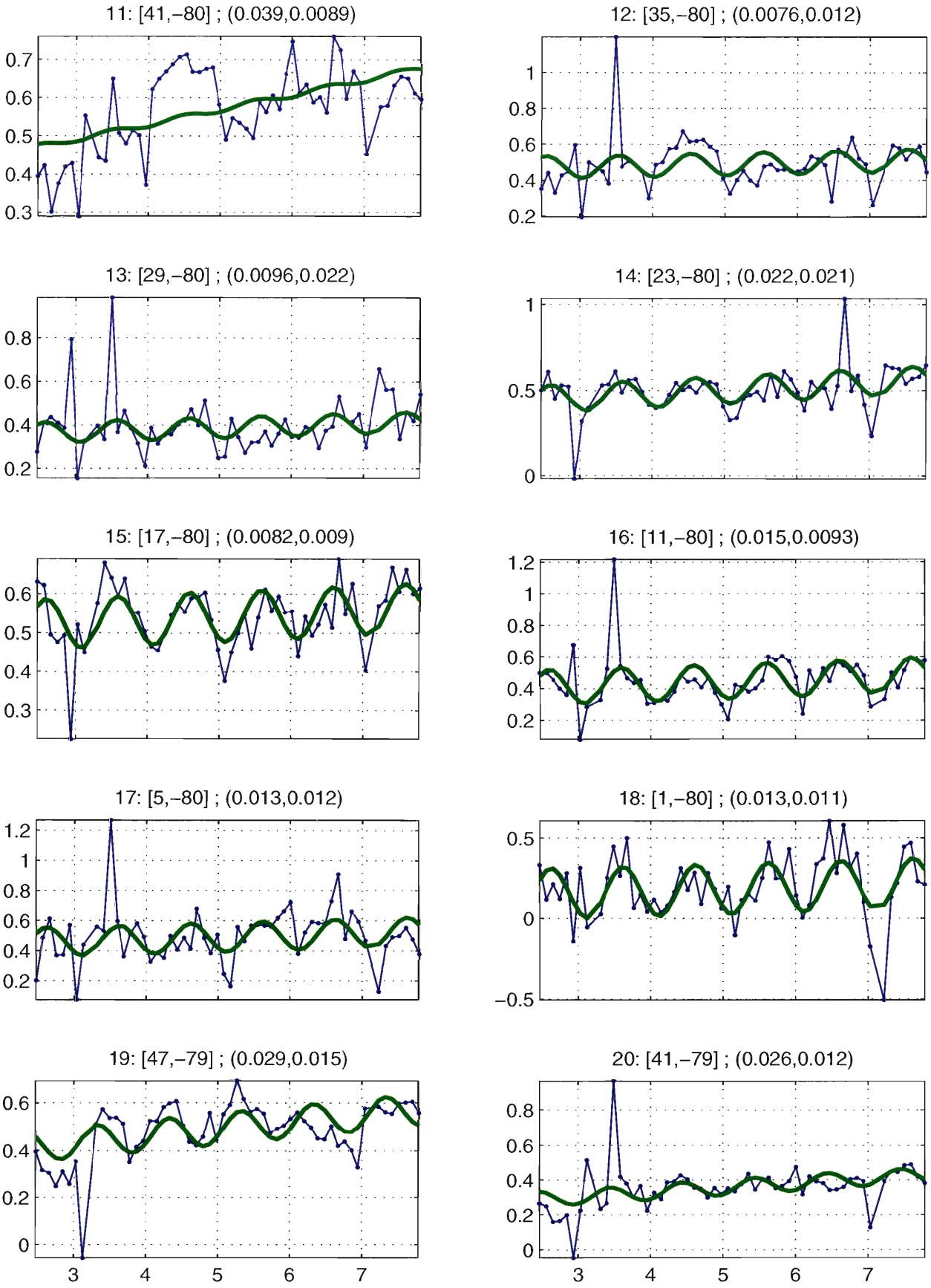
11: [41,−80] ; (0.039,0.0089)
12: [35,−80] ; (0.0076,0.012)
13: [29,−80] ; (0.0096,0.022)
14: [23,−80] ; (0.022,0.021)
15: [17,−80] ; (0.0082,0.009)
16: [11,−80] ; (0.015,0.0093)
17: [5,−80] ; (0.013,0.012)
18: [1,−80] ; (0.013,0.011)
19: [47,−79] ; (0.029,0.015)
20: [41,−79] ; (0.026,0.012)

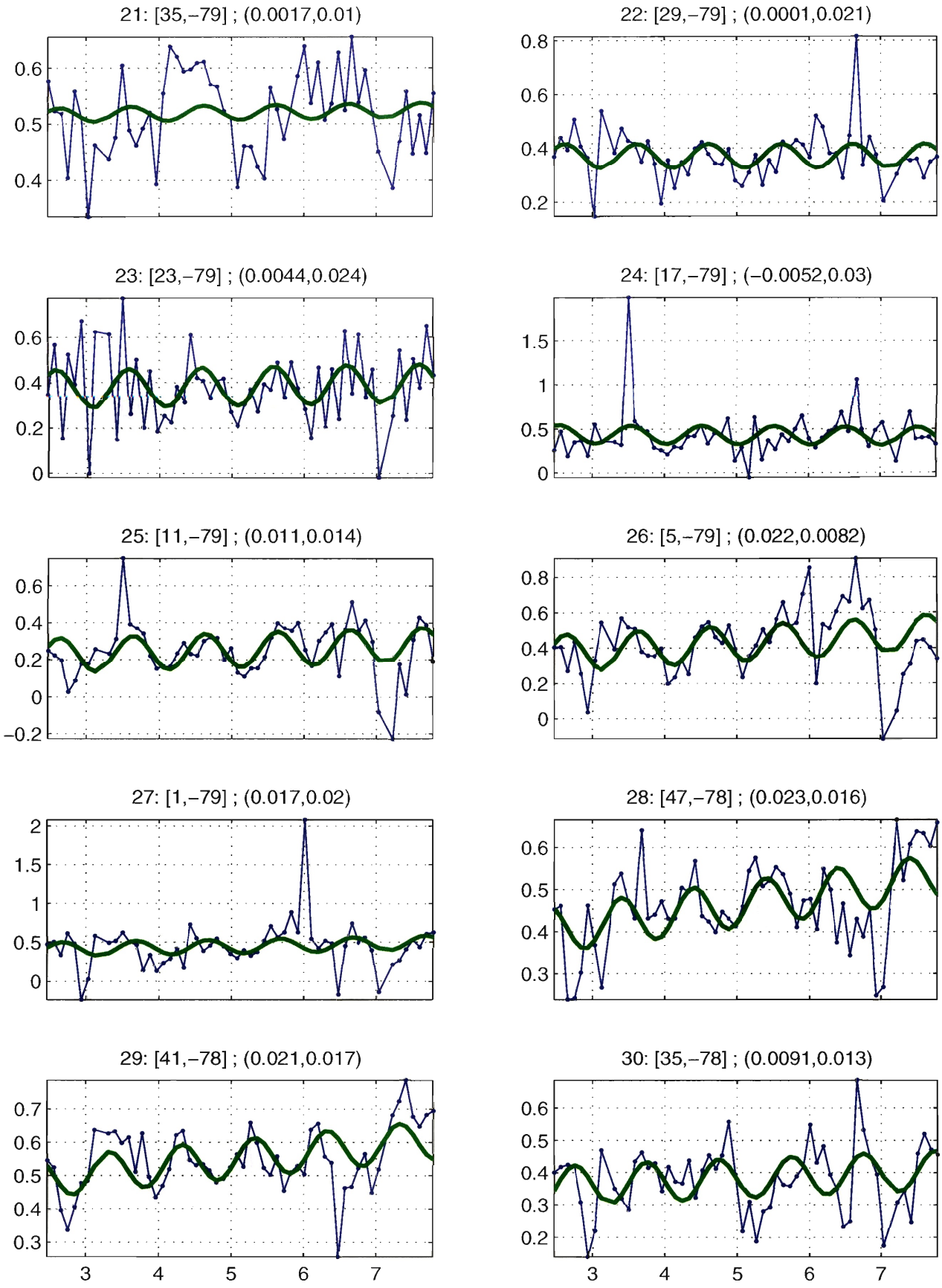
21: [35,−79] ; (0.0017,0.01)
22: [29,−79] ; (0.0001,0.021)
23: [23,−79] ; (0.0044,0.024)
24: [17,−79] ; (−0.0052,0.03)
25: [11,−79] ; (0.011,0.014)
26: [5,−79] ; (0.022,0.0082)
27: [1,−79] ; (0.017,0.02)
28: [47,−78] ; (0.023,0.016)
29: [41,−78] ; (0.021,0.017)
30: [35,−78] ; (0.0091,0.013)

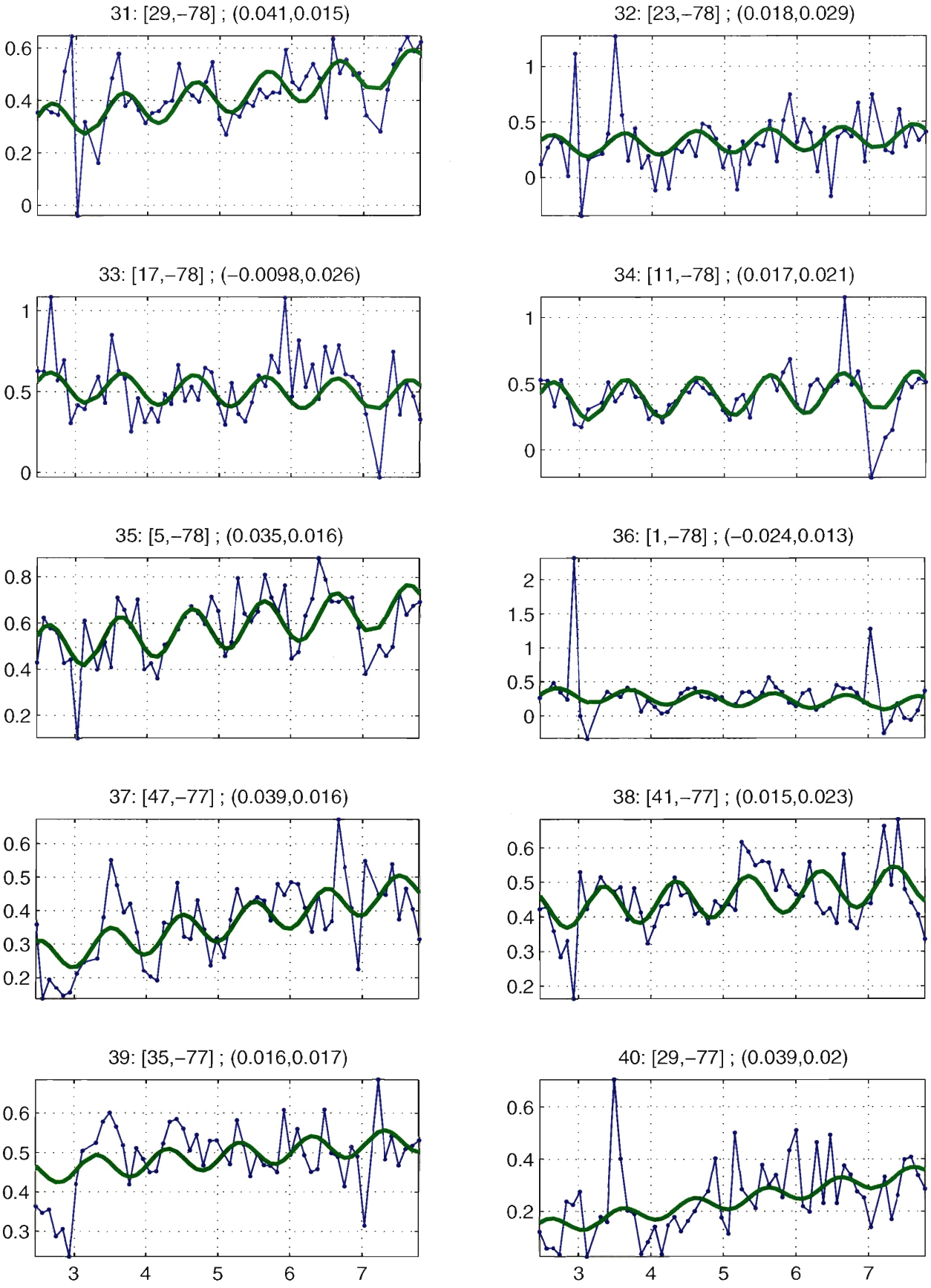
31: [29,−78] ; (0.041,0.015)
32: [23,−78] ; (0.018,0.029)
33: [17,−78] ; (−0.0098,0.026)
34: [11,−78] ; (0.017,0.021)
35: [5,−78] ; (0.035,0.016)
36: [1,−78] ; (−0.024,0.013)
37: [47,−77] ; (0.039,0.016)
38: [41,−77] ; (0.015,0.023)
39: [35,−77] ; (0.016,0.017)
40: [29,−77] ; (0.039,0.02)

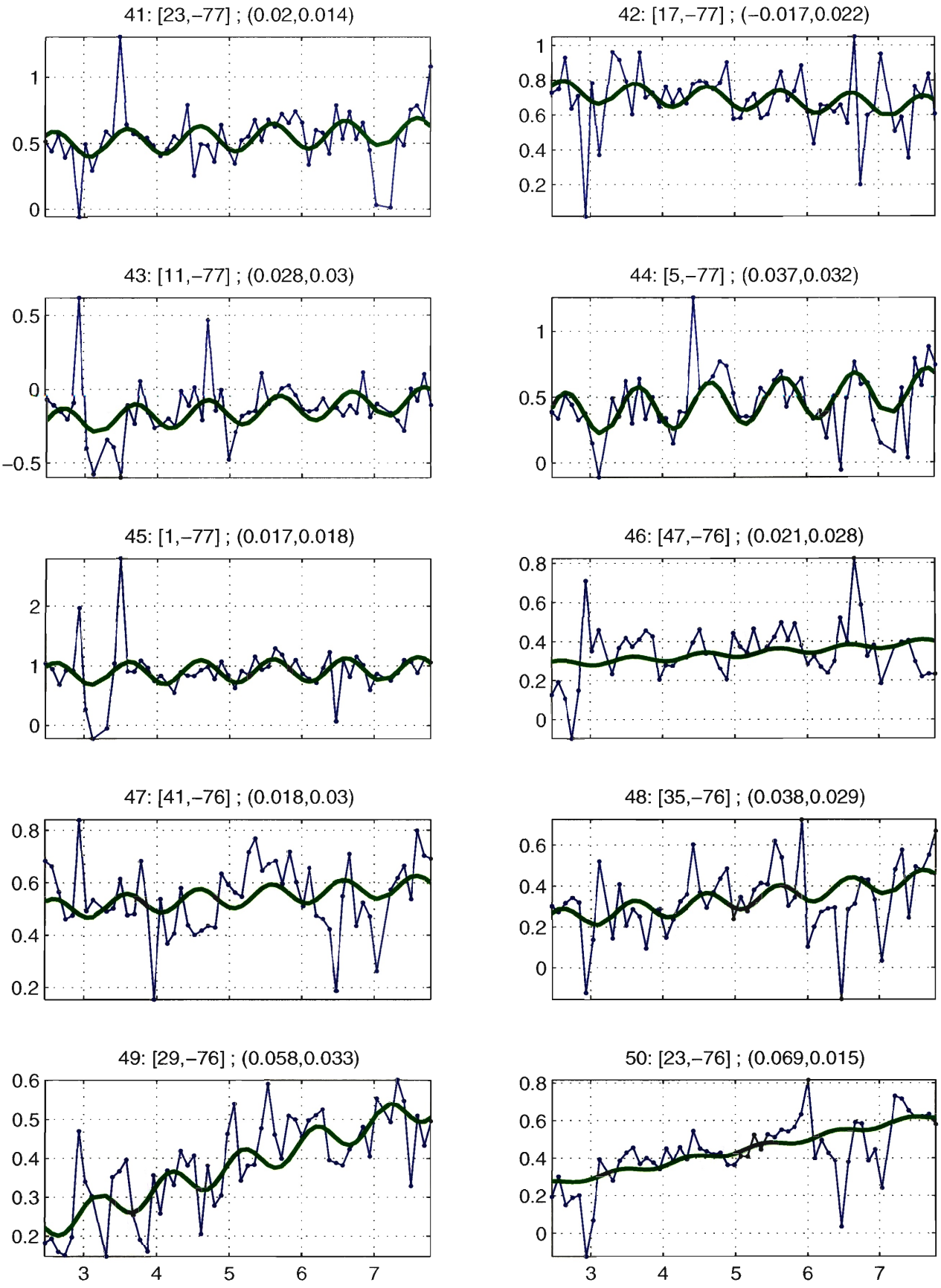
41: [23,−77] ; (0.02,0.014)
42: [17,−77] ; (−0.017,0.022)
43: [11,−77] ; (0.028,0.03)
44: [5,−77] ; (0.037,0.032)
45: [1,−77] ; (0.017,0.018)
46: [47,−76] ; (0.021,0.028)
47: [41,−76] ; (0.018,0.03)
48: [35,−76] ; (0.038,0.029)
49: [29,−76] ; (0.058,0.033)
50: [23,−76] ; (0.069,0.015)

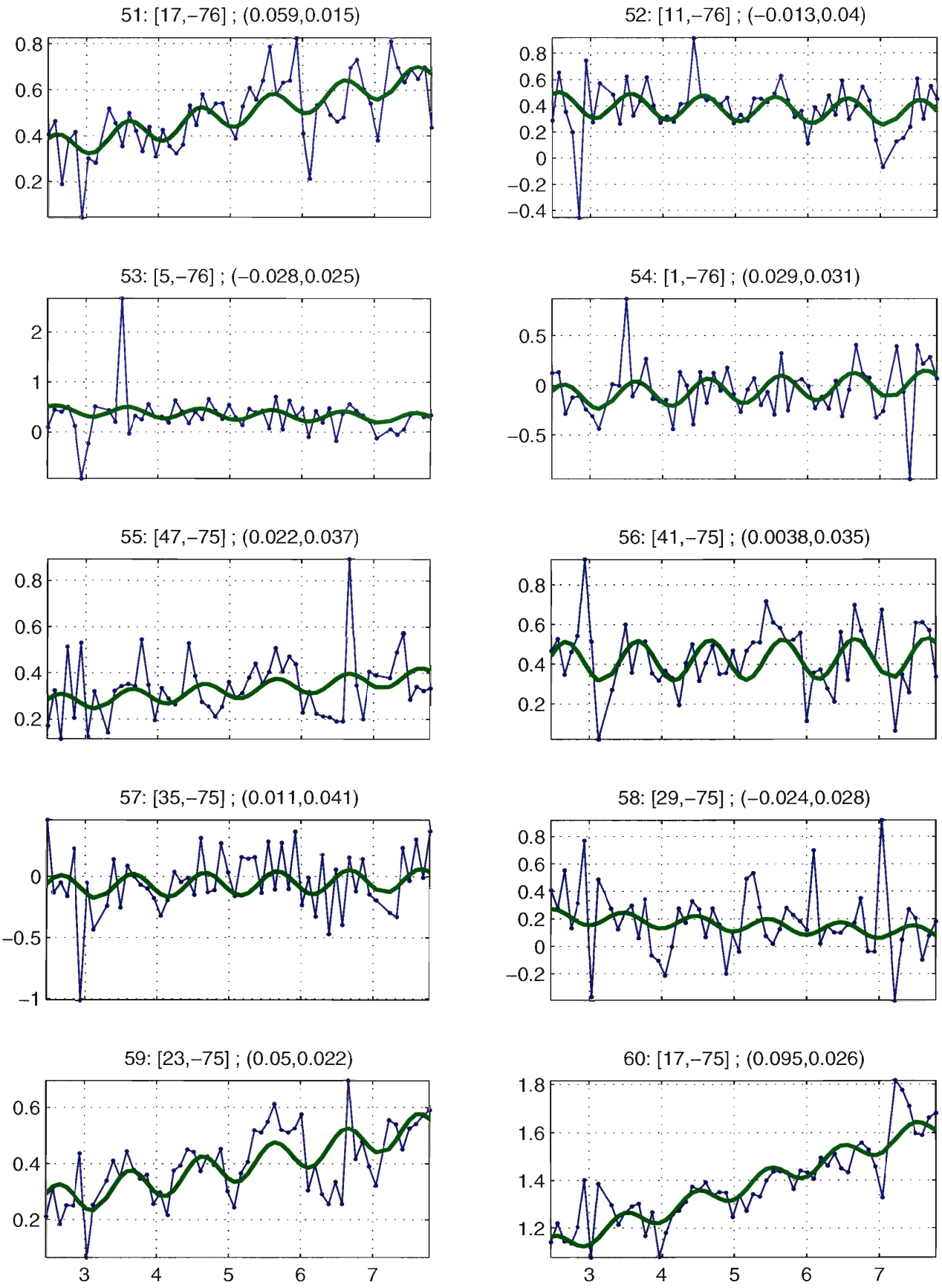
51: [17,−76] ; (0.059,0.015)
52: [11,−76] ; (−0.013,0.04)
53: [5,−76] ; (−0.028,0.025)
54: [1,−76] ; (0.029,0.031)
55: [47,−75] ; (0.022,0.037)
56: [41,−75] ; (0.0038,0.035)
57: [35,−75] ; (0.011,0.041)
58: [29,−75] ; (−0.024,0.028)
59: [23,−75] ; (0.05,0.022)
60: [17,−75] ; (0.095,0.026)

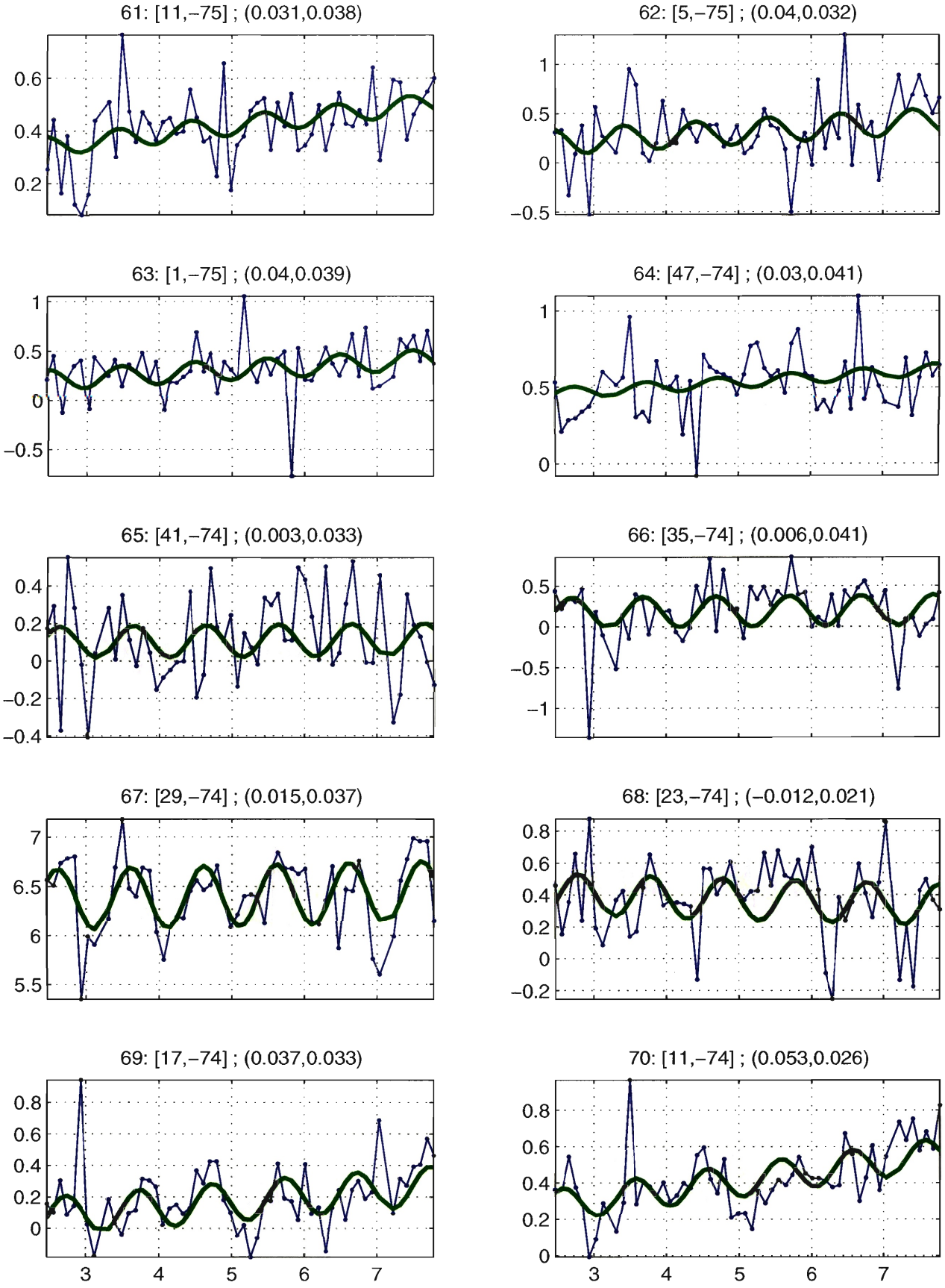
61: [11,−75] ; (0.031,0.038)
62: [5,−75] ; (0.04,0.032)
63: [1,−75] ; (0.04,0.039)
64: [47,−74] ; (0.03,0.041)
65: [41,−74] ; (0.003,0.033)
66: [35,−74] ; (0.006,0.041)
67: [29,−74] ; (0.015,0.037)
68: [23,−74] ; (−0.012,0.021)
69: [17,−74] ; (0.037,0.033)
70: [11,−74] ; (0.053,0.026)

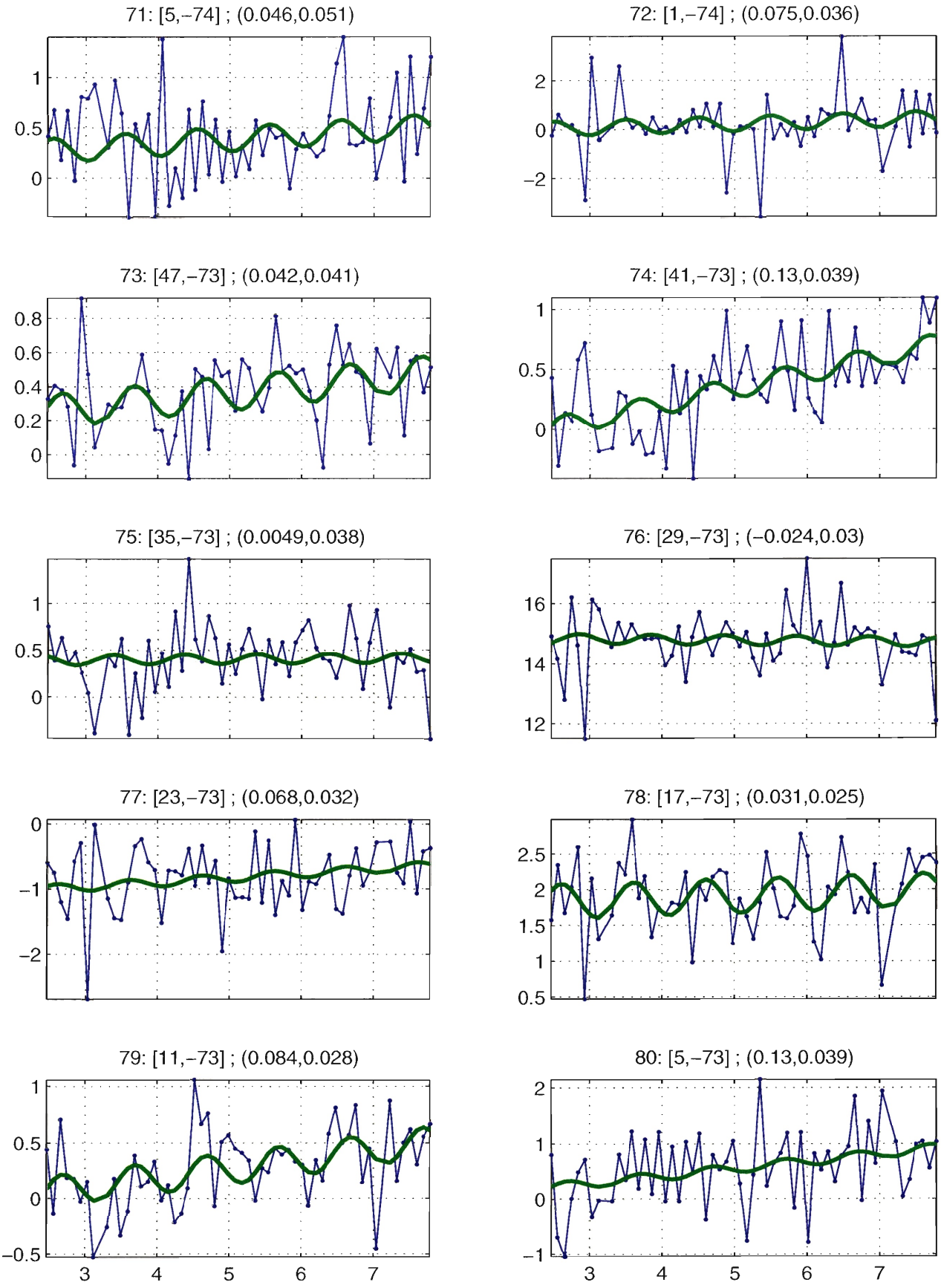
71: [5,−74] ; (0.046,0.051)
72: [1,−74] ; (0.075,0.036)
73: [47,−73] ; (0.042,0.041)
74: [41,−73] ; (0.13,0.039)
75: [35,−73] ; (0.0049,0.038)
76: [29,−73] ; (−0.024,0.03)
77: [23,−73] ; (0.068,0.032)
78: [17,−73] ; (0.031,0.025)
79: [11,−73] ; (0.084,0.028)
80: [5,−73] ; (0.13,0.039)

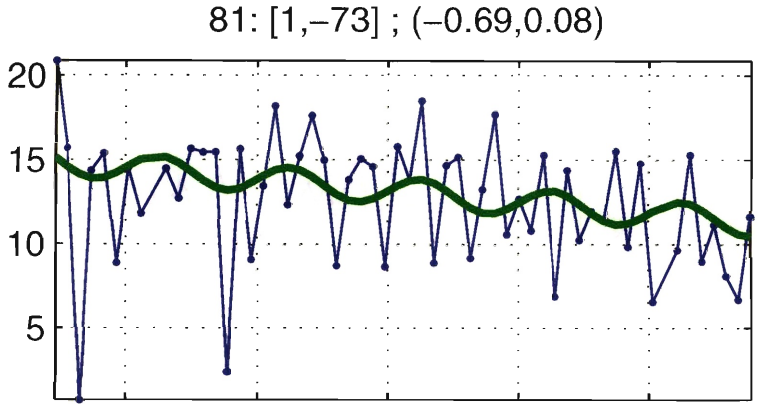
81: [1,−73] ; (−0.69,0.08)
20
15
10
5

Region II

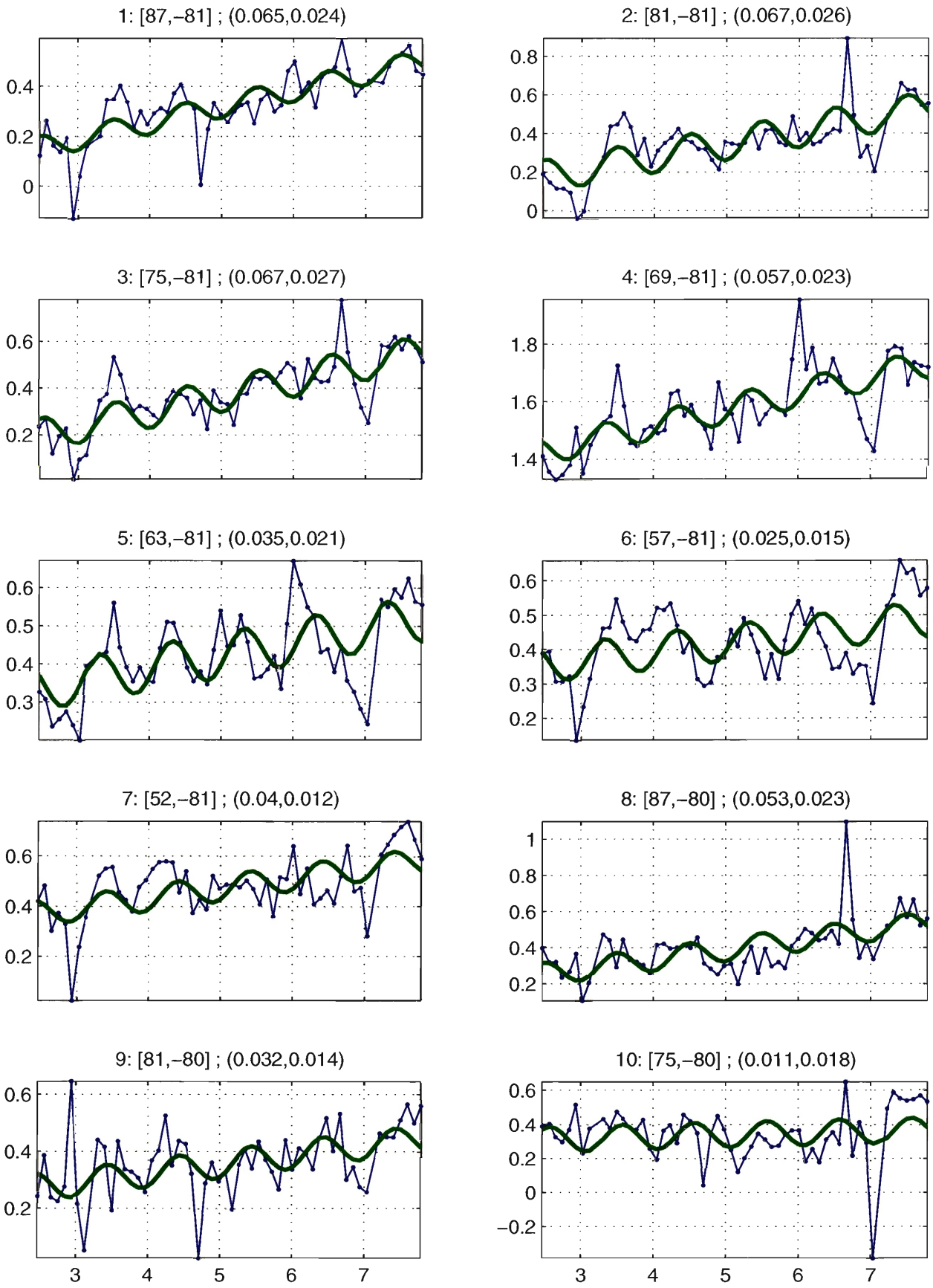
1: [87,−81] ; (0.065,0.024)
2: [81,−81] ; (0.067,0.026)
3: [75,−81] ; (0.067,0.027)
4: [69,−81] ; (0.057,0.023)
5: [63,−81] ; (0.035,0.021)
6: [57,−81] ; (0.025,0.015)
7: [52,−81] ; (0.04,0.012)
8: [87,−80] ; (0.053,0.023)
9: [81,−80] ; (0.032,0.014)
10: [75,−80] ; (0.011,0.018)

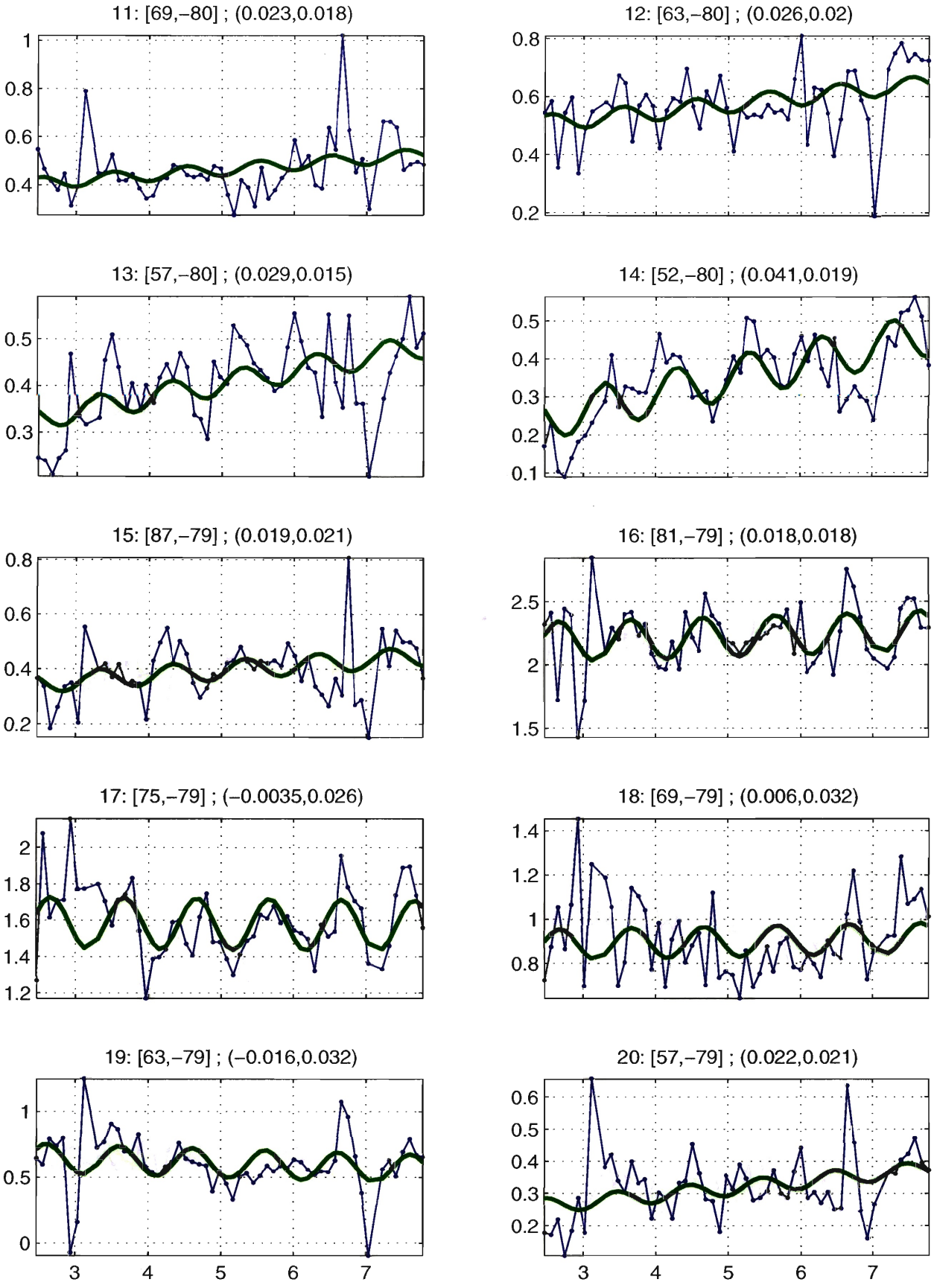
11: [69,−80] ; (0.023,0.018)
12: [63,−80] ; (0.026,0.02)
13: [57,−80] ; (0.029,0.015)
14: [52,−80] ; (0.041,0.019)
15: [87,−79] ; (0.019,0.021)
16: [81,−79] ; (0.018,0.018)
17: [75,−79] ; (−0.0035,0.026)
18: [69,−79] ; (0.006,0.032)
19: [63,−79] ; (−0.016,0.032)
20: [57,−79] ; (0.022,0.021)

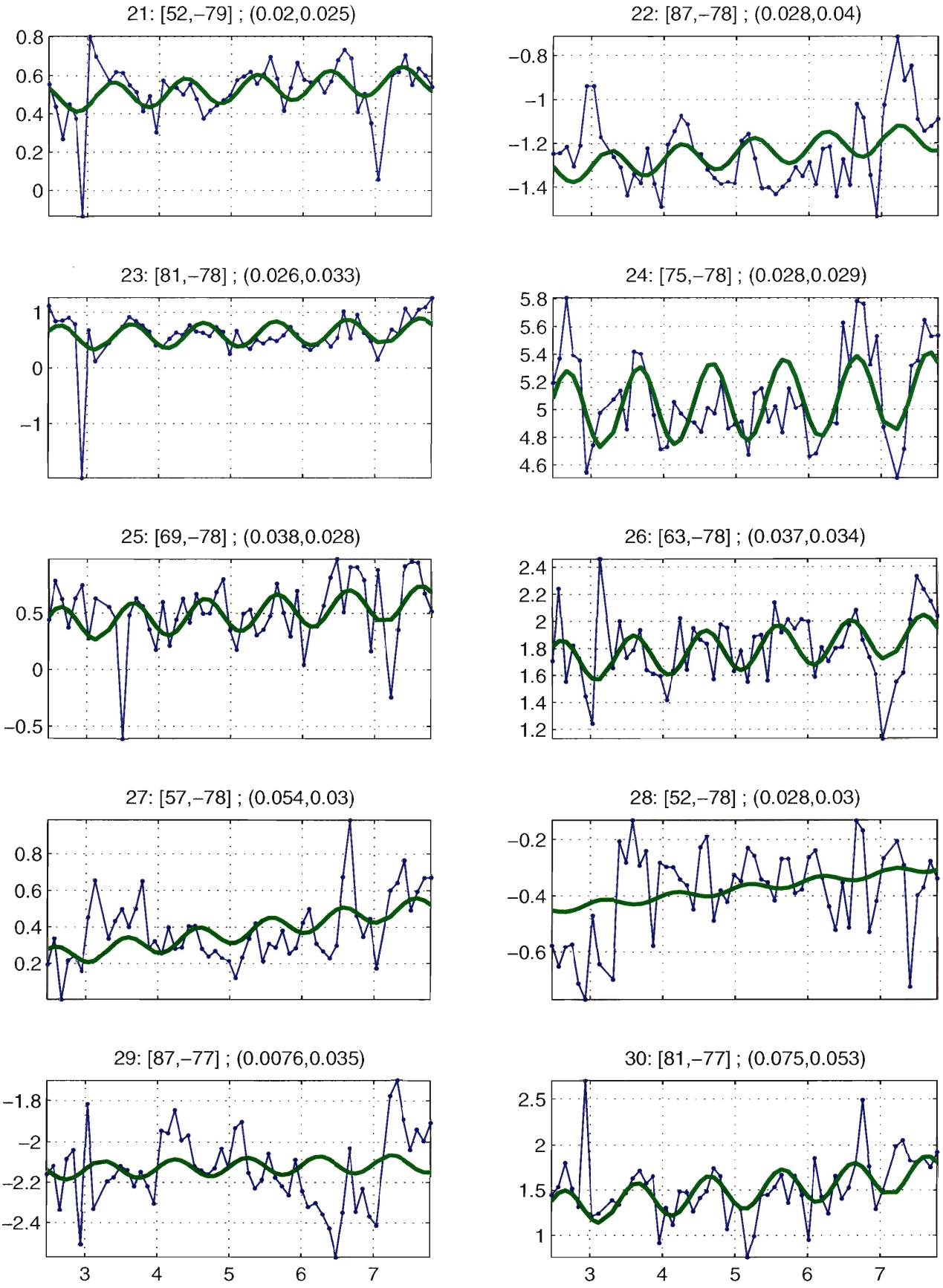
21: [52,−79] ; (0.02,0.025)
22: [87,−78] ; (0.028,0.04)
23: [81,−78] ; (0.026,0.033)
24: [75,−78] ; (0.028,0.029)
25: [69,−78] ; (0.038,0.028)
26: [63,−78] ; (0.037,0.034)
27: [57,−78] ; (0.054,0.03)
28: [52,−78] ; (0.028,0.03)
29: [87,−77] ; (0.0076,0.035)
30: [81,−77] ; (0.075,0.053)

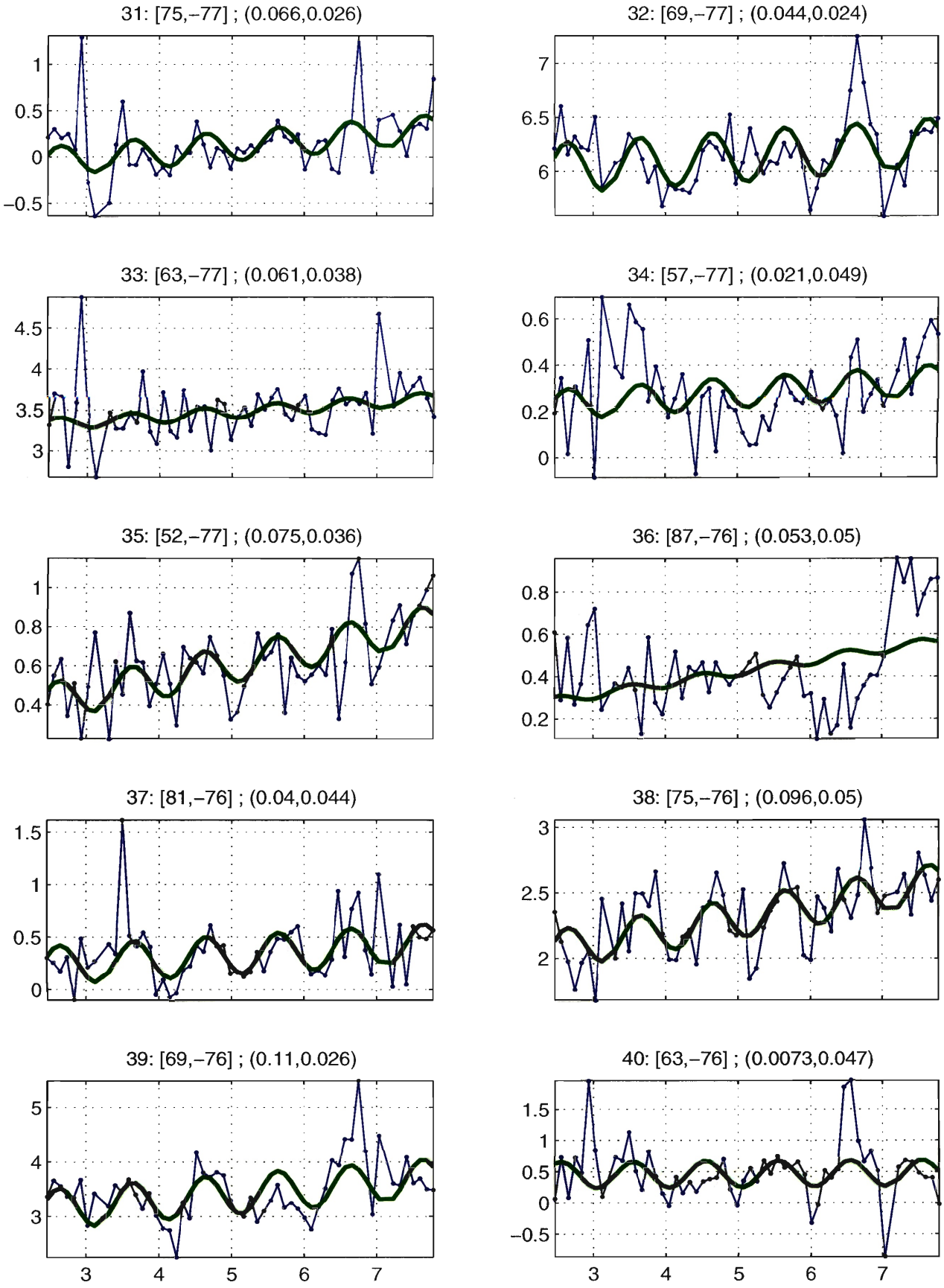
31: [75,−77] ; (0.066,0.026)
32: [69,−77] ; (0.044,0.024)
33: [63,−77] ; (0.061,0.038)
34: [57,−77] ; (0.021,0.049)
35: [52,−77] ; (0.075,0.036)
36: [87,−76] ; (0.053,0.05)
37: [81,−76] ; (0.04,0.044)
38: [75,−76] ; (0.096,0.05)
39: [69,−76] ; (0.11,0.026)
40: [63,−76] ; (0.0073,0.047)

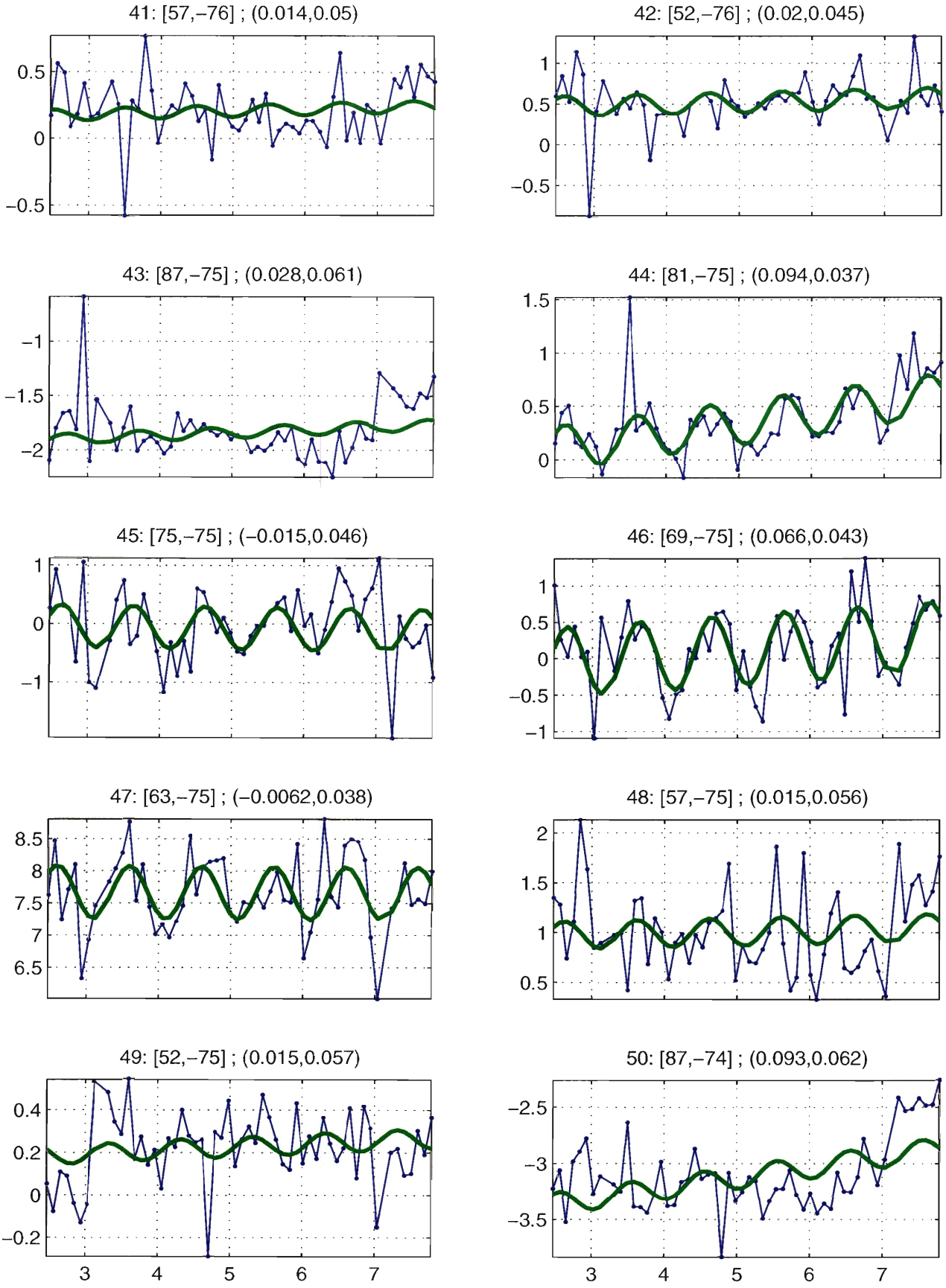
41: [57,−76] ; (0.014,0.05)
42: [52,−76] ; (0.02,0.045)
43: [87,−75] ; (0.028,0.061)
44: [81,−75] ; (0.094,0.037)
45: [75,−75] ; (−0.015,0.046)
46: [69,−75] ; (0.066,0.043)
47: [63,−75] ; (−0.0062,0.038)
48: [57,−75] ; (0.015,0.056)
49: [52,−75] ; (0.015,0.057)
50: [87,−74] ; (0.093,0.062)

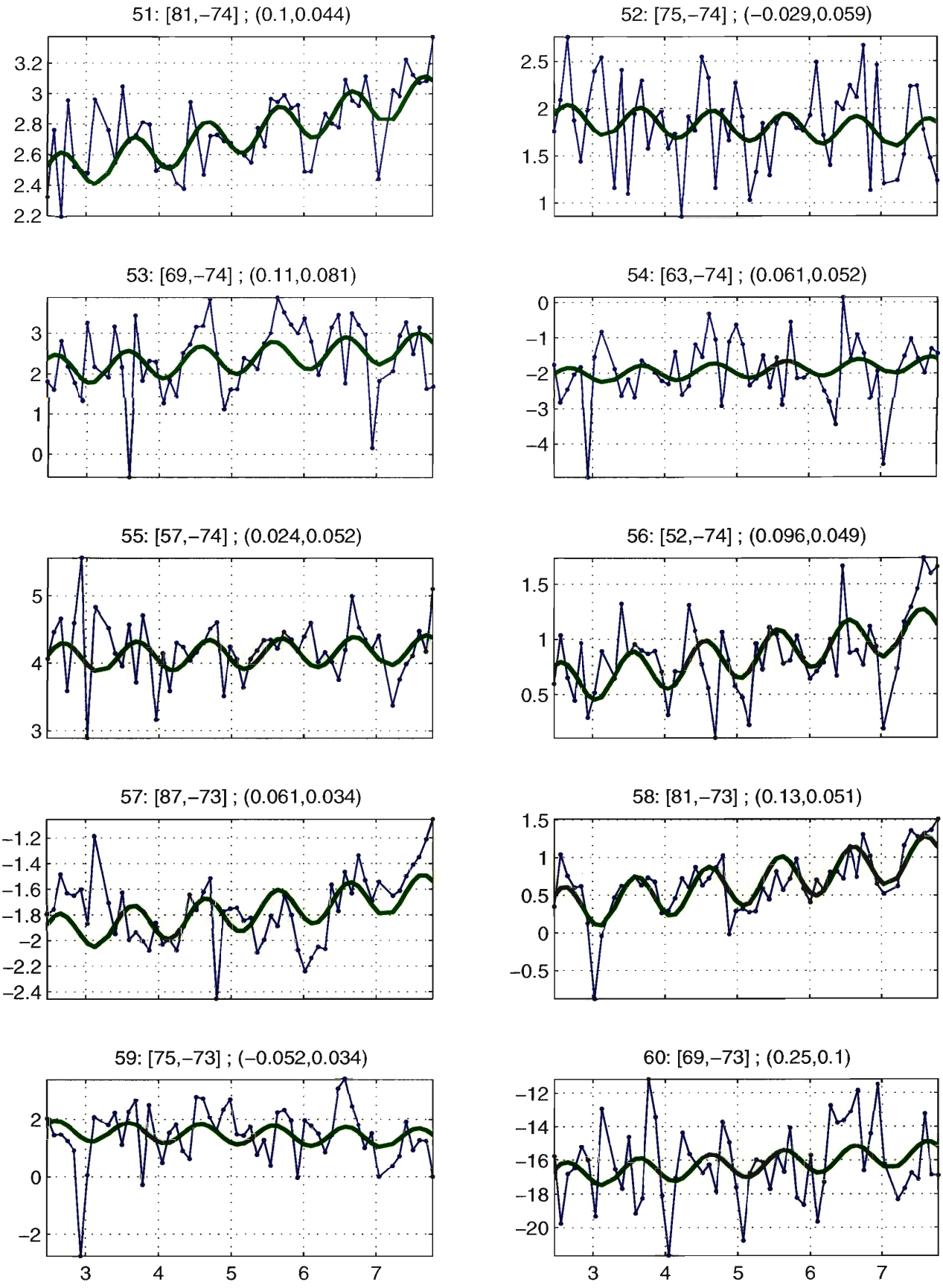
51: [81,−74] ; (0.1,0.044)
52: [75,−74] ; (−0.029,0.059)
53: [69,−74] ; (0.11,0.081)
54: [63,−74] ; (0.061,0.052)
55: [57,−74] ; (0.024,0.052)
56: [52,−74] ; (0.096,0.049)
57: [87,−73] ; (0.061,0.034)
58: [81,−73] ; (0.13,0.051)
59: [75,−73] ; (−0.052,0.034)
60: [69,−73] ; (0.25,0.1)

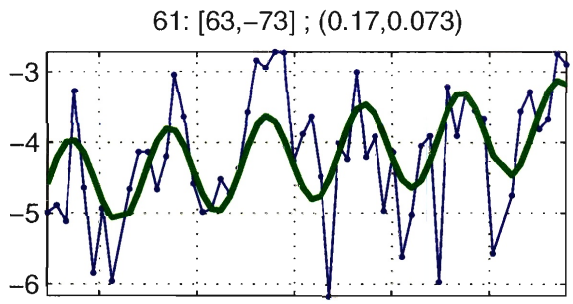
61: [63,−73] ; (0.17,0.073)
−3
−4
−5
−6

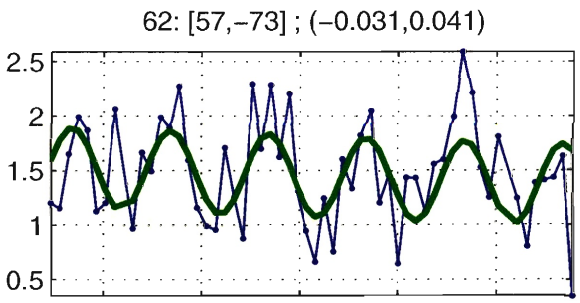
62: [57,−73] ; (−0.031,0.041)
2.5
2
1.5
1
0.5

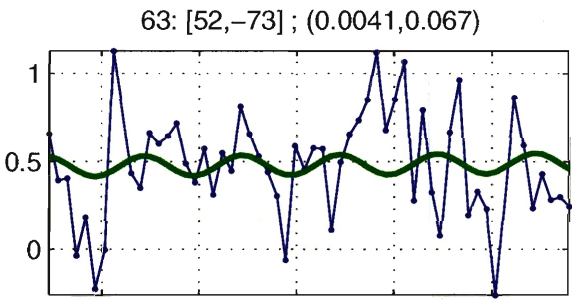
63: [52,−73] ; (0.0041,0.067)
1
0.5
0

Region III

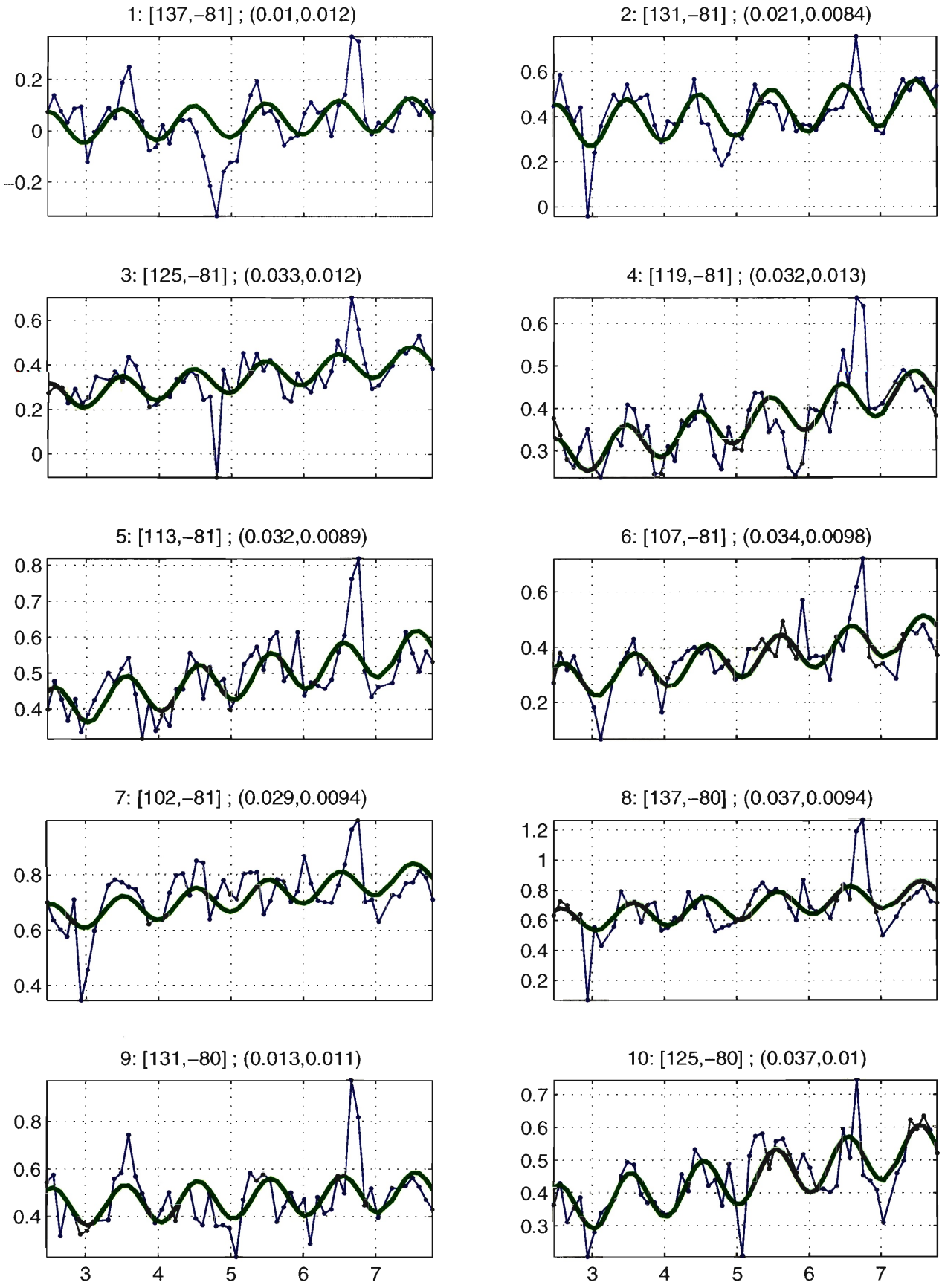
1: [137,−81] ; (0.01,0.012)
2: [131,−81] ; (0.021,0.0084)
3: [125,−81] ; (0.033,0.012)
4: [119,−81] ; (0.032,0.013)
5: [113,−81] ; (0.032,0.0089)
6: [107,−81] ; (0.034,0.0098)
7: [102,−81] ; (0.029,0.0094)
8: [137,−80] ; (0.037,0.0094)
9: [131,−80] ; (0.013,0.011)
10: [125,−80] ; (0.037,0.01)

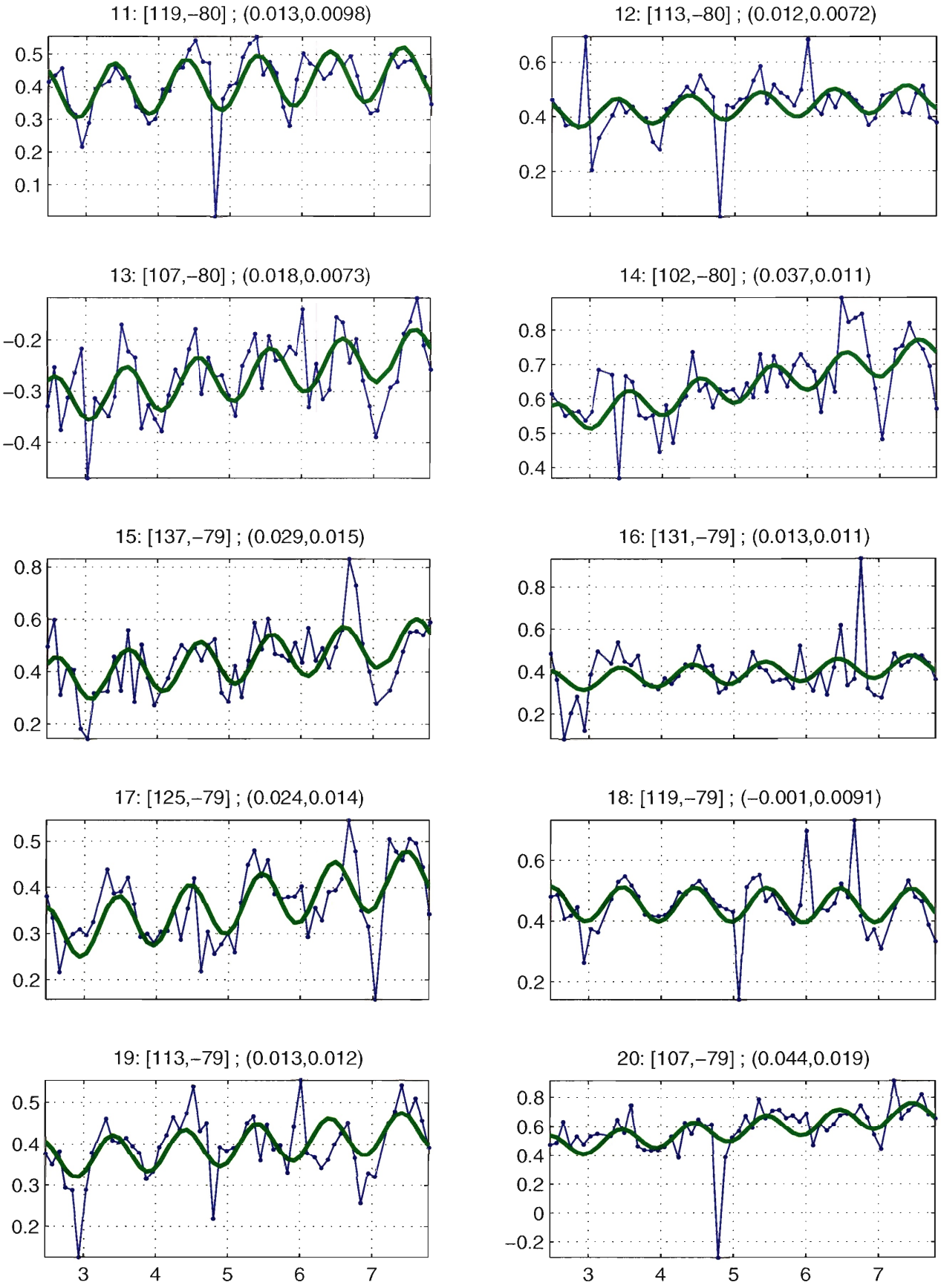
11: [119,−80] ; (0.013,0.0098)
12: [113,−80] ; (0.012,0.0072)
13: [107,−80] ; (0.018,0.0073)
14: [102,−80] ; (0.037,0.011)
15: [137,−79] ; (0.029,0.015)
16: [131,−79] ; (0.013,0.011)
17: [125,−79] ; (0.024,0.014)
18: [119,−79] ; (−0.001,0.0091)
19: [113,−79] ; (0.013,0.012)
20: [107,−79] ; (0.044,0.019)

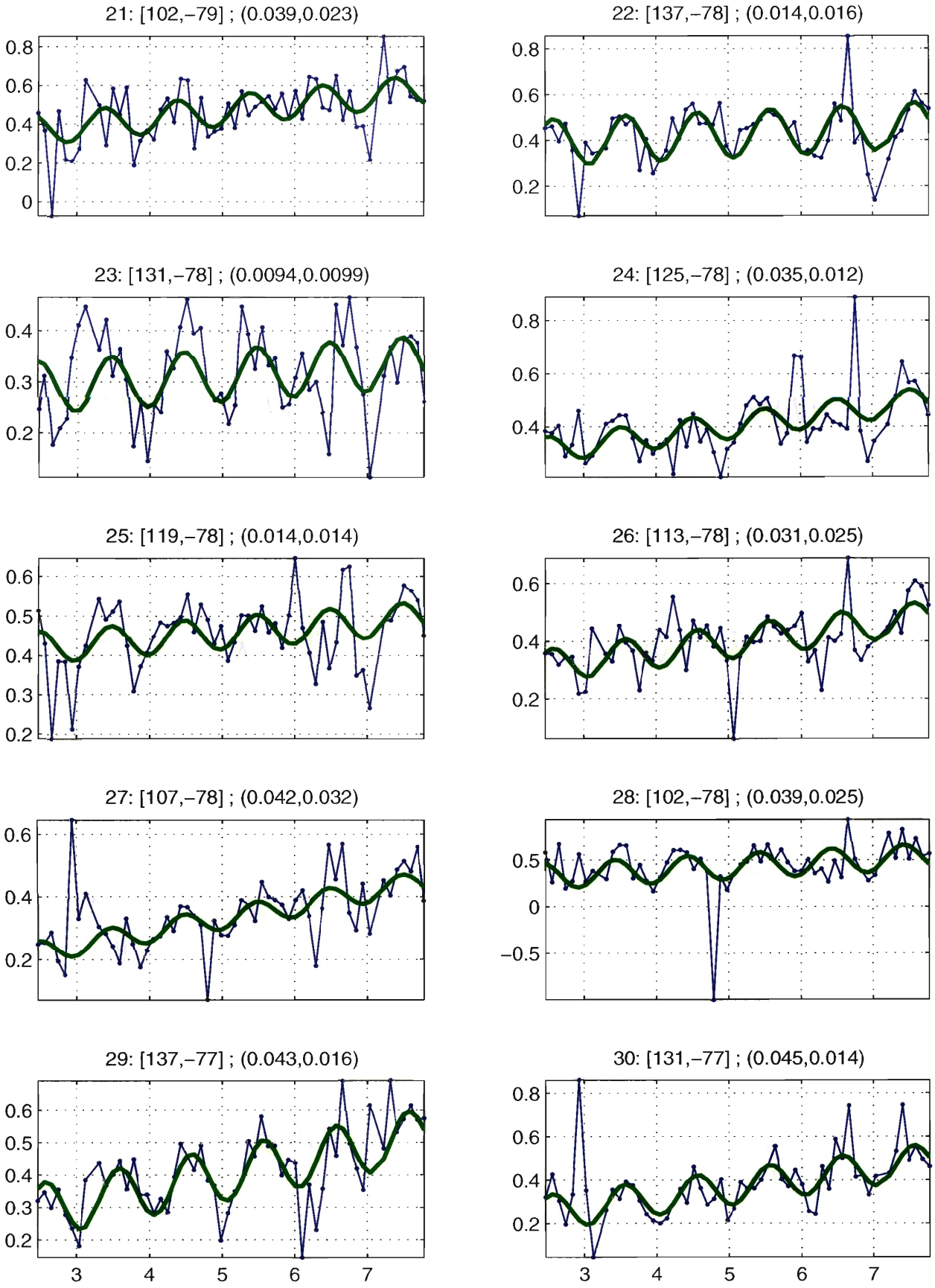
21: [102,−79] ; (0.039,0.023)
22: [137,−78] ; (0.014,0.016)
23: [131,−78] ; (0.0094,0.0099)
24: [125,−78] ; (0.035,0.012)
25: [119,−78] ; (0.014,0.014)
26: [113,−78] ; (0.031,0.025)
27: [107,−78] ; (0.042,0.032)
28: [102,−78] ; (0.039,0.025)
29: [137,−77] ; (0.043,0.016)
30: [131,−77] ; (0.045,0.014)

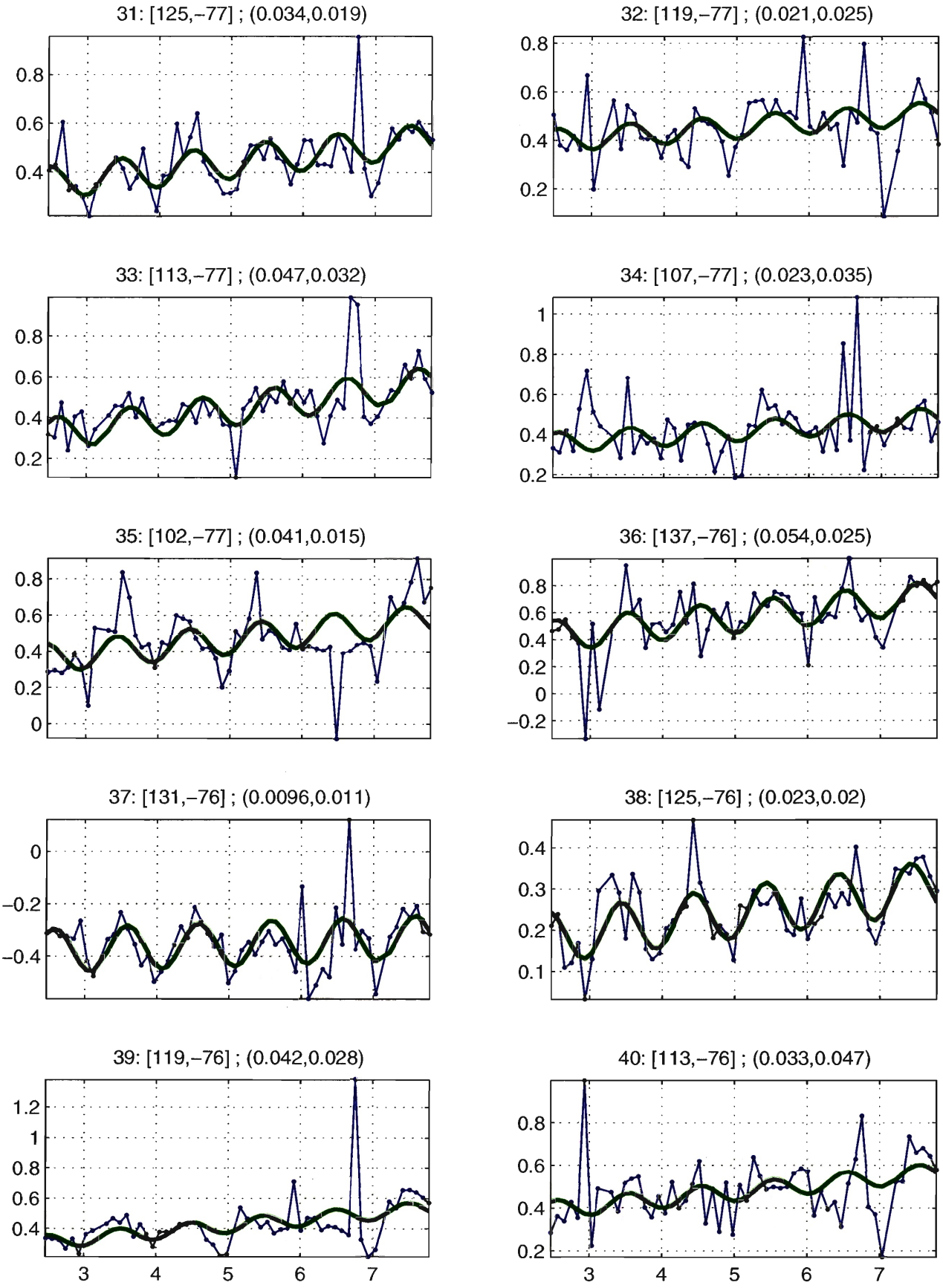
31: [125,−77] ; (0.034,0.019)
32: [119,−77] ; (0.021,0.025)
33: [113,−77] ; (0.047,0.032)
34: [107,−77] ; (0.023,0.035)
35: [102,−77] ; (0.041,0.015)
36: [137,−76] ; (0.054,0.025)
37: [131,−76] ; (0.0096,0.011)
38: [125,−76] ; (0.023,0.02)
39: [119,−76] ; (0.042,0.028)
40: [113,−76] ; (0.033,0.047)

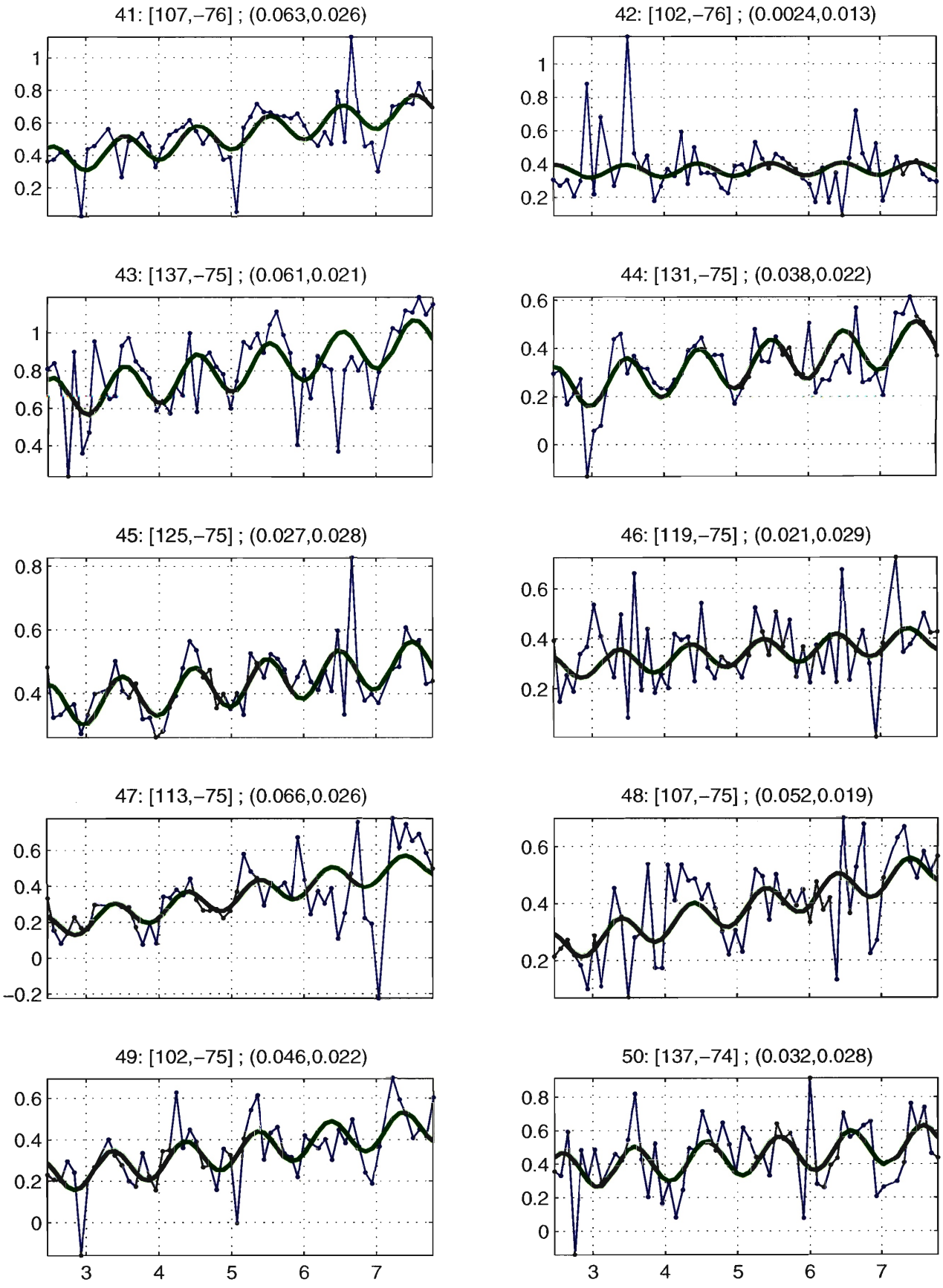
41: [107,−76] ; (0.063,0.026)
42: [102,−76] ; (0.0024,0.013)
43: [137,−75] ; (0.061,0.021)
44: [131,−75] ; (0.038,0.022)
45: [125,−75] ; (0.027,0.028)
46: [119,−75] ; (0.021,0.029)
47: [113,−75] ; (0.066,0.026)
48: [107,−75] ; (0.052,0.019)
49: [102,−75] ; (0.046,0.022)
50: [137,−74] ; (0.032,0.028)

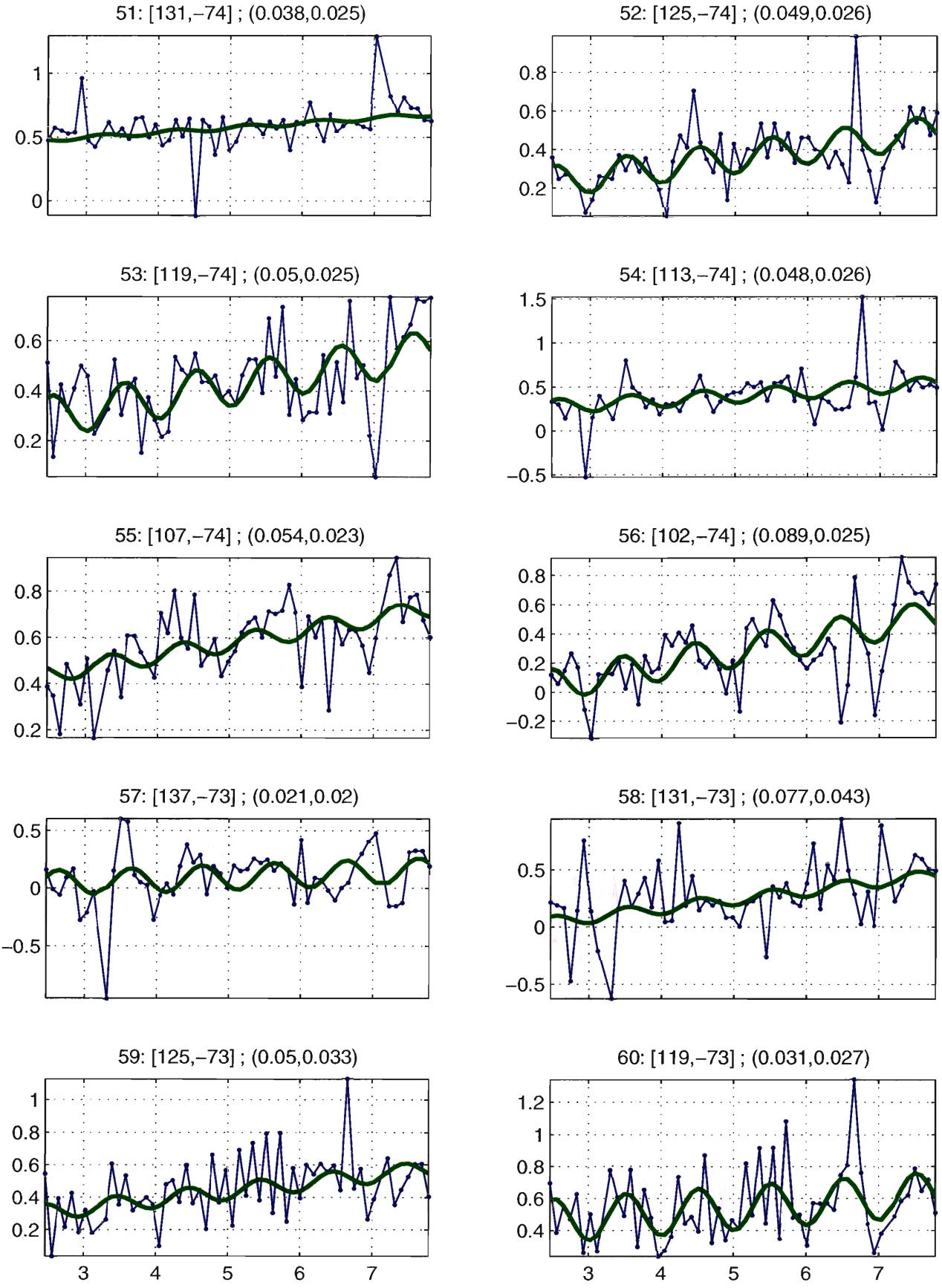
51: [131,−74] ; (0.038,0.025)
52: [125,−74] ; (0.049,0.026)
53: [119,−74] ; (0.05,0.025)
54: [113,−74] ; (0.048,0.026)
55: [107,−74] ; (0.054,0.023)
56: [102,−74] ; (0.089,0.025)
57: [137,−73] ; (0.021,0.02)
58: [131,−73] ; (0.077,0.043)
59: [125,−73] ; (0.05,0.033)
60: [119,−73] ; (0.031,0.027)

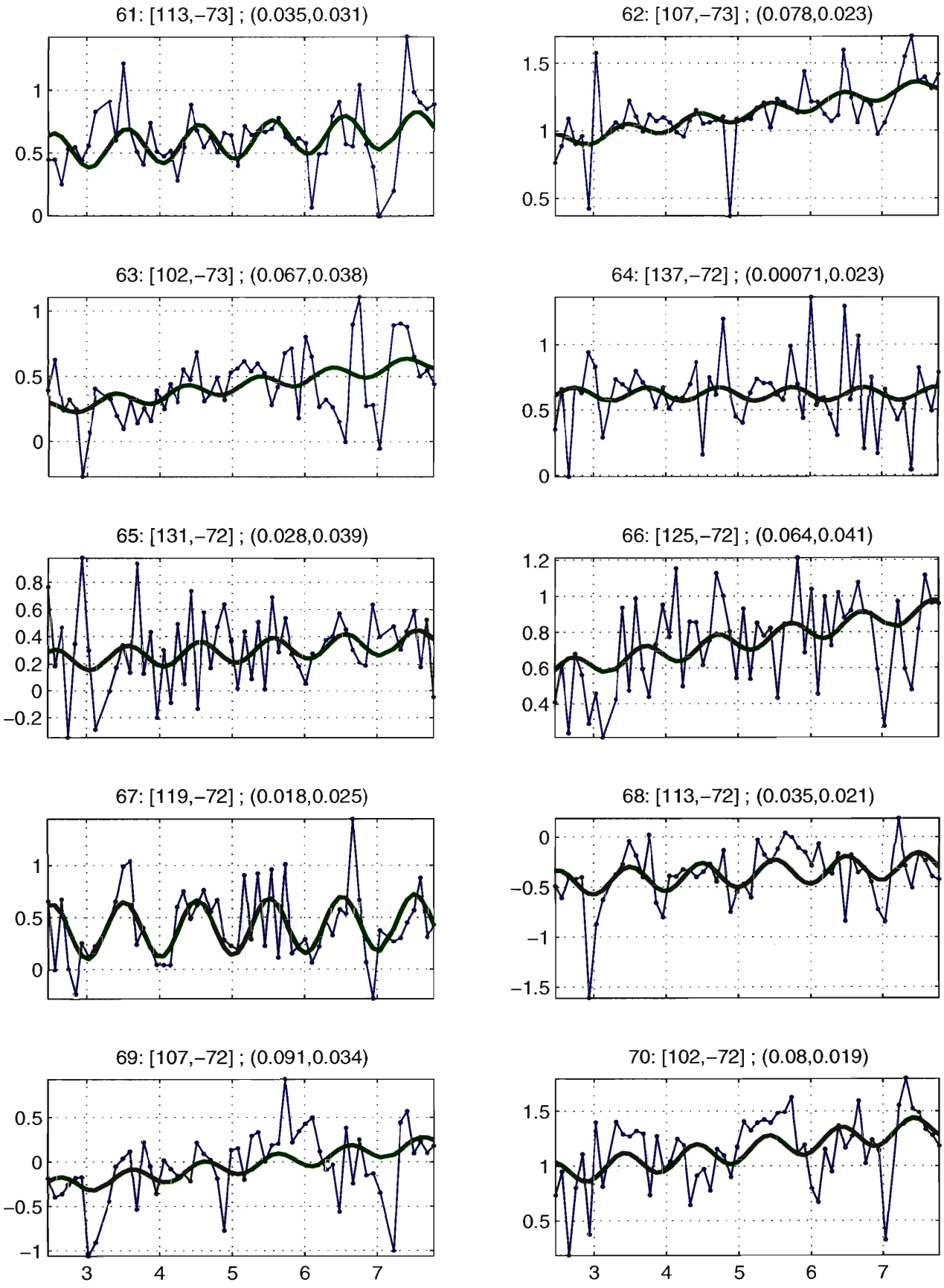
61: [113,−73] ; (0.035,0.031)
62: [107,−73] ; (0.078,0.023)
63: [102,−73] ; (0.067,0.038)
64: [137,−72] ; (0.00071,0.023)
65: [131,−72] ; (0.028,0.039)
66: [125,−72] ; (0.064,0.041)
67: [119,−72] ; (0.018,0.025)
68: [113,−72] ; (0.035,0.021)
69: [107,−72] ; (0.091,0.034)
70: [102,−72] ; (0.08,0.019)

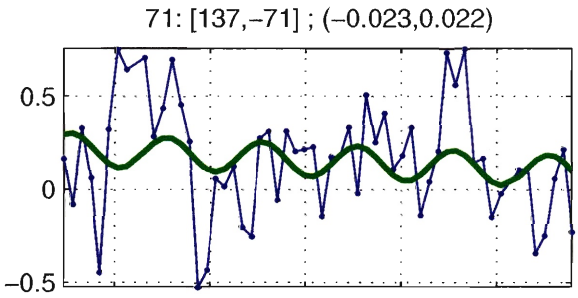
71: [137,−71] ; (−0.023,0.022)
0.5
0
−0.5

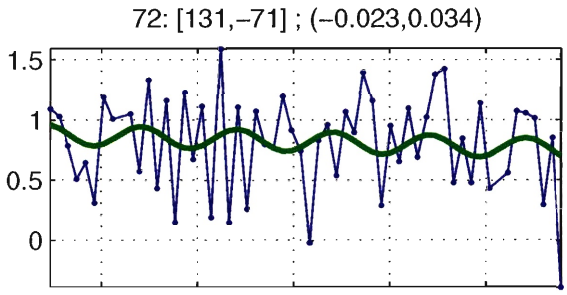
72: [131,−71] ; (−0.023,0.034)
1.5
1
0.5
0

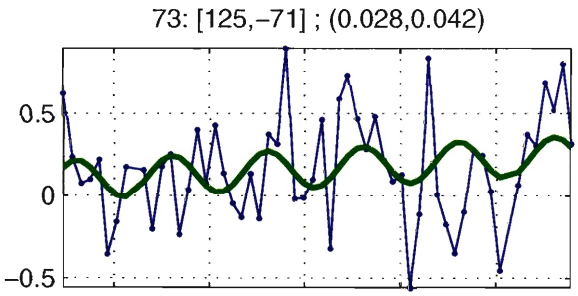
73: [125,−71] ; (0.028,0.042)
0.5
0
−0.5

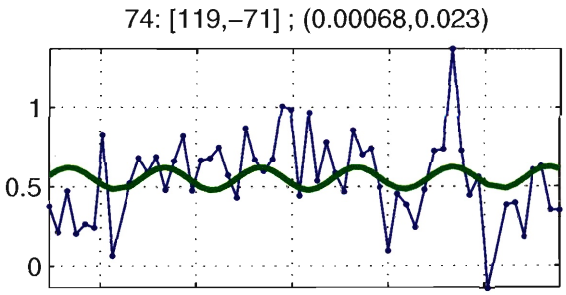
74: [119,−71] ; (0.00068,0.023)
1
0.5
0

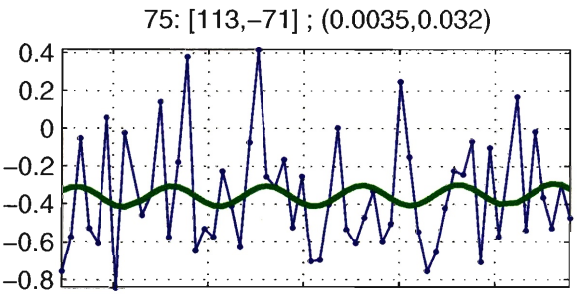
75: [113,−71] ; (0.0035,0.032)
0.4
0.2
0
−0.2
−0.4
−0.6
−0.8

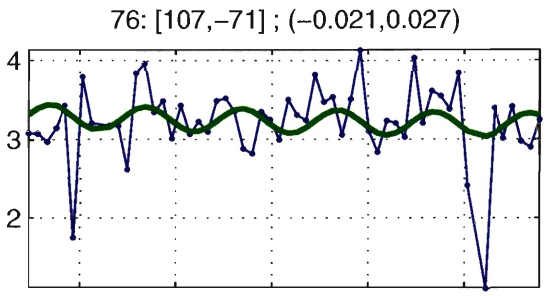
76: [107,−71] ; (−0.021,0.027)
4
3
2

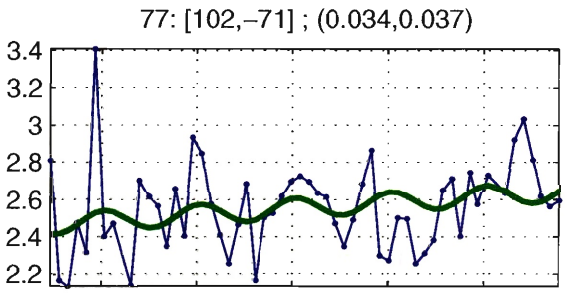
77: [102,−71] ; (0.034,0.037)
3.4
3.2
3
2.8
2.6
2.4
2.2

Region IV

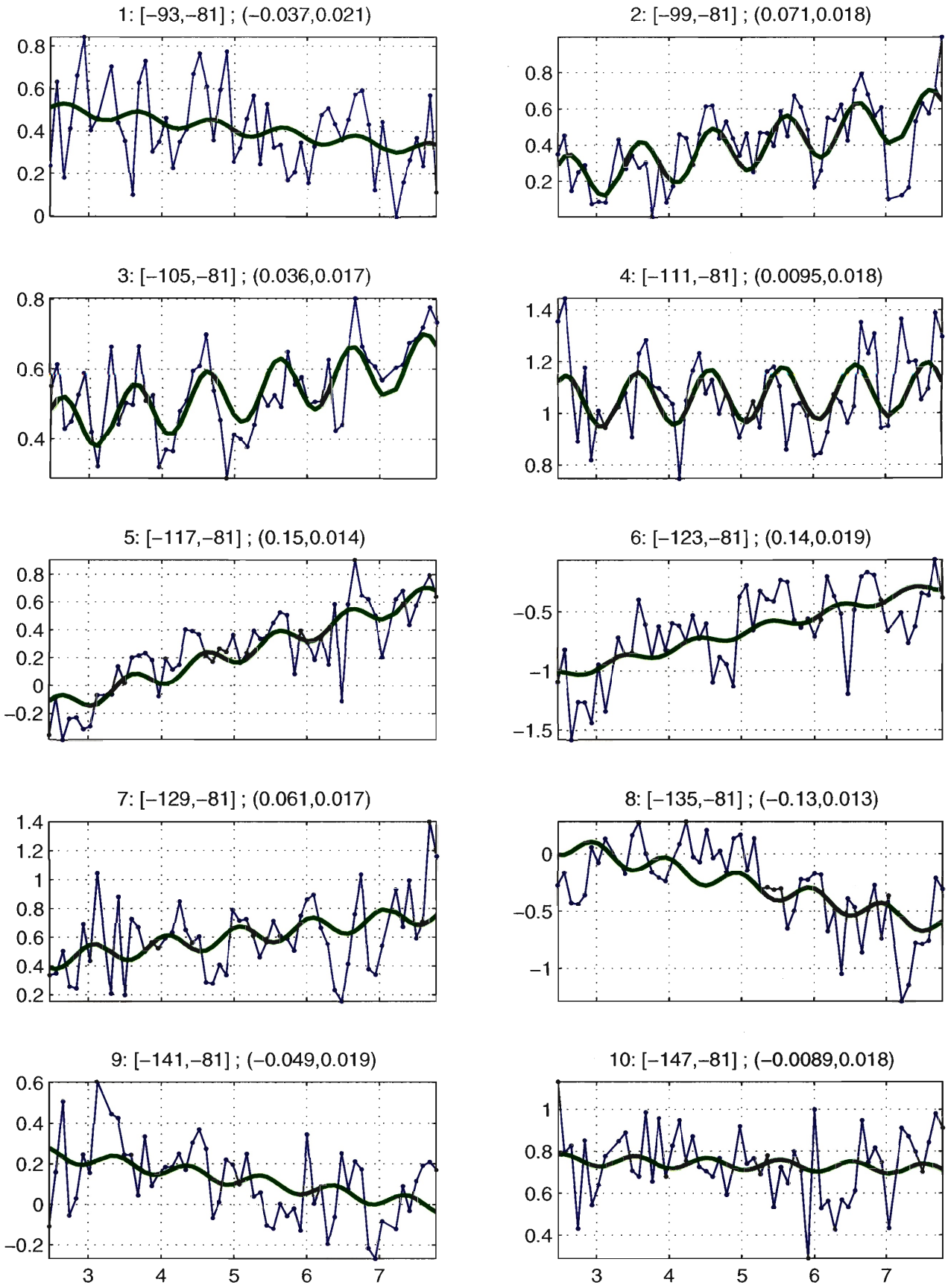
1: [−93,−81] ; (−0.037,0.021)
2: [−99,−81] ; (0.071,0.018)
3: [−105,−81] ; (0.036,0.017)
4: [−111,−81] ; (0.0095,0.018)
5: [−117,−81] ; (0.15,0.014)
6: [−123,−81] ; (0.14,0.019)
7: [−129,−81] ; (0.061,0.017)
8: [−135,−81] ; (−0.13,0.013)
9: [−141,−81] ; (−0.049,0.019)
10: [−147,−81] ; (−0.0089,0.018)

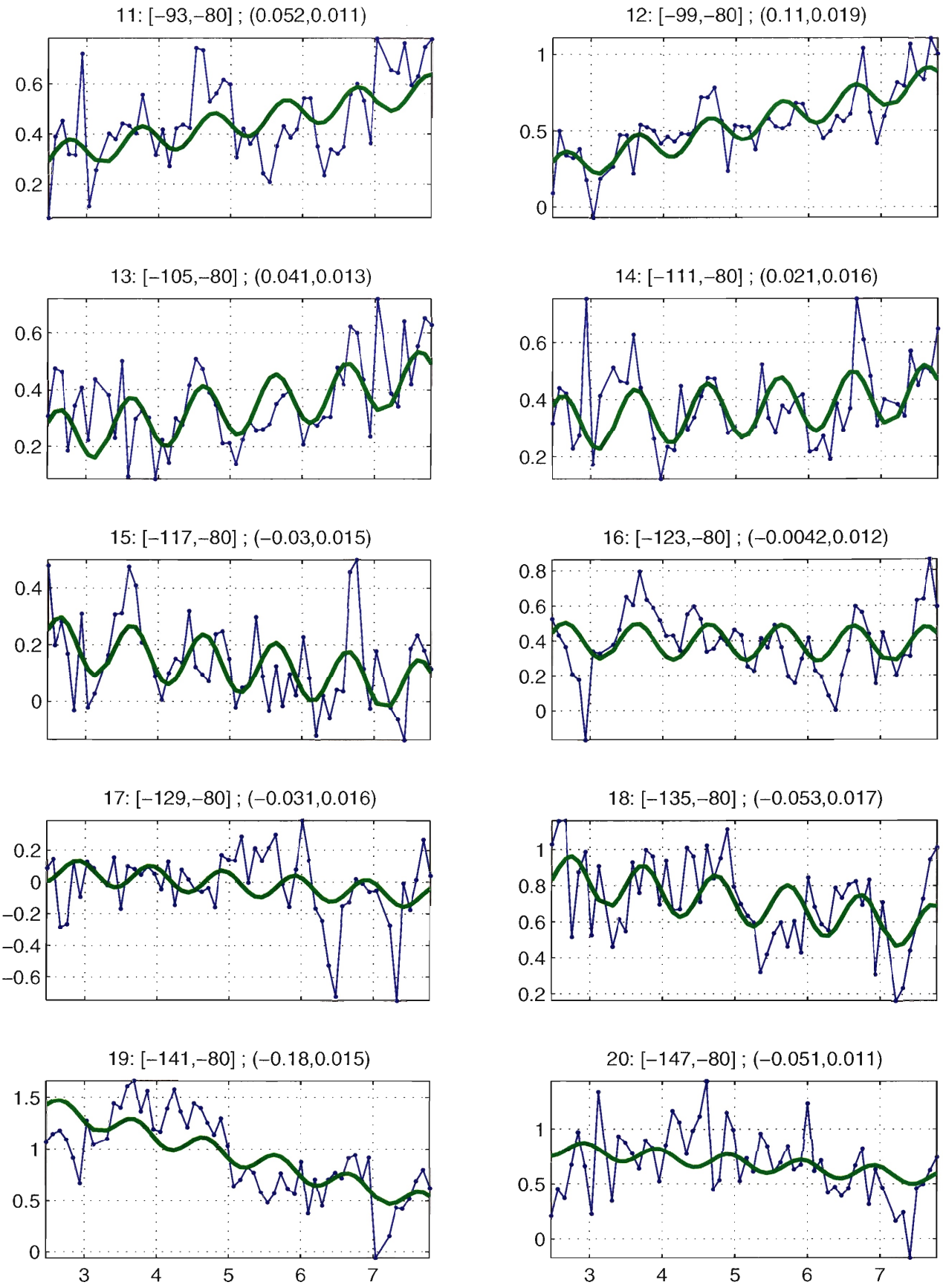
11: [−93,−80] ; (0.052,0.011)
12: [−99,−80] ; (0.11,0.019)
13: [−105,−80] ; (0.041,0.013)
14: [−111,−80] ; (0.021,0.016)
15: [−117,−80] ; (−0.03,0.015)
16: [−123,−80] ; (−0.0042,0.012)
17: [−129,−80] ; (−0.031,0.016)
18: [−135,−80] ; (−0.053,0.017)
19: [−141,−80] ; (−0.18,0.015)
20: [−147,−80] ; (−0.051,0.011)

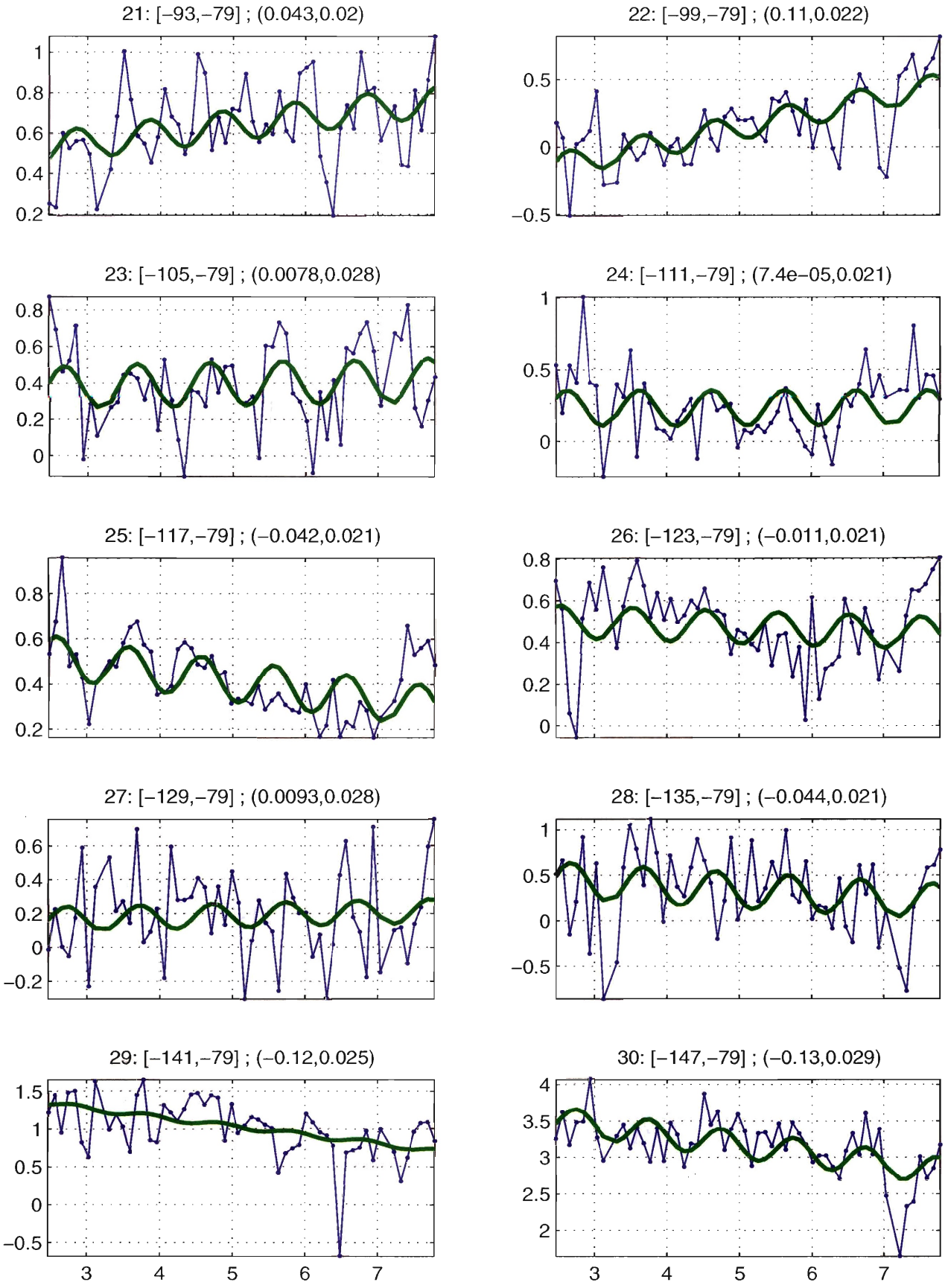
21: [−93,−79] ; (0.043,0.02)
22: [−99,−79] ; (0.11,0.022)
23: [−105,−79] ; (0.0078,0.028)
24: [−111,−79] ; (7.4e−05,0.021)
25: [−117,−79] ; (−0.042,0.021)
26: [−123,−79] ; (−0.011,0.021)
27: [−129,−79] ; (0.0093,0.028)
28: [−135,−79] ; (−0.044,0.021)
29: [−141,−79] ; (−0.12,0.025)
30: [−147,−79] ; (−0.13,0.029)

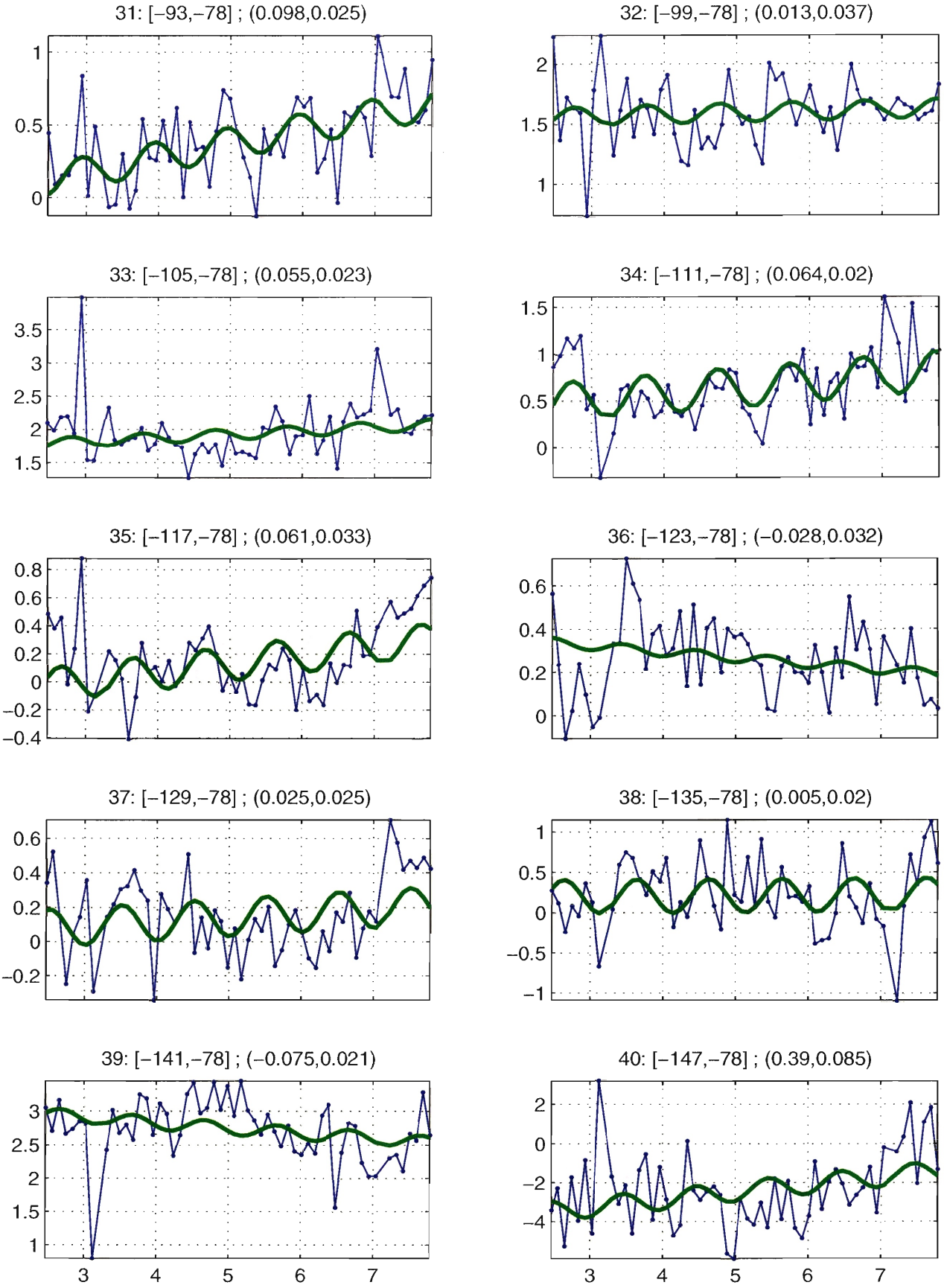
31: [−93,−78] ; (0.098,0.025)
32: [−99,−78] ; (0.013,0.037)
33: [−105,−78] ; (0.055,0.023)
34: [−111,−78] ; (0.064,0.02)
35: [−117,−78] ; (0.061,0.033)
36: [−123,−78] ; (−0.028,0.032)
37: [−129,−78] ; (0.025,0.025)
38: [−135,−78] ; (0.005,0.02)
39: [−141,−78] ; (−0.075,0.021)
40: [−147,−78] ; (0.39,0.085)

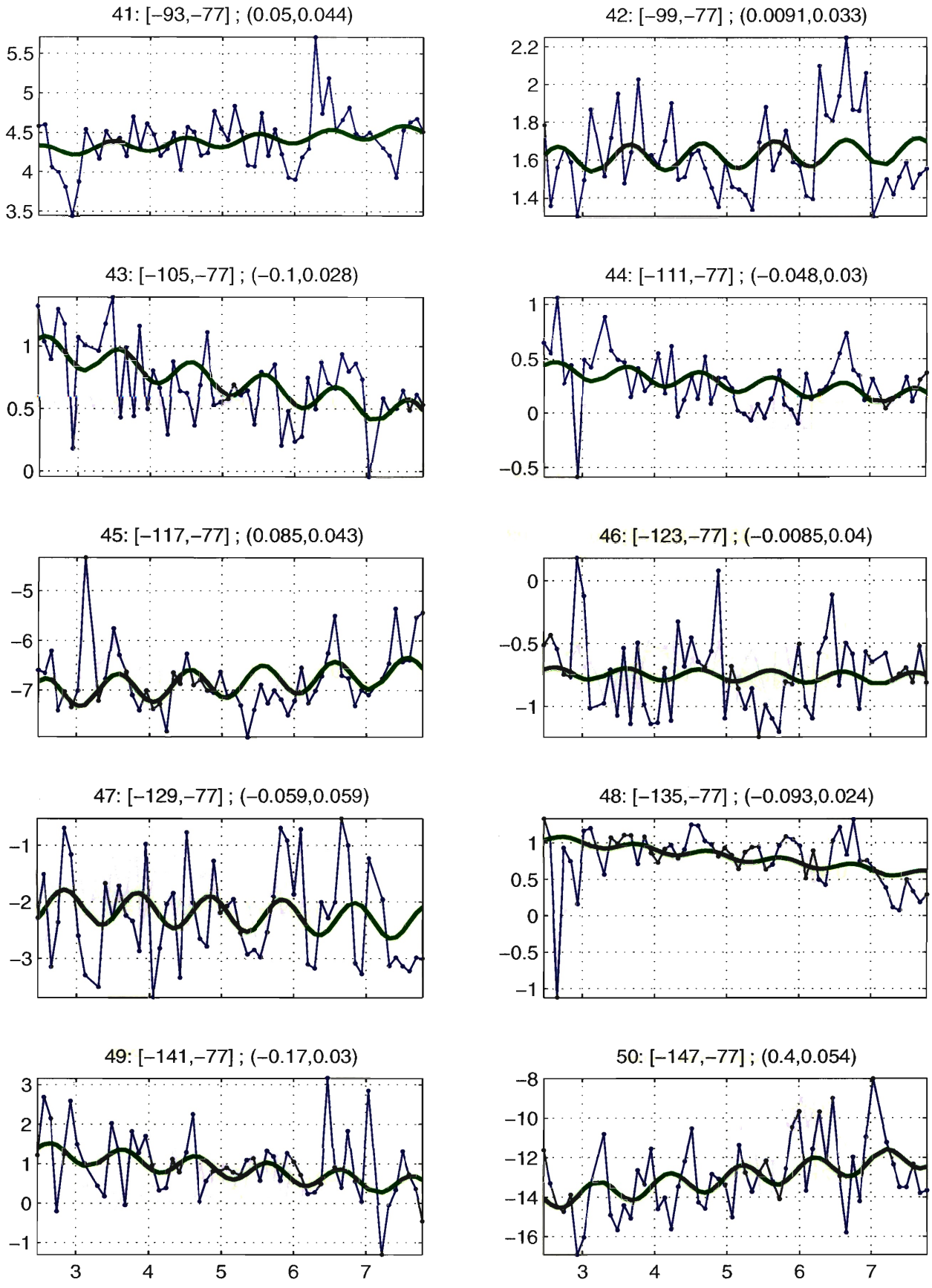
41: [−93,−77] ; (0.05,0.044)
42: [−99,−77] ; (0.0091,0.033)
43: [−105,−77] ; (−0.1,0.028)
44: [−111,−77] ; (−0.048,0.03)
45: [−117,−77] ; (0.085,0.043)
46: [−123,−77] ; (−0.0085,0.04)
47: [−129,−77] ; (−0.059,0.059)
48: [−135,−77] ; (−0.093,0.024)
49: [−141,−77] ; (−0.17,0.03)
50: [−147,−77] ; (0.4,0.054)

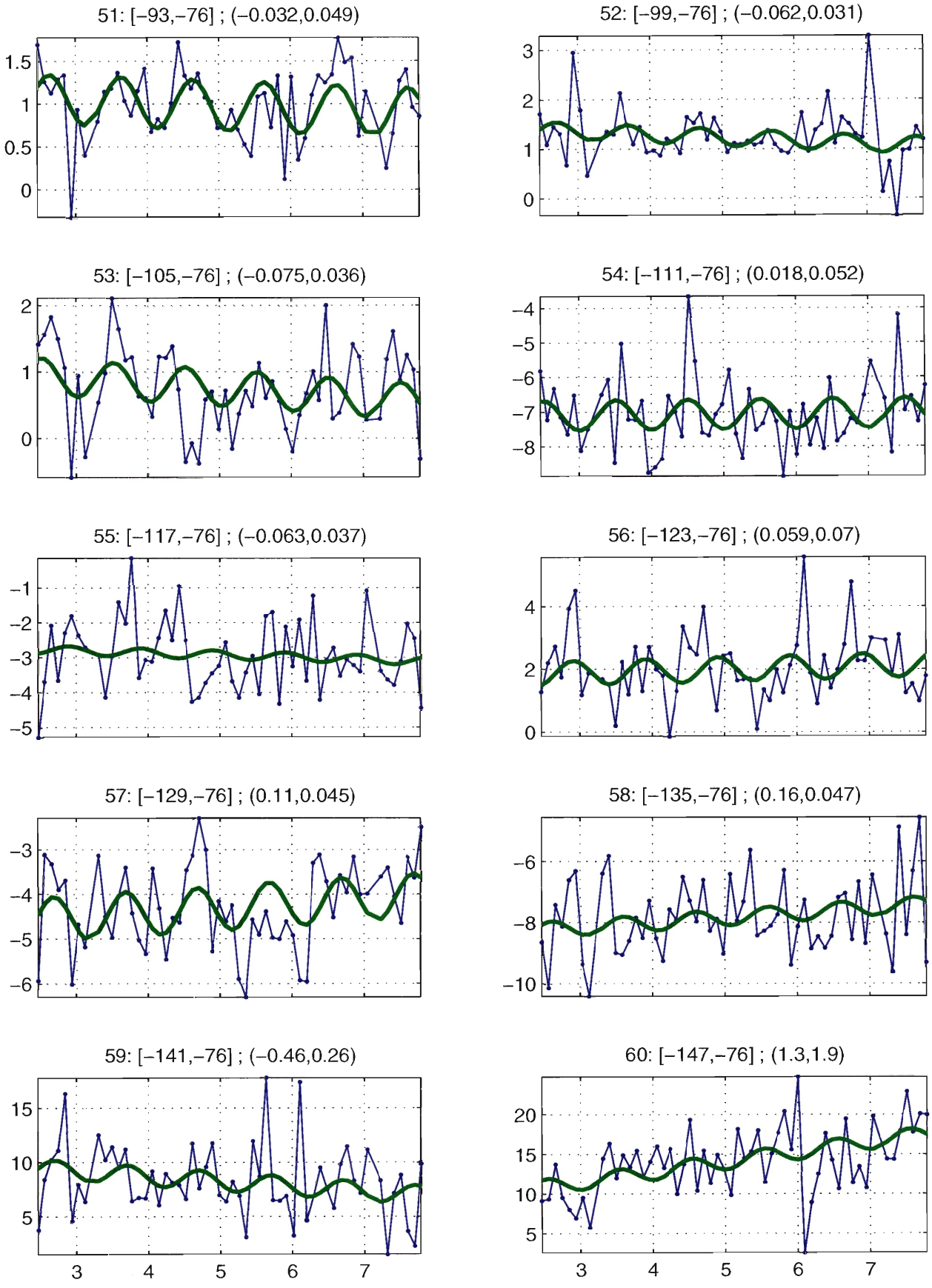
51: [−93,−76] ; (−0.032,0.049)
52: [−99,−76] ; (−0.062,0.031)
53: [−105,−76] ; (−0.075,0.036)
54: [−111,−76] ; (0.018,0.052)
55: [−117,−76] ; (−0.063,0.037)
56: [−123,−76] ; (0.059,0.07)
57: [−129,−76] ; (0.11,0.045)
58: [−135,−76] ; (0.16,0.047)
59: [−141,−76] ; (−0.46,0.26)
60: [−147,−76] ; (1.3,1.9)

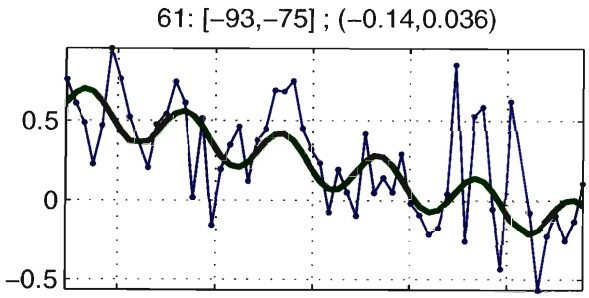
61: [−93,−75] ; (−0.14,0.036)
0.5
0
−0.5

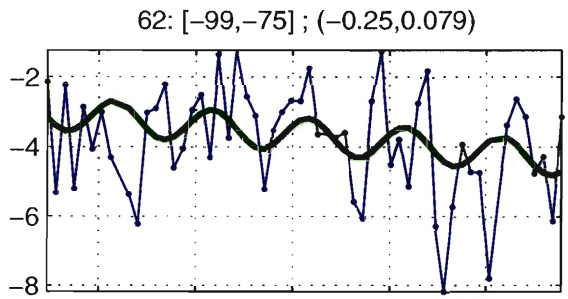
62: [−99,−75] ; (−0.25,0.079)
−2
−4
−6
−8

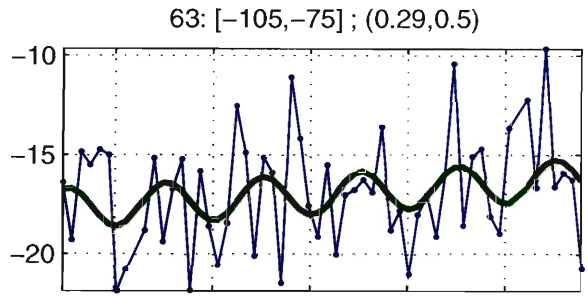
63: [−105,−75] ; (0.29,0.5)
−10
−15
−20

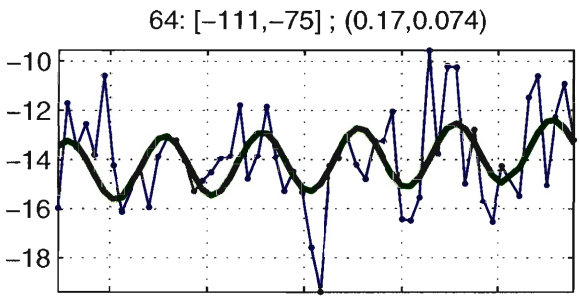
64: [−111,−75] ; (0.17,0.074)
−10
−12
−14
−16
−18

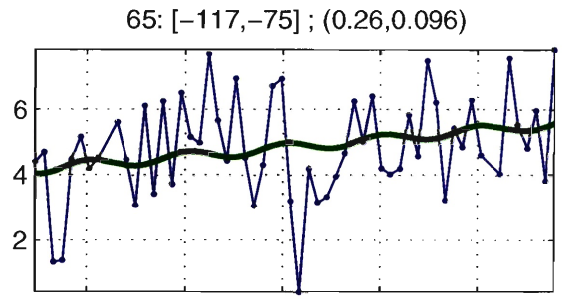
65: [−117,−75] ; (0.26,0.096)
6
4
2

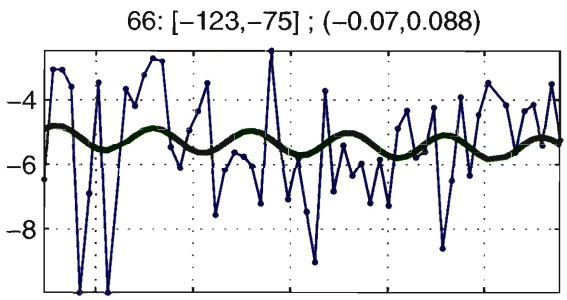
66: [−123,−75] ; (−0.07,0.088)
−4
−6
−8

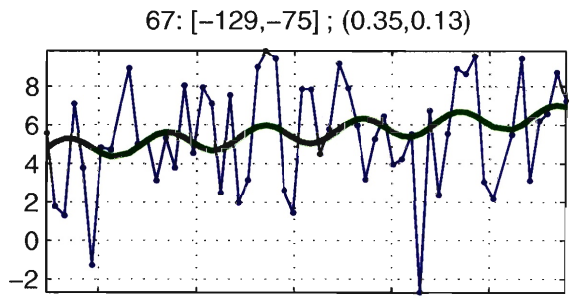
67: [−129,−75] ; (0.35,0.13)
8
6
4
2
0
−2

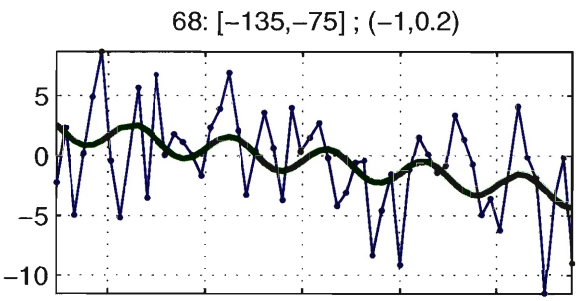
68: [−135,−75] ; (−1,0.2)
5
0
−5
−10

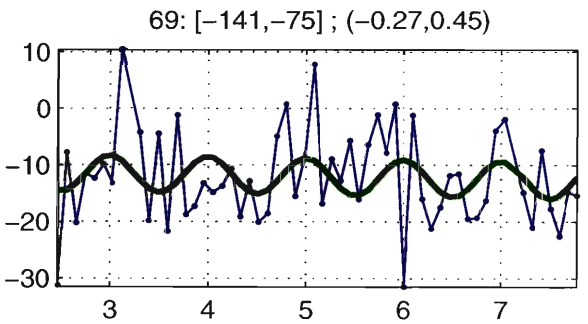
69: [−141,−75] ; (−0.27,0.45)
10
0
−10
−20
−30
3
4
5
6
7

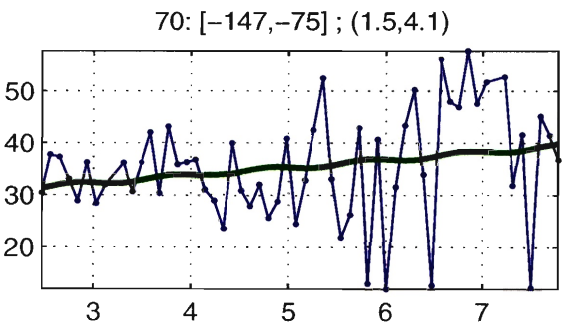
70: [−147,−75] ; (1.5,4.1)
50
40
30
20
3
4
5
6
7

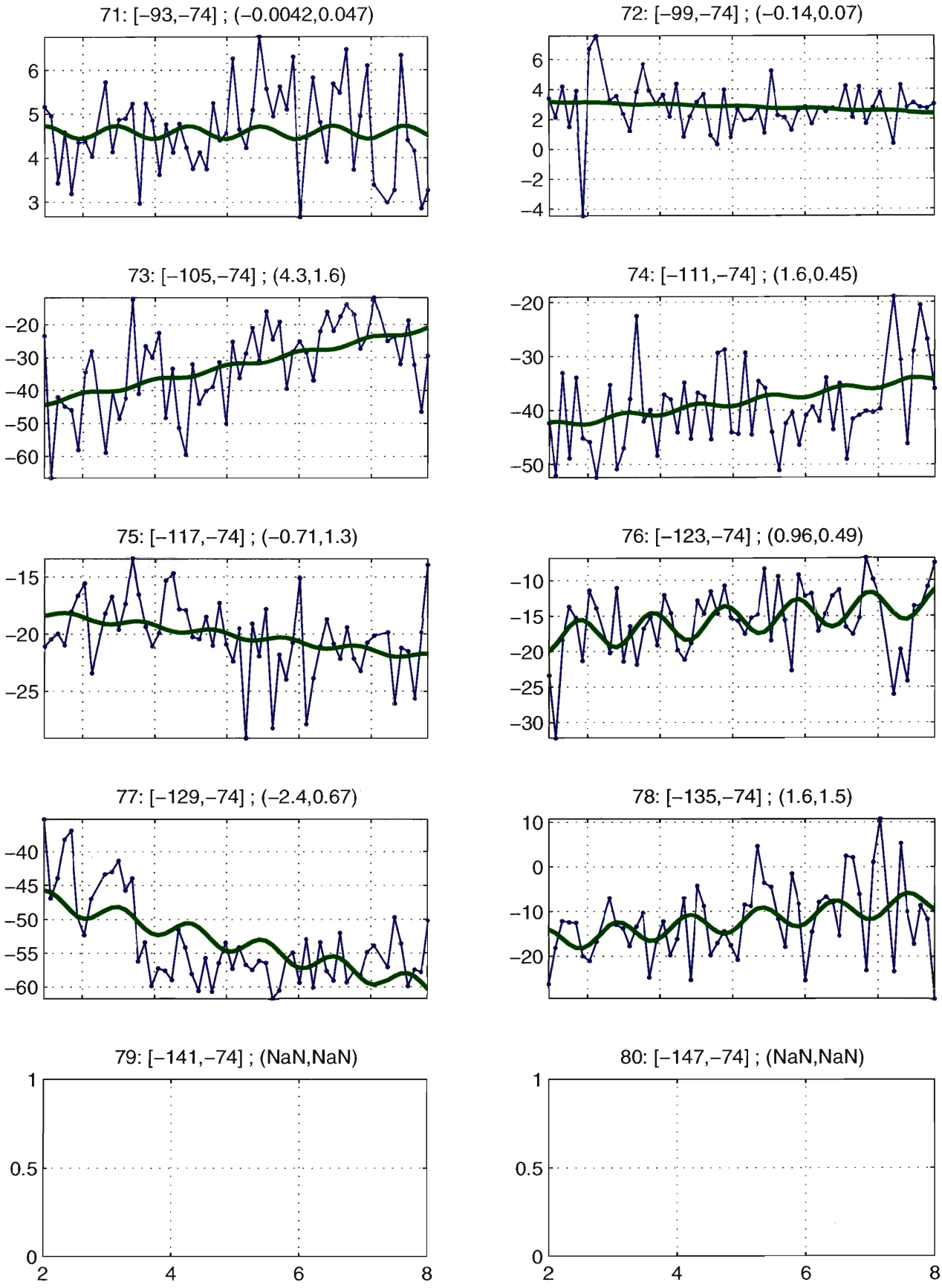
71: [−93,−74] ; (−0.0042,0.047)
72: [−99,−74] ; (−0.14,0.07)
73: [−105,−74] ; (4.3,1.6)
74: [−111,−74] ; (1.6,0.45)
75: [−117,−74] ; (−0.71,1.3)
76: [−123,−74] ; (0.96,0.49)
77: [−129,−74] ; (−2.4,0.67)
78: [−135,−74] ; (1.6,1.5)
79: [−141,−74] ; (NaN,NaN)
80: [−147,−74] ; (NaN,NaN)

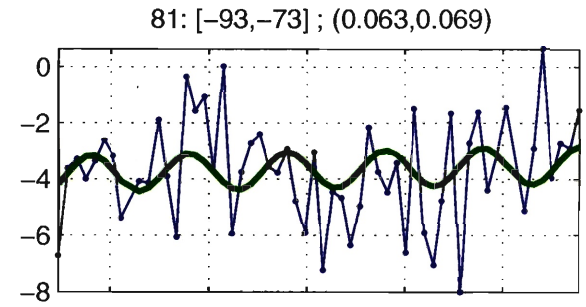
81: [−93,−73] ; (0.063,0.069)
0
−2
−4
−6
−8

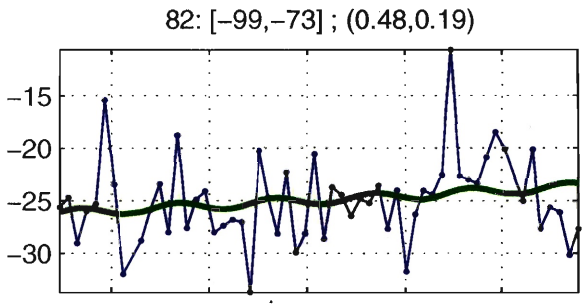
82: [−99,−73] ; (0.48,0.19)
−15
−20
−25
−30

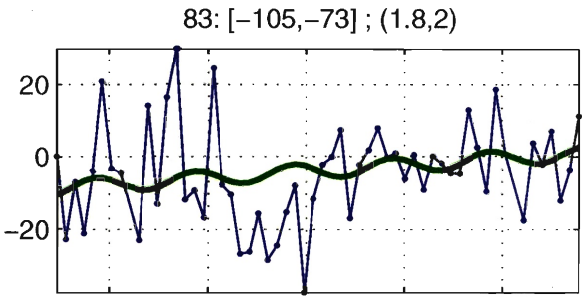
83: [−105,−73] ; (1.8,2)
20
0
−20

Table A.1: Block Kriging Results

lat^o	lon^o	dhdt (m/yr)	σ_{dhdt} (m/yr)	B (m)	σ_B (m)	θ (day)	σ_θ (day)
47.0	-81.0	0.019	0.011	0.034	0.018	404.7	69.6
41.0	-81.0	0.006	0.012	0.047	0.018	141.3	27.3
35.0	-81.0	0.027	0.018	0.081	0.010	155.2	17.5
29.0	-81.0	0.008	0.012	0.081	0.014	167.5	9.9
23.0	-81.0	-0.003	0.009	0.125	0.008	186.1	8.2
17.0	-81.0	0.007	0.015	0.139	0.009	177.5	9.5
11.0	-81.0	0.022	0.013	0.059	0.007	139.9	33.6
5.0	-81.0	0.020	0.009	0.097	0.018	159.7	13.7
1.0	-81.0	0.001	0.018	0.217	0.014	182.0	11.3
47.0	-80.0	0.035	0.008	0.023	0.005	426.8	69.4
41.0	-80.0	0.039	0.009	0.007	0.009	454.8	122.6
35.0	-80.0	0.008	0.012	0.062	0.011	152.7	31.6
29.0	-80.0	0.010	0.022	0.048	0.009	158.4	34.4
23.0	-80.0	0.022	0.021	0.080	0.009	156.4	15.9
17.0	-80.0	0.008	0.009	0.065	0.005	168.5	20.9
11.0	-80.0	0.015	0.009	0.109	0.012	168.9	13.1
5.0	-80.0	0.013	0.012	0.097	0.010	170.5	15.1
1.0	-80.0	0.013	0.011	0.157	0.008	176.0	4.2
47.0	-79.0	0.029	0.015	0.066	0.006	391.3	28.5
41.0	-79.0	0.026	0.012	0.044	0.014	423.7	31.0
35.0	-79.0	0.002	0.010	0.013	0.009	171.3	98.0
29.0	-79.0	0.000	0.021	0.044	0.017	182.4	34.0
23.0	-79.0	0.004	0.024	0.084	0.012	176.5	30.0
17.0	-79.0	-0.005	0.030	0.106	0.017	196.5	26.0
11.0	-79.0	0.011	0.014	0.092	0.009	172.7	22.9
5.0	-79.0	0.022	0.008	0.102	0.015	165.9	18.7
1.0	-79.0	0.017	0.020	0.091	0.012	170.7	22.7
47.0	-78.0	0.023	0.016	0.055	0.014	401.3	29.0
41.0	-78.0	0.021	0.017	0.059	0.008	387.1	40.5
35.0	-78.0	0.009	0.013	0.062	0.010	174.1	36.1
29.0	-78.0	0.041	0.015	0.068	0.010	145.9	26.4
23.0	-78.0	0.018	0.029	0.102	0.025	167.4	45.3
17.0	-78.0	-0.010	0.026	0.095	0.020	190.2	29.1
11.0	-78.0	0.017	0.021	0.147	0.016	173.9	18.2
5.0	-78.0	0.035	0.016	0.095	0.009	153.9	24.6
1.0	-78.0	-0.024	0.013	0.103	0.010	196.4	18.7
47.0	-77.0	0.039	0.016	0.050	0.014	452.1	47.2
41.0	-77.0	0.015	0.023	0.057	0.015	382.9	66.4
35.0	-77.0	0.016	0.017	0.032	0.009	393.3	65.0
29.0	-77.0	0.039	0.020	0.031	0.028	116.8	122.8
23.0	-77.0	0.020	0.014	0.100	0.019	162.9	21.0
17.0	-77.0	-0.017	0.022	0.063	0.025	204.0	50.2
11.0	-77.0	0.028	0.030	0.090	0.018	163.9	42.9
5.0	-77.0	0.037	0.032	0.167	0.013	167.8	26.1
1.0	-77.0	0.017	0.018	0.192	0.019	174.2	8.2
47.0	-76.0	0.021	0.028	0.017	0.015	112.6	127.2
41.0	-76.0	0.018	0.030	0.041	0.023	137.5	63.4
35.0	-76.0	0.038	0.029	0.049	0.018	129.1	37.5
29.0	-76.0	0.058	0.033	0.038	0.030	425.1	107.3
23.0	-76.0	0.069	0.015	0.016	0.014	448.1	220.7
17.0	-76.0	0.059	0.015	0.057	0.026	113.4	33.9
11.0	-76.0	-0.013	0.040	0.097	0.017	203.7	40.9
5.0	-76.0	-0.028	0.025	0.106	0.024	211.3	33.6
1.0	-76.0	0.029	0.031	0.131	0.031	165.2	75.6
47.0	-75.0	0.022	0.037	0.037	0.012	144.3	83.7
41.0	-75.0	0.004	0.035	0.100	0.014	180.1	21.4
35.0	-75.0	0.011	0.041	0.096	0.026	174.9	49.0
29.0	-75.0	-0.024	0.028	0.052	0.015	286.8	91.0
23.0	-75.0	0.050	0.022	0.058	0.020	130.5	44.4
17.0	-75.0	0.095	0.026	0.044	0.016	452.4	66.9
11.0	-75.0	0.031	0.038	0.037	0.029	430.3	146.8
5.0	-75.0	0.040	0.032	0.133	0.022	395.5	21.4
1.0	-75.0	0.040	0.039	0.102	0.034	442.0	26.9
47.0	-74.0	0.030	0.041	0.038	0.011	142.6	92.7

41.0	-74.0	0.003	0.033	0.085	0.020	180.1	45.6
35.0	-74.0	0.006	0.041	0.187	0.034	180.7	30.3
29.0	-74.0	0.015	0.037	0.311	0.024	178.2	9.1
23.0	-74.0	-0.012	0.021	0.130	0.013	188.3	42.3
17.0	-74.0	0.037	0.033	0.124	0.015	165.6	22.1
11.0	-74.0	0.053	0.026	0.089	0.023	126.8	30.6
5.0	-74.0	0.046	0.051	0.121	0.029	125.7	45.2
1.0	-74.0	0.075	0.036	0.304	0.022	446.5	13.7
47.0	-73.0	0.042	0.041	0.101	0.018	156.3	30.8
41.0	-73.0	0.132	0.039	0.087	0.018	121.8	64.9
35.0	-73.0	0.005	0.038	0.052	0.018	372.8	68.2
29.0	-73.0	-0.024	0.030	0.161	0.024	193.7	39.1
23.0	-73.0	0.068	0.032	0.065	0.025	120.8	47.1
17.0	-73.0	0.031	0.025	0.241	0.024	171.0	15.3
11.0	-73.0	0.084	0.028	0.142	0.017	148.9	27.5
5.0	-73.0	0.132	0.039	0.081	0.028	121.5	60.5
1.0	-73.0	-0.686	0.080	0.835	0.035	325.2	10.1
87.0	-81.0	0.065	0.024	0.046	0.011	448.9	53.8
81.0	-81.0	0.067	0.026	0.084	0.011	454.1	24.2
75.0	-81.0	0.067	0.027	0.073	0.024	463.0	43.4
69.0	-81.0	0.057	0.023	0.051	0.018	417.5	75.2
63.0	-81.0	0.035	0.021	0.061	0.017	397.0	49.9
57.0	-81.0	0.025	0.015	0.053	0.009	393.6	34.8
52.0	-81.0	0.040	0.012	0.052	0.013	418.7	44.8
87.0	-80.0	0.053	0.023	0.063	0.018	452.9	55.7
81.0	-80.0	0.032	0.014	0.049	0.011	422.1	46.3
75.0	-80.0	0.011	0.018	0.075	0.014	163.6	16.5
69.0	-80.0	0.023	0.018	0.026	0.013	460.2	47.7
63.0	-80.0	0.026	0.020	0.030	0.012	110.0	54.3
57.0	-80.0	0.029	0.015	0.026	0.005	414.9	102.6
52.0	-80.0	0.041	0.019	0.058	0.012	401.8	46.3
87.0	-79.0	0.019	0.021	0.036	0.009	396.2	82.2
81.0	-79.0	0.018	0.018	0.160	0.017	175.2	24.6
75.0	-79.0	-0.004	0.026	0.142	0.017	184.3	15.7
69.0	-79.0	0.006	0.032	0.070	0.015	177.1	32.5
63.0	-79.0	-0.016	0.032	0.110	0.013	195.6	27.2
57.0	-79.0	0.022	0.021	0.024	0.025	444.5	109.8
52.0	-79.0	0.020	0.025	0.072	0.018	385.5	52.2
87.0	-78.0	0.028	0.040	0.065	0.018	389.1	65.8
81.0	-78.0	0.026	0.033	0.219	0.014	172.3	9.0
75.0	-78.0	0.028	0.029	0.286	0.016	176.0	8.9
69.0	-78.0	0.038	0.028	0.152	0.021	164.1	16.3
63.0	-78.0	0.037	0.034	0.156	0.026	158.1	22.3
57.0	-78.0	0.054	0.030	0.055	0.022	110.1	46.6
52.0	-78.0	0.028	0.030	0.014	0.022	432.2	247.1
87.0	-77.0	0.008	0.035	0.044	0.016	375.2	129.9
81.0	-77.0	0.075	0.053	0.197	0.013	155.7	19.2
75.0	-77.0	0.066	0.026	0.161	0.016	155.0	15.9
69.0	-77.0	0.044	0.024	0.236	0.034	169.2	15.7
63.0	-77.0	0.061	0.038	0.075	0.030	126.0	44.1
57.0	-77.0	0.021	0.049	0.066	0.020	160.8	51.8
52.0	-77.0	0.075	0.036	0.096	0.021	131.8	48.3
87.0	-76.0	0.053	0.050	0.021	0.027	456.3	205.1
81.0	-76.0	0.040	0.044	0.186	0.029	167.1	13.6
75.0	-76.0	0.096	0.050	0.151	0.019	142.9	30.9
69.0	-76.0	0.105	0.026	0.365	0.031	161.3	11.1
63.0	-76.0	0.007	0.047	0.212	0.026	176.2	16.7
57.0	-76.0	0.014	0.050	0.044	0.025	444.2	79.3
52.0	-76.0	0.020	0.045	0.126	0.022	165.6	30.8
87.0	-75.0	0.028	0.061	0.050	0.025	152.4	63.5
81.0	-75.0	0.094	0.037	0.208	0.024	144.4	16.5
75.0	-75.0	-0.015	0.046	0.365	0.038	185.8	10.3
69.0	-75.0	0.066	0.043	0.481	0.023	172.8	8.2
63.0	-75.0	-0.006	0.038	0.408	0.026	184.3	6.7
57.0	-75.0	0.015	0.056	0.141	0.026	173.3	21.6
52.0	-75.0	0.015	0.057	0.047	0.028	384.4	80.7
87.0	-74.0	0.093	0.062	0.101	0.022	108.2	43.5
81.0	-74.0	0.101	0.044	0.127	0.024	137.5	29.9

75.0	-74.0	-0.029	0.059	0.155	0.050	195.1	30.3
69.0	-74.0	0.110	0.081	0.367	0.035	147.2	12.2
63.0	-74.0	0.061	0.052	0.218	0.030	164.8	23.3
57.0	-74.0	0.024	0.052	0.218	0.030	175.6	23.9
52.0	-74.0	0.096	0.049	0.194	0.035	124.8	19.7
87.0	-73.0	0.061	0.034	0.146	0.031	152.9	24.9
81.0	-73.0	0.134	0.051	0.293	0.051	144.7	16.0
75.0	-73.0	-0.052	0.034	0.344	0.040	199.3	15.1
69.0	-73.0	0.245	0.100	0.746	0.033	158.5	10.2
63.0	-73.0	0.168	0.073	0.634	0.038	167.0	7.8
57.0	-73.0	-0.031	0.041	0.376	0.032	187.7	22.8
52.0	-73.0	0.004	0.067	0.058	0.041	375.7	80.5
137.0	-81.0	0.010	0.012	0.064	0.008	412.6	20.7
131.0	-81.0	0.021	0.008	0.099	0.010	429.8	20.9
125.0	-81.0	0.033	0.012	0.062	0.008	435.4	38.7
119.0	-81.0	0.032	0.013	0.047	0.010	437.1	26.9
113.0	-81.0	0.032	0.009	0.057	0.008	118.2	22.0
107.0	-81.0	0.034	0.010	0.068	0.012	138.8	13.3
102.0	-81.0	0.029	0.009	0.050	0.009	456.3	34.6
137.0	-80.0	0.037	0.009	0.084	0.007	131.5	7.4
131.0	-80.0	0.013	0.011	0.082	0.007	149.7	5.6
125.0	-80.0	0.037	0.010	0.076	0.007	112.9	8.7
119.0	-80.0	0.013	0.010	0.081	0.004	377.9	13.7
113.0	-80.0	0.012	0.007	0.049	0.005	383.7	35.0
107.0	-80.0	0.018	0.007	0.047	0.008	132.1	14.2
102.0	-80.0	0.037	0.011	0.045	0.007	101.6	33.2
137.0	-79.0	0.029	0.015	0.088	0.008	149.4	12.9
131.0	-79.0	0.013	0.011	0.050	0.012	398.8	26.3
125.0	-79.0	0.024	0.014	0.060	0.009	421.3	27.1
119.0	-79.0	-0.001	0.009	0.057	0.010	361.3	27.9
113.0	-79.0	0.013	0.012	0.048	0.007	390.5	26.9
107.0	-79.0	0.044	0.019	0.077	0.012	426.4	35.5
102.0	-79.0	0.039	0.023	0.079	0.014	400.0	33.8
137.0	-78.0	0.014	0.016	0.103	0.013	165.7	9.3
131.0	-78.0	0.009	0.010	0.052	0.006	416.2	22.7
125.0	-78.0	0.035	0.012	0.050	0.013	456.2	22.6
119.0	-78.0	0.014	0.014	0.041	0.011	428.5	41.2
113.0	-78.0	0.031	0.025	0.057	0.021	129.1	27.4
107.0	-78.0	0.042	0.032	0.035	0.015	446.4	48.5
102.0	-78.0	0.039	0.025	0.137	0.027	398.4	16.5
137.0	-77.0	0.043	0.016	0.083	0.017	129.8	23.2
131.0	-77.0	0.045	0.014	0.080	0.012	126.4	35.8
125.0	-77.0	0.034	0.019	0.068	0.012	436.6	15.4
119.0	-77.0	0.021	0.025	0.048	0.016	108.0	41.2
113.0	-77.0	0.047	0.032	0.080	0.017	136.2	28.5
107.0	-77.0	0.023	0.035	0.052	0.012	114.2	55.4
102.0	-77.0	0.041	0.015	0.083	0.012	414.7	24.2
137.0	-76.0	0.054	0.025	0.117	0.017	102.3	23.1
131.0	-76.0	0.010	0.011	0.085	0.020	168.7	22.7
125.0	-76.0	0.023	0.020	0.062	0.012	405.5	27.1
119.0	-76.0	0.042	0.028	0.047	0.023	445.7	50.6
113.0	-76.0	0.033	0.047	0.043	0.021	107.8	109.5
107.0	-76.0	0.063	0.026	0.089	0.016	102.7	28.1
102.0	-76.0	0.002	0.013	0.038	0.010	383.9	61.9
137.0	-75.0	0.061	0.021	0.114	0.019	108.4	22.6
131.0	-75.0	0.038	0.022	0.092	0.013	437.7	23.7
125.0	-75.0	0.027	0.028	0.070	0.026	440.7	24.7
119.0	-75.0	0.021	0.029	0.051	0.018	394.5	45.5
113.0	-75.0	0.066	0.026	0.071	0.030	418.8	44.6
107.0	-75.0	0.052	0.019	0.055	0.013	421.2	40.3
102.0	-75.0	0.046	0.022	0.084	0.011	400.9	46.5
137.0	-74.0	0.032	0.028	0.111	0.023	149.3	18.6
131.0	-74.0	0.038	0.025	0.016	0.010	433.8	226.7
125.0	-74.0	0.049	0.026	0.082	0.033	459.6	57.8
119.0	-74.0	0.050	0.025	0.085	0.015	110.6	42.1
113.0	-74.0	0.048	0.026	0.080	0.016	122.5	47.5
107.0	-74.0	0.054	0.023	0.039	0.011	424.9	97.5
102.0	-74.0	0.089	0.025	0.110	0.017	435.7	25.4

137.0	-73.0	0.021	0.020	0.109	0.018	167.7	26.0
131.0	-73.0	0.077	0.043	0.051	0.025	461.2	86.4
125.0	-73.0	0.050	0.033	0.051	0.018	437.6	110.0
119.0	-73.0	0.031	0.027	0.138	0.027	116.2	20.2
113.0	-73.0	0.035	0.031	0.145	0.014	140.3	12.6
107.0	-73.0	0.078	0.023	0.053	0.023	443.0	53.8
102.0	-73.0	0.067	0.038	0.055	0.022	425.1	100.7
137.0	-72.0	0.001	0.023	0.052	0.012	181.8	73.0
131.0	-72.0	0.028	0.039	0.084	0.021	137.4	48.8
125.0	-72.0	0.064	0.041	0.058	0.020	133.0	161.0
119.0	-72.0	0.018	0.025	0.271	0.033	135.6	11.5
113.0	-72.0	0.035	0.021	0.130	0.015	451.8	17.7
107.0	-72.0	0.091	0.034	0.094	0.029	125.1	39.8
102.0	-72.0	0.080	0.019	0.110	0.027	419.4	40.3
137.0	-71.0	-0.023	0.022	0.087	0.021	229.5	55.0
131.0	-71.0	-0.023	0.034	0.086	0.022	336.1	56.8
125.0	-71.0	0.028	0.042	0.118	0.026	160.0	61.0
119.0	-71.0	0.001	0.023	0.071	0.011	182.0	54.3
113.0	-71.0	0.004	0.032	0.055	0.017	176.8	46.8
107.0	-71.0	-0.021	0.027	0.153	0.018	191.3	28.9
102.0	-71.0	0.034	0.037	0.055	0.019	441.6	28.4
-93.0	-81.0	-0.037	0.021	0.030	0.010	235.8	101.1
-99.0	-81.0	0.071	0.018	0.132	0.017	141.3	16.6
-105.0	-81.0	0.036	0.017	0.081	0.016	147.9	16.6
-111.0	-81.0	0.009	0.018	0.104	0.013	170.8	29.3
-117.0	-81.0	0.155	0.014	0.073	0.012	105.3	22.3
-123.0	-81.0	0.143	0.019	0.044	0.010	443.5	75.6
-129.0	-81.0	0.061	0.017	0.071	0.021	430.9	38.5
-135.0	-81.0	-0.133	0.013	0.089	0.014	266.3	34.8
-141.0	-81.0	-0.049	0.019	0.035	0.007	301.1	62.5
-147.0	-81.0	-0.009	0.018	0.027	0.018	238.9	63.5
-93.0	-80.0	0.052	0.011	0.059	0.008	140.5	39.6
-99.0	-80.0	0.111	0.019	0.099	0.010	125.0	12.6
-105.0	-80.0	0.041	0.013	0.096	0.011	148.9	10.5
-111.0	-80.0	0.021	0.016	0.099	0.009	162.6	13.8
-117.0	-80.0	-0.030	0.015	0.096	0.013	205.9	18.1
-123.0	-80.0	-0.004	0.012	0.102	0.010	185.7	10.9
-129.0	-80.0	-0.031	0.016	0.076	0.008	219.3	15.7
-135.0	-80.0	-0.053	0.017	0.128	0.009	205.7	13.4
-141.0	-80.0	-0.176	0.015	0.102	0.009	246.0	17.5
-147.0	-80.0	-0.051	0.011	0.072	0.010	243.1	24.0
-93.0	-79.0	0.043	0.020	0.077	0.007	149.1	23.7
-99.0	-79.0	0.112	0.022	0.093	0.016	125.7	35.6
-105.0	-79.0	0.008	0.028	0.120	0.014	178.4	21.5
-111.0	-79.0	0.000	0.021	0.124	0.013	182.6	21.1
-117.0	-79.0	-0.042	0.021	0.093	0.010	228.9	16.8
-123.0	-79.0	-0.011	0.021	0.079	0.022	218.9	22.8
-129.0	-79.0	0.009	0.028	0.071	0.010	175.0	42.4
-135.0	-79.0	-0.044	0.021	0.198	0.015	196.7	10.7
-141.0	-79.0	-0.118	0.025	0.031	0.007	260.8	61.4
-147.0	-79.0	-0.129	0.029	0.189	0.007	217.4	20.6
-93.0	-78.0	0.098	0.025	0.110	0.019	118.2	27.8
-99.0	-78.0	0.013	0.037	0.078	0.011	173.2	43.6
-105.0	-78.0	0.055	0.023	0.082	0.010	147.9	53.6
-111.0	-78.0	0.064	0.020	0.213	0.010	165.7	10.2
-117.0	-78.0	0.061	0.033	0.124	0.017	149.7	20.4
-123.0	-78.0	-0.028	0.032	0.021	0.020	284.4	82.4
-129.0	-78.0	0.025	0.025	0.110	0.017	109.1	25.1
-135.0	-78.0	0.005	0.020	0.209	0.019	180.8	11.4
-141.0	-78.0	-0.075	0.021	0.095	0.015	224.8	32.7
-147.0	-78.0	0.388	0.085	0.515	0.039	434.6	17.6
-93.0	-77.0	0.050	0.044	0.072	0.022	449.4	58.0
-99.0	-77.0	0.009	0.033	0.070	0.023	173.7	39.0
-105.0	-77.0	-0.101	0.028	0.109	0.015	242.3	17.9
-111.0	-77.0	-0.048	0.030	0.079	0.025	222.9	37.6
-117.0	-77.0	0.085	0.043	0.304	0.031	145.5	13.9
-123.0	-77.0	-0.008	0.040	0.046	0.027	197.7	44.3
-129.0	-77.0	-0.059	0.059	0.301	0.021	196.1	15.9

-135.0	-77.0	-0.093	0.024	0.055	0.011	243.0	76.5
-141.0	-77.0	-0.167	0.030	0.252	0.024	222.2	13.8
-147.0	-77.0	0.397	0.054	0.588	0.056	400.7	10.6
-93.0	-76.0	-0.032	0.049	0.292	0.036	191.5	11.9
-99.0	-76.0	-0.062	0.031	0.174	0.023	203.5	35.6
-105.0	-76.0	-0.075	0.036	0.276	0.017	251.3	12.1
-111.0	-76.0	0.018	0.052	0.439	0.049	140.2	10.0
-117.0	-76.0	-0.063	0.037	0.124	0.038	225.1	50.9
-123.0	-76.0	0.059	0.070	0.390	0.026	167.0	17.4
-129.0	-76.0	0.106	0.045	0.505	0.024	169.2	9.1
-135.0	-76.0	0.159	0.047	0.266	0.054	135.9	26.0
-93.0	-75.0	-0.140	0.036	0.141	0.030	230.3	45.1
-99.0	-75.0	-0.253	0.079	0.498	0.038	334.5	15.4
-111.0	-75.0	0.175	0.074	1.252	0.062	161.6	7.9
-117.0	-75.0	0.265	0.096	0.147	0.042	453.0	39.4
-123.0	-75.0	-0.070	0.088	0.374	0.033	201.0	13.8
-129.0	-75.0	0.347	0.129	0.570	0.086	148.2	22.0
-135.0	-75.0	-1.030	0.196	1.150	0.070	322.7	24.7
-93.0	-74.0	-0.004	0.047	0.146	0.030	358.3	61.5
-99.0	-74.0	-0.144	0.070	0.050	0.037	290.5	146.1
-93.0	-73.0	0.063	0.069	0.664	0.064	176.8	13.1
-99.0	-73.0	0.478	0.189	0.414	0.087	129.5	45.6

Bibliography

W. Abdalati, I. Allison, F. Carsey, G. Casassa, M. Fily, M. Frezzotti, H.A. Fricker, C. Genthon, I. Goodwin, Z. Guo, G.S. Hamilton, R.C.A. Hindmarsh, C.L. Hulbe, T.H. Jacka, K.C. Jezek, R. Kwok, J. Li, U. Nixdorf, G. Paltridge, E. Rignot, C. Ritz, K. Satow, T.A. Scambos, C. Shuman, P. Skvarca, S. Takahashi, R.S.W. van de Wal, D.G. Vaughan, W.L. Wang, R.C. Warner, D.J. Wingham, N.W. Young, and H.J. Zwally. Recommendations for the collection and synthesis of antarctic ice sheet mass balance data. *Global and Planetary Change*, 42:1–15, 2004. The ISMASS Committee.

W. Abdalati, W. krabill, E. Frederick, S. Manizade, C. Martin, J. Sonntag, R. Swift, R. Thomas, W. Wright, and J. Yungel. Airborn laser altimetry mapping of the greenland ice sheet: Application to mass balance assessment. *J. of Geodynamics*, 34:391–403, 2002.

W. Abdalati and K. Steffen. Greenland ice sheet melt extent: 1979-1999. *J. Geophys. Res.*, 106(D24):33983–33988, December 2001.

J B Abshire, X Sun, H Riris, M Sirota, J McGarry, S Palm, D Yi, and P Liiva. Geoscience laser altimeter system (glas) on the icesat mission: On-orbit measurement performance. *Geophys. Res. Letts.*, 2005. in press.

O Aharonson, M T Zuber, D E Smith, G A Neumann, W C Feldman, and T H Prettyman. Depth, distribution, and density of co2 deposition on mars. *J. Geophys. Res.*, 109(E5):10.1029/2003JE002223, May 2004.

R.J. Arthern, D. J. Wingham, and A. L. Ridout. Controls on ers altimeter measurements over ice sheets: Footprint-scale topography, backscatter fluctuations, and the dependence of microwave penetration depth on satellite orientation. *J. Geophys. Res.*, 106(D24):33471–33484, December 2001.

S. Bae and B. E. Schutz. Precision attitude determination (pad). Geoscience Laser Altimeter System (GLAS) Algorithm Theoretical Basis Document, version 2.2, October 2002.

J L. Bamber, R L Layberry, and S P Gogenini. A new ice thickness and bed data set for the greenland ice sheet 1: Measurement, data reduction, and errors. *J. Geophys. Res.*, 106(D4):33773–33780, 2001a.

J.L. Bamber and R. A. Bindschadler. An improved elevation dataset for climate and ice-sheet modelling: validation with satellite imagery. *Annals of Glaciology*, 25: 438–444, 1997.

J.L. Bamber, R L Layberry, and S P Gogenini. A new ice thickness and bed data set for the greenland ice sheet 2: Relationship between dynamics and basal topography. *J. Geophys. Res.*, 106(D4):33781–33788, 2001b.

A.C. Brenner, R. A. Bindschadler, R. H. Thomas, and H. J. Zwally. Slope-induced errors in radar altimetry over continental ice sheets. *J. Geophys. Res.*, 88(C3): 1617–1623, February 1983.

A.C. Brenner, H.J. Zwally, C. R. Bentley, B.M. Csatho, D.J. Harding, M.A. Hofton, J-B Minster, LeeAnne Roberts, J.L. Saba, R.H. Thomas, and D. Yi. Derivation of range and range distributions from laser pulse waveform analysis for surface elevations, roughness, slope, and vegetation heights. Geoscience Laser Altimeter System (GLAS) Algorithm Theoretical Basis Document, version 4.1, September 2003.

R.G. Brown and P.Y.C. Hwang. *Introduction to Random Signals and Applied Kalman Filtering.* John Wiley & Sons, Inc, New York, 3rd edition, 1997. 484p.

J.L. Bufton. Laser altimetry measurements from aircraft and spacecraft. *Proceedings of the IEEE*, 77:463–477, 1989.

J.L. Bufton, J. E. Robinson, M.D. Femiano, and F.S. Flatow. Satellite laser altimeter for measurement of ice sheet topography. *EEE Trans. Geosci. Remote Sensing*, 20 (4):544–549, October 1982.

J.A. Church, J.M. Gregory, P. Huybrechts, M. Kuhn, K. Lambeck, M.T. Nhuan, D. Qin, and P.L. Woodworth. *Changes in Sea Level*, chapter 11, pages 639–693. Cambridge University Press, 2001. in Climate Change 2001 The Scientific Basis, Ed. by Houghton et al.

C. V. Deutsch and André G. Journel. *GSLIB Geostatistical Software Library and User's Guide.* Applied Geostatistics. Oxford University Press, New York, New York, second edition, 1998. 369p.

J. P. DiMarzio, H. J. Zwally, and A. C. Brenner. Comparisons of envisat and ers radar altimetry and icesat laser altimetry for ice-sheet elevation change studies. Presentation at ESA ENVISAT Symposium in Salzburg, Austria, September 2004.

B.C. Douglas. Global sea rise: A redetermination. *Surveys in Geophysics*, 18:279–292, 1997.

M. R. Drinkwater, D. G. Long, and A. W. Bingham. Greenland snow accumulation estimates from satellite radar scatterometer data. *J. Geophys. Res.*, 106(D24): 33935–33950, December 2001.

D P Duda, J D Spinhirne, and E W Eloranta. Atmospheric multiple scattering effects on glas altimetry–part i: Calculations of single pulse bias. *IEEE Trans. Geosci. Rem. Sens.*, 39:92–101, 2001.

1995 EOS. *1995 MTPE EOS Reference Handbook.* NASA / Goddard Space Flight Center, 1995. 281p. Ed. by G Asrah and R Greenstone.

R.G. Fairbanks. A 17,000-year glacio-eustastic sea level record: influence of glacial melting rates on the younger dryas event and deep-ocean circulation. *Nature*, 342: 637–642, 1989.

R. Fifield. *International Research in the Antarctic*. Oxford University Press, New York, 1987. 146p.

M. Frezzotti, M Pourchet, O Flora, S Gandolfi, M Gay, S Urbini, C Vincent, S Becagli, R Gragnani, M Proposito, M Severi, R Traversi, R Udisti, and M Fily. New estimations of precipitation and surface sublimation in east antarctica from snow accumulation measurements. *Climate Dynamics*, 23:803–813, 2004.

H A Fricker, A Borsa, J-B Minster, C Carabajal, K Quinn, and B Bills. Assessment of icesat performance at salar de uyuni, bolivia. *Geophys. Res. Letts.*, 2005. in press.

Helen A. Fricker, Glenn Hyland, Richard Coleman, and Neal W. Young. Digital elevation models for the lambert glacier-amery ice shelf system, east antarctica, from ers-1 satellite radar altimetry. *J. of Glaciol.*, 46(155):553–560, June 2000.

M.B. Giovinetto and H. J. Zwally. Spatial distribution of net surface accumulation on the antarctic ice sheet. *Annals of Glaciology*, 31:178–183, April 2000.

GSFC-website, 2005. http://icesat4.gsfc.nasa.gov/.

D.J. Harding, J.L. Bufton, and J.J. Frawley. Satellite laser altimetry of terrestrial topography: Vertical accuracy as a function of surface slope, roughness, and cloud cover. *IEEE Transactions on Geoscience and Remote Sensing*, 32(2):329–339, March 1994.

T. A. Herring, 2005. per comm.

T.A. Herring and K. Quinn. Atmospheric delay correction to glas laser altimeter ranges. in Geoscience Laser Altimeter System: Algorithm Theoretical Basis Document, version 1.0, February 1999.

J. T. Houghton, B A Callander, and S K Varney. *The 1992 IPCC supplement: scientific assessment.* Cambridge University Press, 1992. in Climate Change 1992: The Supplementary Report to the IPCC Scientific Assessment.

P. Huybrechts, D. Steinhage, F. Wilhelms, and J. Bamber. Balance velocities and measured properties of the antarctic ice sheet from a new compilation of gridded data for modelling. *Annals of Glaciology*, 30:52–60, 2000.

IGARB. Independent glas anomaly review board executive summary. unpublished, November 2003.

S. S. Jacobs, H. H. Helmer, C. S. Doake, A. Jenkins, and R. M. Frolich. Melting of ice shelves and the mass balance of antarctica. *J. of Glaciology*, 38(130):375–387, 1992.

L Jun, 2005. per comm.

P. K. Kitanidis. *Introduction to Geostatistics: applications to hydrogeology.* Cambridge University Press, Cambridge, United Kingdom, jan 1997. 250p.

W. Krabill, W Abdalati, E Frederick, S Manizade, C Martin, J. Sonntag, R. Swift, R. Thomas, W. Wright, and J. Yungel. Greenland ice sheet: High-elevation balance and peripheral thinning. *Science*, 289:428–430, July 2000.

W. Krabill, E. Frederick, S. Manizade, C. Martin, J. Sonntag, R. Swift, R. Thomas, W. Wright, and J. Yungel. Rapid thinning of parts of the southern greenland ice sheet. *Science*, 283:1522–1524, March 1999.

G. Leysinger-Vieli, M J Siegert, and A P Payne. Reconstructing ice sheet accumulation rates at ridge b, east antarctica. *Annals of Glaciol.*, 39, 2004.

N. M. Van Lipzig, E. V. Meijgaard, and J. Oerlemans. The spatial and temporal variability of the surface mass balance in antarctica: Results from a regioanl atmospheric climate model. *Int. J. of Climatol.*, 22:1197–1217, 2002.

M.E. Lisano and B.E. Schutz. Arcsecond-level pointing calibration for icesat laser altimetry of ice sheets. *J. of Geodesy*, 75:99–108, 2001.

S. B. Luthcke, D. D. Rowlands, T. Williams, D. Harding, C. Carabajal, J. Sauber, and J. Bufton. Icesat calibration results from integrated residual analysis. Presentation at ICESat Science Team Meeting in Boulder, CO, October 2004.

S B Luthcke, D D Rowlands, T A Williams, and M Sirota. Calibration and reduction of icesat geolocation errors and the impact on ice sheet elevation change detection. *Geophys. Res. Letts.*, 2005. in press.

T.V. Martin, H. J. Zwally, A. C. Brenner, and R. A. Bindschadler. Analysis and retracking of continental ice sheet radar altimeter waveforms. *J. Geophys. Res.*, 88 (C3):1608–1616, February 1983.

P. S. Maybeck. *Stochastic models, estimation, and control*, volume 1. Academic Press, 1979. NNp.

R S. Nerem and G T Mitchum. *Observation of Sea Level Change from Satellite Altimetry*, volume 75 of *International geophysics series*, chapter 6, pages 121–163. San Diego: Academic Press, 2001a. in Sea Level Rise History and Consequences, Ed. by B C Douglas, M S Kearney, and S P Leatherman.

R S. Nerem and G T Mitchum. *Sea Level Change*, volume 69 of *International geophysics series*, chapter 8, pages 329–349. San Diego: Academic Press, 2001b. in Satellite Altimetry and Earth Sciences, Ed. by L. L. Fu and A. Cazenave.

R.S. Nerem, B.J. Haines, J. Hendricks, J. F. Minster, G.T. Mitchum, and W.B. White. Improved determination of global mean sea level variations using topex/poseidon altimeter data. *Geophys. Res. Lett.*, 24(11):1331–1334, June 1997.

A. Ohmura and N. Reeh. New precipitation and accumulation maps for greenland. *J. of Glaciology*, 37(125):140–148, 1991.

Ricardo A. Olea. *Geostatistics for Engineers and Earth Scientists.* Kluwer Academic Publishers, Norwell, Massachusetts, 1999. 303p.

R. Peltier. Ice age paleontopography. *Science*, 265:195–201, 1994.

H.J. Rim and B.E. Schutz. Precision orbit determination (pod). in Geoscience Laser Altimeter System: Algorithm Theoretical Basis Document, version 2.2, October 2002.

B Schutz, H J Zwally, C Shuman, D Hancock, and J P DiMarzio. Overview of the icesat mission. *Geophys. Res. Letts.*, 2005. in press.

B. E. Schutz. Glas team leader annual report. December 1995.

B. E. Schutz. *Spaceborne Laser Altimetry: 2001 and Beyond.* Norwegian Mapping Authority, Honefoss, Norway, 1998. Plag, H.P. (ed.) Book of Extended Abstracts, WEGENER-98.

B.E. Schutz. Laser footprint location (geolocation) and surface profiles. Geoscience Laser Altimeter System (GLAS) Algorithm Theoretical Basis Document, version 3.0, October 2002.

C A Shuman, H J Zwally, B Schutz, A C Brenner, J P DiMarzio, and V P Suchdeo. Ice sheet elevations from icesat–2003-2004. *Geophys. Res. Letts.*, 2005. in press.

D. E. Smith, M. T. Zuber, H. V. Frey, J. B. Garvin, J. W. Head, D. O. Muhleman, G. H. Pettengill, R. J. Phillips, S. C. Solomon, H. J. Zwally, W. B. Banerdt, T. C. Duxbury, M. P. Golombek, F. G. Lemoine, G. A. Newmann, D. D. Rowlands, O. Aharonson, P. G. Ford, A. B. Ivanov, C. L. Johnson, P. J. McGovern, J. B. Abshire, R. S. Afzal, and X. Sun. Mars orbiter laser altimeter (mola): Experiment summary after the first year of global mapping of mars. *J. Geophys. Res.*, 106 (E10):23689–23722, October 2001a.

D. E. Smith, M. T. Zuber, and G. A. Neumann. Seasonal variation of snow depth on mars. *Science*, 294(5549):2141–2146, December 2001b.

H.W. Sorenson. Least-squares estimation: from gauss to kalman. *IEEE Spectrum*, 7: 63–68, 1970.

J D Spinhirne. Glas science team meeting atmospheric group report. Presentation at ICESat Science Team Meeting in Boulder, CO on Oct 13-14 2005, October 2005.

X. Sun, 2005. per comm.

R. Thomas, T. Akins, B. Csatho, M. Fahnestock, P. Gogineni, C. Kim, and J. Sonntag. Mass balance of the greenland ice sheet at high elevations. *Science*, 289: 426–428, July 2000a.

R. Thomas, B. Csatho, S. Gogineni, K. C. Jezek, and K. Kuivinen. Thickening of the western part of the greenland ice sheet. *Science*, 289(5480):653–658, August 2000b.

J. Turner, W. M. Connolley, S. Leonard, G. J. Marshall, and D. G. Vaughan. Variability of net snow accumulation over the antarctic from ecmwf re-analysis project data. *Int. J. of Climatol.*, 19:697–724, 1999.

D. G. Vaughan, J. L. Bamber, M. Giovinetto, J. Russell, and A. P. R. Cooper. Reassessment of net surface mass balance in antarctica. *J. of Climate*, 12:933–946, April 1999.

I. Velicogna and J. Wahr. A method for separating antarctic postglacial rebound and ice mass balance using future icesat geoscience laser altimeter system, gravity recovery and climate experiment, and gps satellite data. *J. Geophys. Res.*, 107 (B10):2263–2273, October 2002.

D. J. Wingham, A. J. Ridout, R. Scharroo, R. J. Arthern, and C. K. Shum. Antarctica elevation change from 1992 to 1996. *Science*, 282:456–458, October 1998.

D. Yi, J-B. Minster, and C. Bentley. Ocean tidal loading corrections. Geoscience Laser Altimeter System (GLAS) Algorithm Theoretical Basis Document, version 1.0, February 1999.

C. Zelli. Envisat ra-2 advanced radar altimeter: Instrument design and pre-launch performance assessment review. *Acta Astronautica*, 44(7-12):323–333, 1999.

M.T. Zuber, D. E. Smith, S. C. Solomon, D. O. Muhleman, J. W. Head, J. B. Garvin, J. B. Abshire, and J. L. Bufton. The mars observer laser altimeter investigation. *J. Geophys. Res.*, 97(E5):7781–7797, May 1992.

H. J. Zwally, 2005. per comm.

H. J. Zwally and A. C. Brenner. *Ice Sheet Dynamics and Mass Balance*, volume 69 of *International geophysics series*, chapter 9, pages 351–369. San Diego: Academic Press, 2001. in Satellite Altimetry and Earth Sciences, Ed. by L. L. Fu and A. Cazenave.

H. J. Zwally, A C Brenner, H Cornejo, M Giovinetto, J Li, J L Saba, and D Yi. Ice-sheet mass balance from satellite radar altimetry. *Eos Trans. AGU*, 85(47), 2004. Fall Meet. Suppl., Abstract C32A-04.

H. J. Zwally, A. C. Brenner, J. A. Major, R. A. Bindschandler, and J. G. Marsh. Growth of greenland ice sheet: Measurement. *Science*, 246:1587–1589, December 1989.

H. J. Zwally and S. Fiegles. Extent and duration of antarctic surface melting. *J. of Glaciology*, 40(136):463–476, 1994.

H. J. Zwally and Li Jun. Seasonal and interannual variations of firn densification and ice-sheet surface elevation at the greenland summit. *J. of Glaciol.*, 48(161): 199–207, 2002.

H. J. Zwally, B. Schutz, W. Abdalati, J. Abshire, C. Bentley, A. Brenner, J. Bufton, J. Dezio, D. Hancock, D. Harding, T. Herring, B. Minster, K. Quinn, S. Palm, J. Spinhirne, and R. Thomas. Icesat's laser measurements of polar ice, atmosphere, ocean, and land. *J. of Geodynamics*, 34:405–445, 2002.

H. J. Zwally, R H Thomas, and R. A. Bindschadler. Ice-sheet dynamics by satellite laser altimetry. *IEEE proceedings of International Geosciences and Remote Sensing Symposium*, pages 1012–1022, June 1981.